Accretion-ejection mechanisms in the inner disk of T Tauri stars

A study with VLTI GRAVITY

INAUGURAL-DISSERTATION

zur
Erlangung des Doktorgrades
der Mathematisch-Naturwissenschaftlichen Fakultät
der Universität zu Köln

vorgelegt von

Jan Alexander Wojtczak
aus Bergisch Gladbach, Deutschland
Köln 2023

Berichterstatter: (Gutachter)	Prof. Dr. Lucas Labadie Prof. Dr. Stefanie Walch-Gassner
Tag der mündlichen Prüfung:	28. Mai 2024

Contents

Abstract

The study of accretion and ejection in low-mass young stellar objects (YSOs) has seen great advances over the past 20 years. Substantial improvements to instrumental techniques, from spectroscopy to polarimetry and interferometry, have helped to elevate our understanding of the interaction between the strong magnetic fields of T Tauri stars and their innermost disk environments to the point where observations are finally capable of putting some of the long-held paradigms of theoretical astrophysics to the test. Yet, it was only in recent years that a new generation of interferometric instruments has been able to finally spatially resolve these inner disk regions, where magnetised winds and magnetically driven accretion processes are thought to govern the evolution of pre-main sequence stars towards their transitional and eventual main sequence stage. GRAVITY, the near-infrared beam combiner of the Very Large Telescope Interferometer (VLTI) is, without question, currently the spearhead of these efforts. Profiting from an unparalleled combination of sub-mas (milliarcsecond) spatial resolution, high spectral resolution and increased sensitivity, it has unlocked access to interferometric observations of hydrogen emission lines, which trace these magnetic mechanisms in T Tauri stars, for a large number of potential targets.

The fundamental aim of the project described in this thesis was to explore how well spatially resolved observations of the inner regions of T Tauri stars would line up with the theoretical predictions of the magnetospheric accretion paradigm, and, if the model would fall short of the observed reality, how to reconcile potential deviations with our current understanding of these sources. To this end, interferometric data obtained for a sample of 7 T Tauri stars with VLTI GRAVITY was analysed. This data contains the K-band (2 to 2.4 micrometers) continuum emission originating from the hot dust of the inner disk, as well as the Brγ (Bracket-Gamma) hydrogen recombination line at 2.16612 micrometers. At the beginning of the project, this Brγ emission was - following the magnetospheric accretion paradigm - expected to be a direct tracer of the hot gas in the accretion columns close to the stellar surface. Consequently, the Brγ emission origin region should have been restricted to a spatially compact area close to the star, on the order of about 5 R_*. With this in mind, the Brγ spectra, interferometric visibilities and interferometric differential phases were used to spatially constrain the emission region, using GRAVITY's high resolution (R=4000) mode to derive spectrally dispersed characteristic sizes in 13 different spectral channels across the line profile. These sizes were compared against the co-

rotation radii of stars, which served as proxies for the actual magnetospheric truncation radius. Additionally, the relative photocenter offsets of the Brγ emission region were deprojected from the differential phase data for the same spectral channels, creating photocenter shift profiles of the line. The Brγ spectra themselves were scanned for characteristic features of magnetospheric accretion. From the equivalent width of the line profiles, mass accretion rates were estimated, using an empirical relationship established for low-mass YSOs.

The interferometric analysis showed that five out of the seven objects exhibited Brγ emission on extended spatial scales beyond the co-rotation radius, indicating that the accretion columns are not the only source of Brγ radiation in the system. The distribution of photocenters across the line followed complex, multi-axial structures that were not easily attributed to typical rotational profiles, and the the majority of Brγ spectra featured asymmetric line shapes with a blueshifted excess of emission. In order to gain a better understanding of the expected signatures across the line for these observables, I made use of radiative transfer simulations of an axisymmetric magnetospheric accretion model. From the simulated image, synthetic interferometric observables were computed and compared against the observational trends. I found again that the magentospheric accretion scenario was only able to match the two weakest accretors in the sample well, whereas the behaviour of the observables at high red- and blushifted velocities did not align with the model predictions.

In the final part of the project, I extended the radiative transfer simulations to include not only a larger parameter grid, as well as non-axisymmetric magnetospheric configurations, but most importantly an analytical, parametric disk wind model. As, at the conclusion of the GRAVITY survey, it was hypothesised that an additional wind component may be able to reproduce the observed profiles better than the pure magnetospheric accretion model, the goal was to produce simulated images of combined accretion-ejection processes. From these combined images, new sets of synthetic interferometric observables were computed and compared against the observation of the GRAVITY sample object RU Lup. This effort proved to be partially successful, and indeed the simulations showed that in principle, the combination of disk wind and magnetosphere was able to reproduce the spectrum and characteristic sizes across the line. None of the models, however, were able to fundamentally resolve the deviation in scale between the observed and synthetic photocenter shifts.

In this thesis, I will give in detail an account of the means, the methodology, and the results obtained over the course of this project. In Chapter 1, I will briefly introduce the most important physical and observational concepts concerning the inner disk environment, the magnetospheric accretion model, and some additional considerations regarding disk winds.

In Chapter 2 I summarise the most relevant aspects regarding the technique of interferometry, as well as the GRAVITY instrument.

In Chapter 3, I present in detail the methodology behind the analysis of the GRAVITY data .
In Chapter 4, I describe how the radiative transfer code MCFOST was employed to simulate images of the Brγ emission region for various models.
In Chapters 5, 6, and 7, I report the results of the GRAVITY T Tauri Brγ survey. The chapters contain the general trends across the sample of seven T Tauris, the detailed results pertaining to each individual objects, and the early efforts in radiative transfer simulations, using the simple axisymmetric magnetospheric accretion model.
In Chapter 8, I show the results of the advanced radiative transfer modelling, featuring six different models and the comparison of their synthetic observables to the observational results for the sample objects RU Lup.
In Chapter 9, I summarise these results, present the conclusions and outline some potential perspectives for advancing this project.

Part of the work concerning the GRAVITY T Tauri survey has been published in the paper **"The GRAVITY young stellar object survey IX. Spatially resolved kinematics of hot hydrogen gas in the star-disk interaction region of T Tauri stars" - Gravity Collab.: J. A. Wojtczak, L. Labadie et al.** (Gravity Collaboration et al., 2023b).
Part of the work concerning the radiative transfer simulations of the ejection-accretion models will be part of the paper **"The interplay between disk wind and magnetospheric accretion mechanisms in the innermost environment of RU Lup" - J.A. Wojtczak, B. Tessore, L.Labadie et al.** (Wojtczak et al. (2024), in production).
The methodology described in Chapters 3, 4 is based on material used in these two papers, but extended and rewritten to a point that they bear only passing resemblance to the paper contents. The results presented in Chapters 5 to 8 are direct citations of the result and discussion sections presented in the two papers outlined above. They have been integrated into this monography as multiple individual Chapters in accordance with the Promotionsordnung 2020 and in agreement with the coordinators of the BCGS. A reference to the original section in the respective paper is given before every cited section.
I declare hereby that I am the sole creator of all the contents presented in these chapters, and that the co-authors of my papers only contributed to them in the form of - highly valued - discussion and advice.

Erklärung zur Dissertation

"Hiermit versichere ich an Eides statt, dass ich die vorliegende Dissertation selbstständig und ohne die Benutzung anderer als der angegebenen Hilfsmittel und Literatur angefertigt habe. Alle Stellen, die wörtlich oder sinngemäß aus veröffentlichten und nicht veröffentlichten Werken dem Wortlaut oder dem Sinn nach entnommen wurden, sind als solche kenntlich gemacht. Ich versichere an Eides statt, dass diese Dissertation noch keiner anderen Fakultät oder Universität zur Prüfung vorgelegen hat; dass sie - abgesehen von unten angegebenen Teilpublikationen und eingebundenen Artikeln und Manuskripten - noch nicht veröffentlicht worden ist sowie, dass ich eine Veröffentlichung der Dissertation vor Abschluss der Promotion nicht ohne Genehmigung des Promotionsausschusses vornehmen werde. Die Bestimmungen dieser Ordnung sind mir bekannt. Darüber hinaus erkläre ich hiermit, dass ich die Ordnung zur Sicherung guter wissenschaftlicher Praxis und zum Umgang mit wissenschaftlichem Fehlverhalten der Universität zu Köln gelesen und sie bei der Durchführung der Dissertation zugrundeliegenden Arbeiten und der schriftlich verfassten Dissertation beachtet habe und verpflichte mich hiermit, die dort genannten Vorgaben bei allen wissenschaftlichen Tätigkeiten zu beachten und umzusetzen. Ich versichere, dass die eingereichte elektronische Fassung der eingereichten Druckfassung vollständig entspricht."

Teilpublikationen:

"The GRAVITY young stellar object survey IX. Spatially resolved kinematics of hot hydrogen gas in the star-disk interaction region of T Tauri stars" - Gravity Collab.: J. A. Wojtczak, L. Labadie et al. (Gravity Collaboration et al., 2023b).

Part of the work concerning the radiative transfer simulations of the ejection-accretion models will be part of the paper **"The interplay between disk wind and magnetospheric accretion mechanisms in the innermost environment of RU Lup" - J.A. Wojtczak, B. Tessore, L.Labadie et al.** (Wojtczak et al. (2024), in production).

Datum, Name und Unterschrift

10.03.2024 Jan Alexander Wojtczak

1. Introduction: Accretion and ejection mechanisms in the innermost disk of T Tauri stars

1.1. Motivation

Accretion and ejection play a pivotal role in the transition of young stellar objects (YSOs) towards their main sequence stage. The delicate balance between infalling and outflowing matter is responsible for much of the physics that govern the existence of these objects, as they grow from protostars, embedded in envelopes of dust and gas, to pre-main sequence (PMS) objects with their circumstellar accretion disks. From large scale jets around rapidly developing Class-0 and Class-1 objects down to fading winds from the innermost environment of transitional systems in the final years of their YSO stage, the phenomena of accretion and ejection are fundamentally linked, and the co-evolution of the mechanisms that drive them is one of the major influences on those regions around young stars that may eventually see the birth of planetary systems.
This is particularly pertinent for low-mass YSOs, as they offer a glimpse into the distant past of our own solar system. In these objects, the inner disk is dominated by the influence of strong stellar magnetic fields. Interdependent processes like magnetospheric accretion and magnetised winds facilitate the dispersal of the disk and the transitional process towards the main sequence phase, and consequently fundamentally shape the structure of the stellar environment within a few au, where the formation of Earth-like planetary bodies would potentially take place. The study of accretion and ejection mechanisms may thus allow us to find some new insight into the history of our own place in the universe, and gain a greater understanding of the conditions that eventually allowed our own planet, and with it life itself, to come to be. To this end, I begin my thesis with a brief introduction to the basic structure of the innermost disk, as well as to some of the most important aspects behind magnetically driven accretion and ejection mechanisms in T Tauri stars.

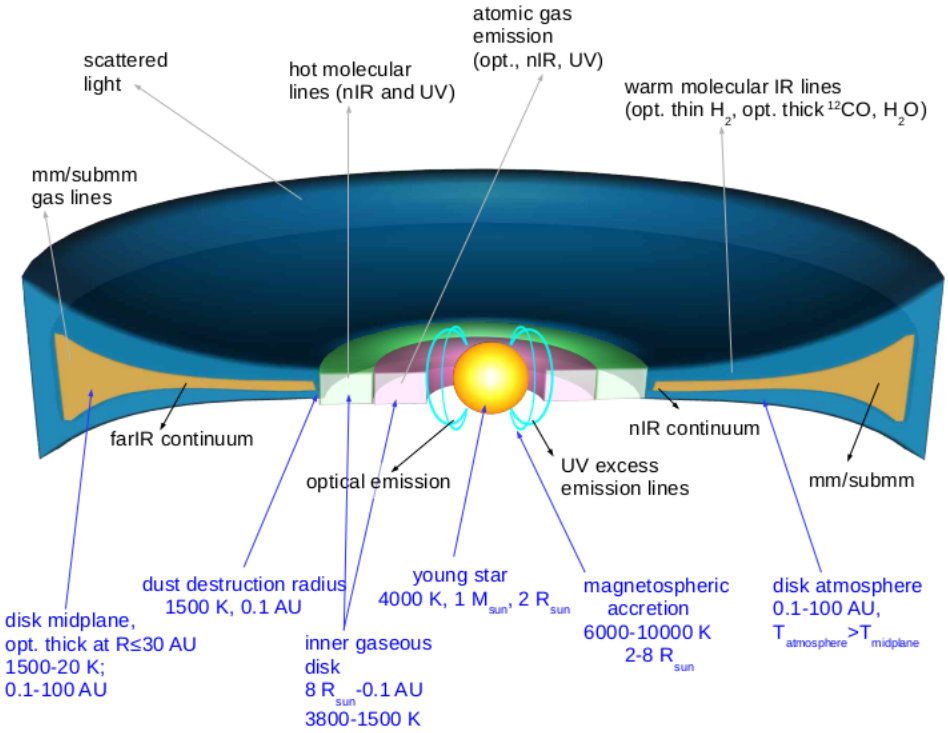

Figure 1.1.: Schematic depiction of the different regions in the circumstellar disk around a T Tauri star. Text in blue indicates the temperature regimes and distances from the stellar axis. Text in black denotes possible types of emission and the region from which they originate. The star-disk system is a complex environment with many concurrent physical processes which require their own tracers. Multi-wavelength observational campaigns are requires to acquire a full understanding of the disk structures and the mechanisms that shape them. **Image credit:** Sicilia-Aguilar et al. (2016)

1.2. The inner disk regions in T Tauri stars

The emergence of circumstellar disks around young stellar objects is direct consequence of the angular momentum problem of star formation. As the molecular material of the stellar cradle begins to collapse into the eventual protostar, conservation of angular momentum would dictate that the forming core should spin up, increasing its rotational velocity to the break-up limit. In this scenario, centrifugal forces would stabilise the cloud fragment against further compression and disrupt the formation process. The creation of a disk is one of the various mechanisms by which the star circumvents this issue, as the redistribution of matter to ranges of 100 au and beyond effectively removes angular momentum from the innermost environment, thus allowing the accretion process to proceed. The circumstellar disk acts consequently also as an accretion disk, since once the young star sheds its envelope and enters the pre-main sequence stage on its evolutionary path, it becomes the sole reservoir of gas and dust from which matter may still be

accreted. At the same time, it serves as the birthplace of planetary systems, and the processing of disk material into planetary bodies is intimately connected to the physics shaping this region. The structure of these disks, as well as the mechanics behind its evolution and dispersal, are of great importance to the final phases of the star formation process.

Circumstellar disks can be broadly divided into two regions, the inner and the outer disk. While there are no exact definitions that delimit these two substructures against each other, the inner disk is commonly understood to be located within a few au around the central star, whereas the outer disk covers a radial extent of several tens to beyond 100 au. The inner disk is often meant to specifically refer to the part that contains everything from the star up to, and including, the transitional border between the optically thick region that is composed of dust and gas, and the optically thin purely gaseous inner disk (Natta et al., 2001)[1], see Fig. 1.1. This transition region is defined by to so-called hot inner rim, where the dust grains are heated to temperatures of around 1500 K, depending on the grain species involved. This temperature is called the sublimation temperature T_{sub}, at which point dust particles are destroyed, i.e. "sublimate" into gas. The distance from the star at which this hot inner rim is located is called the dust sublimation radius r_{sub}. Assuming that the inner rim is heated by direct irradiation from the star, and that the gaseous disk is perfectly transparent to the radiation, a first order estimate of the sublimation radius can be obtained by treating the dust grains as black bodies in thermal equilibrium (Dullemond and Monnier, 2010):

$$r_{sub} = \sqrt{\frac{L_*}{4\pi\sigma T_{sub}^4}} = R_* \left(\frac{T_*}{T_{sub}} \right), \tag{1.1}$$

where σ is the Stefan-Boltzmann constant, and R_*, T_* are the stellar radius and photospheric temperature of the central star, respectively. More advanced modelling will take into account the properties of the dust, see e.g. the relationship given in Monnier and Millan-Gabet (2002), which has been used to compute the sublimation radii shown in Fig. 1.2.

Spectroscopic evidence for the existence of an optically thick circumstellar disk was originally found in the presence of an infrared excess with respect to the pure stellar spectrum, then understood to be caused by the thermal emission of dust grains. At near-infrared (NIR) wavelengths, continuum emission is composed of a photospheric contribution and the emission from the inner dusty disk. The latter is not only composed of the thermal dust emission, but also of a significant additional contribution coming from stellar light scattered on the surface of the disk, as was shown by radiative transfer simulations by Pinte et al. (2008). Through interferometric K-band observations, it is possible to estimate the physical size of the inner disk continuum emission region, which in first order is associated with the sublimation radius. In Gravity Collaboration

[1] While there are again no strict definitions, the additional qualifier "innermost" then typically implies the inner 5 to 15 R_* around the central star, which contain the magnetospheric star-disk interface in T Tauri stars.

et al. (2021b), it was shown that for a sample of T Tauri stars[2] observed with GRAVITY, the size of the K-band continuum emission region strongly correlates with the luminosity of the central star as $R \propto L^{1/2}$, which appears to support the idea of a passively heated inner dust wall bordering a transparent gaseous cavity. However, as depicted in Fig. 1.2, the interferometrically derived K-band size of a Gaussian ring model consistently overestimates the sublimation radius for most of the sample objects, when compared to r_{sub} as directly computed from stellar and dust properties. This discrepancy may imply an advanced evolutionary stage of those disks, in which clearing processes independently of stellar irradiation have already removed part of the dust that once extended to the sublimation radius. When comparing these results to earlier studies by Eisner et al. (2007) on T Tauri stars, it was noted that objects with lower accretion rates deviated more strongly from the size-luminosity relationship, implying that there is a connection between the accretion process and the truncation of the dusty disk.

The purely gaseous inner disk of T Tauri stars extends from the sublimation radius down to the co-rotation radius of the system, on the order of about 5 stellar radii. The co-rotation radius is defined as the radius at which the material in a Keplerian disk rotates at the same angular velocity as the star:

$$r_{co} = \left(\frac{GM_*}{\Omega_*^2} \right)^{\frac{1}{3}}, \tag{1.2}$$

where Ω_* is the angular velocity, M_* the stellar mass and G the gravitational constant (Bouvier, 2013). The significance of the co-rotation radius for the inner edge of the gaseous disk is founded on its connection to the concept of magnetospheric accretion, as it serves effectively as a substitute for the actual magnetospheric truncation radius. A more detailed explanation of the concept and the connection between truncation radius and co-rotation radius will follow in Section 1.3. Simulations of the temperature profiles in low-mass YSOs have shown that the temperature in the inner gaseous disk is not likely to exceed 4000 K (Bertout et al., 1988). As molecular species such as H_2 and CO have dissociation temperatures of about 4500 K (Sicilia-Aguilar et al., 2016), they are perfectly capable of surviving in the inner regions of the gas disk. Through their molecular line emission, they serve as observational tracers of the gas in the innermost disk regions. By contrast, the disk is not hot enough to excite atomic hydrogen lines such as $H\alpha$ or $Br\gamma$, which require temperatures upwards of 6000 K (Tambovtseva et al., 2016). In the inner disk of T Tauri stars, these types of lines are thought to trace specific physical mechanisms responsible for heating the atomic gas. For this reason, hydrogen recombination lines in T Tauri stars are considered to be tracers for processes like magnetospheric accretion.

[2]The T Tauri stars analysed as part of the GRAVITY Brγ T Tauri survey are a subset of the sample from this continuum study.

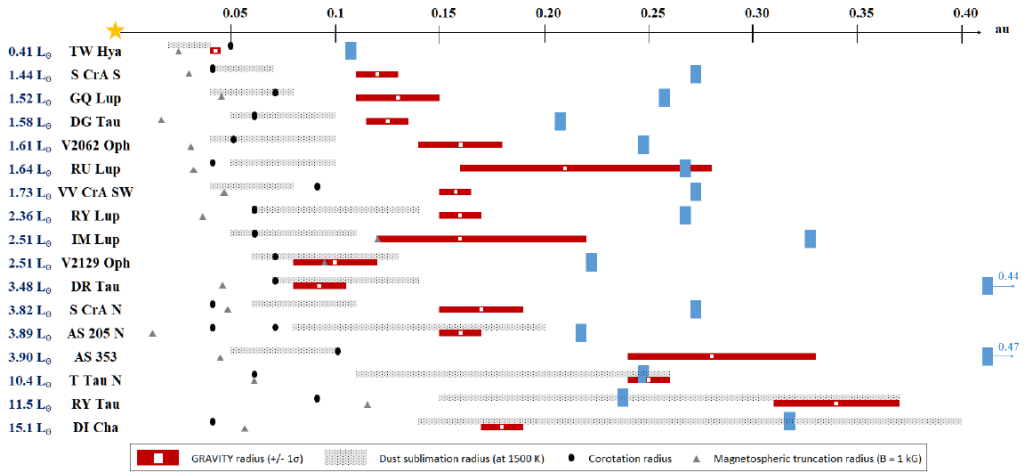

Figure 1.2.: Interferometric K-band sizes, sublimation radii, co-rotation radii, and magnetospheric truncation radii for a sample of T Tauri stars investigated with VLTI GRAVITY. The K-band sizes, derived from a geometrical Gaussian ring model fitted to interferometric visibity data, overestimate the sublimation radii computed from dust and stellar properties. This may indicate that phyiscal processes other than stellar irradiation are clearing out dust in these systems, and could be a characteristic indicator of the disk evolution stage. Note: The magnetospheric truncation radii are not computed correctly here. **Image credit:** Gravity Collaboration et al. (2021b)

1.3. Magnetospheric accretion

A particularly relevant difference between low-mass YSOs and Herbig Ae/Be stars comes to the forefront in the discussion concerning the accretion process in class 2 YSOs. Not only do T Tauri stars exhibit lower stellar masses and photospheric temperatures compared to their intermediate-mass counterparts, they also are known to possess strong magnetic fields, featuring dipolar components with field strengths on the order of 1-2 kG (e.g., Johnstone et al. (2014); Hartmann et al. (2016)). The origin of this distinction is not clear. In the past, it has been attributed to the difference in the make-up of the stellar hull, and the different radiation transport mechanisms that dominate the outer shells, between these two types of objects. As T Tauri stars typically have a large convective outer layer, or may even be fully convective, turbulent dynamo mechanisms have been suspected to induce magnetic dipole fields which then grow more complex with time. However, given the lack of a clear correlation between the rotational periods of T Tauris and the magnetic field strength that would be expected from this scenario, it may be more likely that the observed fields are simply residuals of the primordial magnetic field of the young star's parent cloud (Johns-Krull, 2007). It is possible that the prevalence of strong magnetic fields among low-mass objects is then rather the consequence of faster field decay rates in Herbig stars. This would align with the generally faster evolution of higher mass stars, and is

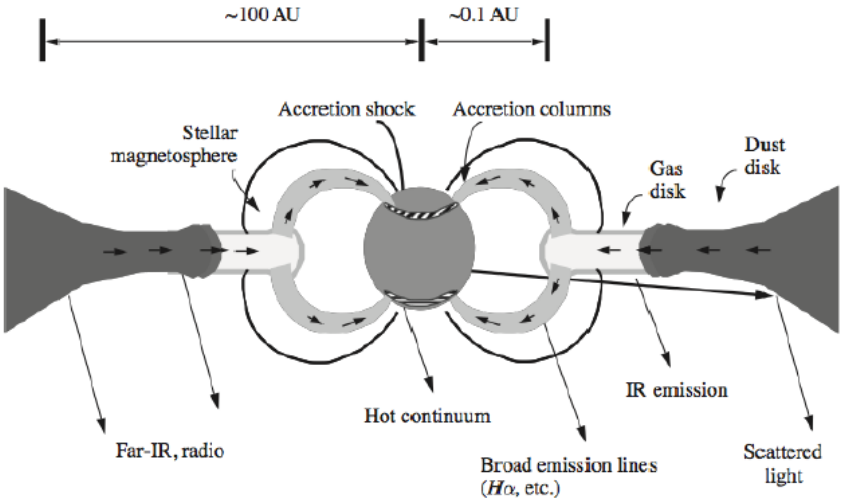

Figure 1.3.: Schematic depiction of a T Tauri circumstellar disk down to sub-au scales, illustrating the axisymmetric magnetospheric accretion scenario.
The inner disk is magnetically truncated by the strong magnetic fields of T Tauri stars, thus preventing gas from being accreted in the disk plane. Instead, it is funnelled onto the star along the magnetic field lines, until it falls onto the stellar surface, heating the shock region in the process. In the axisymmetric case, the dipole axis of the magnetic field and the stellar rotational axis are aligned. The accretion flows are then distributed symmetrically around the stellar axis and the shock region in each hemisphere presents as a heated ring-shaped area. Gas in the accretion columns is magnetically heated, producing atomic line emission from elements such as hydrogen, which due to the velocities in the funnel flows appear as broad emission lines.
Image credit: Hartmann (2009)

at least indirectly supported by a reported correlation between magnetic field decay and stellar mass in main-sequence stars (Fossati et al., 2016).

Regardless of the origin, the kG magnetic fields observed in T Tauri stars have a profound impact on the accretion process during the PMS stage. In the traditional image of accretion in young stars, gas and dust material are spiralling inwards in the disk plane under the gravitational pull of the star and by shedding angular momentum through viscous interaction with the outer layers. This motion extends up to a so-called hot boundary layer in the innermost region of the disk, close to the star, where a large amount of energy and excess angular momentum are released so that the gas may accrete onto the stellar surface (Lynden-Bell and Pringle, 1974). While, in principle, this remains the general model of accretion in Herbig Ae/Be type objects, for T Tauri stars it has been superseded by the paradigm of magnetospheric accretion over the past 20 years (Mendigutía, 2020).

1.3.1. Magnetic truncation of the inner disk and different accretion regimes

The fundamental idea of the magnetospheric accretion model is the notion that the magnetic fields in T Tauri stars are sufficiently strong to exert a force perpendicular to the dipole field lines that would counteract the ram pressure caused by the inwards bulk motion of the gas. We say then that the inner disk is magnetically truncated at a certain radius r_{tr}. Following the simple conceptual derivation of the truncation radius in Bouvier et al. (2007), we set $P_{mag} = \left(\frac{B^2}{8\pi}\right)$ for the magnetic pressure, where B is the field strength of the dipole component, and $P_r = 0.5\rho v^2$ for the ram pressure of the gas, where v is the mean velocity of the bulk motion of the material and ρ is the density distribution. At the equilibrium between both we thus find

$$B^2 = 4\pi\rho v^2. \tag{1.3}$$

To further simplify, we assume first that mass accretes from some spherical shell, so that $\rho = \frac{dM}{dV}$ can be written as

$$\rho = \frac{dM}{4\pi r^2 dr}, \tag{1.4}$$

and then, using $v = \frac{dr}{dt}$, we can derive an expression for the truncation radius:

$$B^2 = \frac{4\pi}{4\pi r_{tr}^2}\frac{dM}{dr}\frac{dr}{dt}v \tag{1.5}$$

$$\iff r_{tr} = \frac{\dot{M}v}{B^2}. \tag{1.6}$$

Here the equation was rewritten in terms of the mass accretion rate $\dot{M} = \frac{dM}{dt}$. Under the assumption that the dipolar field scales radially as $B(r) = B_*\left(\frac{R_*}{r}\right)^3$ with distance r from the dipole axis, this expression can be recast for matter accreting at free-fall velocity $v = \sqrt{\frac{GM}{r_{tr}}}$:

$$r_{tr} = \left(\frac{B_*^4 R_*^{12}}{\dot{M}^2 2GM_*}\right)^{1/7} \tag{1.7}$$

$$\iff \frac{r_{tr}}{R_*} = 7.1 B_3^{4/7}\dot{M}_{-8}^{-2/7}M_{0.5}^{-1/7}R_2^{5/7}, \tag{1.8}$$

The last equality gives the formula in astrophysical units that are particularly convenient for use in the context of T Tauri stars, where B_3 is the stellar magnetic field strength in kG, $\dot{M}_{-8}$ is the mass accretion rate in units of $10^{-8}M_\odot yr^{-1}$, $M_{0.5}$ is the stellar mass in units of 0.5 $M_\odot$ and R_2 the stellar radius in units of 2 $R_\odot$. Inserting typical values for T Tauri stars with M_* = 0.5 $M_\odot$, B_*= 1 kG, R_*= 2 $R_\odot$, and an accretion rate of $\dot{M}$= $10^{-8}M_\odot yr^{-1}$ will yield a truncation radius of

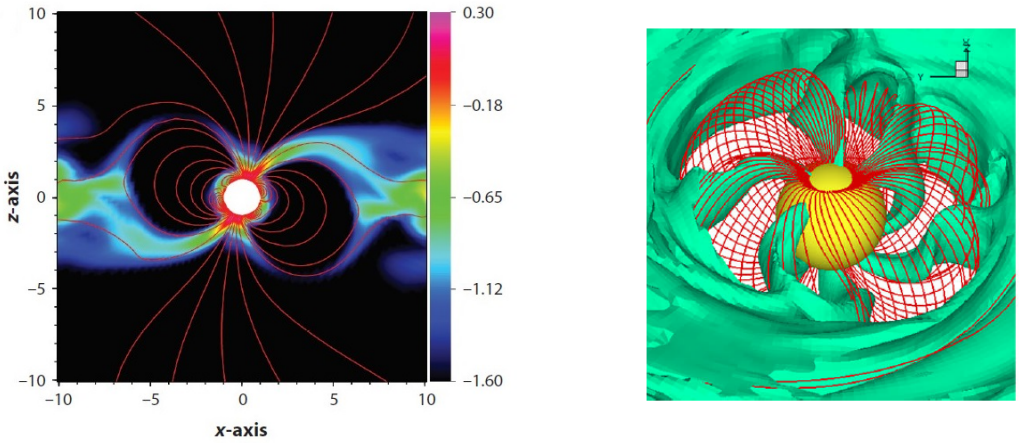

Figure 1.4.: **Left:** 3D MHD simulation of magnetospheric accretion in the T Tauri star V 2129 Oph
The system features a non-zero obliquity, meaning the magnetic field axis is tilted with respect to the rotational axis. This leads to the formation of a single preferential funnel flow per hemisphere, along which matter is transported onto a hot spot shock region. Coordinate axes are in units of stellar radii. The colour map denotes the density in the matter flow in arbitrary units. **Image credit:** Alencar et al. (2012)
Right: Simulation of the chaotic formation of accretion tongues on short time-scales close to the stellar surface when the system is in unstable accretion. **Image credit:** Romanova and Owocki (2015)

about 7 R_*.

In real T Tauri stars, accretion is not spherical but bound to the circumstellar disk, where the material is in Keplerian rotation and does not reach free-fall velocity. This translates to higher densities in the disk and thus an increased ram pressure when compared to the simplified model outlined here. The truncation radius will then be slightly smaller, but remains on the same order of magnitude. More realistic estimates of truncation radii for observed magnetic field strenghts in T Tauris broadly fall in the range of up to 10 R_*, with commonly cited typical values of 4-6 R_* (Hartmann et al., 2016).

Since the gas cannot accrete further than the truncation radius as part of the disk, an inner zone in the close environment of the star will form which is effectively evacuated of disk material in the orbital plane. Instead, gas is funneled along the dipole field lines onto the star, where it will impact the stellar surface at high latitudes, creating a heated shock region in the process. The magnetically dominated environment around the star that is bounded by the truncation radius is referred to as the magnetosphere.

In the naive view of magnetospheric accretion, the dipole axis and the stellar rotational axis are perfectly aligned. In this scenario, the accretion flows are distributed in an axisymmetric configuration, and the accretion shock forms a ring-like region in each hemisphere near the stellar poles, see Fig. 1.3. However, measurements of the magnetic field topology in T Tauri

stars have indicated that many of these objects show tilted dipoles (e.g. Donati et al. (2007); Johnstone et al. (2014)). The angle between the inclined dipole axis and the stellar rotational axis is referred to as obliquity and has been shown to be on the order of 10° (McGinnis et al., 2020). A non-zero obliquity changes the geometry of the funnel flows significantly. Tilting the axis towards the edge of the gaseous disk will lead to the formation of hot spots, i.e. spatially compact regions on the stellar surface onto which the material preferentially accretes. If the obliquity is sufficiently large, only two large accretion columns per hemisphere will remain, which connect the truncation radius to these hot spots.(Bertout et al., 1988; Calvet and Hartmann, 1992). The geometry of the matter flow in such a non-axisymmetric configuration is depicted in the left panel of Fig. 1.4.

The classical view on magnetospheric accretion is based on the idea that the disk is truncated within the co-rotation radius of the system. If the disk were to be truncated outside the co-rotation radius, the differential rotation between the fast magnetosphere and the slow accreting gas would lead to the ejection of matter as it is picked up by the field lines. Numerical MHD simulations (e.g. Romanova and Owocki (2016); Blinova et al. (2016)) indicate that the situation here is more complex, and that one may distinguish between three different regimes of accretion:

- **Stable accretion:** The inner gaseous disk is truncated roughly at, or slightly below, the truncation radius, $r_{tr} \approx r_{co}$. This corresponds to the regular magnetospheric accretion scenario in which accretion columns form at the edge of the magnetosphere and remain stable over long periods of time. From the simulations presented in Romanova and Owocki (2015), the border between the stable and unstable accretion regime is at about 0.7 r_{co}.

- **Unstable accretion:** If the disk is truncated far below the co-rotation radius ($r_{tr} \ll r_{co}$), gas matter penetrates deep into the magnetosphere and is then accreted along a chaotic system of accretion tongues from close to the stellar surface. As a practical consequence, accretion is unsteady and hot spots may form spontaneously, leading to erratic behaviour in simulated light curves (Romanova et al., 2008a). A 3D depiction of the matter flow in such a case is shown in Fig. 1.4, right panel.

- **Propeller regime:** If the disc is truncated at scales larger than the co-rotation radius ($r_{tr} > r_{co}$), angular momentum is transferred from the magnetosphere to the gas entering the funnels. The material is subsequently propelled outwards and ejected from the disk in the form of a centrifugally-driven wind. While the classical picture of magnetospheric accretion implies that no accretion columns would form at all in this case, numerical simulations have shown that the strength of the propeller can vary greatly, depending on the ratio between r_{co} and r_{tr}. For weak propellers, where the truncation radius is only slightly more extended than the co-rotation radius, matter is only partially ejected, while

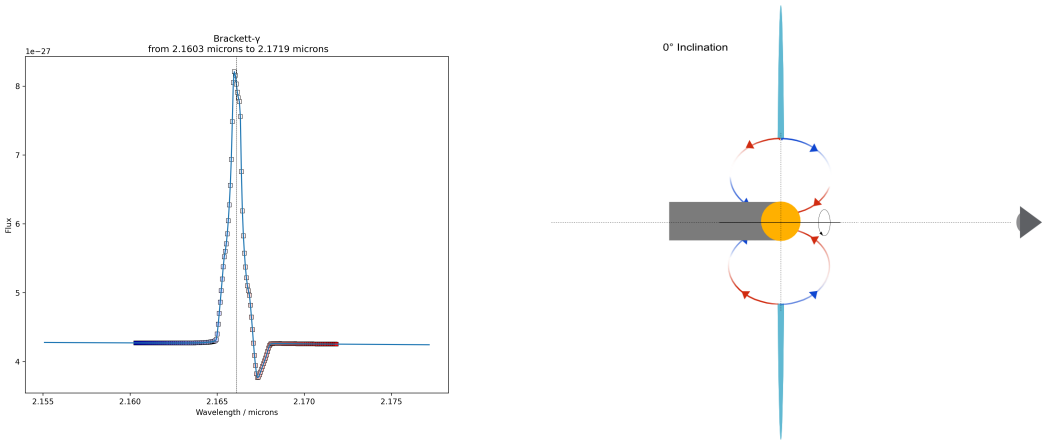

Figure 1.5.: **Left:**The spectrum of a Brγ emission line produced in the accretion funnels of an axisymmetric magnetosphere, observed at zero degrees inclination. The spectrum was computed with the radiative transfer code MCFOST (see Section **??** using the analytical model of magnetospheric accretion introduced in Section 4.3. The red wing of the profile shows an absorption dip, which is commonly referred to as an inverse P Cygni profile.
Right: Cartoon of the geometrical configuration behind the formation of the inverse P Cygni characteristic. If the system is observed pole-on, the redshifted material falling onto the star will be positioned between the observer and the stellar surface. The optically thick accretion flow will then block out part of the photospheric emission, creating the appearance of an absorption dip.

the remaining part is still accreted. For strong propellers with $r_{tr} \gg r_{co}$, accretion comes close to a complete stop.

1.3.2. Observational evidence for magnetospheric accretion

There are a number of potential diagnostics of magentospheric accretion scenario, mostly based on broad atomic emission lines. Hydrogen recombination lines in particular are well established observational tracers of the hot gas in the accretion funnel and have been treated in early observational studies (Camenzind, 1990; Calvet and Hartmann, 1992) as well as radiative transfer simulations (Muzerolle et al., 2001). The link between hydrogen line emission and accretion in T Tauri stars was established by Muzerolle et al. (1998) in the form of an empirical correlation between the line luminosity and the accretion luminosity:

$$\log\left(\frac{L_{acc}}{L_\odot}\right) = a \log\left(\frac{L_{Line}}{L_\odot}\right) + b, \tag{1.9}$$

where the accretion luminosity is defined by the energy released by the material accreting onto the star in free-fall, $L_{acc} = GM_*\dot{M}/R_*$. In Muzerolle et al. (1998), the coefficients a,b were determined to be $a_{Pa\beta} = (1.14 \pm 0.16)$, $b_{Pa\beta} = (3.15 \pm 0.58)$ and $a_{Br\gamma} = (1.26 \pm 0.19)$, $b_{Br\gamma} = (4.43 \pm 0.79)$ for a sample in the Taurus star forming region, using the Paβ and Brγ hydro-

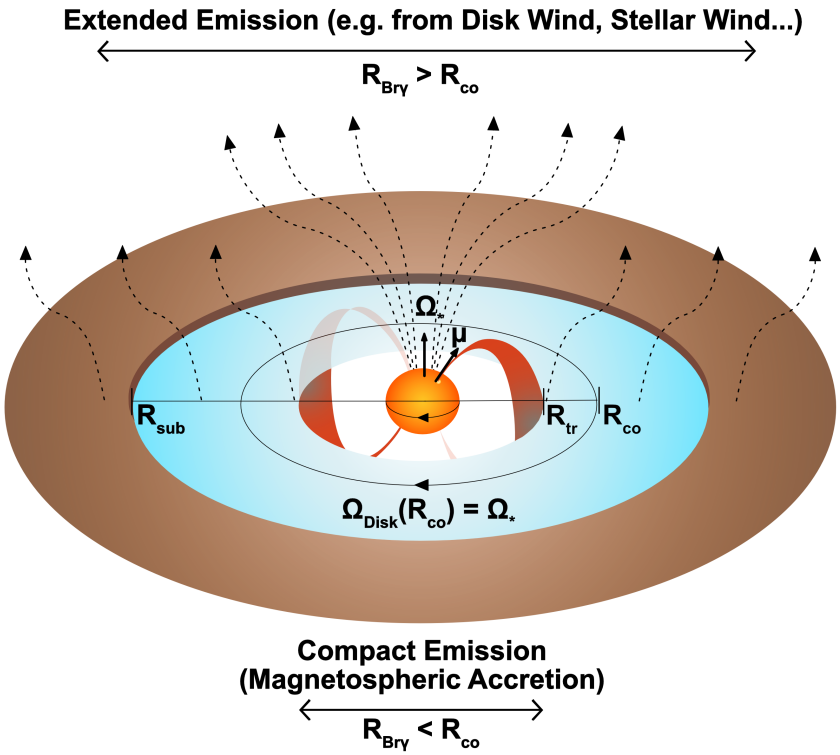

Figure 1.6.: Schematic depiction of the innermost parts of the circumstellar disk of a T Tauri star. Brγ emission in T Tauri stars is associated with the concept of magnetospheric accretion, but outflows caused by certain types of disk or stellar winds (dashed lines) can heat the hydrogen gas to the necessary temperatures to produce Brγ emission as well. Different origin mechanisms can be tied to different spatial scales. Magnetospheric accretion flows (depicted in red) can only stably form in a compact region within the co-rotation radius R_{co}, where the gaseous disk rotates at the same angular velocity Ω as the star. Spatially extended Brγ emission from outside R_{co} cannot be attributed to magnetospheric accretion and must be caused by some other emission component.
This figure specifically shows the common case of a non-axisymmetric magnetosphere, featuring a tilt between the stellar rotational axis Ω_* and the magnetic dipole μ. The obliquity of the magnetosphere leads to the formation of two accretion columns, which funnel gas from a wide arc at the truncation radius onto one primary hot spot per hemisphere.
Note: This figure is a custom creation. It has previously been published in Gravity Collaboration et al. (2023b).

gen lines, respectively. Relying on infrared features is advantageous here, as the measurement of the line luminosity is significantly less affected by interstellar extinction than would be the case for optical lines, such as Hα. This line luminosity to accretion luminosity relationship was re-investigated by Alcalá et al. (2014, 2017) for a sample of T Tauri stars in Lupus, using the VLT X-Shooter spectrograph to acquire high resolution spectra of a number of atomic emission lines. For Paβ and Brγ they found $a_{Pa\beta} = (1.04 \pm 0.08)$, $b_{Pa\beta} = (2.45 \pm 0.39)$ and

$a_{Br\gamma}$ = (1.16 ± 0.07), $b_{Br\gamma}$ = (3.6 ± 0.38), confirming that the relationship holds up very well even between different populations of stars, and that indeed hydrogen line emission is very strongly correlated with accretion in low-mass young stellar objects.

Historically, magnetospheric accretion in YSOs has been mostly viewed through the lens of spectroscopic studies. This was by necessity rather than by choice, considering that the innermost regions of the circumstellar disk around even the closest T Tauri star are not accessible to the most powerful individual telescopes in use even today. The magnetospheric accretion scenario has been found to be well supported spectroscopically, as the model has been able to reproduce a number of different spectral line characteristics at the same time that would otherwise remain unexplained. The presence of accretion columns has been indirectly confirmed through the observation of inverse P Cygni profiles, redshifted absorption features at several hundred km/s, which are found in systems observed at low inclination (Edwards, 1994). The existence of these features is indicative of gas falling onto the star at high latitude from a distance of a few stellar radii, see Fig. 1.5. The observed line width of CO fundamental emission coming from gas in Keplerian rotation around T Tauri stars has been cited as potential evidence for magnetospheric accretion, as they would require an inner disk cavity at scales of less than 9 R_* such as predicted for magnetospheric truncation (Najita et al., 2003). Additionally, rotational modulations of light curves are consistent with the presence of hot spots caused by accretion shocks (Bouvier et al., 1995).

More immediate observational evidence has come to the forefront in recent years through the use of long-baseline interferometry. The sub-milliarcsecond resolution and increased sensitivity available with modern instruments have made spatially resolved observationas of the inner 0.1 in faint T Tauri stars possible. T Tauri Brγ emission in particular has been explored in the works of Eisner et al. (2010, 2014) with the Keck Interferometer (KI), and has also been the focus of recent pioneering studies with the Very Large Telescope Interferometer (VLTI) (Gravity Collaboration et al., 2017; Bouvier et al., 2020). The analysis of the Brγ emission scale in Gravity Collaboration et al. (2020) for the young star TW Hya has attracted attention for being the first direct confirmation of magnetospheric accretion through spatially resolved observations. With the methods of interferometery, the size of the emission region of a tracer line, such as Brγ , may be constrained and compared against known diagnostics, such as the co-rotation criterion. A measured emission region size smaller than the co-rotation radius is considered indicative of accretion. The principal argument here remains that hydrogen line emission in T Tauri stars with an actively accreting magnetosphere is produced predominantly in the funnel flows, where the gas is magnetically heated. Significant Brγ emission at typical mass accretion rates for T Tauri stars has been shown to require temperatures in excess of 6000 K (Muzerolle et al., 1998; Tambovtseva et al., 2016). Even in the close environment of T Tauri stars, with their comparatively

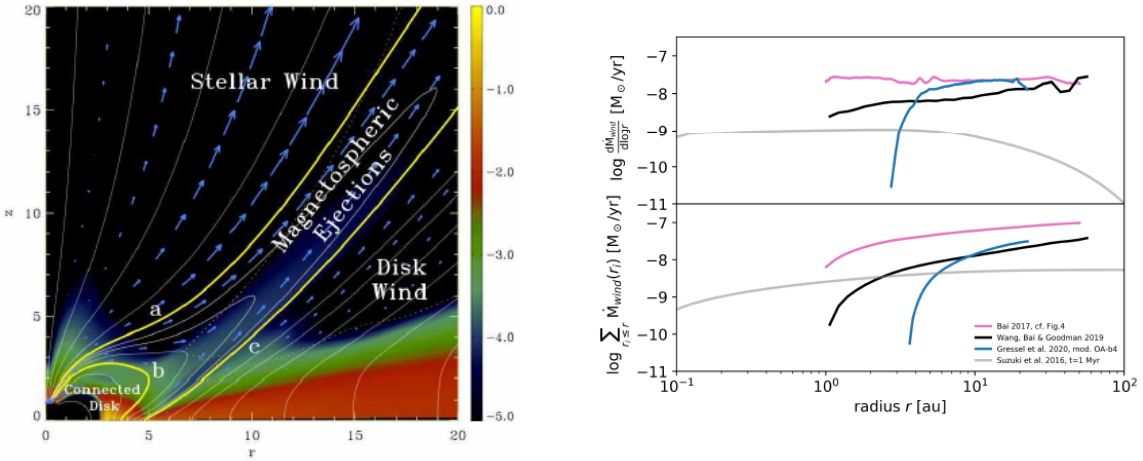

Figure 1.7.: **Left:** Depiction of matter flow simulations in the star-disk interface region. Different types of MHD driven outflow processes in the innermost disk, and the spatial regions they occupy, are shown here. This includes an accretion-powered stellar wind, launched from the polar region of the star along open field lines that connect the stellar magnetic field to the large scale magnetic field of the parent cloud.,ejections from the magnetospheric accretion flows, and the disk wind. The thick yellow field lines delimit the different outflow components. The colour map denotes the density in the system. **Image credit:** Zanni and Ferreira (2013)
Right: Cumulative mass loss up to a radius r as computed from different recent MHD disk wind simulations. The decreasing slopes of the curves indicate that mass loss due to magnetized winds is strongest in the inner regions of the circumstellar disk, with outer regions contributing relatively negligible amounts. **Image credit:** Pascucci et al. (2023)

cool photospheric temperatures and low accretion rates, neither radiative nor viscous heating is sufficiently strong to create the required temperature regime within the gaseous disk itself, such as can be the case for Herbig Ae/Be stars. (Kraus et al., 2008). As a consequence, a very compact emission region is likely to trace part of the magnetosphere itself, whereas an emission region that is significantly more extended than the co-rotation radius is more likely to trace some kind of magnetically driven outflow process, where similar heating mechanisms may lead to Brγ emission. The principle is illustrated in Fig. 1.6.

1.4. Outflows from the innermost disk

Any form of accretion of rotating matter inevitably poses questions concerning the accumulation of angular momentum by the star. Numerical simulations of star-disk interactions in YSOs with strong dipolar magnetospheres have shown that the magnetospheric accretion paradigm does not offer an easy way out of this conundrum. Contrary to earlier expectations, angular momentum is not transferred back to the circumstellar disk via magnetic coupling and no stellar spin

equilibrium is reached. Instead, the accreting star will continue to spin-up until it eventually reaches rotational velocities near the break-up limit (Ferreira, 2013). However, observational studies suggest that T Tauri stars in particular rotate slowly, on the order of 10% of their break-up velocities, nor do they exceed these numbers by much even during their earlier protostellar evolutionary stage (Bouvier, 2013). There is also a robust body of evidence for high-velocity jets around these types of objects (e.g. Agra-Amboage et al. (2014)), suggesting that some form of mass outflow feeding into these large scale structures must be present in the star-disk system. It is clear that magnetospheric accretion in low-mass PMS stars cannot occur without some sort of accompanying ejection mechanism capable of efficiently removing angular momentum from the system.

Outflows in the inner disk of T Tauri stars can be broadly categorised into disk winds, magnetospheric ejections, and stellar winds, depending on the point of origin (Ferreira, 2013). For the disk winds, an additional distinction between magnetically driven disk winds and photoevaporative winds is to be made.

1.4.1. MHD disk winds and photoevaporative winds

Magnetohydrodynamical (MHD) disk winds are outflow processes driven by magneto-centrifugal mechanisms as first described in the seminal work of Blandford and Payne (1982). In principle, they are based on the idea that if the field lines of the large scale magnetic field are inclined away from the polar axis to a sufficient degree, magnetically coupled disk material co-rotating with the field will be expelled from the disk due to centrifugal forces. These types of disk winds are launched when the ratio of thermal gas pressure to MHD pressure, $\beta(z) = \frac{P(z)}{B^2/(8\pi)}$, is $\beta < 1$ (Pascucci et al., 2023). The magnetic field will drive matter along the field lines only if the material is sufficiently ionised. Given that ionisation is higher in regions with lower density, and that density decreases with vertical distance from the midplane, conditions at the disk surface are more favourable to launch the wind. 2D simulations of disk regions ranging from 1 to 20 au have shown typical launch heights of about 5 H (≈ 1 R_*), where H is the thermal pressure scale height of the disk (Bai, 2017). Once launched, dissipative non-ideal MHD processes, such as Ohmic heating or ambipolar diffusion, may dominate the temperature in the gas over photo-heating. In this way, the magnetically heated gas can reach temperatures of up to 10^4 K, creating the environmental conditions that would allow for significant hydrogen emission from spectral lines such as Brγ (Garcia et al., 2001b).

These types of MHD winds are conceptually different from thermal winds, which may be triggered through stellar irradiation of the gas and its subsequent evaporation into a wind. These so-called photoevaporative winds will launch the thermal energy of the gas if large enough to overcome the stellar gravitational field. This dynamic is in itself a function of both the temper-

ature to which the gas is heated by irradiation, as well as the distance from the star. Given the sharp decline in gravitational pull $\propto \frac{1}{r^2}$, launch conditions in the outer regions of the disk are typically more favourable, with critical radii depending on the dominant type of incident photons. If the dominant source of heating comes from extreme ultraviolet (EUV, 13.6 eV to 100 eV), the gas remains gravitationally bound at radii of on the order of 1-2 au. For X-ray (above 100 eV) photons, this critical radius extends to 2-4 au, and for far ultra violet photons (FUV, 6 eV to 13.6 eV) photons the wind may only launch from regions between 3 and 12 au (Pascucci et al., 2023). These scales indicate that photoevaporative processes are unlikely to play a role at the star-disk interface region in the inner 0.1 au.

1.4.2. Stellar winds and magnetospheric ejecta

Other MHD driven outflow processes include accretion-powered stellar winds, which originate from the star itself, as material is expelled along the open field lines emerging from the stellar poles Matt and Pudritz (2005). If the ejected matter remains in co-rotation with the star, and the opening angle of the field lines is wide, such a stellar wind would be highly efficient at removing large amounts of angular momentum per unit mass. However, given that T Tauri stars generally have low rotational velocities, centrifugal forces are not likely to be sufficient to drive the expulsion of matter in this case, and consequently a different pressure mechanism is required to launch the wind. A common idea here is that the gas accreted by the magnetospheric funnel flows creates a shock at the stellar surface as it releases its energy. The shock then generates compressive waves which propagate towards the open field lines at the stellar poles, leading to a turbulent Alfvén wave pressure that would launch the wind material (Ferreira, 2013). These types of winds may reach velocities upwards of 100 km/s, and if observed at low inclination with respect to the observer line of sight, can lead to blueshifted absorption features as the stellar wind blocks out part of the photospheric continuum (Edwards et al., 2006).
In principle, the magnetosphere itself can also act as a source of ejection processes. If the stellar dipolar magnetic field is strongly linked to the surrounding circumstellar disk, differential rotation between the two systems willl lead to an inflation of field lines at mid-latitudes. These field lines undergo a process of expansion and eventual reconnection over a time period of multiple stellar rotations, which will lead to a detachment of accreting material and its ejection along a path in between the open magnetic field lines, see Fig. 1.7, left (Zanni and Ferreira, 2013). These events are dynamic and not steady, and are not likely to be main contributors to mass loss in the inner disk.

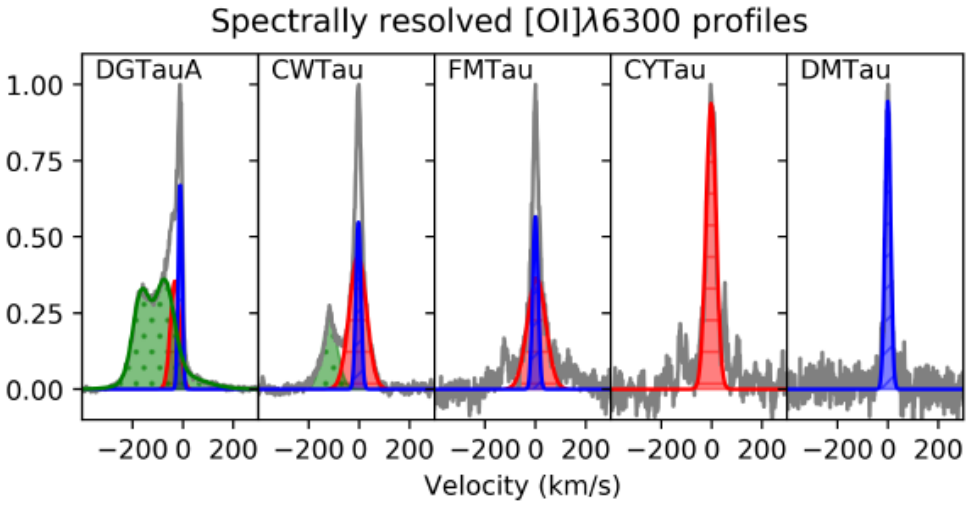

Figure 1.8.: Exemplary disk wind line spectra (grey) from Banzatti et al. (2019) for the [O I] atomic oxygen line at 6300 Å. The figure demonstrates how the wind line profile may be decomposed into different distinct kinematic components: The high velocity component (HVC, green), the low velocity narrow component (LVC NC, blue), and the low velocity broad component (LVC BC,red) **Image credit:** Pascucci et al. (2023)

1.4.3. Observational characteristics

The bulk of the analysis on winds in YSOs has been, historically as today, carried out with the methods of spectroscopy (e.g. Banzatti et al. (2019); Weber et al. (2022)), as only large scale jet structures are large enough for spatially resolved observations with individual telescopes. Spatially unresolved outflows possess a number of tracers, mostly in the form of forbidden emission lines. A prominent example here is the [O I] oxygen line at 6300 Å, which is detected in the overwhelming majority of accreting T Tauri stars, see Fig. 1.8. Other atomic and ionic species suitable to trace outflow processes in Class 2 YSOs through forbidden lines are [S II], [Fe II], as well as molecular lines of H_2 and CO (Lee, 2020; Pascucci et al., 2023). The effects of the wind may also be seen in permitted atomic lines such as Hα or He I 10830 Å, which trace optically thick gas and create blueshifted P Cygni absorption features in the spectra. Forbidden emission lines are often composed of two principal kinematic components: A blueshifted high velocity component (HVC) with an observed blueshift of up to 300 km/s, and a centered low velocity component (LVC) with velocities on the order of 10 km/s. The HVC has in the past been strongly associated with a high velocity microjets, originating in the inner disk on scales of less than 0.5 au. More recently, a possible connection between MHD disk winds launched from the inner disk and the extended jet structures has been suggested, such in the case of HH212, where a launch region for a magnetos-centrifugal wind on scales of 0.05 to 0.3 au was inferred

from ALMA observations (Lee et al., 2017; Tabone et al., 2017).

Both components have been shown to diverge in their coupling to the accretion rate of the system. The mass loss to accretion ratio shows both a larger spread of potential values for the LVC, with $\frac{\dot{M}_{LVC}}{\dot{M}_{acc}} \approx 0.1 - 1$, where as the high velocity components of T Tauri stars appear to sit at a relatively constant ratio of $\frac{\dot{M}_{HVC}}{\dot{M}_{acc}} \approx 0.1$ (Fang et al., 2018). Sperling et al. (2021) showed that for the HVC the decline in mass loss is very strongly coupled to the decreasing accretion rate across different evolutionary stages of low-mass young stars, while the mass loss stemming from the LVC declines much faster than the accretion rate once the star enters the PMS stage.

Interferometric studies in the infrared on wind-based emission in T Tauri stars are comparatively rare, with only Eisner et al. (2010, 2014) applying a simple magnetospheric infall/outflow visibility model to T Tauri data taken with the Keck Interferometer. Studies with the VLTI were, before the advent of GRAVITY, largely restricted to the Herbig Ae/Be stars. Weigelt et al. (2011); Garcia Lopez et al. (2015); Kurosawa et al. (2016) investigated a potential wind in the form of a large-scale Brγ emission region in such intermediate-mass objects with VLTI AMBER, the predecessor instrument to GRAVITY. A first attempt to discuss a possible Brγ outflow in a T Tauri star was made by Gravity Collaboration et al. (2017) with GRAVITY for S CrA N, although while a large scale emission component was detected, its nature remained elusive. The GRAVITY T Tauri Brγ survey (Gravity Collaboration et al., 2023b) expanded upon this work by showing large scale emission for a number of T Tauris, which may indicate the presence of a disk wind. This thesis will present in detail work done by the survey and the additional effort made to constrain the nature of the large scale emission with radiative transfer simulations of a disk wind model.

2. Near-infrared interferometry with VLTI GRAVITY

The contents and equations presented in this chapter draw heavily on well established knowledge about physics in general and interferometry in particular. Sections concerning the theoretical principles of interferometry contain information compiled mainly from Glindemann (2011) and Millour (2014). Technical descriptions of the VLTI and GRAVITY are based on the instrumental manuals publically available on the ESO website. Additional information on the practical observational use of interferometry, including the explanation of interferometric observables and their physical interpretation, and intersections between technological advancements and observations rely on standard treatises such as Berger and Segransan (2007) or Monnier and Millan-Gabet (2002); Monnier (2007); Haniff (2007), with supplemental information taken from the very useful review by Eisenhauer et al. (2023). Given the introductory character of this section, the age of most of these sources and the fact that much of the information presented here is essentially public knowledge among interferometrists, I will refrain from providing individual citations for each argument or equation.

Optical interferometry has been at the forefront of high angular resolution studies into the close environments of young stellar objects ever since the advent of powerful modern long-baseline facilities over the past 20 years. Recent times in particular have seen a growing number of studies focusing on spatially resolved observations of the innermost circumstellar disk in YSOs (Gravity Collaboration et al., 2023a, 2021a,b, 2020; Setterholm et al., 2018). Top-tier optical/infrared interferometers, such as the Center for High Angular Resolution Astronomy (CHARA) Array or the Very Large Telescope Interferometer (VLTI), have benefitted from a number of great technical advancements to the point where once inaccessible regions close to the surface of a young star can be explored in ever increasing detail. The current generation of instruments now routinely allows astronomers to probe even the innermost disk regions of relatively faint sources, such as T Tauri stars, at angular scales in the sub-milliarcsond regime. These improved capabilities present the astrophysical community with opportunities to put long held beliefs about the physical processes governing the star-disk interface to the test. Theoretical frameworks describing the dynamics of ejection and accretion on such small scales have long been discussed in the

context of spectroscopic surveys (e.g. Muzerolle et al. (1998, 2001)), but only now does long baseline interferometry provide the means to also directly trace the spatial signatures associated with those mechanisms.

The most obvious advantage of interferometric techniques lies with the fact that its angular resolution scales with the distance between the two telescopes used, the so called "baseline" B , as $\frac{\lambda}{2B}$. Given that individual telescopes, whose resolution is tied to the size of their primary mirror, are currently[1] limited to diameters of 10 m or less, they cannot hope to compete with the baseline lengths offered at top tier interferometric arrays. This huge advantage, however, comes at a cost, not least of all the fact that the technique is often considered to be unintuitive and its results often difficult to interpret for the uninitiated. This chapter aims to provide a primer for the most important aspects of interferometry, both from a conceptual and an instrumental perspective. The purpose is not to give a full account of the theoretical and mathematical underpinnings of this field, but rather to try walk the reader through a number of key points that hopefully will help to build a fundamental understanding of the interferometric approach and provide some general context for the analysis of GRAVITY data as presented in this thesis.

2.1. Fundamentals of Interferometry

The primary purpose of an astronomical interferometer is to record the interference fringes which are produced when two spatially or temporally displaced signals are brought to superposition. To illustrate the basic principles of fringe formation, it is instructive to recall Young's famous double slit experiment from 1800, as it offers a relatively simple and straightforward analogy to a modern two-telescope interferometer.

Suppose that, at a detector screen, the intensity[2] of an incident electromagnetic wave is proportional to the time average of the squared electric field:

$$I(\mathbf{r}) \propto \left\langle |\mathbf{E}(\mathbf{r}, t)|^2 \right\rangle . \tag{2.1}$$

The intensity takes a particularly simple form for the case of a plane wave travelling in direction z with an electric field component of

$$E(z, t) = E_0 e^{-i(\omega t - kz)}, \tag{2.2}$$

[1] The European Extremely Large Telescope (E-ELT) will use a 40 m primary mirror. Even such an unprecedented technical accomplishment loses,in terms of pure angular resolution, out to the baseline lengths available at current high-end interferometers.

[2] Following the definition in Glindemann (2011), the intensity here is a dimensionless quantity that is proportional to the received flux. The latter is defined by the time average of the Poynting vector.

as the absolute value of a complex number is equal to its amplitude E_0. Since the amplitude is constant, the intensity is then simply $I(\mathbf{r}) \propto E_0^2$ and thus uniform across the screen.

In the double slit experiment, we assume the slits are narrow enough that any incident light passing through them emerges from the other side in the form of a spherical wave:

$$E(r) = \frac{E_0}{r} e^{ikr}. \tag{2.3}$$

Here r refers to absolute value of the position vector, i.e. the radial distance between the slit and some chosen point in space. If we place the detector screen behind a single slit and measure the intensity of a single spherical wave, we will see that the illumination of the screen is dependent on the radial distance from the slit:

$$I(r) = \frac{E_0^2}{r^2}. \tag{2.4}$$

Now consider the case of spherical waves E_1, E_2 emerging from two slits as depicted in Fig. 2.1. The detector now measures the superposition of these two spherical waves, which we can write as

$$E = E_1 + E_2 \tag{2.5}$$

$$\implies E(x) = \frac{E_0}{r_1} e^{ikr_1} + \frac{E_0}{r_2} e^{ikr_2} \tag{2.6}$$

$$= \frac{E_0}{z_1} e^{ik(r_1+r_2)/2} 2cos(k(r_1 - r_2)/2), \tag{2.7}$$

with an intensity of

$$I(x) \propto \frac{E_0^2}{z_1^2} 2(1 + cos(k(r_1 - r_2))) \tag{2.8}$$

$$\implies I(\alpha) \propto (1 + cos(k\alpha)B), \tag{2.9}$$

where x is a coordinate that denotes a position on the detector plane.

In other words, the intensity along the detector alternates between minima and maxima as we increase the deflection angle α. In these equations, z denotes the displacement between the slit screen and the detector and k refers to the absolute value of the wave vector $\mathbf{k}$, with $k = 2\pi/\lambda$. In the last step we introduced B as the displacement between both slits along the slit screen, as well as the angular displacement α between the detector center and the considered point on the detector plane. For visual clarification on the notation, I refer to Figure 2.1.

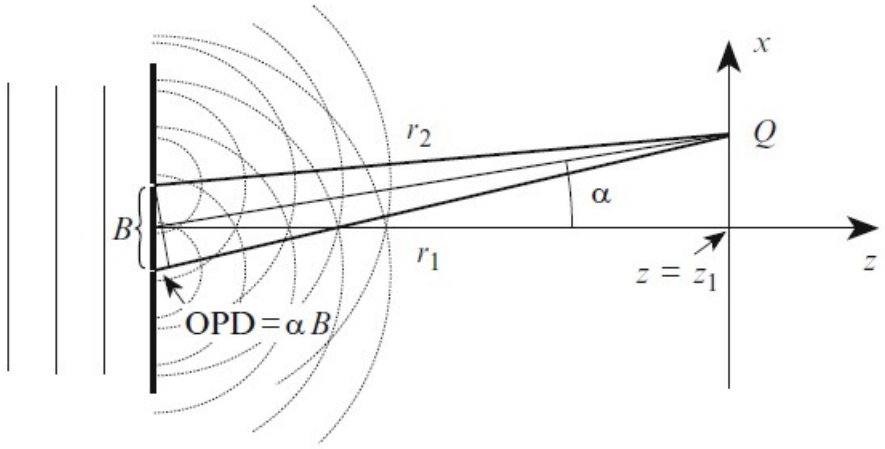

Figure 2.1.: The principal geometry of Young's double slit experiment still serves to illustrate the basic operating principle of current stellar interferometers. The superposition of two coherent spherical waves, emitted from two illuminated slits, leads to a sinusoidal modulation of intensity across the detector, resulting in a pattern of interference fringes. The interference fringes are the primary observable of an interferometer. **Image Credit:** Glindemann (2011)

2.1.1. Interferometric visibility

The periodic intensity modulation described by equation 2.9 gives rise to a pattern of alternating bright and dark fringes. While the mechanics of superposition in a telescope-based interferometer are technically different from the simple double slit experiment, they remain conceptually analogous, and ultimately these interference fringes are the principal observable recorded by an astronomical interferometer. In order to understand how they encode the position and spatial properties of the emission source, it is useful to first consider how the fringes relate to the coherence of the light.

Two beams are considered mutually coherent if they have a constant relative phase and can interfere with each other. The formation of a fringe pattern in the double slit experiment is a manifestation of the coherence of the light emerging from both slits and is tied to the slit displacement B. If B was increased to the point that the optical path difference between the two beams were to exceed the coherence length, the fringe pattern would be lost. Coherence between two electromagnetic signals can be quantified through the mutual coherence function:

$$\Gamma(\mathbf{r}_1, \mathbf{r}_2, \tau) \propto \langle E(\mathbf{r}_1, t+\tau) E^*(\mathbf{r}_2, t) \rangle \,, \tag{2.10}$$

which is proportional to the correlation between the electric fields of the two signals. This general expression considers both spatial coherence, i.e. between the two signals located at different positions $\mathbf{r}_1$,$\mathbf{r}_2$, as well as the temporal coherence between signals with a given time delay τ. The latter case corresponds more to the classical setup of a Michelson-Interferometer,

in which a single beam is brought to interference with a delayed instance of itself via beam splitting and subsequent manipulation of the optical path. This section will keep the focus on the concept of spatial coherence, as it is more immediately relevant to the case of two-telescope interferometry.

In astronomical interferometry, the same wavefront is sampled at the two telescope positions $\mathbf{r}_1$,$\mathbf{r}_2$, If there is no time delay between the measurement at both telescopes, i.e. they receive the light simultaneously, the correlation function simplifies to

$$\Gamma(\mathbf{r}_1, \mathbf{r}_2) \propto \langle E(\mathbf{r}_1) E^*(\mathbf{r}_2) \rangle \,, \tag{2.11}$$

describing now solely the spatial coherence between both electric field components. In this case, instead of Γ, we also write this as $\tilde{v}(\mathbf{r}_1, \mathbf{r}_2)$, as it is more commonly known as the complex visibility function.

The complex visibility function is of pivotal importance to astronomical interferometry due to the Van Cittert-Zernike theorem. The theorem states that for an incoherent source at large distances, the complex visibility function is given by the Fourier transform of the object's brightness distribution I($\mathbf{x}$):

$$\tilde{v}(\mathbf{B}) = \int I(\mathbf{x}) \exp\left(-2i\pi \frac{\mathbf{xB}}{\lambda}\right) dx. \tag{2.12}$$

Here $\mathbf{B}$ is the relative displacement vector, $\mathbf{B} = \mathbf{r}_1 - \mathbf{r}_2$. We refer to this as the baseline between the telescopes. The position vector of a point in the brightness distribution on the sky plane is referred to as $\mathbf{x}$. While a rigorous derivation of Eq. 2.12 is beyond the scope of this introduction, it is useful to consider the implications of the theorem. Suppose that the brightness distribution I($\mathbf{x}$) behaves as a perfect point source at the center of the coordinate system, with I($\mathbf{x}$)=$F \times \delta(\mathbf{x})$. F here is an arbitrary flux value received by the telescopes from the point source. The Fourier integral then evaluates to F at any baseline length,

$$\tilde{v}(\mathbf{B}) = \int F\delta(x) \exp\left(-2i\pi \frac{\mathbf{xB}}{\lambda}\right) dx \tag{2.13}$$

$$= F \exp\left(-2i\pi \frac{\binom{0}{0} \cdot \mathbf{B}}{\lambda}\right) \tag{2.14}$$

$$= F, \tag{2.15}$$

meaning two spatially displaced instances of electromagnetic waves emitted by a point source are completely correlated. The coherent flux is then equal to the total flux received from the

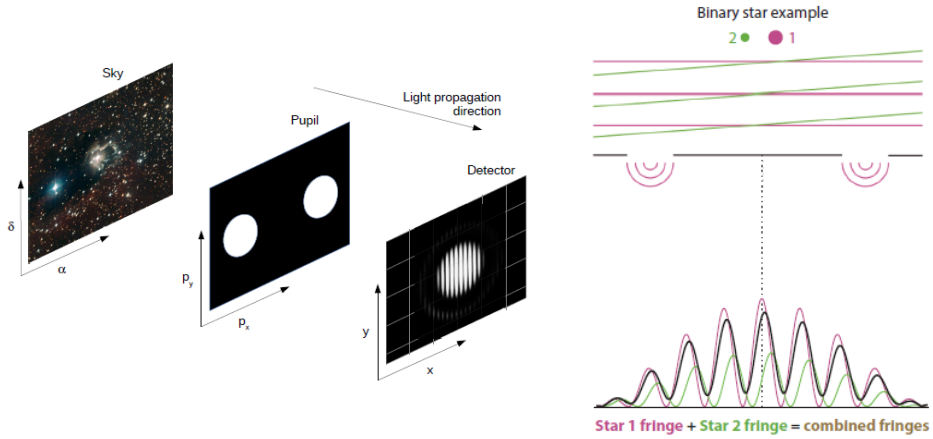

Figure 2.2.: **Left:** Principle of interferometric observations. A sky plane image of some object, represented by an intensity distribution in the telescope field of view, is observed through two telescope pupils seperated by some baseline B. The light from both pupils is brought to interference at the detector, where a set of interference fringes are recorded. **Image credit:** Millour (2014)
Right: Schematic representation of the phase shift introduced by a positional offset of a source, as well as the detrimental effect of incoherent superposition of light from a more resolved object on the contrast of the resulting fringe pattern. **Image credit: Eisenhauer et al. (2023)**

emission source and the interference fringe pattern recorded by the instrument will exhibit the strongest possible contrast between dark and light fringes, as all incoming emission contributes to the pattern. Any brightness distribution that deviates from the centered point source-like geometry will lead to a reduction in the ratio of coherent flux to total flux and thus weaken the fringe contrast. To illustrate this, consider the case of two point sources, which may for example represent a system of individually unresolved binary stars. The first binary component is again centered, the second one is now offset by some angular distance. Due to the angular offset, the individual interference pattern of the secondary source is phase shifted and incoherently adds to the first, blurring the resulting combined fringe in the process. The principle is graphically depicted in Figure 2.2.

This idea can be expanded to conceptualise the fringe formation from any spatially extended source. Instead of a point source, picture now a resolved stellar surface. The brightness distribution is essentially formed by a number of competing point sources with different flux weights, which dilute the resulting interference pattern. We see from this consideration that there is a direct link between the "resolvedness" of an astronomical object, observed at a certain baseline length, and the formation of the interference pattern. The Van Cittert - Zernike theorem describes how this link is used to encode the spatial properties of the brightness distribution in the complex visibility function.

In optical interferometry, a normalised visibility function is typically used instead of the ab-

solute correlated flux to quantify the connection between fringe contrast and spatial properties of the source:

$$\tilde{V}(\mathbf{B}) = \frac{\int I(\mathbf{x}) \exp(-2i\pi \frac{\mathbf{xB}}{\lambda})\, dx}{\int I(\mathbf{x})\, dx}, \tag{2.16}$$

This normalised complex visibility function is the fundament for any form of interferometric data analysis, as all practical interferometrical observables are derived from the complex visibilities. Specifically, as a complex quantity, it features both an amplitude V and a phase component ϕ,

$$\tilde{V}(\mathbf{B}) = V \exp(i\phi), \tag{2.17}$$

which encode different types of information and can thus effectively be treated separately in many cases.

Visibility amplitude

The amplitude V(u,v) of the complex visibility function $\tilde{V}$(u,v), from here on simply referred to as visibility[3], quantifies the ratio of the coherent flux to the total flux coming from the object:

$$F_{coherent} = V \times F_{total}. \tag{2.18}$$

A normalised visibility amplitude of 1 signifies that the received flux is completely coherent. Conversely, a normalised visibility of 0 means that the received flux is completely incoherent and that no interference pattern is formed. Information about the spatial properties of the source can be extracted in the intermediate regime of "partially" resolved sources, for which the normalised visibility amplitudes lies between 0 and 1. The visibility amplitude thus directly quantifies the strength of the fringe contrast:

$$V = \frac{I_{max} - I_{min}}{I_{max} + I_{min}}, \tag{2.19}$$

where I_{min} and I_{max} refer to the brightness of the dark fringe minimum and the bright fringe maximum, respectively. One can associate measurements of the visibility to the size parameters of some source object by presuming certain assumptions about the morphology of its brightness

[3] By convention, interferometrists often refer to the amplitude of the complex visibility function simply as "visibility". This convention will be used throughout this work: If no additional qualification is given, "visibility" will always denote the absolute value of the complex visibility function. There is not much need to recall the full complex visibility beyond this introduction, since phase and amplitude are largely processed individually, but I will explicitly refer to the complex visibility where needed to avoid ambiguity.

distribution. Due to the mathematical attributes of the Fourier transform, in particular the additivity property, one can construct complicated geometric visibility models from relatively simple building blocks, such as point sources, rings or disks. The simplest case of an extended source defined in such a way is again a binary system consisting of two point sources at positions $\mathbf{x}_1, \mathbf{x}_1$:

$$I(\mathbf{x}) = F_1\delta(\mathbf{x}_1) + F_2\delta(\mathbf{x}_2) \tag{2.20}$$

Computing the Fourier transform of this distribution yields:

$$|V|^2 = \frac{1 + f^2 + 2f\cos\left(\frac{2\pi}{\lambda}\mathbf{Bs}\right)}{(1+f)^2}, \tag{2.21}$$

where $\mathbf{s} = \mathbf{x}_1 - \mathbf{x}_2$ is the separation vector and f=$\frac{F_2}{F_2}$ the flux ratio between the stars. See Berger and Segransan (2007) for an explicit derivation. If the visibilities are probed at a sufficient number of baselines, it is possible to fit the separation and flux ratio of the system. This principle extends to other, more complex geometries of I($\mathbf{x}$), and can be used to extract the sizes of disks, rings and other morphologies, as will be discussed in more detail in Chapter 3.2.

Visibility phase

The phase of the complex visibility is directly related to a positional offset on the sky plane. Consider again the case of a point source with I($\mathbf{x}$)=Fδ($\mathbf{x}$), for which we found $\tilde{v}$($\mathbf{B}$)=F. Now suppose the point source is located off-center at some position $\mathbf{x}_0$:

$$I(\mathbf{x} - \mathbf{x}_0) = F\delta(\mathbf{x} - \mathbf{x}_0) \tag{2.22}$$

For this system we equally easily arrive at the normalised complex visibility function by again directly computing the Fourier integral:

$$\tilde{V}(\mathbf{B}) = \frac{\int F\ \delta(\mathbf{x} - \mathbf{x}_0)\ \exp(-2i\pi\frac{\mathbf{xB}}{\lambda})\ dx}{\int F\ \delta(\mathbf{x} - \mathbf{x}_0)\ dx} \tag{2.23}$$

$$\Longleftrightarrow \tilde{V}(\mathbf{B}) = \frac{F\ \exp(-2i\pi\frac{\mathbf{x_0B}}{\lambda})}{F} \tag{2.24}$$

$$\Longleftrightarrow \tilde{V}(\mathbf{B}) = \exp(-2i\pi\frac{\mathbf{x}_0\mathbf{B}}{\lambda}) \tag{2.25}$$

The phase of the complex visiblity is then

$$\phi = \arg(\tilde{V}) \tag{2.26}$$

$$= -2\pi \frac{\mathbf{x}_0 \mathbf{B}}{\lambda} \tag{2.27}$$

$$= -2\pi \frac{x_0 B}{\lambda} \cos(\gamma), \tag{2.28}$$

where $\gamma = \sphericalangle \mathbf{x}_0 \mathbf{B}$ is the angle between the position vector of the point source on the sky plane and the projected baseline vector. $x_0 \cos(\gamma)$ is then the component of the position vector as projected onto the baseline vector. In other words, by measuring the phase of the interference pattern with the interferometer, we could in theory reconstruct the position of the point source by solving

$$x_0 \cos(\gamma) = -\phi \frac{\lambda}{2\pi B} \tag{2.29}$$

for two baselines with orthogonal orientations. While this result is specific to the case of a point source, it has clear implications for any generalised brightness distribution $I(\mathbf{x})$. If we consider again the case of two unresolved binaries, we can express their normalised complex visibility function as

$$\tilde{V}(\mathbf{B}) = \frac{F_1 \exp(-2i\pi \frac{\mathbf{x_1} \mathbf{B}}{\lambda}) + F_2 \exp(-2i\pi \frac{\mathbf{x_2} \mathbf{B}}{\lambda})}{F_1 + F_2}, \tag{2.30}$$

where we used the previous result for the single point source and the linearity property[4] of the Fourier transform to arrive at the total complex visibility function. After substituting $f_{1,2} = \frac{F_{1,2}}{F_1 + F_2}$ and $\phi_{1,2} = -2\pi \frac{\mathbf{x_{1,2}} \mathbf{B}}{\lambda}$, a Taylor expansion up to first order yields:

$$V_{1,2} = f_{1,2} \exp(i\phi_{1,2}) \approx f_{1,2}(1 + i\phi_{1,2}). \tag{2.31}$$

With this we can write an approximate equation for the total complex visibility

$$\tilde{V}(\mathbf{B}) \approx (f_1 + f_2) + i(f_1\phi_1 + f_2\phi_2) \tag{2.32}$$

$$= 1 + i(f_1\phi_1 + f_2\phi_2) \tag{2.33}$$

$$\approx \exp(i(f_1\phi_1 + f_2\phi_2)). \tag{2.34}$$

[4] $FT(I_1 + I_2) = FT(I_1) + FT(I_2)$, see Berger and Segransan (2007) for for other relevant properties.

In the last step we again used the Taylor expansion in order to obtain an approximate expression for the total visibility phase as before:

$$\phi = \arg(\tilde{V}) \tag{2.35}$$

$$\approx (f_1\phi_1 + f_2\phi_2) \tag{2.36}$$

$$= -\frac{F_1 2\pi\frac{\mathbf{x_1 B}}{\lambda} + F_2 2\pi\frac{\mathbf{x_2 B}}{\lambda}}{F_1 + F_2}. \tag{2.37}$$

By rewriting this equation to

$$-\phi\frac{\lambda}{2\pi\mathbf{B}} \approx \frac{F_1\mathbf{x_1} + F_2\mathbf{x_2}}{F_1 + F_2} \tag{2.38}$$

$$= \mathbf{x_{pc}} \tag{2.39}$$

we finally obtain a relationship between the total visibility phase ϕ, and the barycenter of the combined brightness distribution, also more commonly referred to as the *photocenter* $\mathbf{x_{pc}}$.

It is simple enough to intuitively argue that this principal connection between phase and photocenter will be hold for any brightness distribution by considering that any image is essentially made up of individual pixels with different flux weights that behave similarly to a combined system of point sources. It is also possible to give a more general proof for this writing down a series expansion up to first order for a generalised complex visibility function:

$$\tilde{v}(\mathbf{B}) = \int I(\mathbf{x}) \exp\left(-2i\pi\frac{\mathbf{xB}}{\lambda}\right) dx \tag{2.40}$$

$$\approx \int I(\mathbf{x})\, dx - i2\,\frac{\mathbf{B}}{\lambda}\int \mathbf{x}\, I(\mathbf{x})\, dx. \tag{2.41}$$

One can argue similarly to the simple binary case that

$$arg(\tilde{v}) = \arctan(\Im\tilde{v}/\Re\tilde{v}) \approx (\Im\tilde{v}/\Re\tilde{v}) \tag{2.42}$$

$$= -2\pi\frac{\mathbf{B}}{\lambda}\frac{\int \mathbf{x}\, I(\mathbf{x})\, dx}{\int I(\mathbf{x})\, dx}, \tag{2.43}$$

where the integral again defines the photocenter of the brightness distribution. The restriction to the zeroth and first order terms is a good approximation in the regime of "marginally resolved"

objects, where $\mathbf{xB} \ll 1$. A more explicit argument, including the computation of the derivatives for the Taylor expansion in the general case, is presented, for example, in Jankov et al. (2001).

In real-world observations, using the absolute visibility phase to obtain a reliable estimate of the photometric barycenter position is not possible. As will be explained in more detail in Section 2.1.3, atmospheric turbulence introduces randomised short term phase shifts to the absolute phase, which effectively scramble the therein contained information beyond immediate recovery. In practise, this issue is addressed with the introduction of differential observables, namely the *differential phases* and the *closure phases*.

Differential phases

Differential phases are useful when analysing substructures that are restricted to specific wavelength ranges, like absorption or emission lines, which are connected to physically distinct regions with their own photocenters. The basic premise of this observable is that the atmospheric[5] influence is roughly equivalent at each wavelength and is removed by subtracting the phase at one wavelength from the phase at a different wavelength. The differential phase Φ is in practise then computed as the phase of some feature-specific wavelength channel subtracted by a continuum reference phase which is usually taken just outside the feature:

$$\Phi = \phi_{feature} - \phi_{cont} \tag{2.44}$$

$$= -(2\pi \frac{\mathbf{B}\mathbf{x}_{\mathbf{feature}}}{\lambda_{feature}} - 2\pi \frac{\mathbf{B}\mathbf{x}_{\mathbf{cont}}}{\lambda_{cont}}) \tag{2.45}$$

$$\approx -2\pi \frac{\mathbf{B}}{\lambda}(\mathbf{x}_{\mathbf{feature}} - \mathbf{x}_{\mathbf{cont}}), \tag{2.46}$$

where in the last step we assumed that the difference in wavelength between the feature and the reference channels is numerically small enough that $\lambda_{feature} \approx \lambda_{cont} = \lambda$ to simplify the equation. The differential phase then tracks the relative photocenter offset $\mathbf{x}_{\mathbf{feature}} - \mathbf{x}_{\mathbf{cont}}$ between the barycenter associated with the feature and the barycenter associated with the underlying continuum. As a special case, if the photocenter of the continuum is well-centered in the field of view (i.e. it has a non-perturbed phase of zero), the differential phase then recovers the absolute visibility phase and the absolute photocenter position of the feature-specific region. In this work, the term always specifically refers to the differential phases of the Brγ spectral line with respect to the adjacent continuum.

[5] In practice there is also an additional phase shift contribution due to instrumental vibration, but for the purpose of this chapter it is not necessary to distinguish between different origins for random phase variations.

Closure phase

Another way to extract some degree of positional information from the scrambled phase is via the use of closure phases. Consider a triplet of telescopes, all of which are connected to each other with one interferometric baseline each so that the three baselines form a closed triangle. Closure phases are then computed by essentially adding up the different phases measured with the three baselines. The reasoning here is similar to the one behind the differential phase: Since the phase shifts induced by the perturbations are equal but opposite in direction for each adjoining baseline, summing up the phases will remove the atmospheric contribution. The usefulness of this approach when compared to the differential phase lies with the fact that information about the continuum phase can be obtained from the closure phase. This comes at the disadvantage that the closure phase itself is not directly related to a position on the sky any more.

Following the argument presented in Monnier (2007), in order to quantify the impact of turbulence on the visibility, we first introduce the complex gain $\tilde{G}_i$. The gain phase ϕ_i^G represents all phase shifts due to variations in optical path length, such as from fluctuations in air density, that are specific to the i-th telescope. The gain amplitude G_i describes how the measured intensity at the detector is affected by turbulence. A hypothetical direct measurement of the electric field of the incident wavefront would yield the result of the gain applied to the unperturbed signal:

$$\tilde{E}_i^{\,measured} = \tilde{G}_i \tilde{E}_i^{\,true} = G_i e^{i\phi_i^G} \tilde{E}_i^{\,true} \tag{2.47}$$

This translates to the complex visibility, which is related to the electric field via $\tilde{V}_{ij} \propto \tilde{E}_i \cdot \tilde{E}_j^*$, as:

$$\tilde{V}_{ij}^{\,measured} = G_i e^{i\phi_i^G} \tilde{E}_i^{\,true} \cdot G_j e^{-i\phi_j^G} \tilde{E}_j^{\,*true} \tag{2.48}$$

$$= G_i G_j e^{i(\phi_i^G - \phi_j^G)} \tilde{E}_i^{\,true} \tilde{E}_j^{\,*true} \tag{2.49}$$

$$= G_i G_j e^{i(\phi_i^G - \phi_j^G)} \tilde{V}_{ij}^{\,true} \tag{2.50}$$

The total atmospheric phase shift $(\phi_i^G - \phi_j^G)$ for the ij-th baseline then only depends on the individual phase shifts caused by atmospheric variations above the i-th and j-th telescope. Consider now a closed triangles composed of telescopes 1,2,3 with the connecting baselines 1-2,1-3,2-3. Suppose that the atmosphere above all telescopes is perfectly still, except for telescope 2, where turbulence leads to a random phase shift. This would affect baselines 1-2 and 2-3, but leave the phase measured along baseline 1-3 unperturbed.. The phase shift detected at the other two

baselines is equal in magnitude but opposite in direction:

$$\tilde{V_{12}}^{measured} = G_1 G_2 e^{i(0-\phi_2^G)} \tilde{V_{12}}^{true} \tag{2.51}$$

$$\tilde{V_{23}}^{measured} = G_2 G_3 e^{i(\phi_2^G-0)} \tilde{V_{23}}^{true}. \tag{2.52}$$

The measured phase along baseline 1-2 would then be shifted by $-\phi_2^G$, and by $+\phi_2^G$ along baseline 2-3. The closure phase

$$\phi_{123} = \phi_{12}^{measured} + \phi_{13}^{measured} + \phi_{23}^{measured} \tag{2.53}$$

$$= (\phi_{12}^{true} - \phi_2^G) + (\phi_{13}^{true} + \phi_2^G) + \phi_{23}^{true} \tag{2.54}$$

$$= \phi_{12}^{true} + \phi_{13}^{true} + \phi_{23}^{true}, \tag{2.55}$$

is then free of the perturbation terms and only reflects the properties of the source itself.

The closure phase first and foremost encodes of how much a brightness distribution deviates from centrosymmetry. For a centrosymmetric source located at the center of the field of view, the photocenter by defintion is also found at the center of the field of view, and all phases measured along any given baseline orientation will be at zero degrees and the closure phase will then also be at zero degrees[6]. Conversely, non-zero closure phases indicate that the intensity map of the source features some form of asymmetry in the continuum. This information can be used to attempt to fit asymmetries through advanced visibility modelling, or in interferometric image reconstruction.

2.1.2. Sampling the uv plane

Using $\mathbf{x} = \binom{\alpha}{\beta}$ and $\mathbf{B} = \lambda\binom{u}{v}$, Eq. 2.12 can expressed in dependence of uv-coordinates, as usually presented in standard treatises on interferometry:

$$\tilde{v}(u,v) = \int I(\alpha,\beta) \exp(-2i\pi(u\alpha + v\beta) d\alpha d\beta \tag{2.56}$$

α,β quantify the position of a point on the sky plane in angular coordinates. The corresponding coordinates in Fourier space are designated u and v. They are used to define the brightness distribution in the spatial frequency domain and are reciprocal to the sky plane coordinates. Since the

[6]This argument relies on the straightforward and intuitive relationship between phase and position presented in Eq. 2.28. For completeness sake it should be pointed out that the imaginary parts of the Fourier transform vanish at either 0 deg or 180 deg phase, and that the closure phase of a centrosymmetric object can then also be either at 0 deg or 180 deg.

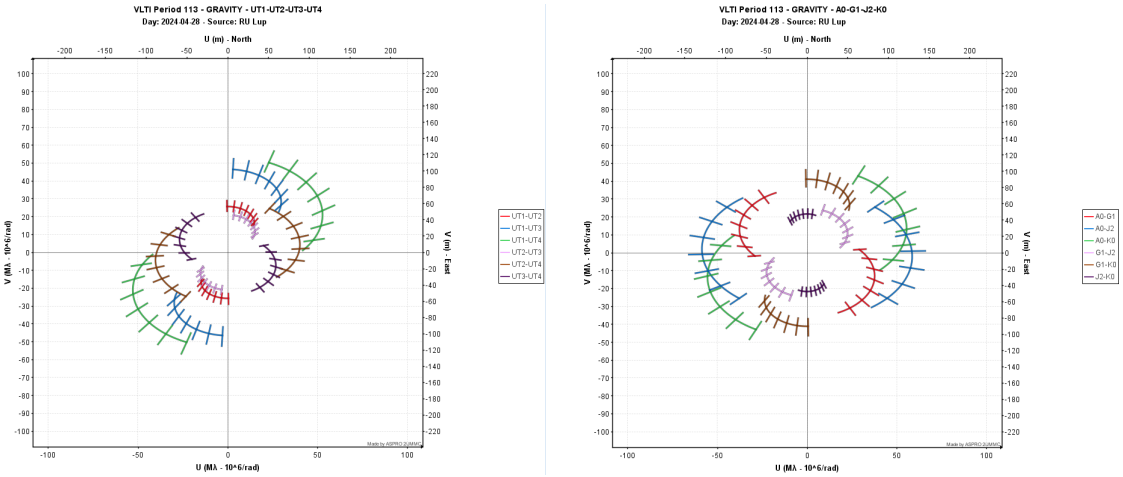

Figure 2.3.: Exemplary uv plane coverage of different baseline configurations of VLTI GRAVITY for a hypothetical observation of the young star RU Lup. The radial dashes indicate the position of a baseline at a certain point in time during the observable period of the target, while the solid tracks show the change in baseleline position as a function of time due to the rotating sky plane.
Left: uv coverage provided by the four UTs. The UTs are immovable and the coverage is thus only variable with the Earth's rotation.
Right: The extended configuration of the ATs. The ATs allow more flexibility in uv coverage as they are movable and four different telesope configurations are offered, which may probe the target at different directions and spatial resolutions.
Image Credit, right: ASPRO, https://www.jmmc.fr/spip.php?rubrique59

latter are given in angular unites, the spatial frequencies are given in units of inverse radians. The uv coordinates are projections of the separation vector **B** onto the pupil plane, i.e. each spatial frequency pair (u,v) is associated with a physical baseline defined by coordinates (B_u, B_v). Note that the baseline here refers to the projected separation between the telescopes relative to the observed object, which depends on its elevation above the horizon. For an object at zenith, the projected baseline equals the on-ground baseline, while for an object just above the horizon, the projected separation is effectively zero, see also Fig. 2.5. This distinction has certain practical implications, as will be explained in the following.

On a basic level, an astronomical interferometer is a tool that samples the Fourier components of a sky plane brightness distribution at those regions accessed by the orientation and length of its baseline. As a consequence, the spatial resolution of the interferometer scales with the length of the baseline as $\frac{\lambda}{2B}$. While long baseline lengths allow the interferometer to explore spatial frequencies that are far beyond the capacity of any indivdual telescope and thus offer unprecedented spatial resolution, this comes at a cost. Whereas a telescope gathers information about large range of spatial frequencies, the interferometer is restricted to those spatial frequencies defined by the projected baseline at any given moment. A two-telescope array, taking a single

measurement at a single point in time at a single wavelength will only probe the observed system at a single spatial frequency along a single axis. While this is an extreme case, the principle difficulty is the same for all optical interferometery in use today: Coverage of the uv plane is typically sparse, which limits the amount of information accessible with an interferometer and necessitates, for example, the need to make assumptions about the morphology of the brightness distribution in order to obtain estimates of its properties.

There are a number of straightforward ways how to increase uv coverage. As the part of the uv space accessed by the instrument depends on the effective baseline length, stretching the observation time will increase the number of uv points. The target's apparent motion on the sky due to earth's rotation then leads to a variation in baseline length and thus increase the number of spatial frequencies probed throughout the night. Another, possibly more obvious solution, is the addition of more telescopes to an interferometric array, which will increase the number of baselines and thus uv points. Increasing the wavelength range of the observation is also possible if the source of interest is a continuum emitter and the scientific analysis is not tied to specific wavelengths, since the spatial frequencies depend directly on the wavelength with $u = \frac{B_u}{\lambda}$.

Finally, there are ways to mitigate the problems posed by sparse uv coverage. Interferometric imaging, which aims to reconstruct the brightness distribution from visibility amplitudes and phase information directly, has benefitted from technical improvements to its algorithms. The use of radiative transfer simulations to derive synthetic observables for specific physical mechanisms may also provide a way forward to better interpret the data gathered by the interferometer by directly connecting the physics of the region with the visibility signatures without the use of geometric models.

2.1.3. The influence of atmospheric conditions

The simple picture of Young's double slit experiment is a useful model to understand the principle guiding the formation of interference fringes, but ultimately deviates significantly from practical astronomical interferometry. Environmental and instrumental factors introduce new complications which restrict the technical applications of interferometry in different ways.

Under real observing conditions, the idealised model of an interferometer measuring the spatial coherence of a flat wavefront at two positions starts to break down due the influence of atmospheric perturbations. Effectively randomised fluctations in air density affect the optical path above the telescopes and lead to distortions along the wavefront that will negatively affect spatial coherence between the received flux at the two telescopes. The effects of atmospheric turbulence also impose a limit on the detector integration time of the interferometer. Since the fluctuations are also time variable, the received signals are only coherent on short time scales defined by the atmospheric coherence time τ_0, which varies with observing conditions. Adaptive

optics and fringe tracking systems were developed to address these particular issues.

Adaptive optics

Without any form of correction for atmospheric perturbation, the largest useful telescope aperture is tied to the Fried parameter r_0. This quantity, also referred to as atmospheric coherence length, is defined as the diameter of a circular area above the aperture, for which the average root mean square wavefront variation caused by turbulence is exactly 1 rad. Since the change of the refractory index induced by the air density fluctuations is wavelength-specific, the Fried parameter also has a wavelength dependency of $r_0 \propto \lambda^{6/5}$. Increasing the diameter of the aperture significantly beyond r_0 will lead to seeing-limited observations, as the blur caused by the instrumental point spread function to a point source increases by a factor $\frac{D}{r_0}$.

For small telescope interferometers, this is not necessarily an issue. The Fried parameter at K-band wavelengths is on the order of 1 m under good seeing conditions. As a consequence, interferometers such as the CHARA array with its 1 m aperture telescopes are not primarily limited by wavefront distortions in terms of the limiting magnitude of potential target objects. Large telescopes, such as used in the Keck Interferometer with their 10 m primary mirrors, on the other hand stand to profit more from active corrections to the perturbations, as with increasing diameter a larger number of turbulent air cells are gathered above the aperture.
Making effective use of large telescopes with diameters beyond the Fried parameter requires the use of adaptive optics (AO) systems for both direct imaging and interferometry. Any AO system features two principal components. First, it requires some kind of sensor that will measure the atmospheric wavefront perturbations of some bright reference object. Second, the information obtained about the wavefronts is then passed to a deformable mirror, where Piezo elements continuously adjust the mirror surface to actively compensate for the distortions in real time.

Fringe tracking

Interferometry in general suffers from a problem of limited exposure times more so than most other fields of observational astronomy. Aside from the geometrical optical path difference introduced by the incident angle of the wavefront, there are additional time-dependent fluctations in OPD due to the influence of the turbulent atmosphere and instrumental vibrations. Since the detection of a fringe pattern is dependent on a nigh-constant phase relationship between the interfering signals, the exposure time must be short enough to minimise the effect of these perturbations. If the short-term optical path variations are dominated by atmospheric turbulence, the coherence time acts as effective upper limit to the integration time for the fringes. However, even at the most suitable locations on earth, the coherence time at optimal conditions is on the order of 20 ms (Eisenhauer et al., 2023), which would limit the sensitivity of the instrument.

These atmospheric limitations can be overcome by the use of adaptive optics systems and a technique called fringe tracking.

While the adaptive optics systems work at the individual telescopes to correct the incident wavefront for atmospheric distortions, fringe tracking aims to compensate for the phase delay between the two interfering signals caused by the instrumental or atmospheric "piston", i.e. the difference in optical path length. In order to do so, the current fringe phase is measured with a phase sensor and compared to a reference fringe position. The measured difference is then passed on to a fast piezo-driven mirror, which will adjust the OPD at high frequency to stabilise the fringe contrast against short term delay fluctuations.

2.2. The VLTI and GRAVITY

2.2.1. An introduction to the VLTI

The Very Large Telescope (VLT) is one of the premier astronomical observational installations in operation today. Since the turn of the millenium, it has delivered numerous high impact results across multiple fields of research, including star formation, the detection of exoplanets and observations of the galactic center. Located on top of Cerro Paranal in the Chilean Atacama desert, it is operated by the European Southern Observatory (ESO) and is one of the world's primary high end tools to study the southern sky at optical and infrared wavelengths. The VLT array consists of four fixed Unit Telescopes (UTs) with 8.2 m primary mirrors, which can be used individually in conjunction with a number of spectographic instruments, such as SPHERE, VISIR, MUSE, or the X-Shooter [7] .

Alternatively, the light gathered by the four UTs can be combined interferometrically, forming possibly the most powerful infrared interferometric array currently available. The full set of telescopes and associated interferometric instruments, including four additional movable 1.8 m Auxilliary Telescopes (ATs), are collectively referred to as the Very Large Telescope Interferometer (VLTI). The main purpose of the VLTI is to unlock those regions of astrophysical interest through spatially resolved observations that lie far beyond the capabilities of even the most powerful telescopes in use today. As the spatial resolution of the interferometer scales with the length of the baseline between two telescopes, the VLTI can fully resolve any structure with an angular diameter of up to 2 milliarcseconds (mas) at 2 μm with its maximum UT baseline length of 130 m, exceeding the spatial resolution of any individual UT (50 mas at 2 μm) by an order of magnitude. By comparison, other top tier platforms such as the Center for High Angular Resolution (CHARA) array, with a maximum baseline of 330 m and six 1 m telescopes, can surpass

[7] Please refer to the documentation provided by ESO for a full list of operational instruments and their respective science cases: https://www.eso.org/sci/facilities/paranal/instruments.html

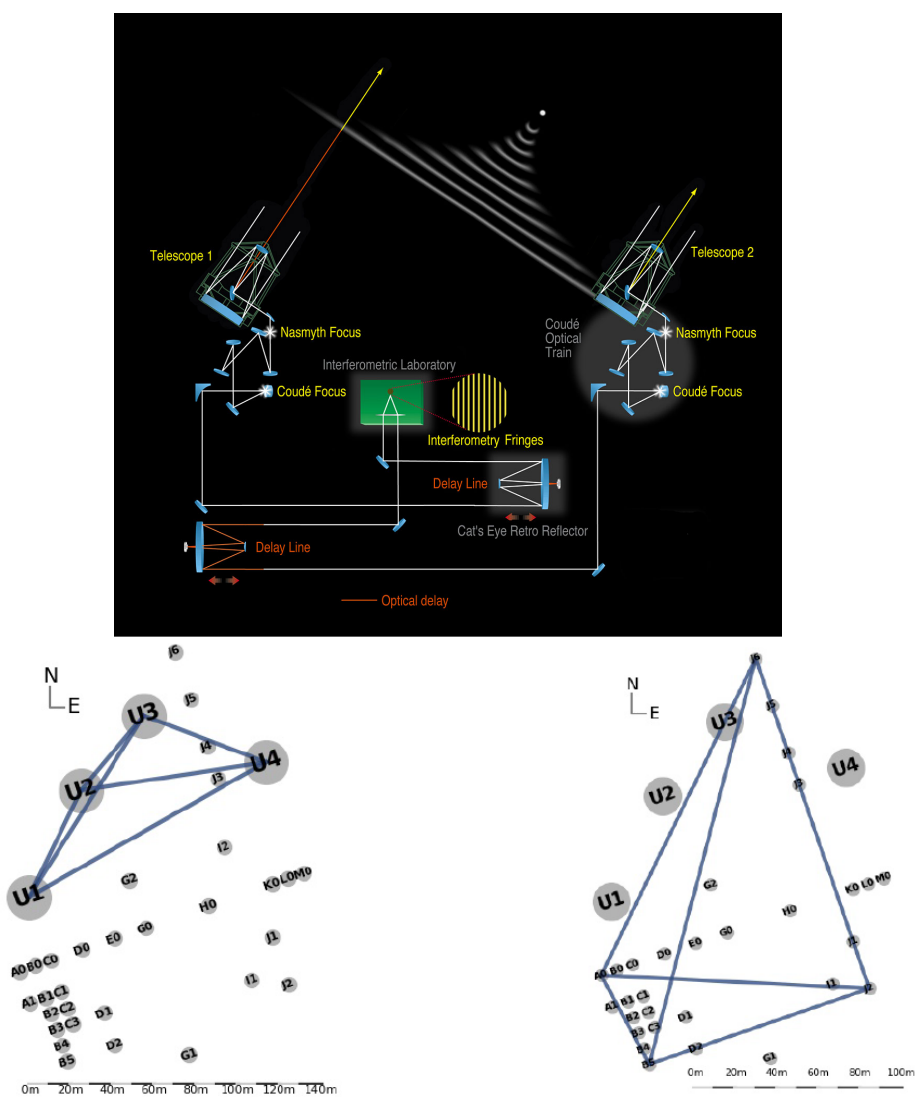

Figure 2.4.: **Top:** Schematic illustrating the basic principle of fringe recording with the VLTI.
Bottom left: On the ground positions of the VLTI Unit Telescopes (UTs) and the baselines spanning between them. The longest baseline between UT1 and UT4 measures 130.2 m.
Bottom right: The so-called "extended configuration" of the VLTI Auxilliary Telescopes (ATs). The ATs can be moved to the different positions indicated on the diagram. Four different total configurations are offered for regular VLTI operations.
Image credit: ESO, Top: https://www.eso.org/public/images/eso0020b/ Bottom: VLTI User Manual Issue 113.0

the VLTI in terms of spatial resolution or uv coverage, but fall short in terms of sensitivity, or vice versa as in the case of the Keck Interferometer (KI) (two 10.4 m telescopes with a single 85 m baseline) or the Large Binocular Telescope Interferometer (LBTI) (two 8.4 m telescopes

with a 23 m baseline).

The ATs are used exclusively as part of the VLTI. They suffer from lower sensitivity when compared to the UTs due to their much smaller diameters, and are thus more limited in their selection of potential targets. The exact limits depend on external factors such as the weather, and the specific instrument being used, and will be briefly discussed in the specific context of GRAVITY later on. The main advantage of the ATs lies with their more flexible positioning on movable tracks, which allows for different baseline configuration that may provide better coverage in the (u,v) plane than the fixed UTs, and additionally also provide a longer maximum baseline at up to 200 m on the ground for the largest configuration.

Interferometric operations of the VLTI are tied to three different current-generation instruments: MATISSE for near- to mid-infrared observations in the L (3.2 to 3.9 μm), M (4.5 to 5 μm), and N-bands (8 to 13 μm), PIONIER for near-infrared observations in the H-band (1.5 and 1.8 μm), and GRAVITY[8], to record interferometric fringes in the near-infrared K-band at wavelengths of 2 to 2.4 μm. All three instruments provide four-way beam combination solutions, meaning that interferometric measurements can be taken with all four telescopes (either UTs or ATs) simultaneously, providing interferometric visibilities amplitudes and phases for six baselines, and closure phases for four unique baseline triangles.

The basic operating principle of the VLTI is common to all of them: Two telescopes are pointed at the science target and sample the light of an incoming electromagnetic wavefront at two separate locations, spatially displaced by the effective baseline length B, which is equivalent to the on-ground baseline length, modulated by the angular distance from the local zenith. The signal is first corrected for atmospheric influence by the adaptive optics systems. The telescopes[9] are equipped with the following systems:

- Multi-Application Curvature Adaptive Optics (MACAO): Deformable mirrors for the UTs, designed to counteract atmospheric distortions of a wavefront through finely tuned adjustments to the mirror surface. To detect the distortions, the system comes with an optical Roddier wavefront curvature sensor.
- Coudé Infrared Adaptive Optics (CIAO): A set of UT infrared wavefront sensors designed for the use with GRAVITY, which work in conjunction with the deformable mirrors of MACAO.
- New Adaptive Optics Module for Interferometry (NAOMI): A set of deformable mirrors and optical wavefront sensors for use with the ATs.

[8]GRAVITY is not an acronym, but rather derives its name from one of the original primary science cases of the instrument: the study of the black hole at the center of the Milky Way galaxy, Sgr A*.

[9]With the impending introduction of GRAVITY+, GRAVITY observations will use a new adaptive optics system called GPAO

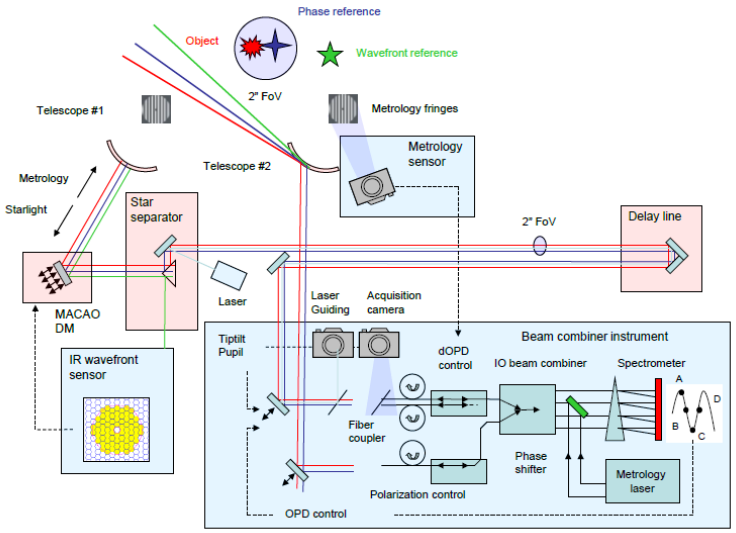

Figure 2.5.: Principal components and optical pathways of GRAVITY for the exemplary case of the UTs using the infrared adaptive optics system CIAO.
Image credit: ESO, GRAVITY User Manual Issue 114.0

The use cases for the UT AO sensors MACAO and CIAO depend on the target attributes and observing conditions. As an infrared sensor, the use of CIAO is primarily suited for observations of deeply embedded targets with no sufficiently bright optical AO guide star nearby. A detailed discussion of the advantages and disadvantages is presented in the VLTI manual published by ESO.

After correction through the adaptive optics, the light is then routed via optical mirrors towards the interferometric laboratory, where the beam combiner and other instruments are situated. Due to the geometrical difference in optical path length, see the top panel of Fig. 2.5, any given wavefront is sampled at two different points in time by the two telescopes that form any baseline. To compensate for this optical path difference, each telescope is equipped with a delay-line. The delay-line consists of a carriage-mounted, movable reflector device designed to flexibly adjust the optical path length. The hereby synchronised incident waves reach the laboratory, where they are brought to interference and a set of fringes is recorded. The characteristics of the beam combiner will be discussed for the specific case of GRAVITY in the following section.

2.2.2. GRAVITY

GRAVITY is the name given to a set of instrumental units, chief among them the Beam Combining Instrument (BCI), working together to allow for interferometric NIR K-band observations with the VLTI. It improves upon its predecessor instrument, the last-generation K-band beam

combiner AMBER, in a number of ways, such as increased uv-coverage by allowing the use of all six baselines simulatenously, and higher sensitivity limits due to improved adaptive optics, the adoption of a dedicated fringe tracker and dual beam interferometry.

At a basic level, a GRAVITY observation works as follows: A bright AO reference star is selected outside the telescopes field of view (2 arcseconds for UTs, 4 arcseconds for the ATs) with the star separators and fed to the wavefront sensors (either the optical sensor of MACAO or the infrared sensor of CIAO for the UTs, or the default sensors of NAOMI for the ATs). After correction of the distorted wavefront with MACAO's deformable mirrors, the light from both a phase reference target and the actual science target is guided to the beam combiner laboratory via the VLTI delay lines. Both objects are located within the telescopes field of view, but how the two beams are handled by the instrument depends on the chosen observation mode. GRAVITY effectively acts as two interferometers with separate beam combiners: The science channel (SC) combiner, which may record spectrally dispersed K-band fringes at one of three different spectral resolution modes (R $\approx$ 22, 500, 4000), and the fringe tracker (FT) (R $\approx$ 22). The instrument can be employed in either single field mode or dual field mode:

- Single field mode: Light from the same source is split 50:50 between FT and SC. For sufficiently bright targets, the fringe tracker can in this way be used to obtain very high accuracy measurements of continuum emission fringes, where spectral resolution is not a concern, while allowing for long integration times on the SC data to provide high resolution spectra and visibilities in order to study wavelength-dependent phenomena (e.g. spectral line emission, absorption features).

- Dual field mode: The fringe tracker records the fringes of a separate bright phase reference object and is then used to stabilise the fringes of a much fainter science target in the same atmospheric isopistonic patch (i.e. the angular area above the telescope with the same OPD). An additional distinction is to be made between the dual field on-axis and off-axis modes: The on-axis mode can be used when the phase reference and the science target are close, with an angular separation of up to 0.6 arcseconds for the UTs or 2.7 arcseconds for the ATs. The path of the light beam is in this case analogous to the single field mode, i.e. it passes the beam splitter and is reduced by 50% for each object. In off-axis mode, the angular separation needs to exceed 0.27 arcseconds (UTs) or 1.17 arcseconds (ATs). Here the light from the science target and fringe tracker target are separated by a roof-top mirror and 100% of the light of each source is then passed on to the instrument. The maximum angular separation corresponds to the telescope field of view.
  Additionally, there is the dual field wide mode, which uses the VLTI star separators to allow an angular separation of up to 30 arcseconds, i.e. the bright reference object can be outside the field of view of the telescopes. This mode currently does not allow for absolute

calibration of the data. Only differential interferometric quantities (differential visiblities, differential phases) can be extracted from these observations. Overleaf Example

There is some overlap between the dual field on- and off-axis separation limits. The limiting K-band magntiudes of SC and FT targets are dependent on the weather conditions and the observation mode. In UT single field mode and at optimal conditions (seeing ≤ 0.6), objects of up to 10 mag can be observed, while in bad conditions (seeing ≥ 1.4) the limit decreases to 8 mag (9 mag vs 7 mag for the ATs, respectively). In dual field mode, using a bright (≤ 10 mag) reference target for the fringe tracker, the limiting magnitude of the science object can be as high as 17.5 mag in off-axis mode (17 mag on-axis) for UT observations under optimal conditions[10].

In dual field mode, the delay line guides the light into a fibre coupler, where the field containing the phase reference and the science target is split and then passed on to the fringe tracker and science channel, respectively, by two separate mono-mode fibres. Both fringe tracker and science beam combiner come in the form of integrated optics chips, which instantaneously sample the fringes using the ABCD method. In this manner, a total of 24 spectra are recorded: one for each of the 6 baselines, sampled at four phase shifted points A,B, C and D. From these spectra, the interferometric observables (i.e. fringe contrast and phase) can be computed.

GRAVITY features a number of other subsystems that provide additional functions. The metrology laser system measures the differential optical path difference between the reference object and the science in dual field mode via split beam interference. The metrology laser is split into three beams, two of which are injected into the FT and SC beam combiners, while the third, stronger beam, is used to amplify the two comparively faint signals after they passed through the instrumental fibers. The beams are finally brought to interference in the pupil plane of the telescopes. This can be used to compute the phase difference and thus the positional offset between both objects, allowing for high precision astrometric measurements.

[10] A full breakdown is available on the ESO page: https://www.eso.org/sci/facilities/paranal/instruments/gravity/inst.html

3. Interferometric data analysis for VLTI GRAVITY

3.1. The GRAVITY spectral data

The treatment of the interferometric visibilities for the Brγ spectral line relies critically on knowledge of the Brγ spectrum itself. Although the complex visibilities are computed as part of the reduction process and already exist in a usable form in the reduced OIFITS file, a robust estimate of the normalised line-to-continuum flux is necessary to extract the pure Brγ emission region properties from the interferometric observables. The process will be described in more extensive detail in Section 3.2. For now it is sufficient to understand that the visibilities, as they are stored in the reduced file, encode information about both the total continuum region and the line emission region at each wavelength. In order to only consider the line emission component, the visibility in each wavelength channel needs to be corrected for the continuum contribution. In this section the steps taken to prepare the GRAVITY spectral data used in Gravity Collaboration et al. (2023b) will be outlined, along with a number of applied corrections, to illustrate one exemplary approach. Note that all steps here exclusively refer to the SC data of the respective observation unless explicitly mentioned otherwise.

3.1.1. Data preparation

Reading out the flux data from the OIFITS file will yield four individiual spectra for the four telescopes of the observation. Atmospheric variations above the different telescopes and other effects may lead to substantially different measured fluxes between them, but since only the continuum-normalised flux ratio is of interest for the visibility modelling, these discrepancies are of no immediate concern. It would be most accurate to produce merged spectra specific to each pair of telescopes and use the baseline-specific flux ratios to further treat the visibilities measured along that baseline. In practise, such a detailed approach is unnecessary as the line-to-continuum flux ratios are typically in strong agreement between all four telescopes. It is consequently sufficient to merge all four spectra into one single combined spectrum, which can

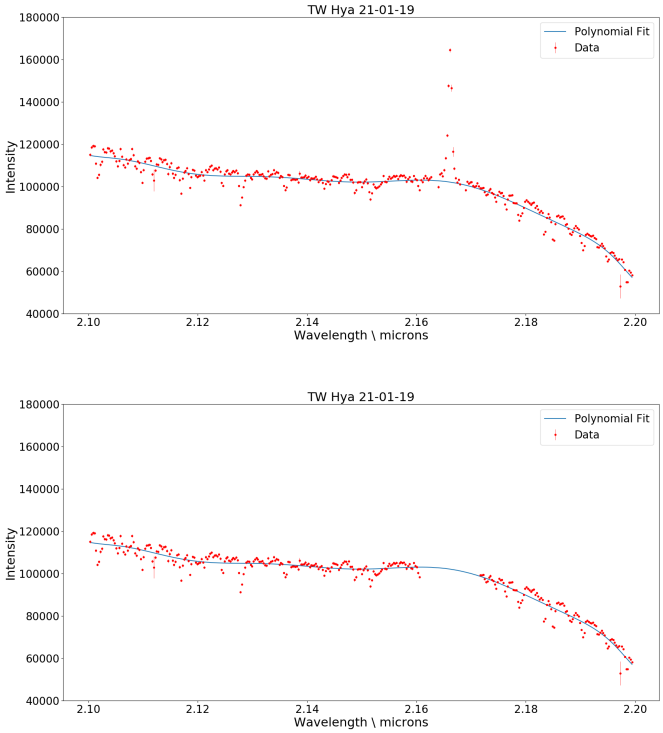

Figure 3.1.: The GRAVITY spectrum of the T Tauri sample object TW Hya.

Top: A polynomial function was fitted to the spectrum in order to fit the continuum level around the Brγ spectral line. The spectral data is then subsequently divided by the polynomial function to obtain a normalised spectrum.

Bottom: Higher order polynomials may end up fitting the base of the spectral line, which potentially removes characteristic asymmetries in the line shape. In order to avoid this effect, the fit was applied to version of the spectrum from which the Brγ line was removed.

be used globally with all baselines.

In GRAVITY high spectral resolution mode, the spectrum is recorded over a wavelength range from 1.98 to 2.4 microns across up to 1742 spectral channels. Channels with a signal-to-noise-ratio (SNR) below a threshold value are flagged by the pipeline and may be cleansed from the data. The flag is part of the OIFITS file and can be accessed in the OI_FLUX table via the keyworld "FLAG":

```
flags=hdu['OI_VIS',10].data.field('FLAG')
```

This will return an array with the shape of the wavelength table and a "True" or "False" entry for each wavelength. After removing flagged channels and other problematic entries, which may occur due to either problems with the raw data or as consequences of issues with the reduction process, the telluric and barycentric corrections are applied. These steps will be explained in

Sections 3.1.2 and 3.1.3, respectively.

A straightforward way to normalise the Brγ line to the continuum is to restrict the spectrum to a wavelength range in the general vicinity of the spectral feature and then fit a polynomial function to the data. The values of the polynomial then represent the continuum radiation and normalisation is achieved by simply dividing the spectrum by the polynomial:

$$S_{normed}(\lambda_i) = \frac{S(\lambda_i)}{f(\lambda_i)}. \tag{3.1}$$

$f(\lambda_i)$ is the fitted polynomial function, interpolated on the observational wavelength grid, and $S(\lambda_i)$ the observational flux value in each spectral channel λ_i.

When treating the data from the GRAVITY T Tauri Brγ study, a third degree polynomial was fitted to a range between 2.1 and 2.2 microns, see Fig. 3.1 for a concrete example of the YSO TW Hya. In addition, the Brγ peak itself was removed before fitting the polynomial to prevent overfitting the base of the spectral line. This particular step may not be necessary for all data sets, but if a spectral line features some form of asymmetry in the wings of the profile, retaining as much of the asymmetry as possible after normalisation may benefit from this procedure. This is particularly true when using higher degree polynomials, which have a tedency to "creep up" into the base of the spectral line.

Depending on the level of noise on the spectral data, it is possible to use the read-out values of the normalised spectrum in each channel as they are to evaluate the flux ratio at each wavelength. A more cautious approach would be to fit the spectral feature with an appropriate function to even out channel-by-channel fluctuations and approximate the underlying inherent flux ratio of the line. A double Gaussian function

$$f(x) = A_1 \exp(-\frac{(x-\mu_1)^2}{2\sigma_1^2}) + A_2 \exp(-\frac{(x-\mu_2)^2}{2\sigma_2^2}) + 1, \tag{3.2}$$

with amplitudes $A_{1,2}$, standard deviations $\sigma_{1,2}$ and means $\mu_{1,2}$ was used to fit the asymmetric line profiles commonly found among most of the objects of the GRAVITY T Tauri survey sample.

Finally, the spectral channels to be used for the visibility analysis need to be selected. In past interferometric studies of line emission, it was common to only consider the central channel of the line or use binning to determine one central component and one blue and redshifted component each. By contrast, for the GRAVITY T Tauri Brγ survey the full capacity of GRAVITY's high spectral resolution mode was employed. Here, a maximum range of ± 6 channels around the central line channel was defined to restrict the analysis to a spectral region largely unaffected by telluric absorption lines. Furthermore, an additional selection criterion was imposed: The flux in each of the 13 spectral channels was compared against the standard deviation σ_{Cont} of the adjacent continuum flux. Only if the line channel flux ratio was found to surpass a threshold of $1+1\sigma_{Cont}$, that channel was then further used in the visibility data analysis.

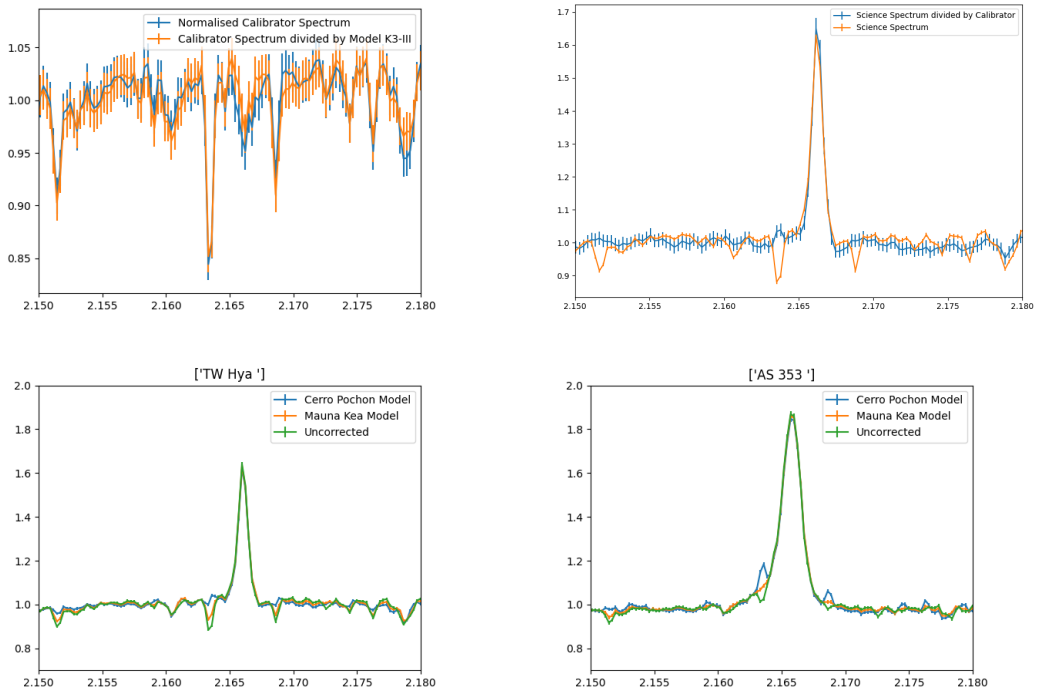

Figure 3.2.: **Top row:** Depicted on the left is the spectrum of the calibrator HD 95470 after division by a synthetic spectrum. Afterwards it was used to remove the telluric lines from the science object TW Hya (right). **Bottom row**: Two examples where the telluric lines were removed by use of synthetic atmospheric models instead. Despite the fact that both spectra were taken with the VLTI, different atmospheric models appear to be preferable for the two objects TW Hya and RU Lup shown here.

3.1.2. Telluric correction

The earth atmosphere features a number of weak absorption lines between 2.1 and 2.2 microns which can be largely attributed to the presence of carbondioxide (CO_2) and methane (CH_4) molecules, see Fig. 3.3. It is possible to correct the spectrum for these absorption features via the use of one of the available calibrator stars. Since any available calibrator was ideally observed in a similar patch of the sky at a similar time as the science object, it is in principle affected by atmospheric absorption to a similar degree, and the calibrator spectrum should feature the same absorption lines at similar line depth as the science spectrum. The calibrator spectrum may be normalised by a fitted polynomial as before, but if there are intrinsic stellar absorption features in the relevant wavelength range, then dividing the calibrator spectrum by a synthetic model of the calibrator spectral type is required first. Herbig stars as calibrators can, for example, be affected by this issue, since they commonly feature Brγ in photospheric absorption.

In practice, there may be issues that prevent the use of the calibrator objects for this purpose.

This was the case for most of the objects in the GRAVITY T Tauri study. Many of the calibrators for the sample objects were Herbig Ae/Be objects with broad photospheric absorption lines which spread into the telluric features, thus preventing the correction as described above. An alternative path to correct for telluric influences lies with the use of synthetic K-band atmospheric spectra. Since they come in the form of transmission coefficients per wavelength, the procedure is straightforward: After interpolating the atmospheric spectrum on the GRAVITY wavelength grid, the flux ratios in each channel can be corrected through division by the corresponding coefficients to obtain the unperturbed science spectrum. The disadvantage of this method is predominantly that the atmospheric conditions at the time of the observation may diverge significantly from the model atmosphere. In the context of the GRAVITY T Tauri survey, it became clear that applying this method consistently to all sample objects was impossible, since each target seemed to favour a different type of model atmosphere. Examples for both approaches are shown in Fig. 3.2.

A correction for these absorption effects may not be strictly necessary when treating specifically the Brγ feature - the two prominent absorption lines close by at 2.163446 and 2.168645 micrometers are just outside the maximum 13 channel range used in Gravity Collaboration et al. (2023b) for the visibility analysis and thus do not affect the result. There is an additional telluric feature close to the center of the nominal Brγ position, but for the GRAVITY sample objects absorption at these wavelengths was sufficiently small as not to affect the overall results in any meaningful way. The biggest remaining issue then is the influence the two telluric absorption lines in the wings of the Brγ feature have on the double Gaussian fit. In order to prevent their presence from diluting the fit of the asymmetries there, the affected points may simply be removed from the spectrum. While this method is comparatively crude, it can be applied consistently to all objects, which is why it was preferred when treating the T Tauri sample.

3.1.3. Barycentric/LSR correction

An additional correction needs to be applied to the observational wavelength grid in order to account for the Doppler shift caused by the motion of the Earth relative to the target object. The correction is specific to the observational date, as the exact radial velocity component of the shift depends on the phase of the Earth's rotation, and the location of the observatory relative to the sky coordinates of the target. Due to the time-sensitivity of the relative motion, the mathematics behind the correction are somewhat cumbersome, but already implemented solutions are available for e.g. Python. The SkyCoord class contained in the Astropy library includes an easy to use function to compute this barycentric velocity correction:

```
from astropy.time import Time
from astropy.coordinates import SkyCoord, EarthLocation
```

```
from astropy.coordinates import ICRS, LSR
import astropy.units as u

# Right ascension and declination of the target
raval=165.46590290601438
decval=-34.704793228437424

#time of observation, converted to MJD
date = ['2019-01-21T06:59:18']
t = Time(date, format='isot', scale='utc')
t = Time(t.mjd, format='mjd', scale='utc')

# location of VLT from ESO website
loc = EarthLocation(lon='-24d37m39.5s',lat='-70d24m15.5s',
      height=2635.43*u.m)
sc = SkyCoord(raval*u.deg, decval*u.deg)

# target radial velocity from SIMBAD
v_rad = 12.3*u.km/u.s

vcorr = sc.radial_velocity_correction(kind='barycentric',
        obstime=t, location=loc)
rv = v_rad + vcorr.to(u.km/u.s)
```

In the example above the radial velocity is corrected by shifting the frame of reference to the earth-sun barycenter.

Even after correcting for the Earth motion, the measured radial velocity of the target is still shifted by some amount caused by the Sun's rotation in the galactic plane. The solar motion is additionaly corrected for by further shifting the reference frame to the so called local standard of rest (LSR). The LSR is defined as the frame of reference of a hypothetical star at the position of the sun that would orbit the galactic center on a circular path at the mean velocity of a local group of stars in the solar neighbourhood (around 100 pc around the Sun). From the point of view of the LSR, close by stars, such as the T Tauri stars of the GRAVITY sample, are effectively at rest. Astropy again offers some default solutions for this correction:

```
#raval, decval as before
#pm_ra_cosdec, pm_dec, distance in pc from SIMBAD or GAIA
# rv is the barycentric radial velocity computed before
obs = ICRS(ra=raval*u.deg, dec=decval*u.deg,
                        pm_ra_cosdec=pmra2*u.mas/u.yr, pm_dec= pmdec*u.mas/u.yr,
                        radial_velocity=rv.value[0]*u.km/u.s, distance = 60*u.pc)

new_rv = obs.transform_to(LSR()).radial_velocity
```

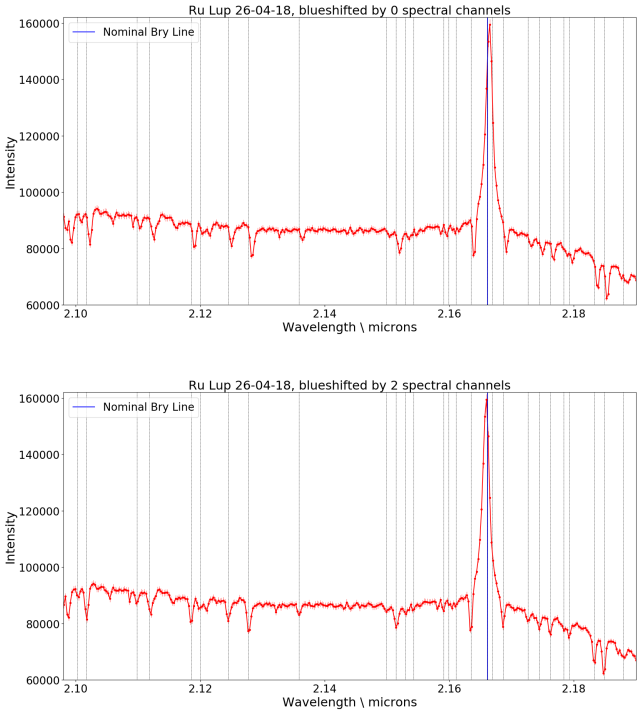

Figure 3.3.: The GRAVITY K-band spectrum from the 2018 epoch of the RU Lup observation, plotted between 2.1 and 2.2 microns. The dashed lines indicate the position of known NIR telluric absorption lines close to the Brγ line.
Top: For RU Lup 2018, the observed position of the aborption lines in the spectrum and the known wavelengths of those lines were offset by about 5 Å. This effect was systematic and affected all observations with GRAVITY before October 2019.
Bottom: The same spectrum shifted by two spectral channels. The observed telluric lines are now in alignment with their known positions.

Once the correct radial velocity is obtained, the wavelength grid needs to be shifted by $\Delta\lambda$

$$\Delta\lambda = \frac{v_{rad}}{c}\lambda_0, \tag{3.3}$$

where v_{rad} is the radial velocity of the object with respect to the LSR, λ_0 is the unshifted wavelength and c is the speed of light. In the case of the GRAVITY T Tauri sample, the total velocity correction lead to shifts of the data by up to 35 km/s.

3.1.4. Spectral shift correction

When treating the sample objects of the GRAVITY T Tauri study, it became clear that part of the sample was suffering from a systematic offset in terms of wavelength that also affected the position of the visibility amplitude signals. The spectra showed both a consistent shift of

about 5 Å with respect to known K-band telluric spectral lines (Fig. 3.3), as well as a relative offset of the position of the Brγ line between the four spectra of the individual UTs. A more thorough investigation showed that the misalignment between the telescope resulted not only in problems when computing the flux ratio, but more importantly also affected the computation of the complex visibilities from the raw data by the pipeline, and thus also both the derived phase and amplitude. A direct practical consequence of this effect was that the spectrally resolved line features in the visibility amplitudes were not well aligned with the peak of the mean spectrum but were rather offset to the left or right, thus affecting the results of the channel-by-channel analysis. Parts of the differential phase data were equally affected, as S-shape signatures were effectively suppressed by the misalignment and appeared like single-peaked profiles.
A correction was implemented as part of the data reduction process, introducing a correction based on a fit of the 24 individual spectra[1] to the known telluric lines close to the Brγ feature. In case the telluric absorption was too weak to clearly identify the lines, or the data too noisy to produce a proper fit, a master correction based on an average shift was applied. An example of this, showing the individual spectra before and after the correction, is presented in Fig. 3.4.

The overall effect of the correction on the interferometric observables was strongest for the differential phases, whereas the visibility data appeared to be relatively less affected. The general impact was highest on the pure line quantities, as shown in Fig. 3.4, right. While the marginally changed shape of spectra and visibility signals after the correction also affect the pure line observables, the dominant effect here stemmed from the relative shift between the mean spectrum and the interferometric observables. When computing the pure line visibility from Eq. 3.19, a different combination of $F_{L/C}$ and V_{tot} values in each channel is used after the correction, as now the visibility peaks are better aligned with the mean spectral peak. The change in pure line visibility caused by the correction is illustrated between Fig. 3.4 top and bottom of the right column.

The spectral shift was detected for all targets of the GRAVITY T Tauri sample that were observed before the grism change in October 2019. Consequently, the correction was applied to all observations other than the 2021 epoch of RU Lup.

[1] GRAVITY, using the ABCD method, records four spectra for each of the six baselines.

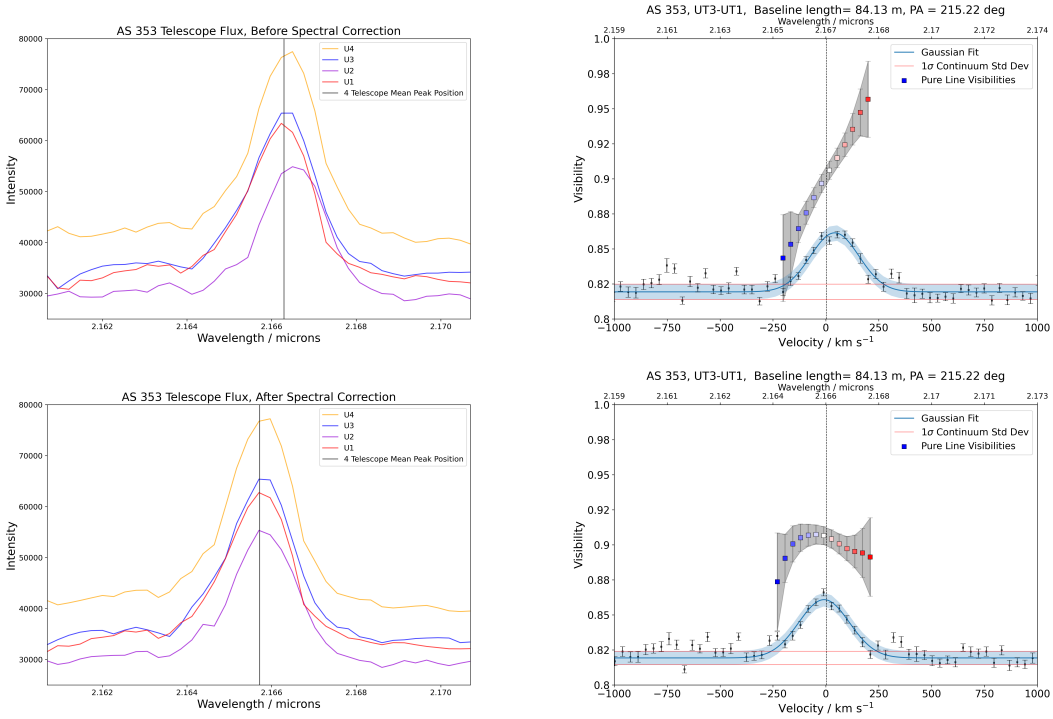

Figure 3.4.: Brγ spectra of the AS 353 observation, taken with the four unit telescopes of the VLTI.
Left column: The spectra before (top) and after (bottom) the application of the spectral shift correction. The vertical line indicates the mean position of the line peak. Before the correction, the individual spectra for most of our objects were misaligned both with respect to the telluric lines and also between each other. **Right column:** The visibility data before (top) and after (bottom) correction for the spectral shift. The impact on the pure line visibility (coloured squares) is significant, mostly due to the change in relative alignment between the flux ratios and visibilities following the correction.

3.2. Visibility analysis in two component systems

3.2.1. Visibility modelling: Pure line visibility amplitude

Consider again the Van Cittert-Zernike theorem introduced in Section 2.1.1:

$$\tilde{v}(\mathbf{B}) = \int I(\mathbf{x}) \exp\left(-2i\pi \frac{\mathbf{xB}}{\lambda})\right) dx. \tag{3.4}$$

Since I($\mathbf{x}$) is the intensity distribution of the combined emission sources in the interferometer's field of view at one particular wavelength, the complex visibility then also encodes the combined properties of all those different sources. While it is entirely possible to determine a size or photocenter offset from this total complex visibility, the overall result will not represent any physical region specifically but rather give a form of average, weighted by the different flux contributions.

In order to extract the specific attributes of a particular component, such as the Brγ emission region, a more thorough modelling of the visibilities is required. To this end, one may use the linearity property of the Fourier transform to construct multi-component visibility functions. This approach will be detailed in the following for the specific example of a system consisting of continuum emission component and a distinct Brγ line emission component. In YSOs, these components are generally thought to represent the stellar photosphere and dust radiation in the continuum on one side, and the hot hydrogen gas of the inner disk on the other side. Since

$$\tilde{\nu}_{tot} = \tilde{\nu}_{Cont} + \tilde{\nu}_{Line}, \tag{3.5}$$

we can write the corresponding normalised **total complex visibility** function as

$$\tilde{V}_{tot} = \frac{F_{Cont}\tilde{V}_{Cont} + F_{Line}\tilde{V}_{Line}}{F_{Cont} + F_{Line}} \tag{3.6}$$

with a total phase ϕ_{tot}, and an amplitude V_{tot}, which encode the photocenter, and spatial geometry, of the emission region, respectively. This function describes the total visibility inside the wavelength channels of the Brγ line. Outside of the region where the line has significant flux (i.e. $F_{Line} \approx 0$), the total complex visibility converges with the continuum complex visibility, $\tilde{V}_{tot} \approx \tilde{V}_{Cont}$.

In order to extract the properties of the line emission region from the total complex visibility, we can simply solve Eq. 3.6 for the **complex pure line visibiltiy** $\tilde{V}_{Line}$. However, at this point it is useful to first introduce the **total line to total continuum ratio** $F_{L/C}$ with

$$F_{L/C} = \frac{F_{Cont} + F_{Line}}{F_{Cont}} = 1 + \frac{F_{Line}}{F_{Cont}}, \tag{3.7}$$

which corresponds to the continuum-normalised flux ratios obtained from the GRAVITY spectra. With this, we can rewrite the total complex visibility function:

$$\tilde{V}_{tot} = \frac{\tilde{V}_{Cont} + \frac{F_{Line}}{F_{Cont}}\tilde{V}_{Line}}{1 + \frac{F_{Line}}{F_{Cont}}} \tag{3.8}$$

$$= \frac{\tilde{V}_{Cont} + (F_{L/C} - 1)\tilde{V}_{Line}}{F_{L/C}}, \tag{3.9}$$

We find then for the complex pure line visibility $\tilde{V}_{Line}$:

$$\tilde{V}_{Line} = \frac{F_{L/C}\tilde{V}_{tot} - \tilde{V}_{Cont}}{F_{L/C} - 1}, . \tag{3.10}$$

$\tilde{V}$ is a complex quantity with a visibility amplitude V and a visibility phase ϕ

$$\tilde{V} = Ve^{i\phi}. \tag{3.11}$$

Since amplitude and phase encode different types of information, it is preferable to be able to treat them separately. The **pure line visibility amplitude** V_{Line}, from which the size of the line emission region is computed, is the absolute value of the complex line visibility introduced in Eq. (3.10)

$$V_{Line} = |\tilde{V}_{Line}| = \left| \frac{F_{L/C} V_{tot} e^{i\phi_{tot}} - V_{Cont} e^{i\phi_{Cont}}}{F_{L/C} - 1} \right|. \tag{3.12}$$

One can use that, for complex numbers z, $|z| = \sqrt{zz^*}$ and $(z_1 + z_2)^* = (z_1^* + z_2^*)$, where the asterisk designates a complex conjugate:

$$V_{Line} = \left[\left(\frac{F_{L/C} V_{tot} e^{i\phi_{tot}} - V_{Cont} e^{i\phi_{Cont}}}{F_{L/C} - 1} \right) \left(\frac{F_{L/C} V_{tot} e^{i\phi_{tot}} - V_{Cont} e^{i\phi_{Cont}}}{F_{L/C} - 1} \right)^* \right]^{1/2} \tag{3.13}$$

$$= \left[\left(\frac{F_{L/C} V_{tot} e^{i\phi_{tot}} - V_{Cont} e^{i\phi_{Cont}}}{F_{L/C} - 1} \right) \left(\frac{F_{L/C} V_{tot} e^{-i\phi_{tot}} - V_{Cont} e^{-i\phi_{Cont}}}{F_{L/C} - 1} \right) \right]^{1/2} \tag{3.14}$$

$$= \left[\frac{1}{(F_{L/C} - 1)^2} \left(F_{L/C}^2 V_{tot}^2 + V_{Cont}^2 - F_{L/C} V_{tot} V_{Cont} \left(e^{i(\phi_{Cont} - \phi_{tot})} + e^{-i(\phi_{Cont} - \phi_{tot})} \right) \right) \right]^{1/2}. \tag{3.15}$$

Using Euler's formula $e^{i\phi} = \cos(\phi) + i \sin(\phi)$ and consequently $e^{i\phi} + e^{-i\phi} = 2\cos(\phi)$, we arrive at

$$V_{Line} = \left[\left(\frac{F_{L/C}}{F_{L/C} - 1} V_{tot} \right)^2 + \left(\frac{1}{F_{L/C} - 1} V_{Cont} \right)^2 - 2 \frac{F_{L/C}}{(F_{L/C} - 1)^2} V_{tot} V_* \cos(\Phi_{tot}) \right]^{1/2}, \tag{3.16}$$

where $\Phi_{tot} = \phi_{tot} - \phi_{Cont}$ is the **total differential phase** of the line, as introduced in Section 2.1.1. In practise the differential phases are usually sufficiently small so that $\cos(\Phi_{tot}) \approx 1$. In this case we can further approximate Eq. (3.16) as:

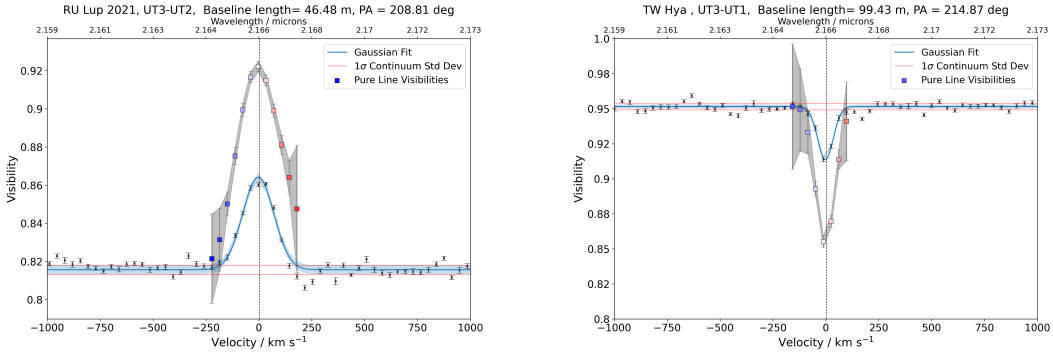

Figure 3.5.: Fitting of the visibility amplitude data.

Left: Visibility data from the UT3-UT2 baseline of the RU Lup observation in 2021. The coloured squares indicate the pure line visibilities after the extraction of the continuum contribution from the Brγ signal as laid out in Eq. (3.19). The errors on the pure line visibility, shaded in grey, were computed from Gaussian error propagation.

Right: Visibility data from the UT3-UT1 baseline of the TW Hya observation in 2019. The total and pure line visibilities here are essentially inverted with respect to the continuum level when compared to the RU Lup plot. This indicates that the total continuum emission region in total is more compact than the line emission region. This could be caused by either a small physical size of the total continuum region, or by a disk-to-star flux ratio that heavily favours the very compact stellar photosphere over the extended dusty disk.

$$V_{Line} \approx \left[\left(\frac{F_{L/C}}{F_{L/C}-1} V_{tot} \right)^2 + \left(\frac{1}{F_{L/C}-1} V_{Cont} \right)^2 - 2 \frac{F_{L/C}}{(F_{L/C}-1)^2} V_{tot} V_{Cont} \right]^{1/2} \tag{3.17}$$

$$= \left[\left(\frac{F_{L/C}}{F_{L/C}-1} V_{tot} - \frac{1}{F_{L/C}-1} V_{Cont} \right)^2 \right]^{1/2} \tag{3.18}$$

$$= \frac{F_{L/C} V_{tot} - V_{Cont}}{F_{L/C}-1}. \tag{3.19}$$

With this result, it is possible to determine a characteristic size of the emission region from the GRAVITY science channel data.

3.2.2. Treatment of GRAVITY visibility amplitudes

Eq. 3.19 connects the pure line visibility amplitude in a straightforward way to three other quantities: the continuum visibility amplitude V_{Cont}, the total visibility amplitude V_{tot}, and the line-to-continuum flux ratio $F_{L/C}$. This representation is very useful because all these quantities

are almost immediately available in the reduced GRAVITY OIFITS file.

As before, the visibility data should be cleansed of flagged or otherwise problematic entries. This process needs to be consistent with the spectral and phase data, i.e. only those data points which are usable for all three observables simultaneously should remain. Additionally, the reduced OIFITS file contains both the pipeline-computed squared visibility amplitude and a separate pipeline-computed regular visibility amplitude. While in principle both quantities should be, and usually are, consistent with each other, problems during the reduction process can lead to discrepancies. The squared visibility amplitude is commonly considered to be the preferred visibility, since the V^2 is more directly related to the measured intensity of the incident radiation. If possible it should be used to compute the regular visibility amplitude by the user directly (i.e. as V= $\sqrt{V^2}$), but in some cases there may be faulty entries in the OIFITS OI_VIS2 table, while the corresponding OI_VIS1 entries are not affected. Some user judgement may be necessary here.

Similar to the treatment of the spectral data, the visibilities can be fitted with a single peaked Gaussian function to account for noise-induced channel-to-channel fluctuations:

$$f(x) = A \exp(-\frac{(x-\mu^2)}{2\sigma^2}) + B, \tag{3.20}$$

with amplitude A, mean μ, standard deviation σ and offset B. The readout value of the total visibility V_{tot} in each considered spectral channel is then the value of the fitted function f at that wavelength, while the offset B defines the continuum visibility V_{Cont}. It is recommended to rely on the fringe tracker data for the continuum measurement over the science channel data. While deviations between the FT and SC continua were for most data sets from the GRAVITY T Tauri study on the order of 2% or less, the fringe tracker is considered to offer a more robust estimator of the continuum visibility due to less V^2 degradation at short integration times. When treating the GRAVITY T Tauri sample, the SC data was adjusted to the FT continuum level by taking the average continuum visibility of the five FT channels, V_{FT}, and then multiplying the total visibility in each channel with $\frac{V_{FT}}{V_{Cont}}$.

From this procedure and the previous treatment of the spectral data, a triplet of values ($F_{L/C}$, V_{tot}, V_{Cont}) has now been obtained for each spectral channel in the line. Restricting them further to those channels that meet the line flux selection criterion, the pure line visibility can be computed from Eq. 3.19. The uncertainties on the pure line flux can be computed for the pure line flux via standard error propagation:

$$\Delta V_{Line} = \frac{1}{F_{L/C}-1} \sqrt{(\Delta V_{tot} F_{L/C})^2 + (\Delta V_{tot}^{Cont})^2 + (\Delta F_{L/C} \frac{V_{tot}^{Cont} - V_{tot}}{F_{L/C}-1})^2} \tag{3.21}$$

Here ΔV_{tot} is the uncertainty on the total visibility, given by the instrumental error bar computed by the GRAVITY pipeline, ΔV_{Cont} is the standard error $\frac{\sigma_{FT}}{5}$ of the five averaged fringe tracker visibilities, and $\Delta F_{L/C}$ is the uncertainty on the flux ratio, also defined by the pipeline-derived instrumental uncertainty. Figure 3.5 shows the visibilities, both total and pure line, for two different baselines of two different objects.

3.2.3. Geometric Modelling

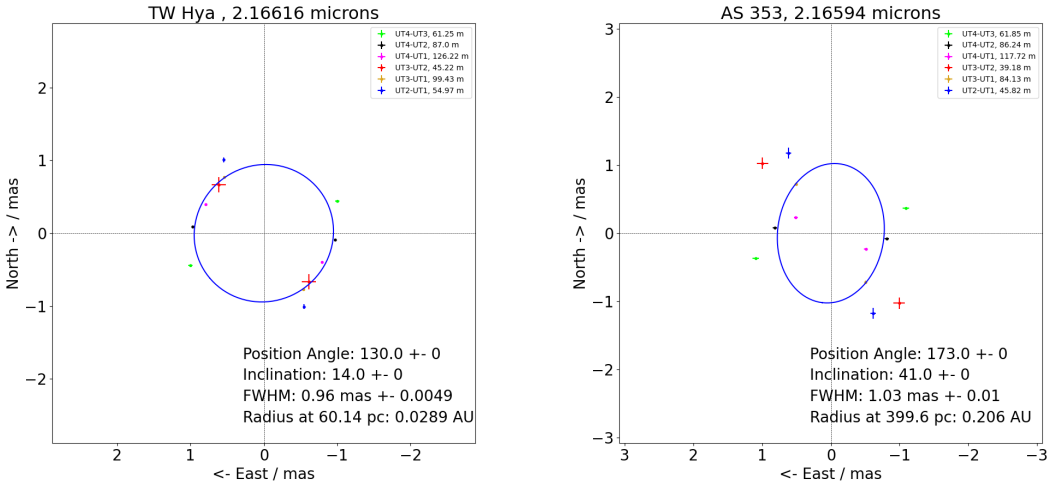

Figure 3.6.: Fit of the geometrical model to the visibilities.

Left: An ellipse representing the full width half maximum of a Gaussian disk 2D line emission region as projected onto the six baselines of GRAVITY in a single spectral channel. Shown here is the emission region at the central channel of the Brγ line of TW Hya. The inclination and position angle were fixed in accordance with those values obtained from the continuum fit of the same GRAVITY data and presented in Gravity Collaboration et al. (2021b). In this case the fixed ellipse is a gpod fit to the spectral line emission region.

Right: The corresponding line emission region plot for the central Brγ channel of AS 353. It is clear from the distribution of the underlying projected sizes that the emission region would not fit any form of inclined disk model particularly well. This is indicative of a more complex morphology of the emission intensity distribution.

The Van Cittert-Zernike theorem connects the intensity distribution I(**x**) on the sky to the visibilities. By presuming a certain morphology for I(**x**), it is possible to derive a analytical expression for the visibility function that explicitly refers to some form of size property of the brightness map. This was already illustrated for the case of a binary system consisting of two unresolved stars, where the resulting visibility amplitude was a function of the binary separation. This principal idea can be extended to different morphologies to obtain geometric models for the

visibility functions. A uniform disk, for example,

$$I(\rho) = \frac{4}{\pi\theta^2} \text{ if } \rho \leq \theta/2, \text{ else } 0, \tag{3.22}$$

is commonly used to give a first order description of the resolved surface of a star with an angular diameter θ. ρ refers to an angular radial coordinate on the sky, $\rho = \sqrt{\alpha^2 + \beta^2}$ (see Eq. 2.56). Evaluating the Fourier integral will yield a visibility function of the form

$$V(B, \lambda) = 2\frac{J_1(\pi\theta B/\lambda)}{\pi\theta B/\lambda}, \tag{3.23}$$

where B is the length of the projected baseline with which the visilibity was measured, and J_1 is the first order Bessel function.

Analysis of the inner disk region often make use of different disk or ring models to model brightness profiles with radial dependency. Ring models in particular can be used to construct a visibility function for a temperature gradient disk model by essentially integrating over a number of rings up to some outer radius and weighing their different flux contributions. Another popular choice when attempting to model the inner disk is a Gaussian disk model, i.e. a disk with a centrally peaked intensity that then drops off radially as a Gaussian function:

$$I(\rho) = \frac{1}{\sqrt{\pi/4ln(2)}\Theta} \exp\left(\frac{-4ln(2)\rho^2}{\Theta^2}\right), \tag{3.24}$$

where ρ is again a radial coordinate as before and Θ is now the full width half maximum (FWHM) of Gaussian distribution, and thus the characteristic size parameter of this model. The Gaussian disk model offers a simple way to approximate disk-like regions with a hot, bright inner center and a colder, darker outer region without having the define a more complex stacked visibility function. In Gravity Collaboration et al. (2023b)[2], a simple Gaussian disk model was used to fit the Brγ line emission region of the GRAVITY T Tauri sample.

The visibility function of the Gaussian disk model is then:

$$V(B, \lambda) = \exp\left(-\frac{(\pi\Theta B)^2}{4ln(2)\lambda^2}\right). \tag{3.25}$$

B here is again the length of the projected baseline and Θ the angular FWHM in radians.

$$V_{Line} = \exp\left(-\frac{(\pi\Theta B)^2}{4ln(2)\lambda^2}\right). \tag{3.26}$$

[2]Other recent works featuring the Gaussian disk model to fit a line emission region are Gravity Collaboration et al. (2021a, 2020).

If the line emission region in the two component visibility model is to be modelled by a Gaussian disk, one can set V(B,λ) = V_{Line}, By inverting Eq. (3.26), the angular characteristic size of the Gaussian disk as measured at any one single baseline can then be computed from the pure line visibilities:

$$\Theta_{Line} = \sqrt{-4\ln(2)\ln(V_{Line})}\frac{\lambda}{B\pi} \tag{3.27}$$

The uncertainties on the projected sizes are then again computed via error propagation:

$$\Delta\Theta_{Line} = \sqrt{\frac{-\ln(2)}{\ln(V_{Line})}}\frac{\lambda}{B\pi}\frac{\Delta V_{Line}}{V_{Line}}, \tag{3.28}$$

where ΔV_{Line} is the error on the pure line visibility amplitude computed from Eq. 3.21.

The intensity of any given point of the emission region is through Eq. 3.24 fully defined by the radial distance from the coordinate center. This only corresponds to the image seen by the observer in the specific case of a pole-on observation, i.e. when the disk-like system is seen at zero degrees inclination with respect to the observer line of sight. In reality, the disks around young stars, and thus presumably also the line emission regions of those systems, are often observed at non-zero inclinations. The image that is then fed to the interferometer is the projection of the inclined disk onto the 2D sky plane and is thus elliptical in shape. The projection effect can be accounted for in uv space by manipulating the visibility function (see Berger and Segransan (2007) for a detailed explanation) accordingly. Alternatively, the inclination can be included in real space by treating the sizes that were obtained for each baseline of the observation as projections Θ_i of the zero-inclination FWHM Θ onto the baselines B_i. The true, inherent FWHM of the disk structure can then be recovered by fitting an ellipse, defined by the size of the major axis, the position angle and the inclination. The major axis is equivalent to the FWHM, the position angle (PA) measures the angular distance between the major axis and the North axis on the sky plane, and the inclination (inc) is the angle between the polar axis of the disk[3] and the observer line of sight. Fitting such a three-parameter system can be done in a number of ways with varying complexity, but for such a simple configuration a straightforward χ^2 minimisation will deliver robust results if the distribution of projected sizes indeed follows an elliptical shape. The χ^2 of any given ellipse is defined by

$$\chi^2 = \sum_i \frac{(\Theta_{Ellipse,i} - \Theta_{Data,i})^2}{\Delta\Theta^2_{Data,i}}, \tag{3.29}$$

where $\Theta_{Ellipse,i}$ is the size of the ellipse in the direction of the i-th baseline, $\Theta_{Data,i}$ is the computed FWHM along the i-th baseline, and $\Delta\Theta_{Data,i}$ is the propagated error computed from Eq.

[3]In YSO disks this, in first order, corresponds to the stellar rotational axis.

(3.28). Uncertainties on the disk parameters can be estimated from the covariance matrix defined by

$$Cov(i, j) = (U^{-1})_{i,j}. \tag{3.30}$$

The matrix elements of U can be derived from the partial derivatives of the χ^2 with respect to the fit parameters:

$$U_{i,j} = \frac{1}{2}\frac{\partial^2\chi^2}{\partial i \partial j}, \tag{3.31}$$

where i, j would represent Θ, PA or inc of the ellipse. The diagonal elements of the covariance matrix then give the squared parameter uncertainties σ^2_{Θ}, σ^2_{inc}, σ^2_{PA}.

The ellipse fit method, illustrated in Fig. 3.6, was used in the GRAVITY study of Brγ emission in T Tauri stars. One of the advantages of fitting the disk structure in real space lies with the fact that it is straightforward to recognise discrepancies between the geometric model and the underlying distribution of projected sizes. The Brγ emission region in T Tauri stars is not necessarily well described by an inclined disk, and the ellipse fit allows more easily to visually judge whether this may be caused by baseline resolution effects or the inherent complexitiy of the intensity map.

The geometric distribution of the UTs leaves a gap in uv coverage at a position angle of about 130 degrees North to East. Regardless of the fitting method used, this lack of coverage introduces a bias in favour of elongated ellipses which fall into this gap. In order to counteract this effect, the PA and inclination of the ellipse were fixed at the values obtained from the GRAVITY continuum data for the inner dusty disk (Gravity Collaboration et al., 2021b) under the implicit assumption that the Brγ emission region and the continuum disk are roughly aligned in terms of inclination. While this is a strong assumption, one advantage of this approach is that the continuum fits also make use of AT data sets for the T Tauri sample objects, which do not suffer from the coverage issue of the UTs. Since the ATs were not sensitive enough to detect the Brγ line in the T Tauri sample objects, however, their use in this case was restricted to continuum data. Consequently, with PA and inclination fixed, only the FWHM of the Gaussian disk remained as a free parameter of the fit.

In the GRAVITY T Tauri study, the Gaussian disk model was used to derive a FWHM for all sample objects, regardless of how well the disk model appeared to fit the projected sizes or how well line and continuum PA and inclination agreed with each other. Since the priority of the study was to discover common trends or characteristics according which different types of objects could be grouped together, consistency in the approach was in first order of greater interest than more complex geometric modelling. The derived sizes, which were obtained for each

selected spectral channel individually, are therefore best interpreted as characteristic sizes, given that they are dependent on both the geometrical model used and the assumptions made for the fit. They recover trends both between different sample objects and across multiple line channels for individual objects. While they are very much connceted to the physical size of the emission region, some care needs to be taken not to overinterpret how much detail they can deliver about the line emission region.

3.3. Differential phase analysis in two component systems

3.3.1. Visibility modelling: Pure line differential phases

Consider again the complex pure line visibility function:

$$\tilde{V}_{Line} = V_{Line} e^{i\phi_{Line}} = \frac{F_{L/C} V_{tot} e^{i\phi_{tot}} - V_{Cont} e^{i\phi_{Cont}}}{F_{L/C} - 1}. \tag{3.32}$$

In order to extract the **pure line differential phase** $\Phi_{Line} = \phi_{Line} - \phi_{Cont}$, both sides of Eq. 3.32 need to be multiplied by a factor $e^{-i\phi_{Cont}}$:

$$V_{Line} e^{i\phi_{Line}} e^{-i\phi_{Cont}} = \frac{F_{L/C} V_{tot} e^{i\phi_{tot}} e^{-i\phi_{Cont}} - V_{Cont} e^{i\phi_{Cont}} e^{-i\phi_{Cont}}}{F_{L/C} - 1} \tag{3.33}$$

$$\Longleftrightarrow V_{Line} e^{i\Phi_{Line}} = \frac{F_{L/C} V_{tot} e^{i\Phi_{tot}} - V_{Cont}}{F_{L/C} - 1} \tag{3.34}$$

$$\Longleftrightarrow e^{i\Phi_{Line}} = \frac{F_{L/C}}{F_{L/C} - 1} \frac{V_{tot}}{V_{Line}} e^{i\Phi_{tot}} - \frac{1}{F_{L/C} - 1} \frac{V_{Cont}}{V_{Line}}, \tag{3.35}$$

and via use of Euler's formula, $e^{i\Phi} = cos(\Phi) + isin(\Phi)$, this may further be rewritten as

$$\begin{aligned} cos(\Phi_{Line}) + isin(\Phi_{Line}) = &\left(\frac{F_{L/C}}{F_{L/C} - 1} \frac{V_{tot}}{V_{Line}} cos(\Phi_{tot}) - \frac{1}{F_{L/C} - 1} \frac{V_{Cont}}{V_{Line}} \right) \\ &+ i \left(\frac{F_{L/C}}{F_{L/C} - 1} \frac{V_{tot}}{V_{Line}} sin(\Phi_{tot}) \right). \end{aligned} \tag{3.36}$$

By comparison of the imaginary coefficients, we finally arrive at

$$sin(\Phi_{Line}) = \frac{F_{L/C}}{F_{L/C} - 1} \frac{V_{tot}}{V_{Line}} sin(\Phi_{tot}). \tag{3.37}$$

The pure line differential phase can thus be computed as

$$\Phi_{Line} = arcsin\left(\frac{F_{L/C}}{F_{L/C}-1}\frac{V_{tot}}{V_{Line}}sin(\Phi_{tot})\right), \tag{3.38}$$

from the pure line visibility V_{Line}, the total visibility V_{tot}, the line-to-continuum flux ratio $F_{L/C}$, and the total differential phase Φ_{tot}. All of these quantities can be obtained from the reduced GRAVITY data.

It is worth considering what the pure line correction represents physically when treating the differential phase. In the case of the pure line visibility, flux contributions of the continuum emission region were removed to determine a size which may be attributed to the source of the line emission alone. If the continuum was represented by dust and the line emission region by hydrogen gas, the total visibility represents a hypothetical combined region, while the pure line visibility is linked to the size of the hydrogen gas region only. The same is true in principle for the pure line differential phase. The photocenter offset that is encoded in the total differential phase is the offset of a hypothetical combined emission region, since there the spectral channels within the line contain both flux from the hydrogen transition itself, but also the underlying continuum. The pure line differential phase only encodes the photocenter offset of the emitting hydrogen region. It may be tempting to think that the the continuum contribution is already removed by subtracting the continuum phase from the total line phase, but the differential nature of the observable has a different interpretation entirely. The total differential phase Φ_{tot}

$$\Phi_{tot} = \phi_{(Cont+Line)} - \phi_{Cont}, \tag{3.39}$$

encodes the photocenter position of the total emission region relative to the photocenter of the continuum, as was explained in Section 2.1.1, i.e. how much the total photocenter is shifted with respect to the unknown position of the continuum photocenter. The pure line differential phase gives the photocenter offset of only the line emission region, still relative to the unknown continuum photocenter position. In other words, the continuum phase subtraction removes the absolute positional information from the phase, but not the flux contribution.

3.3.2. Treating GRAVITY visibility phase data

Extracting the pure line differential phase from the GRAVITY OIFITS file is a broadly analogous process to the treatment of the visibility amplitude data. One principal difference is that the OIFITS file contains information about the absolute, atmospherically scrambled, phase. In order to compute the differential phase, the continuum phase must be subtracted. However, unlike in the case of the visibility data, the phase data is typically sloped. The obvious approach here is

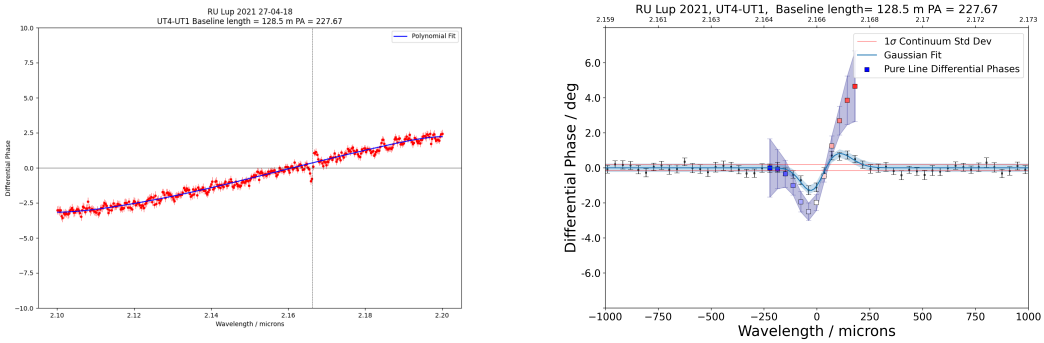

Figure 3.7.: Fitting of the differential phase data.

Left: Absolute phase data from the UT4-UT1 baseline of the RU Lup observation in 2021 over a wavelength range of 2.1 to 2.2 microns. The phase is sloped, thus necessitating the fit of a polynomial function to determine the continuum phase, which is in turn then subtracted from the absolute phase of the Brγ line channels.

Right: Continuum-subtractd differential phase data betweeb 2.159 and 2.173 microns. Here the coloured squares indicate again the pure line differential phases, corrected for the flux contributions of the continuum via Eq. 3.38.

to fit a polynomial function to the slope, as in the case of the spectral data. After interpolating the polynomial on the GRAVITY wavelength grid, the phase data in each wavelength channel is then subtracted by the value of the polynomial to obtain the total differential phase Φ_{tot}. See Fig. 3.7 (left) for an example of such a polynomial fit for one object and baseline.

The phase data is often significantly noisier than the visibility amplitude data, so fitting a Gaussian function to determine the read-out value per channel is strongly recommended, if the analysis is to be extended over the full range of line channels. Differential phase data may often feature so called S-shapes, meaning that the profile shows a blue and redshifted peak, which are inverted with respect to each other, as depicted in Fig. 3.7 (right). These types of profiles may be fitted with a double Gaussian function, but consequently either some form of automated solution needs to be implemented to distinguish single peaked and double peaked signals, or the baselines featuring S-shapes need to be identified in advance.

The uncertainties on the pure line differential phase can be computed from error propagation via:

$$\Delta\Phi_{Line} = \frac{\sin(\Phi_{Line})}{\sqrt{1 - sin^2(\Phi_{Line})}} \sqrt{(\Delta\phi \frac{\cos(\Phi_{tot})}{\sin(\Phi_{tot})})^2 + (\frac{\Delta V_{tot}}{V_{tot}})^2 + (\frac{\Delta V_{Line}}{V_{Line}})^2 + (\frac{\Delta F_{L/C}}{F_{L/C} - 1})^2}, \quad (3.40)$$

where ΔV_{tot} is the pipeline-derived instrumental uncertainty on the total visibility, ΔV_{Line} is the computed uncertainty on the pure line visibility, $\Delta F_{L/C}$ is the pipeline-derived instrumental uncertainty on the flux ratio, and $\Delta\Phi_{tot}$ is the pipeline-derived instrumental uncertainty on the total differential phase.

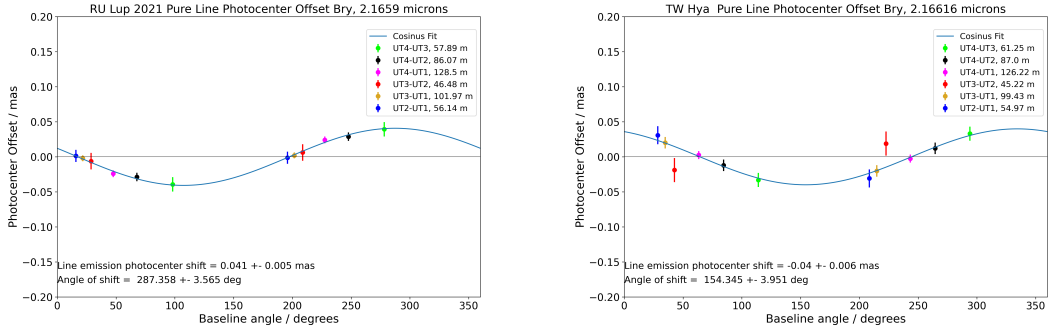

Figure 3.8.: Deprojection of the baseline-specific photocenter shifts to obtain the inherent photocenter offset of the emission region. The six baselines of GRAVITY yield a total of 12 different pairs of projected photocenter shift angle and magnitude, to which a cosine function was fitted to determine the inherent photocenter shift of the line emission region.
Left: The cosine fit for one spectral channel of the RU Lup 2021 observation. All projected shifts follow the sinusoid form of the function almost perfectly, thus constraining the inherent photocenter well. 3.43.
Right: The equivalent plot for one spectral channel of the TW Hya observation. At the shortest baseline (red), the computed projected shift seems to deviate from the cosine. This may be caused by noise in the differential phase data, alternatively it could also indicate a resolution effect. Since the shortest baseline features the lowest spatial resolution, the innermost parts of the emission region may be effectively invisible to it. In such a case, the baseline would see a different inherent photocenter.

3.3.3. Extracting the photocentre offset of the line emission region

In Section 2.1.1, it was demonstrated how the relative photocenter position of the emission region at a certain wavelength approximately relates to the differential phase between that wavelength and some reference channel. This relationship, defined by Eq. (2.46), connects the measured pure line differential phase Φ_i at a baseline $\mathbf{B}_i$ to an angular photocenter offset $\mathbf{P}$ on the sky plane, as projected onto that baseline vector:

$$\Phi_{Line,i} \approx -2\pi \frac{\mathbf{B_i}}{\lambda} \mathbf{P}. \tag{3.41}$$

In order to obtain the inherent photocenter shift $\mathbf{P}$ of the line emission region, the offsets p_i measured with each of the six GRAVITY baselines need to be deprojected. Thee procedure is comparatively straightforward, as, unlike in the case of the visibilities, no particular model assumptions are necessary. Rewriting Eq. (3.41) as

$$\Phi_{Line,i} \approx -2\pi \frac{\mathrm{B_i} \cdot \mathrm{P} \cos(\delta_i)}{\lambda}, \tag{3.42}$$

where δ_i is the relative angle between the baseline vector and the vector of the inherent photocenter offset $\mathbf{P}$, and then substituting $\mathrm{p}_i = \mathrm{P} \cos(\delta_i)$, utlimately leads to the well known relationship

between differential phase and shift along a baseline (Le Bouquin et al., 2009):

$$p_{Line,i} \approx -\frac{\Phi_{Line,i}\,\lambda}{2\pi B_i}, \tag{3.43}$$

with the associated uncertainties

$$p_{Line,i} \approx -\frac{\Delta\Phi_{Line,i}\,\lambda}{2\pi B_i}. \tag{3.44}$$

Using Eq. (3.43), is possible to convert the GRAVITY differential phases into angular shifts in the direction of the baseline vector. Since the photocenter offset is necessarily anti-symmetric with respect to 180 degree inversion, i.e. a projected shift p_i at a baseline angle θ_i is equivalent to a shift of -p_i at an angle of $\theta_i \pm$ 180 deg. The six baselines of GRAVITY then define a set of 12 pairs (p_i, θ_i) for each spectral channel individually. In principle, the inherent photocenter shift could be determined from solving the resulting system of equations since the projection relationship is exact. In practicse, uncertainty in the measurement of the differential phase and baseline resolution effects may lead to sets of value pairs that are not exactly compatible with the same inherent offset. In order to better take into account these discrepancies between measurements and true shifts, fitting a cosine function of the form

$$p_{\mathrm{Line,i}} = P\cos(\Psi - \theta_i), \tag{3.45}$$

where Ψ is the angle and P is the magnitude of the inherent photocenter offset vector **P**, to the set of points will deproject the baseline-specific offsets. P and Ψ are then determined from the fit. The principle is illustrated in Fig. 3.8 for two different exemplary targets in one spectral channel each.

4. Radiative transfer simulations of the Brγ emission region

While both accretion and ejection mechanisms feature certain characteristics against which we may compare observational signatures, the interpretation of interferometric data often remains challenging. Making proper use of GRAVITY's high spectral resolution mode in particular is difficult, as no clear baselines for the behaviour of the interferometric observables across the line channels have ever been established. A potential way forward here lies in the use of radiative transfer simulations of accretion and ejection processes. From simulated images of the Brγ emission region, synthetic interferometric observables may be computed in order to serve as a point of reference for future observational results. To this end, analytical models of magnetospheric accretion and magnetically driven disk winds were used in combination with the radiative transfer code MCFOST in order to produce intensity maps, such as shown in Fig. 4.1, in the wavelength range of the Brγ line.

4.1. The radiative transfer problem of atomic line emission

The generalised descriptions of radiative transfer for atomic lines, which are meant to provide more context in terms of mathematical formalism to the actual practical implementation in MCFOST, are largely based on Rutten (2003). Information specific to the use in MCFOST is taken from Tessore et al. (2021, 2023), and private communication with the author of those papers.

The computation of an emission region image pertaining to some atomic line transition necessitates knowledge of the surface brightness of any image pixel. This surface brightness is determined by the specific intensity I_ν, which defines the energy radiated per unit area dA, unit time dt, unit solid angle dΩ and unit frequency dν. In other words, the specific intensity is the energy radiated by some point P of a surface element in the direction of a unit vector **n** along a single ray of light. This relates to the specific flux density F_ν, emitted from the same point into a solid angle Ω in direction **n**, as

$$F_\nu = \int_\Omega I_\nu \cos(\theta)\, d\Omega, \tag{4.1}$$

where θ is the angle between the normal vector of dA and the direction of **n**. The specific flux depends on the solid angle over which the radiation is received and is thus dependent on the distance from the source object. The specific intensity, by contrast, is independent of the observer and only depends on the parameters that set the properties of the emission region itself in terms of emission and absorption. The surface brightness of any point can then be obtained by solving the radiative transfer equation along a ray of length ds in the direction **n** at some frequency ν:

$$\frac{dI(\nu, \mathbf{n})}{ds} = -\chi(\nu, \mathbf{n})I(\nu, \mathbf{n}) + \eta(\nu, \mathbf{n}), \tag{4.2}$$

The emissivity $\eta(\nu, \mathbf{n})$ here defines the energy added to the beam from emission in some local volume V:

$$dE(\nu, \mathbf{n}) = \eta(\nu, \mathbf{n})\, dV\, dt\, d\nu\, d\Omega, \tag{4.3}$$

and relates to the specific intensity added along some geometric path length s in the direction of the beam as

$$dI(\nu, \mathbf{n}) = \eta(\nu, \mathbf{n})\, ds. \tag{4.4}$$

The linear extinction coefficient $\chi(\nu, \mathbf{n})$ specifies the amount of energy taken from the beam as it travels along a path s through some volume of particles with density n and with cross-section $\sigma(\nu, \mathbf{n})$ so that $\chi(\nu, \mathbf{n}) = n\sigma(\nu, \mathbf{n})$

$$dI(\nu, \mathbf{n}) = -\chi(\nu, \mathbf{n})I_\nu\, ds. \tag{4.5}$$

The transfer equation (4.2) then describes the balance of photons added by emission processes in the radiant medium and those subtracted by absorption processes to define the change in specific intensity along a path s. Suppose now that this medium is a monoatomic hydrogen gas, defining an atomic system with electronic levels denoted by i,j so that j > i, i.e. j denotes the upper and i denotes the lower state. The emissivity and opacity can then be written as

$$\eta_{i,j} = n_j U_{ji}(\nu, \mathbf{n}) \tag{4.6}$$

$$\chi_{i,j} = n_i V_{ij}(\nu, \mathbf{n}) - n_j V_{ji}(\nu, \mathbf{n}) \tag{4.7}$$

where $n_{i,j}$ are the populations of the i-th and j-th state, respectively, and U_{ij}, V_{ij} are radiative transfer coefficients of emission and absorption, so that

$$U_{ab} = \frac{h\nu}{4\pi} A_{ab}\psi(\nu, \mathbf{n}) \tag{4.8}$$

$$V_{ab} = \frac{h\nu}{4\pi} B_{ab}\phi(\nu, \mathbf{n}). \tag{4.9}$$

The indices denote two states a and b without any kind of specific order between them. A_{ab} here is the Einstein coefficient of emission and defines the transitional probability from upper to lower state under spontaneous de-excitation, while B_{ab} is the Einstein coefficient of absorption, describing transitions under radiative excitation (b > a) or stimulated emission (a > b). The emission and absorption profiles $\psi(\nu, \mathbf{n})$, $\phi(\nu, \mathbf{n})$ are probability distribution functions due to natural line broadening, centered on the transition frequencies. It common to assume here that $\phi(\nu, \mathbf{n}) = \psi(\nu, \mathbf{n})$. The total emissivity and opacity are obtained by evaluating the sum of equations (4.6) and (4.7) over all transitions and atoms, and other sources of absorption in the system, such as dust.

If the populations of the electronic states and the properties of the radiant medium, such as the velocity and temperature of the gas, are known, then the specific intensity can be computed from the radiative transfer equation in a straightforward way:

$$I(\nu, \mathbf{n}, \tau_2) = I(\nu, \mathbf{n}, \tau_1)e^{-(\tau_2-\tau_1)} + \int_{\tau_1}^{\tau_2} S(\nu, \mathbf{n}, \tau)e^{-(\tau-\tau_1)}\ d\tau. \tag{4.10}$$

$S(\nu, \mathbf{n}, \tau_2) = \frac{\eta(\nu,\mathbf{n},\tau)}{\chi(\nu,\mathbf{n},\tau)}$ is the source function, τ denotes the optical depth with $\tau = \int -\chi(\nu, \mathbf{n})\, ds$.

In local thermodynamic equilibrium (LTE), the distribution of excitation levels in any atomic or ionic species follows Boltzmann statistics and is characterised by the temperature alone. The distribution of ionic populations of the same species are described by the Saha ionisation equation. The population of any level in LTE is then given by the combined Saha-Boltzmann distribution and completely determined by the local temperature and electronic density in the emission region:

$$\left[\frac{n_c}{n_i}\right]_{LTE} = \frac{1}{N_e}\frac{2g_c}{g_i}\left(\frac{2\pi m_e k_B T}{h^2}e^{-\Delta E_{ci}/k_B T}\right), \tag{4.11}$$

where n_i is the number density of atoms in excitation level i, n_c is the population of ions of ionisation level[1] c, $g_{c,j}$ the statistical weights of these levels, m_e the electronic mass, k_B the Boltzmann constant, T the temperature and ΔE_{ci} the ionisation energy from i to c. This implies that the population levels are not themselves influenced by the radiative processes at all. The source function S_ν is in this case equal to the Planck function $B_\nu = \frac{2h\nu^3}{c^2}\frac{1}{e^{\frac{h\nu}{k_B T}}-1}$. In reality, the population numbers are dependent on the intensity emitted as the radiant matter goes through a process of excitation and de-excitation caused by photon emission and absorption between the different particles within the medium. Atomic line transfer is then a non-local thermodynamic equilibrium (non-LTE) problem and an accurate modelling requires an iterative treatment of the population changes.

[1] The ionisation level here refers to the number of electrons removed from the neutral atom.

Non-LTE treatment of radiative line transfer assumes that the populations are in statistical equilibrium (SE), meaning the level populations and radiation fields are constant in time so that

$$\frac{dn_i(\mathbf{r})}{dt} = \sum_{j\neq i}^{N} n_j(\mathbf{r})P_{ji} - n_i(\mathbf{r})\sum_{j\neq i}^{N} P_{ij} = 0. \tag{4.12}$$

The total number of transitions from any other state j into the i-th state is then equal to the sum of all outgoing transitions from the i-th state to any other state per unit time, defined by the transition rates $P_{ji,ij}$ and the population densities $n_{i,j}$. The transition rates themselves are the sums of the radiative and collisional transitions R_{ij} and C_{ij}, respectively, with $P_{ij} = R_{ij} + C_{ij}$. The collisional rates are functions of the local temperature and the transition frequency, and determined by the Maxwell distribution of the gas particles. The radiative transition rates by contrast are determined by

$$R_{ab} = \int d\Omega \int \frac{1}{h\nu}\left[U_{ab}(\nu,\mathbf{n}) + V_{ab}(\nu,\mathbf{n})I(\nu,\mathbf{n})\right]\, d\nu, \tag{4.13}$$

and rely on the transition coefficients, which are in themselves functions of the populations, emissivity and opacity and thus are products of the radiative transfer code. A common approach to the computation of the iteration steps follows the Λ-iteration method, which reformulates the radiative transfer equation in terms of an operator equation:

$$I(\nu,\mathbf{n}) = \Psi(\nu,\mathbf{n})[\eta(\nu,\mathbf{n})]. \tag{4.14}$$

$\Psi(\nu,\mathbf{n})$ here is a matrix operator that includes the population levels and opacities of the system. After determining the initial atomic populations, the emissivity is computed from these population levels, which in turn is then used to compute the intensity. From these results, the transition coefficients are derived and subsequently new level populations are finally obtained. The process is repeated in consecutive iteration steps until a convergence threshold has been met. In this manner, the final surface brightness of the image can be obtained in principle. In practise, this method will only converge in optically thin media. Different methods are necessary to solve this problem in optically thick regions, like ALI (accelerated λ-iteration), which simultaneously solves the RT and SE equations at each iteration step.

4.2. Non-LTE line emission radiative transfer with MCFOST

MCFOST (Pinte et al., 2006, 2009) is a 3D Monte Carlo and ray-tracing based radiative transfer code, capable of computing both dust continuum and atomic line emission in multi-level atomic systems under non-local thermodynamical equilibrium conditions (Tessore et al., 2021, 2023). Its primary use case is the computation of emission region images in star-disk systems,

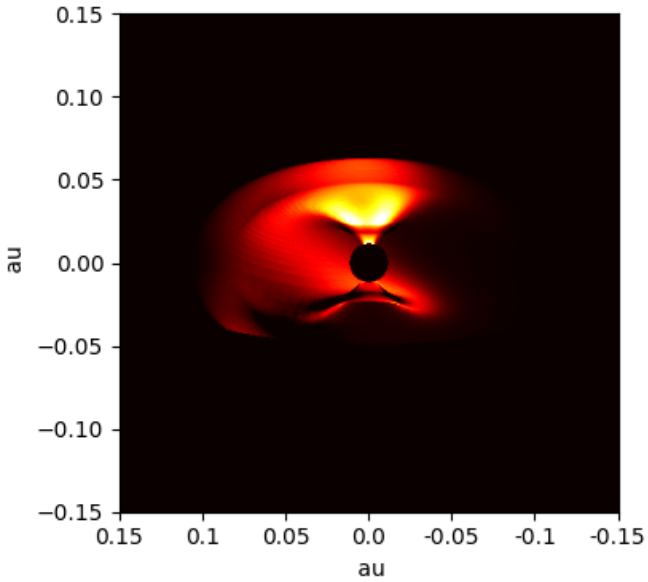

Figure 4.1.: An example of a magnetospheric accretion model image, produced with the MCFOST radiative transfer code. Shown here is the continuum-subtracted Brγ emission region of a purely axisymmetric rotating magnetosphere with no additional emission components. Channel line maps like this can be used to compute artificial interferometric observables which we are then able to compare to real observational data.

including the line transfer of atomic populations in the close environment of young stars. At the present state it allows for the use of cylindrical, spherical and unstructured grid types on which the relevant model quantities may be defined at the grid cell level. These cells contain the velocity fields, particle densities, and temperatures, which set the environmental conditions for the radiative transfer of the emission region. Radially defined cells in the case of the spherical and cylindrical grids are spaced logarithmically to allow for a higher cell densities in the central regions of the grid. The cell quantities may be defined arbitrarily in three dimensions, either by providing pre-defined inputs in the form of tables with the relevant properties for each cell, or through the use of parametric models such as presented in Sections 4.3 and 4.4. The cell contents must remain constant throughout the simulation, i.e. the simulations cannot be time-dependent.

MCFOST-art[2], the collection of line radiative transfer modules, exclusively relies on ray-tracing to obtain solutions to the atomic line radiative transfer equation defined by Eq. 4.2.
Its main purpose is to concurrently solve the transport equation and the statistical equilibrium equation in an iterative loop until convergence is achieved. As initial inputs it takes an atomic model file, featuring the electronic transitions, oscillator properties and associated energy levels, along with the provided cell grid contents from the parametric models used. Some care needs

[2]"art" here stands for "atomic radiative transitions".

RT code	Dust	Atomic/molecular lines	Native grid mesh options	Parallelisation	Availability
MCFOST	Yes	ALI / MC ALI	Structured (Cyl., Sph.), unstructured, irregular	openMP	Fully public
RADMC-3D	Yes	Sobolev	Structured (Cub., Sph.), AMR	openMP	Fully public
LIME	Yes	MC ALI	Unstructured	openMP	Fully public
Torus	Yes	Sobolev	Structured, AMR	MPI	Partially public
Magritte	no	ALI	Stuctured (Cyl., Sph.), unstructured, irregular, AMR	MPI	Fully public

Table 4.1.: Overview of different radiative transfer codes with non-LTE atomic line transfer modules. The "Atomic/-molecular lines" column specifies the solution used by each RT code. In order from most to least accurate, there is the deterministic accelerated lambda iteration method (ALI), a probabilistic implementation of the accelerated lambda iteration method using a Monte Carlo approach (MC ALI), and the Sobolov approximation for large velocity gradients.
In the "Native grid mesh option" column, "structured" refers to the option of fixed grids with cubic, spherical or cylindrical structure (Cub., Sph., and Cyl., respectively). "Unstructured" refers to the implementation of some form of Voronoi tesselation, where the mesh grid points are distributed as a cloud of points with no specific axes of symmetry. "Irregular" refers to the option to scale cell sizes according to some predefined relationship (e.g. logarithmic spacing for cells on a spherical grid). "AMR" stands for "adaptive mesh refinement", which offers a dynamical method to irregularise specific parts of the grid. Note that structured grids may be effectively created from unstructured grids in any case. The information in this column only specifies which options are included natively in the code.
In the "Parallelisation" column, "openMP" (open multi-processing) refers to parallelisation on the CPU threads of a single computer, whereas "MPI" (message passing interface) specifices the capacity for distributed computing on multiple machines simultaneously. Both methods may be combined, and the availability of MPI implies the capacity for openMP parallelisation as well.

to be taken when combining cell definitions from two different parametric model components, such as the accretion region and the disk wind detailed in the following sections. As any cell may only carry the information of one model, a careful definition of both model regions via their geometric parameters is necessary to avoid overwriting existing cell information. All interactions between the different components come purely in the form of radiative transfer between them and the induced population changes.

MCFOST offers different options for initialising the atomic level populations. The may be determined from evaluating the densities under LTE conditions, or alternatively, through methods such as collisional-radiative switching (Hummer and Voels, 1988) if the initial LTE guess leads to slow or no convergence. After evaluating the background opacities of continuum sources (e.g. free-free transitions, bound-free transitions) that are not strongly affected by the following

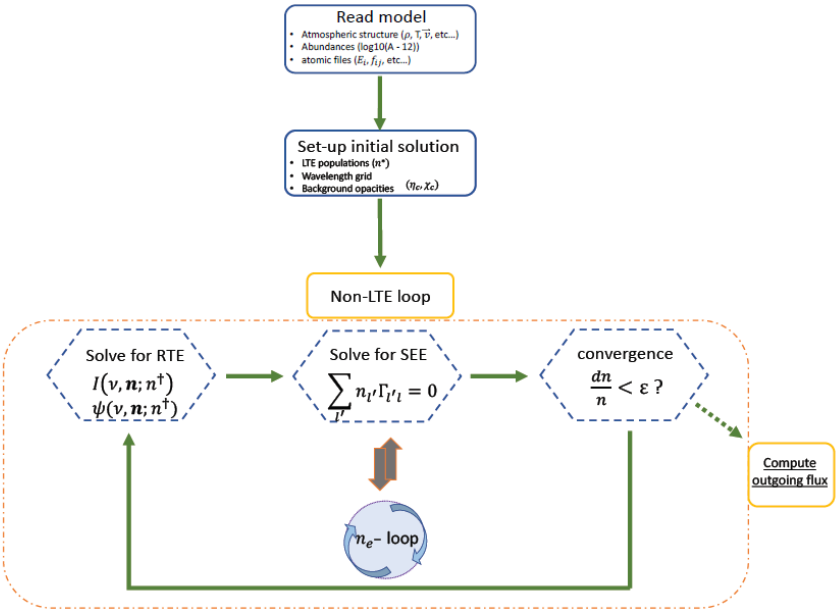

Figure 4.2.: Representation of the iteration loop for the non-LTE problem of line radiative transfer as implemented in MCFOST. I(ν,**n**,n†) is the specific intensity radiated at frequency ν along a beam in the direction of the unit vector **n** at at population levels n†. The † indicates that this step references population numbers from a previous iteration step. ψ is a matrix operator representing the atomic populations and opacities, and Γ is an operator representing the transitional rates in the statistic equilibrium equation (SEE). After the SEE has been solved, the change in population levels attributed to the current iteration step is compared against a treshold value ϵ. If the threshold is not met, the new populations are used to solve the radiative transfer equation (RTE) in the next iteration. Electronic densities n$_{e^-}$ are computed iteratively through their own sub-loop simultaneously to the SEE through a Newton-Raphson scheme.
Image credit: Tessore et al. (2021)

iteration, the non-LTE loop is initialised. MCFOST uses the multilevel-ALI (MALI) method (Rybicki and Hummer, 1991; Uitenbroek, 2001) to determine a solution to the statistical equilibrium equation (4.12), for practical purposes rewritten in terms of a matrix operator Γ_{ab}:

$$\sum_a n_a \Gamma_{ab} = 0. \tag{4.15}$$

Here Γ_{ab} is defined by the transitional rates with

$$\Gamma_{ab} = R_{ab} + C_{ab} - \delta_{ab} \sum_c \left[R_{ac} + C_{ac} \right]. \tag{4.16}$$

Finally, from the solution of the statistical equilibrium equation, new atomic populations are derived which are compared against the result of the previous loop iteration. If the convergence criterion

$$\left\| 1 - \frac{n^\dagger}{n} \right\| < \epsilon, \tag{4.17}$$

is met, the loop concludes and the radiated flux from the image pixels is computed. The threshold value ϵ here may be arbitrarily defined by the user and is typically on the order of 10^{-3} to 10^{-4}. The criterion compares the newly computed population levels n against the result of the previous loop $n^{\dagger}$, and convergence is achieved if the marginal change to the population levels after a new iteration becomes sufficiently small to say that a quasi-stable non-LTE configuration of atomic states was found.

For a more complete description of the implementation of the line radiative transfer problem, I refer to Tessore et al. (2021). Beyond the pure gas emission region, the simulated images used in this thesis also feature a photospheric continuum contribution which may come in the form of either a point source, a uniformly radiating sphere, or a sphere featuring limb-darkening. The brightness profiles of these stellar objects may either be derived from a simple black body spectrum, or from more complex synthetic stellar spectra. Also, while MCFOST is fully capable of simultaneously computing the radiative transfer in a continuum-emitting disk, such a contribution was not included in any of the model systems used in this work, but rather handled on the level of the synthetic interferometric observables, as will be explained in Section 4.5. For a thorough treatment of dust radiative transfer with MCFOST, I refer to Pinte et al. (2006, 2009).

4.3. The magnetospheric accretion model

Note: Based on Section 3 of ***"The interplay between disk wind and magnetospheric accretion mechanisms in the innermost environment of RU Lup" - J.A. Wojtczak, B. Tessore, L.Labadie et al.*** *(Wojtczak et al. (2024), in production).*

Under the magnetospheric accretion paradigm, the inner disk is magnetically truncated at a certain distance R_m from the central star, at which point gas is funneled along the magnetic field lines and transported onto the stellar surface near the poles. In order to compute the emission produced in such a system with the MCFOST code, we employ the model presented in Hartmann et al. (1994); Kurosawa et al. (2006, 2011), and Lima et al. (2010) to define the hydrogen mass density ρ, the temperature profile T(R) and the poloidal velocity v_p along the field lines.

In the axisymmetric scenario, i.e. when the magnetic dipole is completely aligned with the stellar rotational axis, there is no azimuth-dependency of the density, temperature or velocity profiles. As the magnetosphere looks identical from every azimuth angle, the system is thus completely characterised by any 2D slice of the 3D distributions and can be parameterised on a 2D spherical coordinate grid centered on the stellar position. With a radius r and a polar angle θ, the geometry of the field lines is defined by

$$r = R_m \, sin^2(\theta). \tag{4.18}$$

where R_m is the anchoring point of a field line on the disk. The fundamental assumption of magnetospheric accretion is that the stream of matter within the magnetosphere follows the geometry of the field lines. The poloidal velocity of the gas accreting onto the star is defined by

$$v_p(r) = \left[\frac{2GM_*}{R_*}\left(\frac{R_*}{r} - \frac{R_*}{R_m}\right)\right]^{1/2}. \tag{4.19}$$

Thus, the gas is assumed to have no velocity at the truncation radius and then accretes onto the star via free fall motion under the gravitational pull, which defines then the absolute velocity parallel to the field line anchored at R_m at any radius r. Since the magnetospheric funnel is not infinitely thin, we define an inner and an outer magnetospheric radius R_{mi} and R_{mo}, respectively, and a width δR so that $R_{mo} = R_{mi} + \delta R$. The velocity along any field line with an anchor point R_m between these boundaries is fully defined by Eq.4.3 for a given set of stellar parameters and a radius. In addition, a toroidal velocity in the plane perpendicular to the field lines is determined from the magnetic moment of the star, which is defined implicitly by the accretion rate and magnetospheric boundaries, and the stellar rotational period, so that line broadening effects at non-zero inclinations are properly taken into account.

The density along the magnetic field lines follows

$$\rho = C\frac{B_p}{v_p}, \tag{4.20}$$

where B_p is the poloidal magnetic field strength and C is a constant along any given field line. The constant C is obtained by integrating the mass flux over the ring-shaped shock region and acts as an effective normalisation constant to ensure the mass flux onto the star is consistent with the density and velocity profiles within the accretion columns. Thus, the density finally reads

$$\rho = \frac{\dot{M}_{acc}}{4\pi(1/R_{mi} - 1/R_{mo})}\frac{r^{-5/2}}{(2GM)^{1/2}}\sqrt{\frac{4 - 3\frac{r}{R_m}}{1 - \frac{r}{R_m}}}, \tag{4.21}$$

where $\dot{M}_{acc}$ is the mass accretion rate. The area of the shock is defined by the topology of the field lines anchored at R_{mi} and R_{mo}. From Eq. 4.3, one can solve for the intersection with the stellar surface, arriving at bounding latitudes $\theta_{o.i}$

$$sin(\theta_{o,i})^2 = \frac{R_*}{R_{mo,mi}}. \tag{4.22}$$

The shock region itself is another source of continuum emission, acting as an additional black body with a temperature determined by the energy released by the infalling material.

The temperature profile within the funnel flows has been determined self-consistently in the past (Martin, 1996), but the results did not well reproduce known observational profiles (Muzerolle et al., 1998, 2001). We follow Kurosawa et al. (2006); Lima et al. (2010) by adapting

the Hartmann et al. (1994) temperature profile based on a volumetric heating rate $\propto \frac{1}{r^{-3}}$. The temperature along the funnel is then computed based on an assumed energy balance between the radiative cooling rates presented in Hartmann et al. (1982) and the volumetric heating rate. The profile is normalised to a maximum temperature along the funnel T_{mag}, which we set as a parameter in our model.

For the non-axisymmetric scenario, we introduced an additional free parameter: the dipole tilt angle β_{ma} relative to the direction of the stellar rotational axis. We refer to this angle as the "obliquity" of the system. For this non-axisymmetric case, there is no simple analytical formula such as Eq. 4.3 to compute the density along the different field lines. The resulting density can, however, be approximately described based on the axisymmetric density relationship given in Eq. 4.3 as

$$\rho = C\frac{B}{v} \approx CB\frac{\rho_{axi}}{B_{axi}} \tag{4.23}$$

, where ρ_{axi} and B_{axi} are obtained for the axisymmetric dipole ($\beta_{ma} = 0°$) see also Tessore et al. (2023). , the normalisation constant C is obtained numerically, again imposing consistency between the mass accretion rate and the mass flux onto the star. For a full description of the magnetic field components in the non-axisymmetric case, we refer to Mahdavi and Kenyon (1998).

In summary, our magnetospheric accretion model is fully characterised by the **stellar parameters** R_*, M_*, P_*, the **mass accretion rate** $\dot{M_{acc}}$, the **inner anchor point** R_{mi} and **width** δR_{mag} of the accretion columns, and the **obliquity** β_{ma}.

4.4. The disk wind model

Note: Based on Section 3 of ***"The interplay between disk wind and magnetospheric accretion mechanisms in the innermost environment of RU Lup" - J.A. Wojtczak, B. Tessore, L.Labadie et al.*** *(Wojtczak et al. (2024), in production).*

In order to ensure a high degree of flexibility when adjusting the outflow component in the system, we chose to adapt the kinematic disk wind model described by Knigge et al. (1995). Their model follows the basic principle of the magneto-centrifugal disk wind as proposed by Blandford and Payne (1982), which features a mass outflow arising from a disk in Keplerian rotation along a range of open field lines anchored at the disk midplane. It is fundamentally a parametric description of a disk wind, designed to allow for straightforward manipulation of the parameter space to be explored, whilst still approximately reproducing the attributes of a proper, self-consistently treated, MHD wind model.

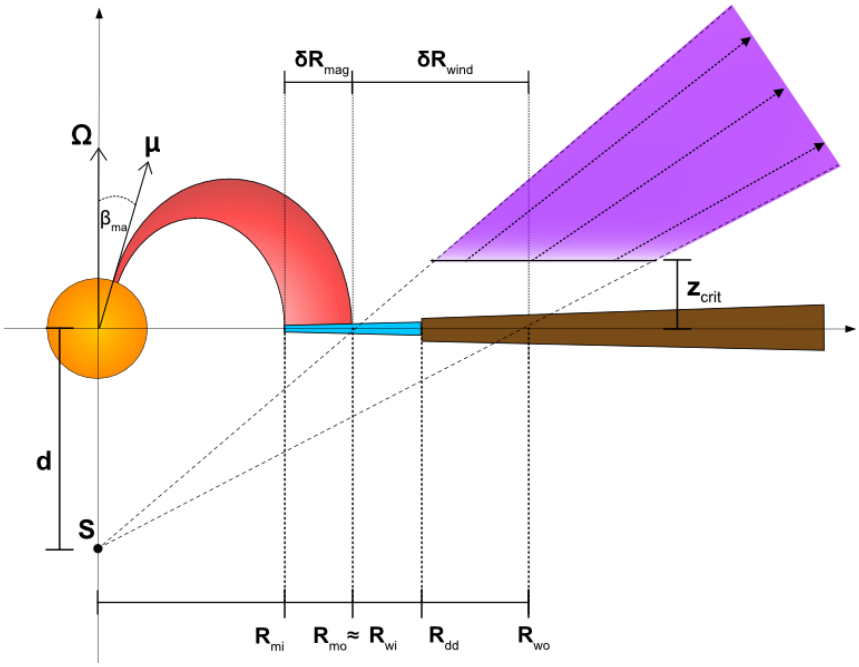

Figure 4.3.: A schematic depiction of the magnetospheric accretion and disk wind models. Shown here are the geometrical parameters defining each component. These are: The rotational axis $\boldsymbol{\Omega}$, the magnetic dipole axis $\boldsymbol{\mu}$, the magnetic obliquity $\boldsymbol{\beta_{ma}}$, the wind focal point (**S**) displacement **d**, the inner and outer radius $\boldsymbol{R_{mi}}$ and $\boldsymbol{R_{mo}}$, and width $\boldsymbol{\delta R_{mag}}$, of the magnetosphere, the inner and outer radius $\boldsymbol{R_{wi}}$ and $\boldsymbol{R_{wo}}$, and width $\boldsymbol{\delta R_{wind}}$, of the wind, the dark disk radius $\boldsymbol{R_{dd}}$ beyond which the disk becomes completely opaque, and the cutoff $\boldsymbol{z_{crit}}$ at which the isothermal wind instantly reaches its 10^4 K temperature.
The lower hemisphere parts of wind and magnetospheric funnel are omitted in this depiction for the sake of clarity.

The geometry of the model is biconical, featuring gas streams which follow a set of magnetic field lines lying on conically shaped surfaces, see Fig. 4.3. In Kurosawa et al. (2006, 2011), this structure is well described by three geometric parameters, which come in the form of the focal point distance d, as well as an inner and outer wind boundary radius $R_{wi,o}$. The focal point defines the origin of the magnetic field lines for one hemisphere, which is vertically displaced from the midplane along the disk axis by the focal point distance. The inner and outer radii of the wind then give the radial distance from the star at which the closest and furthest field lines intersect the midplane, thus defining the effective wind region in our system as the set of conical surfaces between these two radii. We further extend these parameters by an additional quantity z_{crit}, which describes the critical height z above the midplane at which the wind reaches its final constant temperature of 10^4 K. Since our implementation treats the wind as isothermal, the critical height acts as a vertical lower end cutoff, effectively defining a starting height for the Brγ emitting component. This approach, which essentially approximates a temperature profile

along the vertical axis with little heating at first and then a very sharp rise in temperature close to z_{crit}, was chosen to simplify the question of the temperature structure in the gas streams. Below z_{crit}, the gas is assumed to be cold and effectively transparent at NIR K-band wavelengths. The isothermal temperature of 10^4 K was chosen due to practical considerations, as the Brγ wind emission is significantly reduced below this threshold at typical wind densities, and in particular drops off rapidly below 9000 K. The range at which the wind temperature could be reasonably treated as a free parameter of the model is thus narrow to the point that we only consider this temperature.

The velocity profile of the wind can, as previously for the magnetosphere, be separated into a poloidal component v_p, which defines the velocity along the open field line, and a toroidal component v_t. The latter is largely driven by the fact that any field line, at its point of emergence from the disk surface, is effectively in Keplerian rotation about the stellar axis. At the disk midplane it thus is defined by

$$v_{t,0}(R_w) = \sqrt{\frac{GM_*}{R_w}}, \tag{4.24}$$

where R_w is the distance from the star to the field line anchor point. To determine the local toroidal velocity at a non-zero height as the gas stream rises above the disk, it is assumed that the specific angular momentum of the stream with respect to the z axis is conserved. We can then write (Kurosawa et al., 2011)

$$v_t(R) = v_{t,0}(R_w)\frac{R_w}{R}, \tag{4.25}$$

to parametrise the toroidal velocity in the direction of the wind stream at any point (R= $\sqrt{x^2 + y^2}$, z) on the field line, where R is the projection of the point vector **r** onto the radial axis. In other words, R is the cylindrical distance between the field line point for which v_t is to be evaluated and the rotational axis.

The poloidal velocity in the direction of the gas stream is defined by a radial velocity law

$$v_{p,l}(R_w) = c_s(R_w) + [f v_{esc} - c_s(R_w)]\left(1 - \frac{R_s}{l + R_s}\right)^{\beta_{wind}}, \tag{4.26}$$

where R_s is the wind scale length, which we set to 10 R_{wi}, while c_s(R) is the sound speed at the launch point:

$$c_s(R_w) \approx 10\sqrt{\frac{T(r)}{10^4 K}}\ (km\ s^{-1}), \tag{4.27}$$

and l is the distance between the anchor point of the field line and the point **r** on the field line. Finally, f is a scale factor that determines the terminal velocity of the wind as a factor of the

local escape velocity at the point of emergence. In our models, we keep f=2 constant, while the temperature profile in the disk follows

$$T(R_w) = T_{in} \cdot \left(\frac{R_w}{R_{in}}\right)^{\gamma}, \tag{4.28}$$

where we set the temperature at the inner edge of the disk T_{in} to 2000 K and the radial parameter γ =-0.5. β_{wind} is the only parameter left free to be manipulated in order to regulate the wind velocity of our model.

The initial gas density in the disk plane is computed as

$$\rho_0(R_w) = \frac{\dot{m}(R_w)}{v_{p,0}(R_w) cos\delta} \tag{4.29}$$

In this context, δ is the angle between field line and the disk rotational axis, while $\dot{m}$ refers to the local mass loss rate per unit surface area. It is connected to the temperature profile of the disk via

$$\dot{m}(R) \propto T(R)^{4\alpha}, \tag{4.30}$$

i.e. the local mass loss profile follows the temperature gradient if α=0.25 and is uniform across the disk if α=0. This also implies

$$\dot{m}(R) \propto R^{p}, \tag{4.31}$$

where p=4$\gamma\alpha$, due to T(R)$\propto$ R$^{\gamma}$ as shown in Eq. 4.28. The exact proportionality constant is determined from normalising the profile so that integrating the local mass loss rates of all the wind stream lines between the inner and outer radius adds up to the global mass loss rate $\dot{M}_{loss}$:

$$\dot{m}(R) = \dot{M}_{loss} \left(\frac{p+2}{R_{wo}^{p+2} - R_{wi}^{p+2}}\right) \frac{R^p}{4\pi}. \tag{4.32}$$

The density profile in the wind follows from mass continuity along the gas streams

$$\rho(R) = \rho_0(R_w) \frac{R_w}{R} \frac{dR_w}{dR} \frac{v_{p,0}(R_w)}{v_{p,l}(R)} \tag{4.33}$$

$$= \rho_0(R_w) \frac{R_w}{R} \left(\frac{d}{R cos\delta}\right)^2 \frac{v_{p,0}(R_w)}{v_{p,l}(R)} \tag{4.34}$$

$$= \frac{\dot{m}(R_w)}{v_{p,l}(R) cos\delta} \left(\frac{d}{R cos\delta}\right)^2, \tag{4.35}$$

where in the final step we used the result from Eq. 4.29. With this, the density profile in the wind streams is fully described.

In addition to the cutoff height z_{crit}, we lastly introduce a second new parameter that is not part of the original model description in Knigge et al. (1995). The dark disk radius R_{dd} defines the distance from the central star at which the midplane of the cell grid becomes completely opaque to all photons, effectively creating a thin black layer that blocks all radiation from the other side of the disk. This "dark disk" extends from R_{dd} to the edge of the cell grid, while any cell within the radius is completely transparent to all radiation. This again is very much a simplified approach to approximate the real influence of optically thick dust at certain distances in the midplane, but is sufficient to allow us to modulate the proportion of radiation from the back side of the disk that is going to contribute to our profiles.

This again is very much a simplified approach to approximate the real influence of optically thick dust at certain distances in the midplane, but is sufficient to allow us to modulate the proportion of radiation from the back side of the disk that is going to contribute to our profiles.

We finally note that the disk wind model is axisymmetric and thus effectively two-dimensional. While it is technically possible to combine a 2D wind with a 3D non-axsisymmetric magnetospheric accretion model, we point out that such an approach would ignore the interactions between wind and accretion that arise in numerical treatments of such combined systems. In such a scenario, we would expect an azimuth dependence in the density of the wind and thus also an azimuth dependence of z_{crit}, which we do not consider in our analytical approach. In summary, we define the disk wind model component by setting the stellar parameters R_*, M_*, P_* , the **global mass loss rate** $\dot{M}_{loss}$, the exponent regulating the **local mass loss per unit area** α, the exponent regulating the **radial velocity law** β_{wind}, the **inner radius** R_{wi} and **width of the wind** δR_{wind}, the **dark disk radius** R_{dd}, the **focal point displacement** d, and the **temperature cutoff** z_{crit}.

4.5. Synthetic interferometric observables

The intensity maps produced with MCFOST from the parametric models of magnetospheric accretion and disk winds are not directly comparable to observational interferometric results, since the uv space probed by a typical VLTI GRAVITY observation is limited and insufficient to accurately reconstruct the complete Brγ brightness distribution. As explained in Section 2.1.1, geometrical modelling of the visibilities and deprojections of the phase information are instead used to extract information regarding the spatial properties of the emission region from the complex visibilities. Translating the simulated image into such corresponding interferometric quantities is not technically challenging, but necessitates some careful consideration as to what

exactly is being represented by the synthetic data in order to ensure comparability.

Fourier transformation of the simulated image will produce a set of synthetic complex visibilities which represent the image in the uv-plane. Standard solutions utilising high performance algorithms, such as the Fast Fourier Transformation (FFT), are readily available in default libraries for languages like Python. In practise, however, a simple evaluation of the Fourier integral

$$\tilde{v}(u,v) = \int I(\alpha,\beta)\ \exp\left(\frac{-2i\pi}{\lambda}(B_u\alpha + B_v\beta)\right)\ d\alpha d\beta, \tag{4.36}$$

where $B_{u,v}$ is the component of the baseline vector along the u,v axes in meters and α,β are the angular coordinates of the image pixels, has proven to be the superior method for computing synthetic visibilities for a large amount of models. While standard FFT packages indeed offer fast computational times, they also map the entirety of the image to the spatial frequency domain instead of only those uv points probed by the baseline vector **B**. Computing the integral in Eq. 4.36 will restrict the operation to only one complex visibility $\tilde{v}(\mathbf{B},\lambda)$ per uv point, i.e. per spectral channel and baseline. If the baseline array and wavelengths used correspond to the observational configuration, then only those uv points probed by the observation will be considered and the overall computation time is reduced. The visibility amplitude and the phase can then be recovered as

$$V(\mathbf{B},\lambda) = \mathrm{abs}(\tilde{v}(\mathbf{B},\lambda)) \tag{4.37}$$

$$\phi((\mathbf{B},\lambda) = \arg(\tilde{v}(\mathbf{B},\lambda)). \tag{4.38}$$

These quantities are specific to **B** as they encode the projections of the geometric features along a specific baseline alignment at a resolution defined by the baseline length.

The model images feature the Brγ gas emission region, as well as a stellar continuum. If the model includes magnetospheric accretion, then the stellar continuum is composed of a photospheric and an accretion shock contribution, otherwise it consists of the photospheric emission only. For sufficiently high particle densities and temperatures, certain model configurations may also show the hydrogen emission region contribute to the continuum radiation through bound-free transitions. A dusty disk emitting in the K-band continuum on the other hand, which we would expect to be encoded within the observational visibilities and fluxes, is completely omitted from the simulated images. This potential discrepancy between the observed intensity map and the simulated intensity map is not inherently problematic for the comparison between synthetic and observational data. There are in general two different ways process the synthetic data to make them comparable to the observations:

- The pure line quantities are extracted as described in Section 2.1.1 from the total image visibilities and total image differential phases. Both the observational and synthetic pure

line observables describe the total extent of the coherent Brγ flux from the emitting hydrogen in the inner disk and are thus directly comparable. Any discrepancy between them is then caused by the model diverging from the system that is to be modelled.

- The missing disk contribution in the image may be added to the interferometric equations. The total image flux ratios, visibilities, and phases are modified to make them comparable to the total observational observables. This approach requires more work, but it allows to explore variations in the continuum parameters and their impact on the total observables. If only the sizes and photocenter offsets of the gas emission are of interest, this method is ultimately unnecessary as the pure line visibilities computed from the modified observables and the pure line visibilities computed from the unmodified image observables are identical, if the modification is implemented correctly. Regardless of whether the visibilites and phases are to be modified to include the dusty disk, the modification of the line-to-continuum flux ratio is necessary to compare the synthetic Brγ spectrum to the observational spectrum obtained with GRAVITY.

Extracting the pure line visibilities from the image observables is straightforward. The treatment of the synthetic observables is largely analogous to that of the observational data described in Section 3.2. If no noise is applied to the simulated image or the resulting complex visibilities, then the process of fitting a Gaussian function to smooth out channel-to-channel fluctations is unnecessary and the actual read-out values from each spectral channel can be used directly without issue. The pure line visibility is extracted as before via

$$V_{Line} = \frac{F^{Im}_{L/C} V^{Im}_{tot} - V^{Im}_{Cont}}{F^{Im}_{L/C}}, \tag{4.39}$$

where the superscript "Im" specifies that all the quantities on the right-hand side of the equation are specific to the image. One of the core points to consider here stems from an important implicit result that is contained within the pure line visibility equation. The extraction of the continuum-corrected visibilities does not depend on the nature of the continuum or its composition. In Equations (3.19) and (4.39), the continuum sources encoded within the total observables differs by the dusty disk and potentially also the shock region, yet the equations are completely identical in form. As long as consistent quantities are combined with each other to remove the appropriate continuum influence for the system in question, the resulting pure line observables will be identical. In practical terms, this means that the normalised total flux of the simulated image needs to be combined with the total line and total continuum visibilities in Eq. (4.39), as they contain all information from the simulated emission sources. If on the other hand the total

image visibilites are modified to add a disk contribution, then the normalised flux needs to be modified consistently in order to extract the same pure line visibility.

4.5.1. Modified flux ŕatio of the model

Consider first the original total line to total continuum flux ratio $F'_{L/C}$ of the model image, composed only of the Brγ line emission region and a stellar continuum:

$$F'_{L/C} = \frac{F_* + F_{Line}}{F_*} \tag{4.40}$$

$$= 1 + \frac{F_{Line}}{F_*}. \tag{4.41}$$

We now define the modified flux ratio $F_{L/C}$ to include disk contribution to the total flux. In treatments of the K-band continuum data, which typically traces a much more spatially extended region, the modelling of an additional so called halo component is common. This halo refers to a part of the emission region that is within the field of view of the telescopes and thus contributes to the measured flux, but is so spatially extended that it is overresolved at all baselines, with a visibility $V_{Halo} = 0$. The modified expression featuring both halo and disk flux is then

$$F_{L/C} = \frac{F_* + F_{Disk} + F_{Halo} + F_{Line}}{F_* + F_{Disk} + F_{Halo}} \tag{4.42}$$

$$= \frac{1 + \frac{F_{Line}}{F_*} + \frac{F_{Disk}+F_{Halo}}{F_*}}{1 + \frac{F_{Disk}+F_{Halo}}{F_*}} \tag{4.43}$$

$$= \frac{F'_{L/C} + \frac{F_{Disk}+F_{Halo}}{F_*}}{1 + \frac{F_{Disk}+F_{Halo}}{F_*}}. \tag{4.44}$$

In Eq. (4.44) the new ratio is recast in terms of the original flux ratio of the model cube and the infrared excess $\frac{F_{Disk}+F_{Halo}}{F_*}$. The total infrared excess needs to be known for this modification, or alternatively may be derived from fitting the spectral data. In this case both the Brγ emission model parameters and the infrared excess of the continuum are to some degree uncertain. Determining the continuum flux ratios from a separate fit of the GRAVITY continuum data is in most cases the better choice.

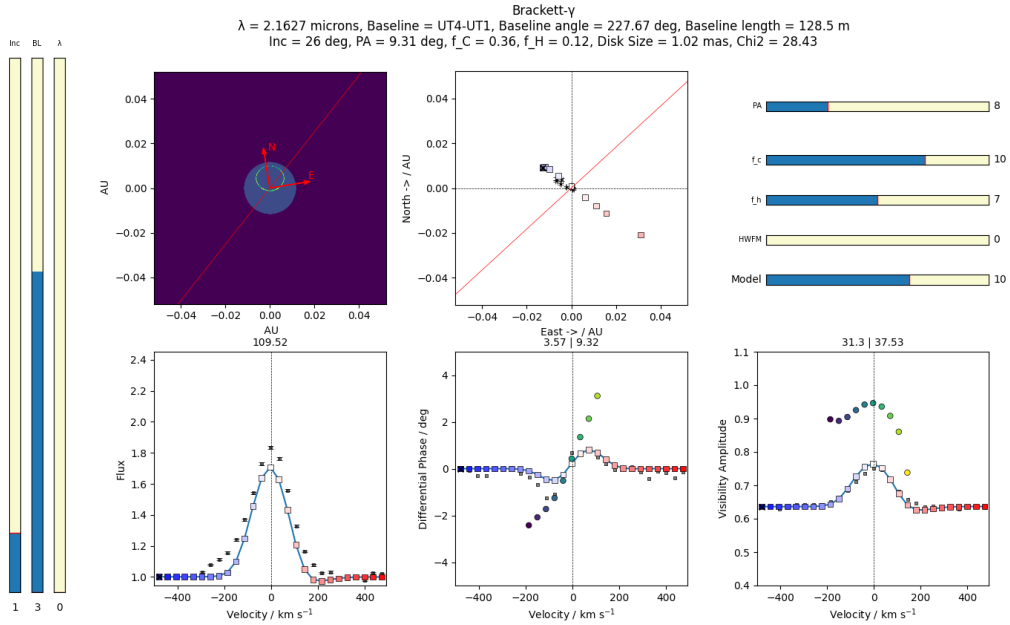

Figure 4.4.: A simple visualisation tool for synthetic interferometric model data. Setting the sliders allows for interactive adjustments to the model parameters.
Shown here is an early iteration of the tool, used as part of the GRAVITY T Tauri study to compare modified total model observables to the total observational quantities obtained with GRAVITY for RU Lup in 2021. The panels show, from top left to bottom right, the model image at one wavelength, the photocenters of the emission region, the line-to-continuum flux ratio, the total differential phases, and the total visibilities. Model data points are depicted in colour-coded squares, observational data in grey. Pure line observables computed from the model are shown in colour-coded dots. The red line indicates the orientation of the selected baseline.

4.5.2. Modified visibility amplitude of the model

By modelling the visibility components of the total image visibility V'_{tot}, we derive the expression already given in Eq. (4.39)[3]:

[3]In Section 3.2, we derived this form of the pure line visbility equation under the assumption that the differential phase is small enough so that $\cos(\phi) \approx 1$. The same assumption is made here implicitly to simplify the algebra.

$$V'_{tot} = \frac{F_* V_* + F_{Line} V_{Line}}{F_* + F_{Line}} \tag{4.45}$$

$$= \frac{V_* + \frac{F_{Line}}{F_*} V_{Line}}{1 + \frac{F_{Line}}{F_*}} \tag{4.46}$$

$$= \frac{V_* + (F'_{L/C} - 1) V_{Line}}{F'_{L/C}}. \tag{4.47}$$

Following the same approach as for the modified flux ratio, the total visibility for a system including an additional halo and disk continuum contribution is

$$V_{tot} = \frac{F_{Line} V_{Line} + F_* V_* + F_{Disk} V_{Disk} + F_{Halo} V_{Halo}}{F_{Line} + F_* + F_{Disk} + F_{Halo}} \tag{4.48}$$

$$= \frac{V_* + \frac{F_{Line}}{F_*} V_{Line} + \frac{F_{Disk}}{F_*} V_{Disk}}{1 + \frac{F_{Line}}{F_*} + \frac{F_{Disk}+F_{Halo}}{F_*}} \tag{4.49}$$

$$= \frac{F'_{L/C} V'_{tot} + \frac{F_{Disk}}{F_*} V_{Disk}}{F'_{L/C} + \frac{F_{Disk}+F_{Halo}}{F_*}}. \tag{4.50}$$

Here, as a first step, $V_{Halo} = 0$ was substituted, and the equation subsequently re-expressed in terms of the original total model visibility Eq. (4.47). The modified total visibility is finally written in dependence of the original model flux ratio $F'_{L/C}$, the original total model visibility V'_{tot}, the total infrared excess $\frac{F_{Disk}+F_{Halo}}{F_*}$, and the disk-attributed infrared excess $\frac{F_{Disk}}{F_*}$. The total disk visibility encodes the geometric properties of the partially resolved part of the continuum-emitting disk and can, for example, be computed from a geometric disk model, after the inclination and the position angle of the disk were properly into account. Alternatively, using $\frac{F_{Line}}{F_*} = (F_{L/C} - 1)(\frac{F_{Disk}+F_{Halo}}{F_*} + 1)$ and $V_{Cont} = \frac{\frac{F_{Disk}}{F_*} V_{Disk} + V_*}{F_{Disk}+F_{Halo}+1}$, Eq. (4.49) can be recast into a form analogous to Eq. 4.39:

$$V_{tot} = \frac{V_{Cont} + (F_{L/C} - 1) V_{Line}}{F_{L/C}}. \tag{4.51}$$

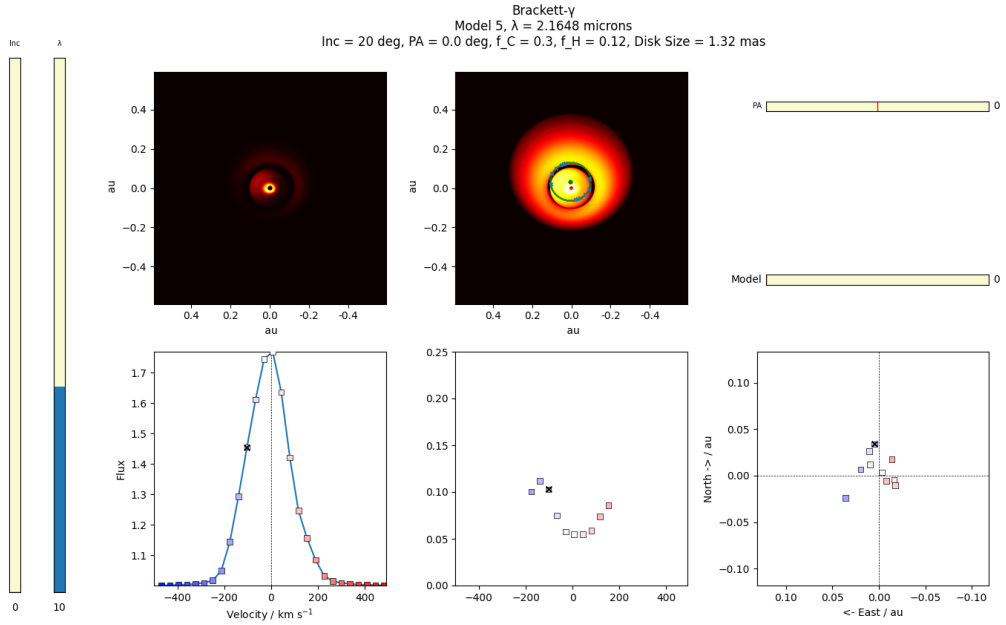

Figure 4.5.: A variant of the visualisation tool that only displays the final results from the fit of the geometric model and the deprojected photocenter shifts, without any baseline-dependency. The panels are, from top left to bottom right: The model image at linear and logarithmic normalisation, the line-to-continuum flux ratio, the HWHM derived with the Gaussian disk model, and the photocenter shifts. The focus on the resulting sizes was more relevant when trying to reproduce the observational size profile of RU Lup with more complex models of combined magnetospheric accretion and disk wind components.

In this case the disk information is contained within the general continuum visibility. This equation will yield the - at this point well known - expression for the pure line visibility, proving that the exact composition of the continuum is irrelevant to the correction.

4.5.3. Modified differential phase of the model

The pure line differential phase can be extracted from the unmodified model observables as:

$$\Phi'_{Line} = arcsin\left(\frac{F'_{L/C}}{F'_{L/C}-1}\frac{V'_{tot}}{V_{Line}}sin(\Phi'_{tot})\right). \tag{4.52}$$

The equivalent relationship for the modified model cube follows self-evidently from Eq. 4.51

$$\Phi_{Line} = arcsin\left(\frac{F_{L/C}}{F_{L/C}-1}\frac{V_{tot}}{V_{Line}}sin(\Phi_{tot})\right), \tag{4.53}$$

in analogy to the derivation presented in Section 3.2.
As previously discussed, the pure line quantities by definition should be equal, $\Phi_{Line} = \Phi'_{Line}$. Through this equality one can then relate the total differential phase of the modified model to the total differential phase of the original model system as

$$\frac{F'_{L/C}}{F'_{L/C}-1}\frac{V'_{tot}}{V_{Line}}sin(\Phi'_{tot}) = \frac{F_{L/C}}{F_{L/C}-1}\frac{V_{tot}}{V_{Line}}sin(\Phi_{tot}) \tag{4.54}$$

$$\iff sin(\Phi_{tot}) = \frac{F'_{L/C}}{F_{L/C}}\frac{F_{L/C}-1}{F'_{L/C}-1}\frac{V'_{tot}}{V_{tot}}sin(\Phi'_{tot}) \tag{4.55}$$

$$= \frac{F'_{L/C}V'_{tot}}{\frac{F_{Disk}+F_{Halo}}{F_*}V_{Disk} + F'_{L/C}V'_{tot}}sin(\Phi'_{tot}). \tag{4.56}$$

The total differential phases for a system including a disk continuum can thus be computed from the infrared excess, the disk visibility and the unmodified image observables as

$$\Phi_{tot} = \arcsin\left(\frac{F'_{L/C}V'_{tot}}{\frac{F_{Disk}+F_{Halo}}{F_*}V_{Disk} + F'_{L/C}V'_{tot}}sin(\Phi'_{tot})\right). \tag{4.57}$$

4.5.4. Treatment of the synthetic data

Ultimately, following the modifications outlined in this section, or simply extracting the pure line observables right away, will yield a set of flux ratios over some chosen wavelength range, as well as one visibility and differential phase per baseline and spectral channel. These synthetic data may be compared against the GRAVITY data directly, either in form of the total or pure line quantities, or they can be processed in the same way as the observational data to derive a characteristic size and a relative photocenter shift of the emission region.

Either way, as a first step the model should be rotated to the same orientation as the observational target it is to be compared against. The images produced by MCFOST always align the stellar rotational axis with the vertical image axis, whereas any observed object will usually feature a non-zero position angle. While it is possible to rotate the total image entirely, it may be more convenient to simply add the PA to the baseline angle and hereby effectively rotate the baseline configuration to the observational frame of reference. Of course, this requires knowledge of the source PA. If this is not available, the observables may also be computed over a large range of possible position angles in order to find some form of best fit solution.

As the model images are computed over an arbitrarily chosen wavelength grid at essentially perfect spectral resolution, the data needs to be spectrally degraded to be comparable to the observation. In order to do so, the flux, visibilities and differential phases are first convolved with a Gaussian kernel with a FWHM equal to the 2.5 Å channel width of GRAVITY's high spectral resolution mode, and then interpolated on the observational wavelength grid. It is not necessary to also spatially degrade the image before computing the complex visibilities, since the interferometric resolution is set by the baseline length and thus already integrated into the evaluation of the Fourier integral.

When modifying the total observables, the disk contribution can be added as described by Equations (4.44) and (4.49). Doing so requires definition of the disk and halo contributions to the total flux, as well as the size of the disk and its inclination and PA. If these parameters are not well constrained, again a grid of possible paramter combinations may be used to determine a best fitting solution. The disk visibility contribution is at non-zero inclinations specific to the direction of the baseline and the positional parameters of the disk. For an angular disk size parameter Θ, the projected size along a baseline can be converted into a baseline-specific visibility via

$$\Theta_i^{projected} = \Theta \sqrt{\cos^2(\phi_i + \theta) + \cos^2(inc)\sin^2(\phi_i + \theta)} \tag{4.58}$$

$$\implies V_{Disk,i}^{projected} = \exp\left(-\frac{(\pi\Theta \sqrt{\cos^2(\phi_i + \theta) + \cos^2(inc)\sin^2(\phi_i + \theta)}B)^2}{4\ln(2)\lambda^2} \right), \tag{4.59}$$

where θ is the position angle of the disk, inc is the disk inclination, and ϕ_i is the baseline angle of the i-th baseline.

Over the course of this project, having access to an easy way to explore the impact of different model parameters on the resulting observables proved to be of great advantage. A simple tool, depicted in Figures 4.5 and 4.4 with an interface which allows the user to interactively switch between different parameter configurations, was written and used to this end. The visualiser offers the possibility to vary the inclination, position angle, disk and halo fluxes, and disk size, as well as the underlying model file itself, and allows the user to attribute different sizes and photocenter shifts easily to the images and other observables of those spectral channels for which they were derived.

4.6. Parameter dependencies of the models

Note: The content of this section is a direct citation from Appendix A of ***"The interplay between disk wind and magnetospheric accretion mechanisms in the innermost environment of RU***

	P_r	ΔP [%]	ΔFlux [%]	ΔSize [%]	ΔPC [%]	Mean Δ [%]	ξ_{Flux} [%]	ξ_{Size} [%]	ξ_{PC} [%]	ξ_{Tot} [%]
T_{mag}	8600 K	16	22	27	73	41	134	167	448	250
R_*	2.5 $R_\odot$	24	5	21	27	17	22	86	111	73
R_{mi}	7 R_*	43	10	29	39	26	23	69	90	61
P_*	7 days	45	3	6	38	16	7	14	84	35
$\dot{M}_{acc}$	23 10^{-8} $M_\odot yr^{-1}$	22	8	4	11	8	35	16	52	35
δR_m	2 R_*	50	12	4	26	14	24	8	51	28
M_*	0.8 $M_\odot$	38	7	4	12	8	20	10	32	21
T_*	4050 K	2	0	0	0	0	2	0	4	2
Average		30	8	12	28	16	33	46	109	63

Table 4.2.: **Magnetospheric accretion model response properties.** All quantities marked with Δ are mean parameter variations of the magnetospheric accretion model, given in relation to the reference parameter P_r. ξ denotes the resulting responses of the computed synthetic observables (line-to-continuum flux ratio, characteristic emission region size and emission region offset), as computed according to Eq. 4.61.

Lup'' - J.A. Wojtczak, B. Tessore, L.Labadie et al. *(Wojtczak et al. (2024), in production).*

While the parameter descriptions laid out in sections 4.3 and 4.4 may outline the general impact of a parameter change on the densities and velocities in the system, they cannot straightforwardly connect the effect of such a variation with the resulting emission line profiles, and possibly even less so with the interferometric quantities. Due to the complex interplay between atomic populations, radiative transitions and the spatial distribution of velocities and densities, it is more instructive to directly analyse the effective change in line strength, emission region size and photocenter distribution when increasing or decreasing a single parameter by a certain margin. In this manner, both the total sensitivity of the model as well as the partial sensitivities of these individual quantities to changes in a specific parameter may be constrained and compared. The limitations to this approach lie predominantly in the need to compute a new model for each parameter change and the time investment required to do so. Given the relatively large amount of parameters that we consider, in principle, fit for variation up to a point, we limit this analysis to one increase and one decrease relative to the parameter value of an arbitrarily chosen reference model. The step size of the variation is not set consistently but rather chosen based on relevant upper and lower limits from the literature for parameters which have known observational constraints, like the stellar radius or mass. Other parameters, for which such constraints are not available, are varied to a degree that results in a similar change in the line-to-continuum

flux ratio. While a purely theoretical study of the models would certainly look at a broader range of parameter changes, we remind that the purpose of this analysis was primarily to determine which quantities were the most relevant to the interpretation of specific observational results.

We differentiate between individual parameters based on their influence on the results. To this end, we present multiple ways to quantify the impact. First, we consider the relative change ΔO as a percentage of the respective reference model parameter:

$$\Delta O = \left| \frac{O_v - O_r}{O_r} \right|. \tag{4.60}$$

Here, O is one of the observables we compute from the model images, i.e. line-to-continuum flux ratio, characteristic size of the emission region or photocenter offset of the emission region. The subscript v designates that the observable belongs to the variation model, while r designates the reference model. We choose to employ a relative measure of the change primarily due to the very different scales between these three observables. If we were to consider the absolute change, the large flux ratio values would dominate the average over the small sizes and photocenter shifts. In particular, we consider here the mean relative change between the parameter increase and the parameter decrease. We further compute the unweighted average of this metric over all considered wavelengths across the Brγ feature. Then, we subsequently set this value in relation to the relative parameter step ΔP, which is computed analogously according to Eq. 4.60 for a variation model parameter P_v and a reference model parameter P_r. Thus, we arrive at a measure for the relative mean observable change, adjusted by the parameter step size. We refer to this quantity as the model observable O response ξ_O to a parameter P change ΔP.:

$$\xi_O = \frac{\Delta O}{\Delta P} \tag{4.61}$$

4.6.1. Stellar parameters

The photospheric contribution to the continuum emission is modelled as a blackbody which radiates at an effective temperature T_* over a surface area defined by the stellar radius R_*. In addition, the stellar mass M_* and stellar rotational period P_* affect the velocities in the magnetospheric funnel flows and wind outflows. While in Gravity Collaboration et al. (2023b) we assumed those parameters to be relatively well defined for the test case of RU Lup, a more thorough review of the literature showed a significant spread of reported figures for this object. Consequently, we chose to adapt a broader range of possible parameter values, treating them effectively as a semi-free parameter in our model exploration. This is discussed in more concrete detail in Section 8.4.

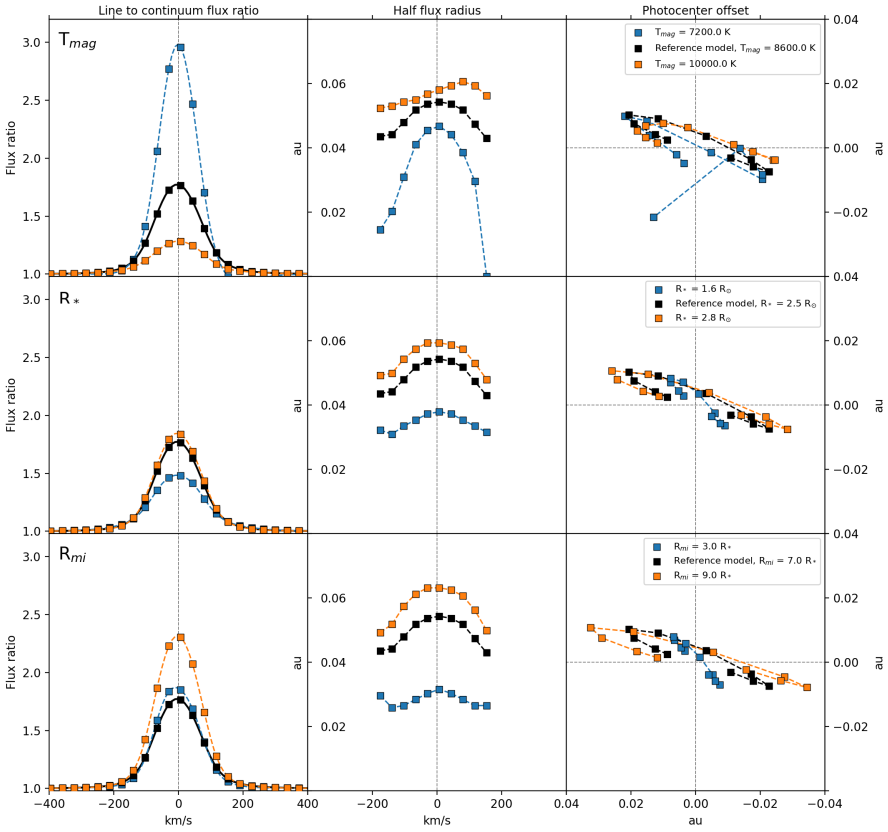

Figure 4.6.: Observable dependencies on parameter changes for the top three **magnetospheric accretion** parameters as ranked in Table 4.2. The left column depicts the changes in continuum normalised line flux. The center column shows a characteristic interferometric size, obtained as the half width at half maximum (HWHM) of a geometric Gaussian disk model. The right column illustrates the spatial distribution of line emission photocenters at different velocity channels.

4.6.2. Magnetospheric accretion

In Table 4.2 we present the relative effects of a parameter change on the magnetospheric accretion model observables, as well as the response metrics computed based on Eq. 4.61. When ranked by their respective ξ_{Tot} values, the maximum temperature in the magnetospheric funnel flows T_{mag}, the stellar Radius R_* and the inner magnetospheric truncation radius R_{mi} come out top in terms of their overall impact on the resulting model observables. Figure 4.6 shows the deviations of the line profile, the size and photocenter shifts from the reference model for the

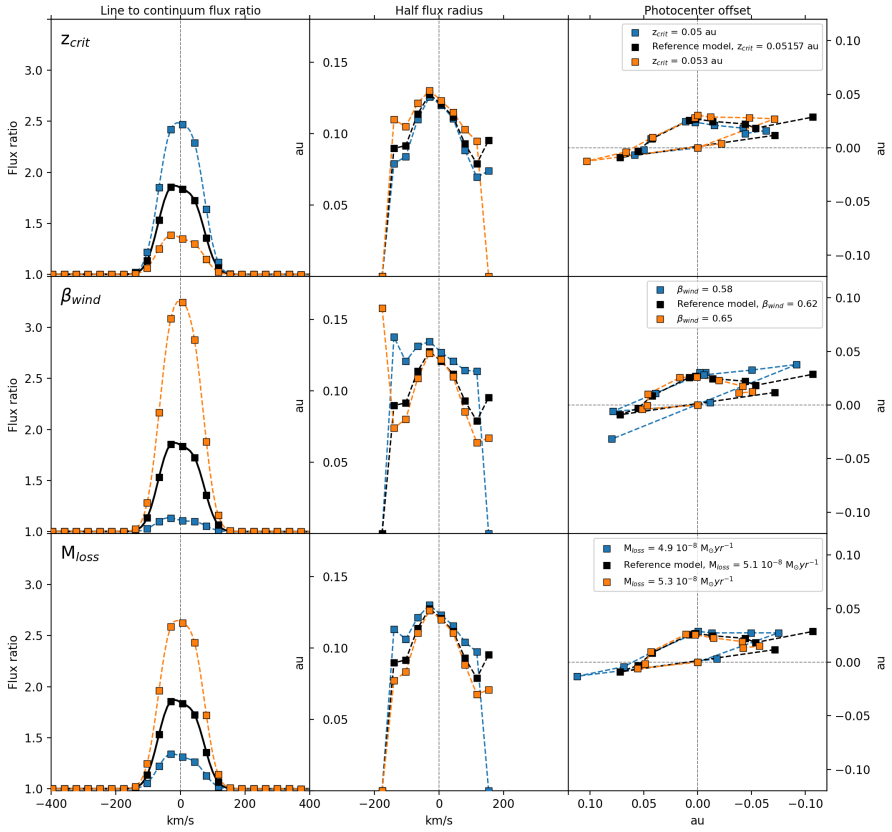

Figure 4.7.: Observable dependencies on parameter changes for the top three **disk wind** parameters as ranked in Table 4.3. The left column depicts the changes in continuum normalised line flux. The center column shows a characteristic interferometric size, obtained as the half width at half maximum (HWHM) of a geometric Gaussian disk model. The right column illustrates the spatial distribution of line emission photocenters at different velocity channels.

across all channels of the Brγ feature for these quantities. Here, the effect of a magnetospheric temperature variation on all three observables stands out as particularly noteworthy when taking into account the relatively small variation step width. The relative changes in photocenter shifts and sizes are on the order of factor 2 to 4 higher when compared even to the other two high impact parameters, and on the order of factor 10 when compared to the mass accretion rate of the system, for which the variation step width of 22% is similar to T_{mag} at 16%. Figure 4.6 shows that an increase in magnetospheric temperature from the reference value of 8600 K leads to a decrease in continuum-normalised flux and simultaneously to an increase in the emission regions

	P_r	Δ P [%]	Δ Flux [%]	Δ Size [%]	Δ PC [%]	Mean Δ [%]	ξ_{Flux} [%]	ξ_{Size} [%]	ξ_{PC} [%]	ξ_{Tot} [%]
z_{crit}	0.0516 au	3	15	14	35	21	522	473	1195	730
β_{wind}	0.62	6	27	21	63	37	487	376	1114	659
M_{loss}	5.1 10^{-8} $M_\odot yr^{-1}$	4	18	15	36	23	465	375	922	588
δR_w	7.1 R_*	20	40	29	94	54	200	147	469	272
R_{wi}	5 R_*	14	15	11	69	31	104	75	489	223
d_{fp}	15 R_*	33	39	34	138	70	118	103	413	211
R_*	2.5 $R_\odot$	24	11	14	93	39	46	57	386	163
R_{dd}	14.5 R_*	34	14	12	141	56	40	36	408	161
M_*	0.8 $M_\odot$	38	41	29	88	53	109	78	234	140
α_{wind}	0.4	25	26	18	47	31	104	72	190	122
T_*	4050 K	5	3	2	7	4	68	44	140	84
P_*	7 days	45	0	0	0	0	0	0	0	0
Average		21	21	17	67	35	188	153	497	279

Table 4.3.: **Disk wind model response properties**. All quantities marked with Δ are mean parameter variations of the disk wind model, given in relation to the reference parameter P_r. ξ denotes the resulting responses of the computed synthetic observables (line-to-continuum flux ratio, characteristic emission region size and emission region offset), as computed according to Eq. 4.61.

characteristic size. The former suggests that, at such high temperatures, a significant amount of continuum emission is produced in the accretion columns due to bound-free transitions as the hydrogen becomes increasingly ionised. The larger characteristic size stems from a flatter distribution of flux across the entire magnetosphere, which leads to a spatially more extended full width at half maximum of the Gaussian disk model used to fit the characteristic size. For the same reason, the photocenter appears slightly less extended, as the more evenly distributed emission throughout the very hot magnetosphere symmetrises the emission region relative to the reference model.

Similar reasoning can be applied when breaking down the effects of other parameter changes, although in the case of the stellar radius one should take care to separate the physical influence of the radius from model scaling effects. Since we define the size of our truncation radius and magnetospheric widths in units of stellar radii, we are effectively changing the absolute physical size of the magnetosphere by varying the stellar radius, and thus also the position of the field line anchor points as they appear in those equations. This in turn explains why the impact a stellar radius variation seems to beat an adjustment of the truncation radius, both in terms

of ξ_{Tot} and also in the partial metric for the characteristic size alone. The characteristic size of the system is a product of both R_{mi} and, albeit to a significantly lesser degree, δR_m, which are both defined in units of R_*, whereas setting the truncation radius directly will only affect R_{mi}.

By contrast, it appears that the stellar mass M_* and photospheric temperature T_* only marginally influence the outcome of the computations. This is particularly true for the photospheric temperature, which, even when accounting for the very small parameter variation of about 2%, produces a negligible change in observables compared to the other quantities. The low impact of T_* on the interferometric quantities is not surprising, given that the characteristic size of the emission region is based on the continuum extracted pure line visibilities and the pure line differential phase. The fact that some variation in photocenter shift with changing photospheric temperature can be observed at all is likely caused by the shifting weights between the stellar continuum and the magnetospheric continuum. Indeed, the former will produce a small non-zero continuum phase at higher inclinations due to the presence of the ring-like shock region close to the pole, while the magnetospheric continuum is centrosymmetric for an axisymmetric configuration, such as used here.

Finally, the stellar period does not affect the flux ratio or characteristic size to the same degree as R_*, but has a comparable effect on the photocenter shift, due to increased line broadening at higher rotational velocities of the star. Since the magnetospheric funnels rotate at the same velocity, observing the rotating gas stream at a non-zero inclination will lead to a broader line profile. The change in flux ratio caused by this is not necessarily large, as demonstrated by the low ξ_{Flux} of only 7%. The redistribution of flux to higher velocities, however, translates to a relatively large change in magnetospheric symmetries at those velocities, and thus the more drastic variations in the photocenters per velocity component.

4.6.3. Disk wind

In Table 4.3 we present an analogous ranking of the response metric ξ_{tot} for the disk wind model. It demonstrates that again three parameters perform significantly stronger compared to the rest in terms of their impact on the three observables. For the wind model, we find that the critical height z_{crit}, the velocity law parameter β_{wind} and the global mass loss rate $\dot{M}_{loss}$ have far above average impact on the resulting line profiles, characteristic sizes and photocenter shifts. The response metrics for these three parameters are broadly similar across the three observables. For each of them, the step width-weighted parameter variation causes a particularly large relative change in the photocenter profile, for which the ξ_{PC} is about a factor two larger than the corresponding flux ratio metric, whereas the respective ξ_{Size} values are similar to, but slightly smaller than, the flux ratio metric. In Figure 4.7 we show the corresponding changes in flux ratio, size and photocenter offset.

It is obvious that a higher cutoff z_{crit} of the wind leads to a weaker line-to-continuum ratio. This is expected, as the density along a stream line falls with increasing distance from the mid-plane. As a consequence, by choosing a higher cutoff, we effectively remove the denser parts of the wind from the model, thus lowering the Brγ emission contribution of the wind. The size, on the contrary, increases slightly when the cutoff is higher, since the effective inner diameter of the brightness distribution is enlarged due to the collimation angle of the field lines, see Fig. 4.3. The maximum shift magnitude among the photocenter offsets is even more extended for the same reason.

By contrast, for both mass loss rate and the velocity law exponent, parameter increases lead to stronger flux ratios, but smaller emission region characteristic sizes and more compact photocenter shift profiles. For the wind velocity exponent β_{wind}, this behaviour is straightforward to understand. A higher value for β_{wind} decreases the acceleration of the wind. In turn, in requires the wind to travel further to reach the same velocity, which leads to the size increase due to the angle of the stream lines. The velocity also influences the density inversely, as the density of gas particles in a slow moving outflow is higher, and so is subsequently then the gas emission. The change in characteristic size and photocenter offsets following such a parameter variation is most pronounced at high velocities. As there is now more or less, for decreasing or increasing β_{wind} respectively, gas moving at those high velocities, the region appears larger or smaller at those wavelengths. The parallel decrease in flux ratio that comes with a larger region is largely irrelevant to the characteristic size, as long as the hydrogen is dense enough to produce Brγ emission, since the characteristic size is obtained from the continuum-corrected visibilities.

An analogous argument can be made for the changes induced by a variation of the global mass loss rate. The local mass loss rate $\dot{m}$(R) at a certain distance R from the central star is $\propto \dot{M}_{loss}$, so a high global mass loss rate leads to an increase in local mass loss at every distance and thus increased wind density at every distance. However, in this case, the α_{wind} parameter, as well as the chosen collimation angle of the wind stream lines, lead to a stronger increase in density closer to the inner edge of the disk. Under such circumstances, a fit of a Gaussian disk model would yield a smaller characteristic size.

The stellar parameters appear to again have some of the weakest effects on the three observables. The rotation period in particular does not affect the model at all, since the angular velocity component of the wind is fully determined by Keplerian velocity at the stream line anchor point. As a notable difference compared to the magnetospheric model, the stellar radius seems to rank below both inner radius and width of the wind region, even though both are defined in units of R_* and thus naively the same reasoning as laid out there should apply. The equations governing the density and velocity profiles of the wind model, however, show that dependencies on length scales and sizes mostly come in the form of a ratios between different different projected radial

distances, which are all defined in stellar radius units. It follows then that these quantities are relatively less affected by a change in R_*. It is also the case here that the most impactful distance scale, the cutoff height z_{crit}, is defined in absolute astronomical units and does not vary with the stellar radius.

Finally, we note that the dark disk radius parameter R_{dd}, which we introduced to regulate the amount of detected flux from the back side of the disk, is of below average influence according to its computed ξ_{Tot}. While this is true when considering the overall profile changes induced by a variation in R_{dd}, it does not properly illustrate the effect on profile symmetry. The dark disk radius R_{dd} is the only parameter that allows us to directly adjust the relative strength between blue and red wings of the observable profiles. This unique quality of the parameter is not well reflected in the response metric, given that we consider average metrics over the entire relevant wavelength range.

5. The GRAVITY Brγ T Tauri survey, part one: Introduction and global trends

Note: The contents of this chapter are direct citations from ***"The GRAVITY young stellar object survey IX. Spatially resolved kinematics of hot hydrogen gas in the star-disk interaction region of T Tauri stars" - Gravity Collab.: J. A. Wojtczak, L. Labadie et al.*** *(Gravity Collaboration et al., 2023b), specifically Sections 2, 4 and 5.1.*
Here I present an overview of the observational sample which was then analysed, using the methodology described in Chapters 3 and 4 of this thesis. The global trends that were uncovered by this analysis are also presented in this chapter, including a summary of the results, the computation of mass accretion rates from the line luminosity, and the relationship betweeen accretion rates and size of the Brγ emission region.
The data of the observations listed in Table 5.2 are publically available via the ESO archive: https://archive.eso.org/.

5.1. Sample overview and observations

5.1.1. Sample

We have studied a total of seven T Tauri sources, which in the context of this work will be referred to as the GRAVITY T Tauri sample. The targets in the sample consist of a number of mostly strong accretors with mass-accretion rates of the order of $10^{-8} M_{\odot}\ yr^{-1}$, masses of less than 1.5 $M_{\odot}$, and stellar luminosities ranging up to 4 $L_{\odot}$. The majority are mid K-type stars with surface temperatures in the span between 4000 K and 4900 K and ages of 1 to 2 million years or younger. Their individual properties are summarised in Table 5.1.

5.1.2. Observations

The individual sources of the sample were observed between 2016 and 2021 with VLTI GRAVITY, the latest generation K-band beam combiner based at the ESO facilities of the VLTI at Cerro Paranal, Chile. The analysis of the Brγ emission region relies exclusively on observations taken with the four Unit Telescopes (UTs) with their 8.2 m primary mirrors. The Auxiliary

Name	Sp. Type	T_{eff} [K]	d [pc]	M_* [$M_\odot$]	L_* [$L_\odot$]	R_* [$R_\odot$]	$\dot{M}_{acc}$ [$10^{-8}\,M_\odot yr^{-1}$]	Age [Ma]	References
AS 353	K5	4450	399.6 ± 4.2	1 ± 0.2	3.9 ± 0.67	3.32 ± 0.29	7.9 - 45	≤ 1	Rei et al. (2018), Prato et al. (2003)
RU Lup	K7	4050	157.5 ± 1.3	0.6 ± 0.2	1.64 ± 0.22	2.60 ± 0.17	1.8 - 30	1-2	Herczeg and Hillenbrand (2008), Siwak et al. (2016)
VV CrA SW	K7	4050	156.6 ±1.2	0.6 ± 0.2	1.73 ± 0.24	2.67 ± 0.19	3.33 - 22	1-2	Sullivan et al. (2019)
TW Hya	K6	4200	60.14 ± 0.07	0.9 ± 0.1	0.41 ± 0.05	1.21 ± 0.07	0.13 - 0.23	4-12	Donati et al. (2011), Venuti et al. (2019)
S CrA N	K5-K6	4300	160.5 ± 2.2	0.9 ± 0.2	3.82 ± 0.54	3.52 ± 0.25	7.8 - 50	≤ 1	Sullivan et al. (2019)
DG Tau	K6	4200	125.2 ± 2.3	0.8 ± 0.2	1.58 ± 0.37	2.37 ± 0.28	4.6 - 74	1-2	Gahm et al. (2018), White and Ghez (2001), White and Hillenbrand (2004)
DoAr 44	K2-K3	4840	146.3 ± 0.6	1.5 ± 0.2	1.61 ± 0.21	1.80 ± 0.12	0.63 - 0.9	3-6	Manara (2014), Espaillat et al. (2010)

Table 5.1.: Properties of the stars of the T Tauri sample. References are referring to the lower and upper limit $\dot{M}_{acc}$ literature values. We note that R_* was computed from effective temperature and stellar luminosity. Other properties were adopted from Gravity Collaboration et al. (2021b).

Telescopes (ATs), while providing better coverage in the uv plane and potentially higher spatial resolution at the longest baselines, are usually not sensitive enough to detect the relatively faint emission signal of Brγ originating from T Tauri type stars.

The standard UT configuration combines the four telescopes to a total of six baselines, spanning up to 130 m in length on the ground and providing a spatial resolution of up to $\frac{\lambda}{2B}$, which translates into 1.6 to 1.7 mas when observing in the near infrared between 2 and 2.4 micrometres. With the exception of S CrA N, all of the sources were observed in single field mode, meaning the fringe data were simultaneously recorded on the separate detectors of the instrument's fringe tracker (FT) and science channel (SC).

The FT data were recorded at low spectral resolution (R=22) in six spectral channels over the range of the entire K-band. While the fringe tracker data in its own right can be utilised in the analysis of the K-band continuum, its main purpose with respect to the investigation of the hydrogen emission lines is to allow for longer integration times in the SC than would otherwise be feasible by stabilising the fringes against small perturbations of the atmosphere (Lacour et al., 2019). We made use of the FT capability to take the SC observations in GRAVITY's high resolution mode (R=4000) with a width of ~ 5 Å, or 75 km/s, per channel, enabling us to spectrally resolve the Brγ feature and trace the gas kinematics over a range of up to ± six channels from the centre of the line, depending on the strength of the feature in the individual sources.

The observations of the different targets are subdivided into a set of short term runs of about 5 minutes in length, each of which was saved as a separate file, stretching over a total observation

Table 5.2.: Log of observations.

Source	Date	Time (UTC)	Configuration	Calibrator	Airmass	Seeing [arcsec]	Files
DG Tau	21.01.2019	01:31 - 03:06	U1-U2-U3-U4	HD 37491	1.59	0.65	10
TW Hya	21.01.2019	06:59 - 08:24	U1-U2-U3-U4	HD 95470	1.03	0.51	13
AS 353	21.04.2019	08:44 - 10:22	U1-U2-U3-U4	HD 183442	1.31	0.34	12
RU Lup 2018	27.04.2018	03:23 - 04:30	U1-U2-U3-U4	HD 142448	1.27	0.57	8
RU Lup 2021	30.05.2021	01:58 - 03:19	U1-U2-U3-U4	HD 99264	1.31	0.64	8
S CrA N	20.07.2016	05:30 - 06:13	U1-U2-U3-U4	HD 188787	1.10	0.56	6
VV CrA	20.06.2019	02:53 - 04:04	U1-U2-U3-U4	HD 162926	1.31	0.77	3
DoAr 44	22.06.2019	02:04 - 05:46	U1-U2-U3-U4	HD 149562, HD 147701, HD 147578	1.04	0.68	28

Time denotes the beginning of the first and the last file of the observation.

time of around 1 1/2 hours for most of the objects, although the observation of DoAr 44 went on for notably longer with a total time of slightly over 4 hours. Measurements of suitable calibrator stars in a sufficiently close part of the sky were predominantly taken either up to 45 minutes before the beginning or after the end of the telescope run and thus potentially probing the sky under close but not entirely identical atmospheric conditions. For the 2021 epoch of the RU Lup observation, no calibrator close to the target was available for the night, so that an object in a significantly different part of the sky had to be used for data calibration.
Weather conditions for the relevant nights were mostly stable with typical seeing values of around 0.5 to 0.7 arcseconds, however, due to the relatively long observation of DoAr 44, we note a larger fluctuation of the seeing throughout the night and deteriorating atmospheric conditions towards the end of the run.
The GRAVITY data on TW Hya, S CrA and DoAr 44 was previously published in Gravity Collaboration et al. (2020), Gravity Collaboration et al. (2017), and Bouvier et al. (2020), respectively. A log of the observations of the T Tauri sample is given in Table 5.2.

5.1.3. Data and methodology overview

Through our GRAVITY observation, we obtained K-band spectra between 2 and 2.4 microns, showing clear Brγ features at around 2.16 microns with peak line-to-continuum flux ratios spanning a range of values from 1.91 in the extreme case of AS 353 down to only 1.19 for the faintest line we observed for DoAr 44. The uncertainties on the flux ratios, derived from the instrumental error bars given by the pipeline, are of the order of 0.01 for the majority of the T Tauri sample, although in the case of VV CrA we note a severe increase to around 0.03, even though the dispersion of the continuum flux values remains comparable to the dispersion found for the other sources.

The continuum visibility data in the vicinity of the Brγ feature for the different objects in the sample ranges from visibilities of about 0.7 to amplitudes close to 1, indicating that the total line emission region and the surrounding continuum were partially resolved over the entire K-band at baseline lengths between 40 m and 130 m for all of the targets. The Brγ visibilities signals are single peaked and in most cases well aligned with the position of the feature in the corresponding spectrum.
There are clear distinctions in terms of visibility signal strength at the Brγ line between the different sources. Particularly clear and strong features were observed in both epochs of RU Lup, where the difference between Brγ peak and surrounding continuum can be as high as 0.12 (Fig. A.3), compared to the relatively faint signals detected at the position of Brγ for DoAr 44 with a line to continuum difference in visibility of only about 0.01 at even the longest baselines.
Noise levels can equally vary greatly, with low continuum dispersion in wavelength regions adjacent to the Brγ line again for RU Lup, where we measure a continuum standard deviation of 0.0023, compared to the very noisy data obtained for VV CrA (Fig. A.6) where the continuum standard deviation can go up to 0.035.
We found non-zero differential phases at the position of Brγ at several baselines for each target in the sample, with typical absolute phase values of around 0.5° to 1°, although the largest measured differential phase goes up to 6.3°. S-shaped features, as expected for systems in rotation, can be observed for some sources at some baselines (e.g. RU Lup 2021, UT4-UT1, see Fig. A.3), but are rather exceptional and notably absent from many other targets. The features appear single peaked in many cases, but the peak is not aligned with the line centre, suggesting that in such cases a potential S-shape might be masked by one of the two constituent peaks being somehow attenuated.
The differential phase data is significantly more noisy when compared to the visibilities. Standard deviations in the continuum adjacent to Brγ , even for sources with clear differential phase Brγ peaks, are on average the order of 0.4°. For the very noisy data of VV CrA the continuum dispersion even goes up to 2° in standard deviation.
The closure phases at the position of Brγ are consistent with the closure phases of the nearby continuum throughout the sample with no clear Brγ signal visible for any of the sources. The continuum closure phases for most of our objects are close to 0°, although small offsets of around 1° can be detected at certain baseline triangles for AS 353, RU Lup, and DoAr 44 (Fig. A.1, A.3, and A.7, respectively). For VV CrA (Fig. A.6) we found again a comparatively large dispersion of closure phase values, with standard deviations across the different triangles reaching up to 4°.
The data were treated by using the total line to continuum flux ratio and continuum quantities to remove the influence of the continuum on the interferometric observables. This way a 'pure line' Brγ visibility and differential phase was extracted from the total observables in each of

the chosen spectral channels and then further used to determine the size and photocentre of the Brγ emission region. Based on a simple geometric Gaussian disk model (Berger and Segransan, 2007), we extracted the half-flux radius (or half width half maximum, HWHM) in each channel, as well as the relative offset of the photocentre with respect to the position of the continuum photocentre. This treatment was applied to a number of spectral channels based on the previously explained flux selection criterion to analyse the change of those derived properties across the different velocity components of the Brγ line, see, for example, Fig. 6.1. A full explanation of the process is given in Chapter 2.

5.2. Sizes and Photocenter shifts across the sample

In this section we first present a breakdown of the general results obtained from the GRAVITY T Tauri data, introduce some additional concepts relevant to the interpretation, and give an overview over the global trends we were able to identify across the entire sample. In the following sections, we then proceed to go over each source individually in detail and contextualise our findings by drawing upon relevant references, if and where available. Table 5.3 summarises key results concerning the characteristics of the Brγ emission region and accretion properties, respectively. Figures 5.1 and 5.2 serve as a visual overview of the sample results with regards to the most important criteria we use to interpret our results.
The sample consists of mostly strong Brγ emitters, with normalised peak line to continuum flux ratios between 1.91 and 1.53 for six out of our eight data sets and ranging down to 1.19 for the weakest emitter DoAr 44. Many of the objects exhibit line shapes that are asymmetric, featuring an excess of blueshifted emission. We approximate this asymmetry by fitting a superposition of two Gaussian functions to the data, basically dividing the feature into a narrow centred low velocity component and a broader offset high velocity component. Whether these Gaussian components can necessarily be directly attributed to specific physical phenomena, such as additional outflows on top of an accreting magnetosphere, is not certain. Inverse P Cygni features, as expected to be seen when observing magnetospheric accretion columns at low inclination, are generally absent from the line profiles of the sample, even for those objects observed at a close to pole-on configuration, such as TW Hya. The width and offset of the broad component, and thus of the total emission line, can vary significantly throughout the sample, even between two epochs of the same target (RU Lup), although the overall strength of the asymmetry correlates with the peak flux ratio and is also reflected in the equivalent widths. We computed the line luminosities for each object from the equivalent widths and K-band magnitudes from 2MASS

	AS353	RU Lup 2018	RU Lup 2021	TW Hya	DG Tau	DoAr 44	S CrA	VV CrA
$F_{L/C}$	1.91	1.86	1.83	1.61	1.29	1.19	1.53	1.65
FWHM [km s^{-1}]	233	183	187	121	224	137	175	150
W10% [km s^{-1}]	594	607	420	241	445	274	524	416
μ_{HV} [km s^{-1}]	-97	-55	-50	-183	-	-	-273	-75.49
μ_{LV} [km s^{-1}]	3	2	6	1	-	-	3	0.84
$FWHM_{HV}$ [km s^{-1}]	520	586	295	482	-	-	549	598.54
$FWHM_{LV}$ [km s^{-1}]	204	154	154	116	-	-	170	141.32
EW [Å]	-19.62 ± 0.91	-16.82 ± 1.76	-13.47 ± 0.43	-7.11 ± 0.76	-5.80 ± 0.35	-2.65 ± 0.38	-8.71 ± 0.66	-10.09 ± 0.99
L_{acc} [$L_\odot$]	3.07 ± 0.17	0.98 ± 0.12	0.76 ± 0.03	0.03 ± 0.00	0.33 ± 0.02	0.07 ± 0.01	1.74 ± 0.15	1.64 ± 0.19
$\log\dot{M}_{acc,inst}$ [$M_\odot yr^{-1}$]	-6.38 ± 0.44	-6.76 ± 0.48	-6.87 ± 0.48	-8.74 ± 0.49	-7.40 ± 0.47	-8.46 ± 0.49	-6.56 ± 0.44	-6.52 ± 0.47
$\dot{M}_{acc,inst}$ [10^{-8} $M_\odot yr^{-1}$]	$41.48^{+41.35}_{-20.16}$	$17.31^{+20.78}_{-8.54}$	$13.38^{+15.79}_{-6.66}$	$0.18^{+0.32}_{-0.1}$	$3.95^{+4.44}_{-2}$	$0.35^{+0.38}_{-0.19}$	$27.72^{+28.96}_{-13.57}$	$29.77^{+34.39}_{-14.59}$
PA [°]	173 ± 3	99 ± 31	101 ± 31	130 ± 32	143 ± 12	137 ± 4	1 ± 6	91 ± 6
i [°]	41 ± 2	16^{+6}_{-8}	20^{+6}_{-8}	14^{+6}_{-14}	49 ± 4	32 ± 4	27 ± 3	32 ± 3
Continuum HWHM [au]	0.28 ± 0.05	0.21 ± 0.06	0.21 ± 0.06	0.042 ± 0.003	0.13 ± 0.01	0.16 ± 0.02	0.17 ± 0.02	0.16 ± 0.01
Brγ HWHM [au]	0.206 ± 0.003	0.076 ± 0.001	0.061 ± 0.001	0.029 ± 0.001	0.143 ± 0.004	0.050 ± 0.002	0.071 ± 0.011	0.081 ± 0.005
R_{tr} [au]	0.04 - 0.08	0.04 - 0.07	0.04 - 0.08	0.05 - 0.07	0.05 - 0.09	0.09 - 0.11	0.05 - 0.10	0.04 - 0.07
R_{co} [au]	0.10	0.04	0.04	0.05	0.06	0.05	0.04	0.10
Continuum HWHM [R_*]	18.13 ± 3.59	17.36 ± 5.10	17.36 ± 5.10	7.47 ± 0.70	11.32 ± 1.61	19.07 ± 2.69	10.38 ± 1.42	12.64 ± 1.04
Brγ HWHM [R_*]	13.32 ± 1.16	6.32 ± 0.43	5.01 ± 0.35	5.13 ± 0.33	12.93 ± 1.56	5.93 ± 0.47	4.36 ± 0.75	6.56 ± 0.59
R_{tr} [R_*]	2.83 - 5.30	3.28 - 6.14	3.53 - 6.61	8.31 - 12.35	4.50 - 8.42	10.62 - 12.68	3.36 - 6.29	2.86 - 5.36
R_{co} [R_*]	6.47	3.31	3.31	8.89	5.44	5.96	2.44	7.25

Table 5.3.: Results for equivalent widths, mass-accretion rates, and characteristic sizes of the Brγ emission region. $F_{L/C}$ is the total line to continuum flux ratio at the centre of the line. FWHM and W10% are the line widths at 50% and 10% of the peak flux, respectively. μ is the position of the high (HV) or low velocity (LV) component from the double Gaussian fit to the spectrum.
The Brγ half-flux radius (HWHM) is given for the central channel. R_{co}, continuum HWHM, PA, and i were adopted from Gravity Collaboration et al. (2021b). Accretion luminosities were estimated from the line luminosities based on the empirical relationship in Eq. 5.1. The instantaneous mass-accretion rates were then computed as in Eq 5.2. R_{tr} is given based on Eq. 5.4 for magnetic field strengths between 1 kG to 3 kG and using the mass-accretion rates derived from the equivalent widths (EW). The asymmetric error bars on the absolute values of $\dot{M}_{acc,inst}$ represent the 25th and 75th percentiles of the distribution. Other error bars denote 1σ uncertainties.

(Cutri et al., 2003). We then used the empirical relationship from Alcalá et al. (2014),

$$log\left(\frac{L_{acc}}{L_\odot}\right) = a \cdot log\left(\frac{L_{Line}}{L_\odot}\right) + b \tag{5.1}$$

with a=1.16 ± 0.07 and b=3.6 ± 0.38, to estimate the accretion luminosities and subsequently determined the corresponding mass-accretion rates via (Hartmann et al., 1998)

$$\dot{M}_{acc} = \left(1 - \frac{R_*}{R_{in}}\right)^{-1} L_{acc}\frac{R_*}{GM_*} \approx 1.25 L_{acc}\frac{R_*}{GM_*}, \tag{5.2}$$

which describes the relationship between the gravitational energy released and radiated away by the mass falling in from the truncation radius. For the right hand side approximation we follow the common convention of using $R_{in} \approx 5\ R_*$ as a typical size for truncation radii.
These results are summarised in Table 5.3. They are also shown in Fig. 5.1, where we present both the instantaneous mass-accretion rates as well as a range based on the lowest and highest previous estimates found in the literature. Based on this comparison, we found that our mass-accretion rates tend to fall into the range established by past observations, even if mostly towards the higher end for the stronger accretors. The uncertainties on the coefficients a,b of Eq. 5.1 translate into relatively large and asymmetric error bars on the absolute value of L_{acc} and consequently also $\dot{M}_{acc}$. We used a Monte-Carlo approach to determine the final uncertainties on the accretion rate, rather than Gaussian error propagation not applicable here.
We fitted the visibility data with a 2D Gaussian in order to find the half-flux radii (HWHM) of the pure Brγ emission region, using the inclination and position angles of the K-band continuum emission region presented in Gravity Collaboration et al. (2021b) to constrain those two parameters in our fit. The HWHMs we obtained through this process are, across the entire sample, of the order of less than 0.21 au at their greatest extent, ranging down to regions as compact as 0.03 au. In terms of stellar radii, the central channel sizes vary from up to 13 R_* to less than 5 R_*, although the majority of objects show clustering (see Figures 5.2, 5.1) in a range from 4 to 7 R_*, which is fairly typical for magnetospheric radii (Bouvier et al., 2007). This clustering can be observed across the entire range of mass-accretion rates of our small sample, so that a correlation between those sizes and accretion rates cannot be established here. Equally, within our sample we do not detect a clear correlation of those Brγ sizes with the luminosity of the objects, as opposed to the NIR continuum sizes, which were shown to correlate as per $R \propto L^{1/2}$ (Gravity Collaboration et al., 2021b). However, it is apparent from Fig. 5.2 that the two weakest accretors in the sample (TW Hya and DoAr 44) also show most clearly an emission region smaller than the co-rotation radius, whereas most of the other objects show Brγ emission coming from beyond the co-rotation radius.

Changes in HWHM in the spectral channel across the Brγ line can be significant, with largest to smallest size-in-channel ratios being around 1.2 to 1.5 for many of the objects, although in extreme cases this can go up to almost 2, whilst others show a relatively flat profile relative to their error bars. Under a magnetospheric accretion scenario, a decrease of size towards the edges of the line (i.e. higher velocities) would be naively expected, as the gas at the highest velocities should be in free fall close to the star. In our sample, only one source (TW Hya) clearly shows this decrease, whereas most of the other objects show either a straight increase with a minimum at the centre channel or even a mixed profile with a decreasing size at low velocities and

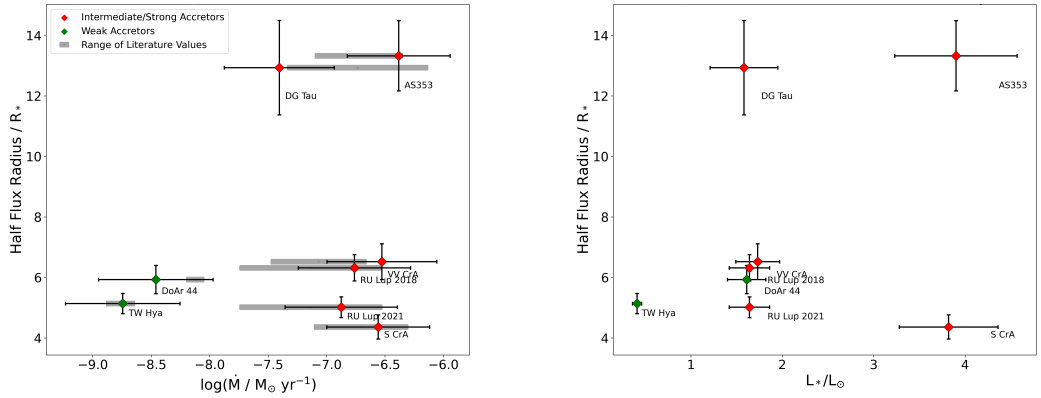

Figure 5.1.: Relationships between Brγ emission region sizes and selected stellar properties.

Top: Fitted HWHM of the Brγ pure line emission region of the central channel versus the mass-accretion rate. The latter is depicted in two forms: Once as a grey bar which denotes the range of $\dot{M}$ values found in the literature on the respective source, then as the instantaneous mass-accretion rate, which was derived from the equivalent width of the GRAVITY Brγ spectra. The colour coding represents the classification of the sample objects as either weak (green) or intermediate to strong accretors (red). Most of the T Tauri stars cluster in a 4-7 R_* range, which is of the order of typical magnetospheric sizes.

Bottom: Brγ HWHM versus accretion luminosities. The colour coding corresponds to the upper plot.

then an increase as we move to higher velocities. These mixed profiles could be indicative of a multi-component Brγ emission region, although in many cases the extent of these more complex signatures is within the uncertainties.

An important point of reference in the search for the origin of Brγ emission is the co-rotation radius, since we know that the inner disk must be truncated inside the R_{co} so that stable magnetospheric accretion columns can form. If the dominant driver of Brγ emission is magnetospheric accretion, we expect that the Brγ emission region would be of the order of the co-rotation radius or even slightly more compact. The co-rotation radius is defined as the radius at which the angular velocity of the rotating disk matches the angular velocity of the star Ω_* (Bouvier, 2013):

$$R_{co} = \left(\frac{GM_*}{\Omega_*^2}\right)^{1/3}. \tag{5.3}$$

Stellar angular velocities are determined from measurements of the rotational period of the star or the v sin(i). We refer to Gravity Collaboration et al. (2021b) for the relevant values for our sample objects. The co-rotation radii are given in Table 5.3. Of course, the best way to determine whether the size of the Brγ emission region corresponds to the size of the magnetosphere in any object would be to compare the region size against the magnetospheric truncation radius directly. The truncation radius can be computed from stellar parameters, if the strength of the magnetic

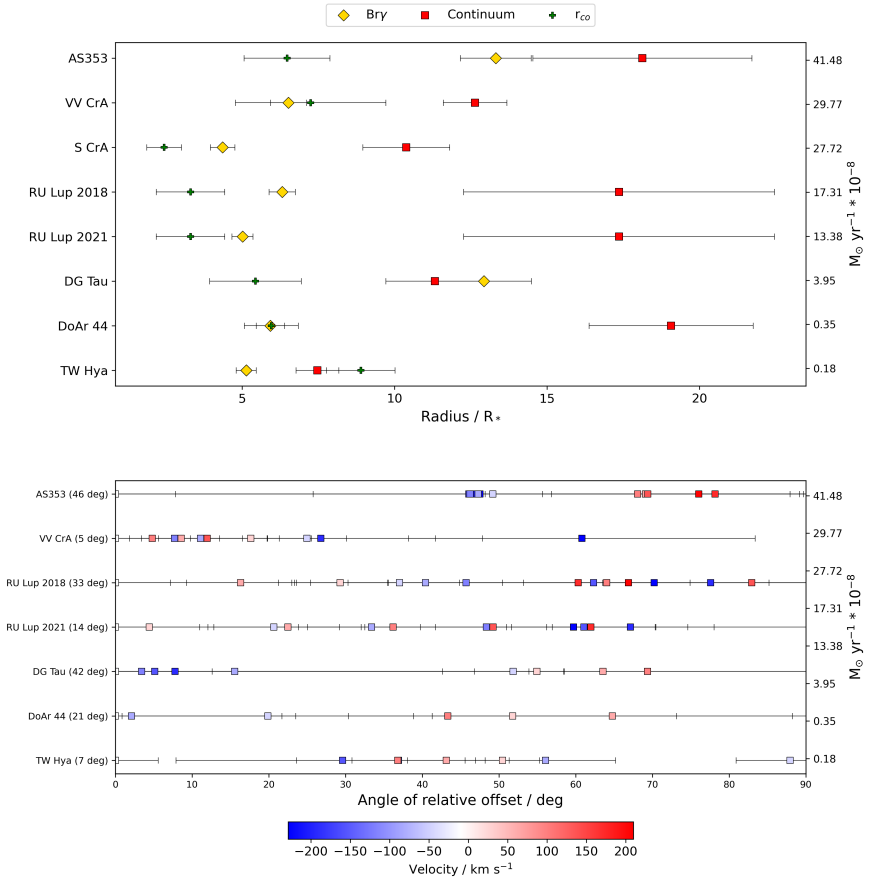

Figure 5.2.: Sample overview for emission region sizes and photocenter shifts.

Top: Brγ half-flux radii (yellow), compared to K-band NIR continuum half-flux radii (red) and co-rotation radii (green) across the sample. We note that Brγ region and continuum HWHMs are based on a Gaussian disk and a Gaussian ring model, respectively, which should approximately reflect the differences in the morphology of both regions. The objects are given in order of descending mass-accretion rate.

Bottom: The distribution of photocentre shift angles across the line for the entire sample. The x-axis shows the minimum difference angle between the relative shift vector and the position angle of the continuum disk. The white channel serves as the point of reference for the relative shift vector. An angle of 0° means the photocentre shift vector is aligned with the disk axis, as would for example be expected for a disk in rotation. A difference angle of 90° indicates that the shift vector is perpendicular to the disk axis. A clustering of points close to a certain difference angle indicates an alignment of the photocentre shifts along a preferential axis. VV CrA shows a monoaxial distribution of photocentres, while for other targets more complex profiles with multiple alignments are indicated. The number stated in brackets after the object name gives the average error on the angle for the five central channels.

dipole field is known:

$$R_{tr} = 12.6 \frac{B_3^{4/7} R_2^{12/7}}{M_{0.5}^{1/7} \dot{M}_{-8}^{2/7}}. \tag{5.4}$$

In this notation we follow the convention used in Hartmann et al. (2016), for example. We note that $M_{0.5}$ is the stellar mass in units of 0.5 $M_\odot$, R_2 the stellar radius in units of 2 $R_\odot$, B_3 the surface field strength of the dipolar magnetic field at the stellar equator in kG, and $\dot{M}_{-8}$ the mass-accretion rate in units of $10^{-8} M_\odot yr^{-1}$. The resulting truncation radius is given in units of $R_\odot$. The derivation is conceptually discussed in Bessolaz et al. (2008).

Measurements of magnetic field strengths in T Tauri stars are scarce, so that we cannot rely on the truncation radius as a primary criterion to identify strong magnetospheric accretion cases. Even so, we can still use general estimates of R_{tr} as complementary information. Building upon the approach laid out in Gravity Collaboration et al. (2021b), we set a range of 1 - 3 kG for B and compute the truncation radii for this range as presented in Table 5.3 from the relevant stellar properties.

An overview of the emission region sizes in the central line channels, compared to the respective co-rotation radii and the NIR K-band continuum sizes taken from Gravity Collaboration et al. (2021b), can be found in Fig. 5.2. The sample can generally be divided into targets with emission regions of the order of the co-rotation radius (DoAr 44, TW Hya), those with more extended Brγ emission than the co-rotation radius, but still close to typical magnetospheric radii around 5 R_* (RU Lup, S CrA N, and VV CrA SW), and those with highly spatially extended Brγ regions outside the typical range of magnetospheric sizes (AS 353, DG Tau). This separation partially corresponds to the distinction between weak accretors ($\dot{M}_{acc} < 1 \cdot 10^{-8} M_\odot yr^{-1}$, again DoAr 44 and TW Hya) and the intermediate to strong accretors, which we indicated in Fig.5.1 via the different colours. While the weak accretors do appear to conform to the co-rotation criterion with compact emission regions, the situation is more complex for objects with higher accretion rates, as there is no clear correlation between the relative region sizes and the mass-accretion rates for those targets.

Magnitudes for the observed photocentre displacements are of the order of 0.07 au or below. For multiple targets the entire photocentre profile across the line is sufficiently compact to be within or close to 1 R_*, although such a compact concentration of photocentres does not necessarily correlate with the size of the emission region. The photocentre profiles are complex and not easily classified, although a broad distinction can be made between targets that show quasi-rotational profiles, featuring distinct blue and red arms aligned along a common axis, targets with compact profiles that lack any clear structures, and complex profiles which again appear potentially as a superposition of multiple components. In Fig. 5.2 we give an overview over the possible alignment of the photocentre shifts across the line with different axes. To account for the offset of the profiles from the plot centre, we compute the difference vectors between each point and the centre channel (shown as a white square) and then compute the minimum angular difference between the angle of the difference vector and the NIR continuum disk axis

position angle. The resulting value is a measure of how well aligned the photocentre offsets are relative to the disk axis. The plot can be interpreted in a meaningful way by considering the degree of clustering, and at which angles the clustering occurs. A concentration of points in a narrow angular range (AS 353) indicates that the photocentre shift is aligned along a single axis. If the clustering range is close to zero, the photocentres are aligned with the disk semi-major axis, which is something that would be expected from a disk in Keplerian rotation. If the points cluster at 90°, the photocentres might be aligned with some form of polar outflow (red wing in DG Tau). An even spread of points indicates an absence of recognisable structures and a random distribution of photocentres (TW Hya). The figure clearly shows the previously introduced distinction between simple alignments and complex patterns, where we see multiple clusters (DG Tau and RU Lup).

It is important to remember that the differential phases track the relative offset of the Brγ emission region from the overall photocentre of the continuum. In Fig. 6.1, for example, the centre of the plot is the combined photocentre of the star and other continuum emitting components such as the dusty disk. If the dusty disk is perfectly centrosymmetric, its own photocentre coincides with that of the star and the overall continuum photocentre matches the position of the star. If the continuum photocentre, however, is not centrosymmetric, either offset from the star or with an asymmetric brightness distribution, then the zero position in those plots can significantly deviate from the stellar position. We therefore make use of the closure phases to extract information about the continuum asymmetry. For the majority of our sample objects the closure phases themselves are close to zero and thus suggest a centrosymmetric continuum. We then instead use the uncertainty given by the phase dispersion to derive an uncertainty on the stellar position. To do this we follow Gravity Collaboration et al. (2021b) by fitting an azimuthally modulated ring model to the continuum closure phase data. The results are depicted as red circles on the photocentre profile plots, showing that indeed in the majority of the cases the centre channel photocentre could conceivably be centred on the stellar position.

6. The GRAVITY Brγ T Tauri survey, part two: discussion of individual objects

Note: The contents of this chapter are direct citations from ***"The GRAVITY young stellar object survey IX. Spatially resolved kinematics of hot hydrogen gas in the star-disk interaction region of T Tauri stars" - Gravity Collab.: J. A. Wojtczak, L. Labadie et al.*** *(Gravity Collaboration et al., 2023b), specifically Section 5.2.*
Here I present in detail the results that were obtained for each object in the sample, using the methodology described in Chapter 3 of this thesis. The results for the characteristic size, the photocenter shifts, and the spectra itself are discussed in the context of known characteristics for each object.

6.1. AS 353

With a peak line to continuum flux ratio of 1.91 and an equivalent width of -19.6 Å, AS 353 (Fig. 6.1) is the strongest Brγ emitter in the GRAVITY T Tauri sample. These measurements are consistent with the results of a spectroscopic survey of young binaries done in 1996 by Prato et al. (2003), who found an equivalent width of -21.1 Å for the Brγ emission line of this object. We do not find a significant change in size across the Brγ line for the emission region, with all channels appearing consistent within their respective uncertainties with a half flux radius of 0.206 au at the centre of the line. This puts the emission region at about twice the size of the co-rotation radius at 0.1 au, but still well within the NIR continuum HWHM of 0.28 au. However, when comparing these quantities, it is important to point out a certain amount of confusion surrounding the distance estimate to the AS 353 system. Since the system is thought to be connected with the Aquila star forming region (Rice et al., 2006) and thus to the complex of dark interstellar clouds of the Aquila rift, accurate measurements of the distance have historically been difficult to obtain. Previous works such as Edwards and Snell (1982) refer to a distance of 150 pc, which was also adopted by Prato et al. (2003) with a estimated error of 50 pc based on the idea that AS 353 is in front of the Aquila rift at 200 ± 100 pc (Dame and Thaddeus, 1985). More recent high accuracy parallax measurements of AS 353 taken by GAIA and released as part of DR2 and DR3 put the binary at a comparatively remote 400 pc (Gaia Collaboration, 2020), which is the value

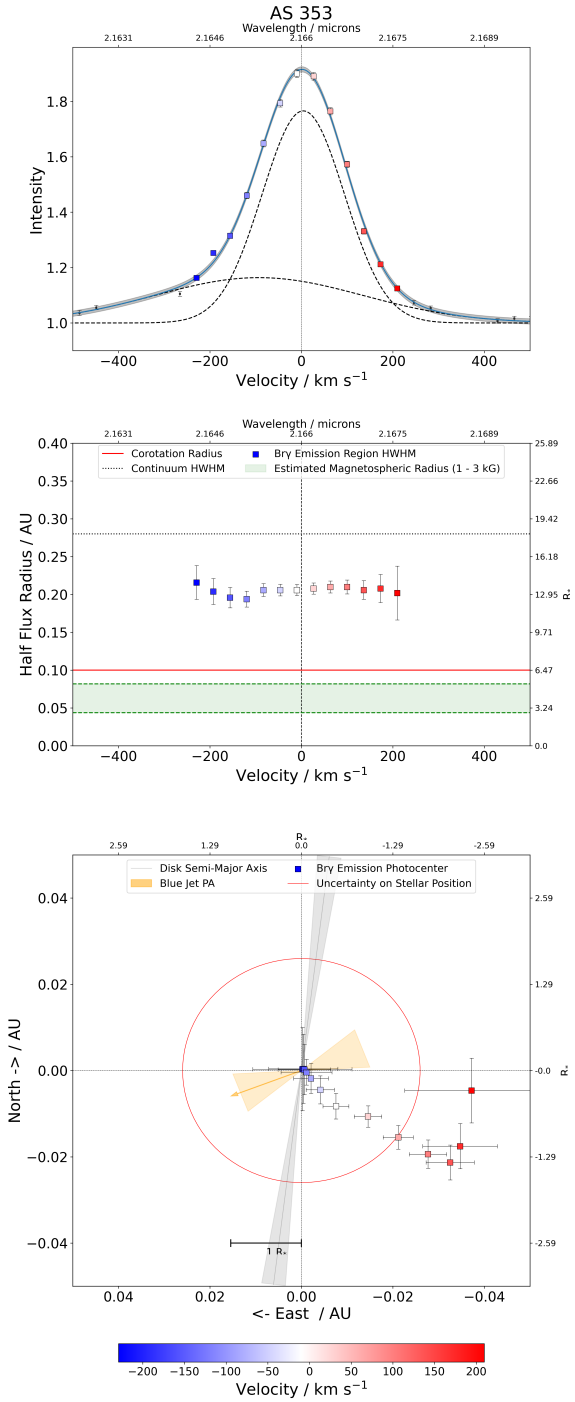

Figure 6.1.: Spectrum (top), size (middle), and photocentre shift (bottom) profiles for AS 353. Shaded regions indicate uncertainties.

we adopt in this paper. This is supported by other recent studies covering parts of the Aquila rift, such as the work of Ortiz-León et al. (2017), which presents astrometric measurements that put the WS40/Serpens cloud complex at 436 ± 9.2 pc. Still, even relatively recent publications like the interferometric study of Eisner et al. (2014) use the 150 pc estimate to convert their angular scales into physical sizes. For the Brγ emission region size Eisner et al. (2014) report an angular ring diameter of 1.06 mas and a subsequent ring radius of 0.08 au, which, if converted to the more recent distance measurements, would translate to a radius of 0.21 au. This, within a 1σ error bar, agrees with our findings, despite the fact that their model does not take into account the relatively high inclination of 41° of the inner disk of AS 353. Conversely, if our results were to be converted into a physical size based on a 150 pc distance, we would obtain a half flux radius of 0.077 au, meaning something more compact than the co-rotation radius. However, based on the fact that the most recent distance measurements for AS 353 independently came to similar results, we consider the 400 pc estimate to be robust. As such, the very large extent of the emission region indicates that the Brγ emission is likely produced through some form of disk wind outflow launched from the inner gaseous disk.

This could be supported by the spatial profile of the Brγ line photocentres, which shows similarity to a rotational profile, albeit not aligned with the disk and severely truncated in the blue wing. It is possible that such an asymmetric structure, with a maximum photocentre displacement of 0.039 au, or 2.5 R_*, in the red wing, is caused by the interplay of disk and jet. The AS 353 system is connected to the Herbig-Haro object HH32 and drives a large-scale outflow at a very high inclination of 70° (Curiel et al., 1997) with a fainter blue component and multiple more prominent redshifted knots. At a smaller scale, Hα emission originating from a blueshifted jet was reported at a position angle of (111 ± 18)° by (Takami et al., 2003). This is, within the respective uncertainties, close to perpendicular to the NIR continuum disk axis of (173 ± 3)° (Gravity Collaboration et al., 2021b).

Assuming that the weaker emission in the blue knot observed in HH32 translates to a similar asymmetry for the small-scale jet, a superposition of two distinct photocentre shift profiles, one aligned with the jet axis and the other coming from the rotating base of a disk wind and thus aligned with the disk semi-major axis, could lead to the observed distribution of photocentres. This is also supported by the closure phase data, which indicates that the position of the star is consistent with the centroid of the central velocity channel within an uncertainty of 0.026 au.

6.2. RU Lup

RU Lup was observed in two distinct epochs in 2018 and 2021 (Fig. 6.2). It appears as the second strongest Brγ emitter of our sample of T Tauri YSOs, exhibiting a peak flux line to con-

tinuum ratio of 1.86 and 1.83, respectively. From the Brγ line we compute an equivalent width of 16.8 Å in 2018 and 13.5 Å in 2021, which reflects the narrower shape of the feature in the more recent epoch. Using the empirical relationship presented before, we use the Brγ EW to estimate the accretion luminosity to be (0.98 ± 0.12) $L_\odot$ and (0.76 ± 0.03) $L_\odot$, respectively. By comparison, the X-Shooter measurements from 2012 presented in Alcalá et al. (2014) put the equivalent width at 9.6 Å and the accretion luminosity of the RU Lup system at 0.5 $L_\odot$. Using the accretion luminosity, stellar radius and stellar mass of RU Lup, we compute the instantaneous mass-accretion rate to be $17.31^{+20.78}_{-8.54}$ and $13.38^{+15.79}_{-6.66} \cdot 10^{-8}$ $M_\odot yr^{-1}$, while they arrive at a more moderate accretion rate of $4.3 \cdot 10^{-8}$ $M_\odot yr^{-1}$ largely due to their significantly higher estimate of the stellar mass. Similar accretion rates can be found in Manara (2014), although higher rates similar to the ones we derived were also presented in the past (Siwak et al., 2016).

The Brγ emission region was marginally resolved across all channels at even the shortest baselines, giving us an extremely clear size profile across different velocity components of the line. For 2018 we detect a minimum half flux radius of 0.076 au (6.3 R_*) at the line centre, which increases to 0.1 au (8.3 R_*) at the edges of our selected channel range. A similar size profile presents itself in 2021, where the central minimum is at 0.061 au (5 R_*), while in the extreme blue channel the half flux radius increases again to 0.1 au, but only 0.088 au (7.3 R_*) au in the red wing. Such changes of the order of 30% to 50% are particularly noteworthy when taking into account the high signal to noise in both visibilities and flux data, and the resulting very small uncertainties we obtain for the half flux radii. While the region in both epochs is significantly more compact than the NIR continuum at 0.21 au (17.4 R_*), Brγ emission does appear to extend beyond the co-rotation radius of 0.04 au (3.3 R_*) at both epochs. Both the absolute size, the relative size variation and the pronounced blueshifted excess emission are not characteristic for a scenario where Brγ emission is exclusively, or even dominantly, driven by magnetospheric accretion itself, but rather imply the existence of a more extended outflow component, possibly in the form of a disk or stellar wind.

The Brγ signals in the differential phases are relatively weak and translate into a distribution of different velocity photocentres that is quite complex and not easily interpreted. While the maximum shift is of the order of less than 1 R_*, there seem to be substructures in the profile that align themselves along 2-3 different axes. One for the low velocity channels which are, within a 1σ uncertainty, broadly aligned with the semi-major axis of the inner NIR continuum disk at (99 ± 31)° and also the large-scale outer disk as measured with ALMA at 121° (Huang et al., 2018). Then there are two parallel axes which run almost perpendicular to the low velocity axis, although between the two epochs, the red and blue arms are not equally well aligned. The overall profile gives the appearance of a 'crescent' type shape which seems to rotate by about 45° towards the north from 2018 to 2021. We find that in 2018 the blue arm of the profile

is almost perfectly aligned with the average PA of the blueshifted jet at (229 ± 10)° (Whelan et al., 2021), while in 2021 this is true for the red arm. It is noticeable that the arm closest to the jet axis in each case is relatively straight while the other arm appears somewhat distorted in shape, although the effect is within the uncertainty on the photocentre displacements. While it is tempting to conclude that some form of polar outflow is responsible for this behaviour, a stellar wind would not explain why the blue arm runs anti-parallel to the jet direction in 2018. The complexity of this case would require a better understanding of what a superposition of different photocentre distributions caused by different Brγ origin mechanisms would look like in order to comment on this behaviour in a more meaningful way.

6.3. VV CrA SW

The GRAVITY K-band spectrum for the VV CrA (Fig.6.3) primary shows a Brγ emission feature that lacks the pronounced blueshifted excess detected in many of the other objects in the sample. The line shape appears more Lorentzian, featuring broader wings which contain more of the flux than in a Gaussian profile. Flux ratios vary from 1.65 at the centre of the line to 1.05 at the edges of our selected channel range. We computed a Brγ equivalent width of 10.1 Å, which appears significantly weaker than than the 30 Å reported by Sullivan et al. (2019) based on archival K-band NIRSPEC data from 2008. Even by visual comparison, the GRAVITY and NIRSPEC spectra around the Brγ line appear quite distinct, as the NIRSPEC data shows both a peak flux ratio of about 2 and a higher excess of blueshifted emission, leading to an asymmetric shape similar to those observed for other objects of the GRAVITY sample. By contrast, Scicluna et al. (2016) present Brγ spectra taken with CRIRES in 2013 which are visually closer to ours, also displaying quasi-Lorentzian line shape that is slightly skewed towards the blue wing. Their equivalent width of 9 Å is also consistent with our findings, although due to their very different stellar parameters, their estimate of the mass-accretion rate is significantly lower ($4 \cdot 10^{-8}\ M_{\odot}\mathrm{yr}^{-1}$) than the $29.77^{+34.39}_{-14.59} \cdot 10^{-8}\ \mathrm{M}_{\odot}\mathrm{yr}^{-1}$) we derived from our data.
At the centre channel we obtain a size of 0.081 au (6.5 R_{*}) for the emission region, while the change across the line appears to be mostly within the significant uncertainties, which are amplified by the low flux and high visibilities in the wings of the feature. Even so, there is seemingly an increase in size towards the line edges and especially the over blueshifted channels, where the half flux radius goes up to 0.127 au (10.2 R_{*}). In the channels close to the line centre, Brγ emission originates from within the co-rotation radius at 0.09 au (7.3 R_{*}). If we were to interpret the two Gaussian components we fitted to the spectrum physically, this could signify the presence of an additional emission source at scales beyond the co-rotation radius, which is responsible for the broad component, while the narrow component, which is dominant in the centre, traces

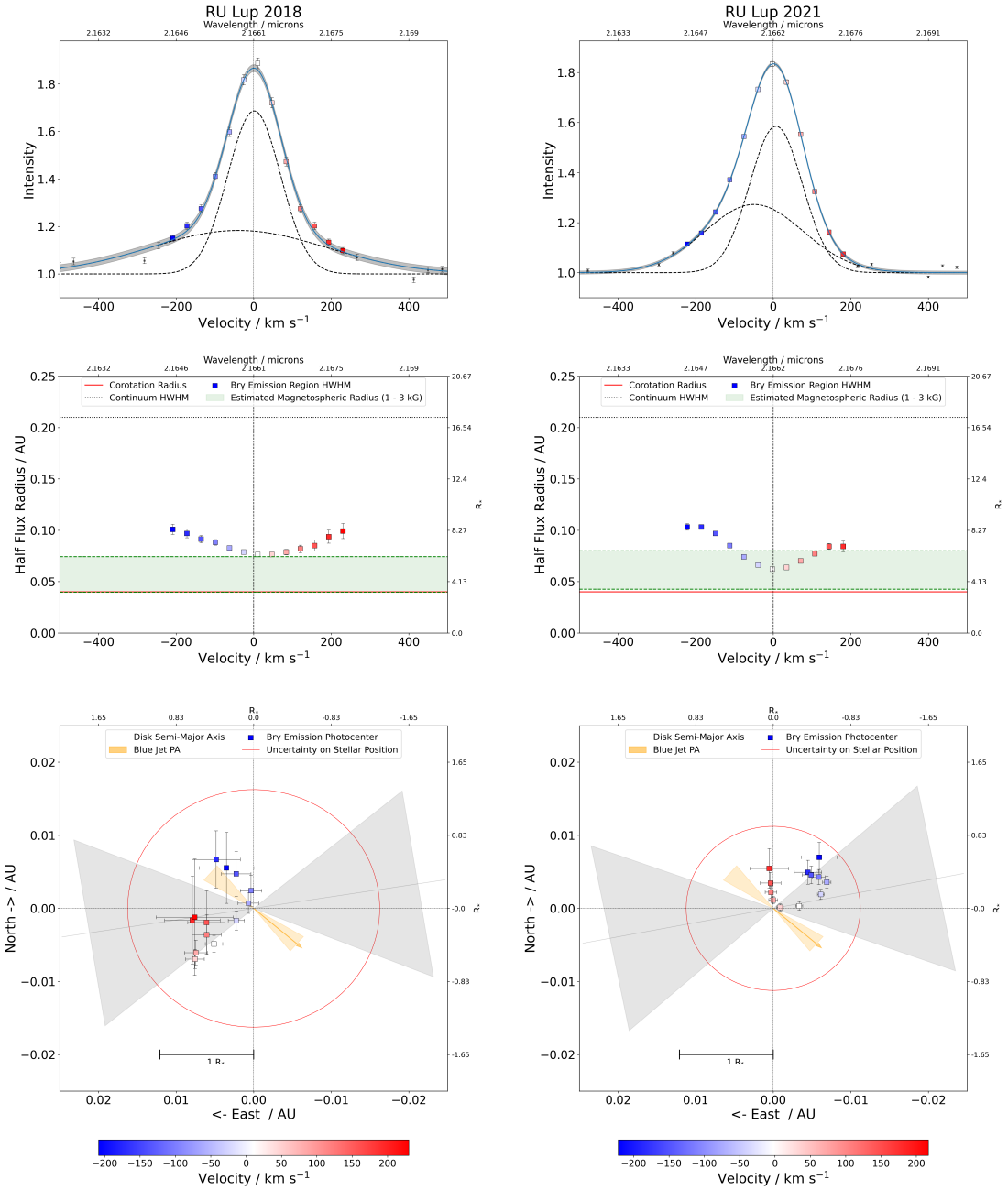

Figure 6.2.: Spectrum (top), size (middle), and photocentre shift (bottom) profiles for the two epochs of RU Lup in 2019 and 2021. Shaded regions indicate uncertainties.

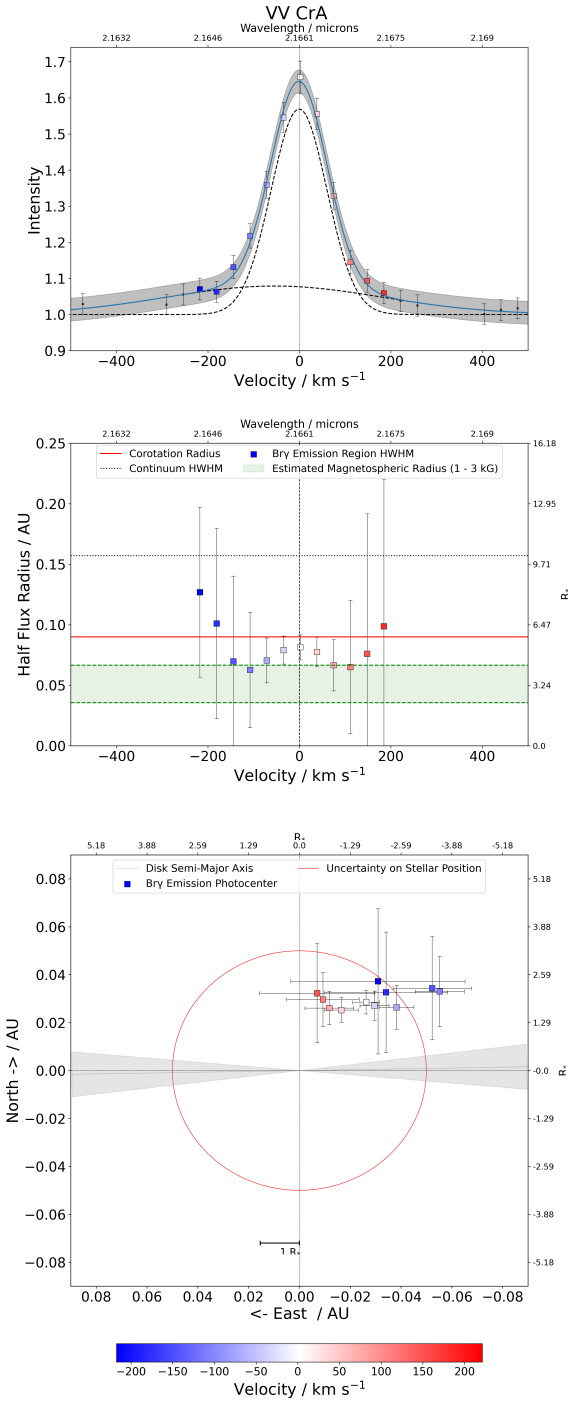

Figure 6.3.: Spectrum (top), size (middle), and photocentre shift (bottom) profiles for VV CrA SW. Shaded regions indicate uncertainties.

the emission coming from the magnetosphere. This is further supported by the fact that within the range of the narrow component, we first see a decrease in size as would be expected for the case of magnetospheric accretion. A combination of a disk wind launched from the inner disk and a system of accretion columns would be a suitable candidate to explain the radius profile, although the large uncertainties do not allow us to conclude this definitively.
A contributing wind could also explain the distribution of photocentres across the line, as the separation between red and blue arm is similar to a rotational profile which is aligned with the position angle of the NIR continuum disk at (91 ± 6)°. Such an alignment is typical for a disk in rotation, and a wind launched from such a rotating disk might be expected to display a similar displacement of photocentres, see for example Goto et al. (2012). Again, the low signal to noise ratio in our differential phase data results in very large error bars, making any kind of commentary ultimately speculative, but it is notable that the maximum shift (3.8 R_*) we detect for a photocentre is significantly larger both in absolute terms and as a fraction of the size of the Brγ emission region than what we find for any of the other targets in the sample. This implies that there is some influence which distorts the symmetry of the Brγ brightness distribution at larger scales than what we usually see.

6.4. DG Tau

GRAVITY observations of the DG Tau (Fig. 6.4) Brγ flux show a weak spectral line, with a peak flux ratio of only 1.29, the second lowest in the sample, and a FWHM of about ± 224 km/s. The original assumption of DG Tau as one of the strongest accretors in the sample appears at odds with the small equivalent width of only 5.79 Å, from which we estimate a mass-accretion rate of just $3.95^{+4.44}_{-2} \cdot 10^{-8}$ $M_\odot yr^{-1}$. This puts this observation at the very low end of a range of previously reported accretion rates, some of which can surpass the current result by an order of magnitude (see e.g. Iguchi and Itoh (2016). Such a degree of variation among past results indicates either high variability in accretion itself, some form of temporary obscuration of the central star and the Brγ emission region, or a combination of similar factors leading to an attenuated Brγ feature.
Fits of the continuum data with a Gaussian ring model have constrained the inner dust disk PA at (143 ± 12)° (Gravity Collaboration et al., 2021b), so that we were not able to detect a misalignment between the K-band continuum and the outer disk at 135.4° position angle as measured by ALMA at 870 μm (Güdel et al., 2018). The semi-major axis of the inner dusty disk appears almost perpendicular to the reported jet PA (Solf and Boehm, 1993) of 226°. By contrast, there appears to be a significant divergence in terms of inclination between the outer disk at 37° and

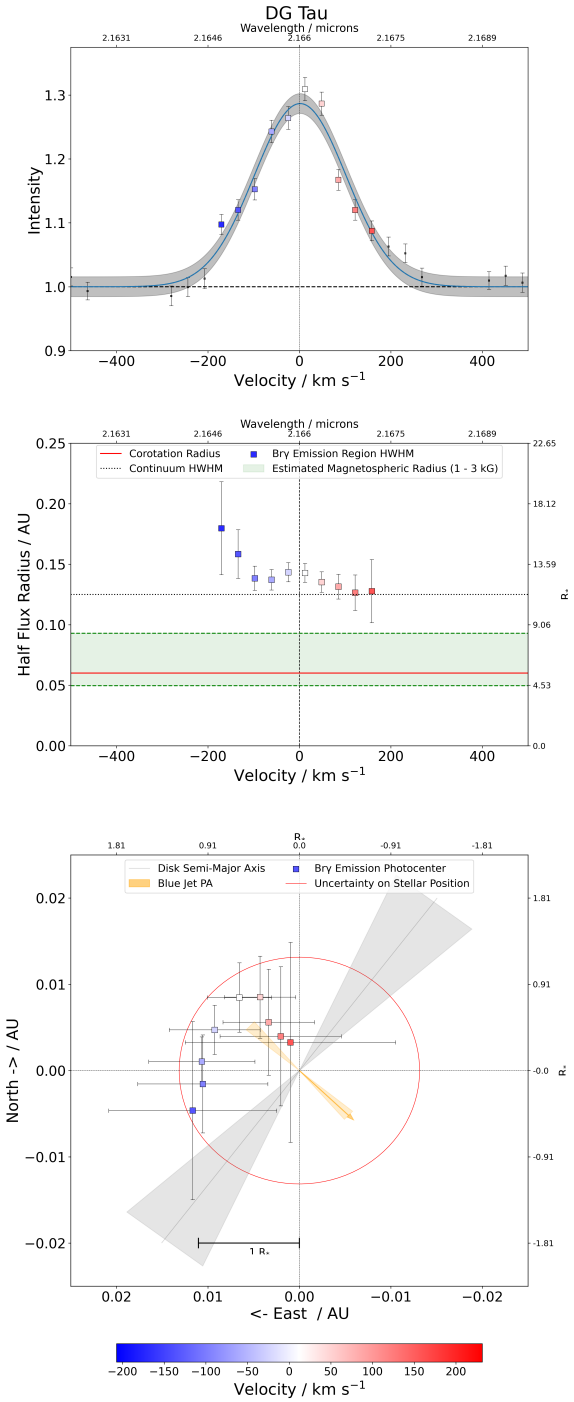

Figure 6.4.: Spectrum (top), size (middle), and photocentre shift (bottom) profiles for DG Tau. Shaded regions indicate uncertainties.

the inner disk at (49 ± 4)°. The known jet inclination of 46° (Eislöffel and Mundt, 1998) agrees with the GRAVITY result, which suggests that the inner disk is aligned with the magnetic field. For DG Tau, Brγ visibility signals tend to be faint, with multiple baselines showing no recognisable Brγ feature at all. The absence of a clear detection for some of the baselines cannot be directly attributed to a lack of spatial resolution as there seems to be overall no clear correlation between strength of signal and baseline length. At a central channel half-flux radius of 0.143 au (12.9 R_*), the emission region stretches far beyond the co-rotation radius and even slightly beyond the NIR continuum HWHM of 0.125 au, which makes it a unique case within our sample. Our results appear more extended when compared to those of Eisner et al. (2014), who examined the Brγ feature of DG Tau with the Keck Interferometer (KI) and found a uniform ring radius of 0.12 au in Brγ versus 0.17 au in the NIR continuum for an assumed distance of 140 pc. If updated to the more recent distance estimate of 125 pc from GAIA DR3, this would translate into 0.10 au and 0.15 au, respectively. As the Brγ line recorded with KI shows an equivalent width of 6.9 Å and is thus broadly similar in strength and width to the one measured with GRAVITY, this discrepancy is likely the result of differing methods in determining the region size. Due to their reliance on a single baseline, they fit a uniform ring model without taking into account possible inclination effects. While the methodology section of their paper does reference a 'circumstellar emission' which seems similar in approach to the pure line emission used in our analysis, it is not clear whether the reported Brγ radius is based on this or the total visibilities. If the latter is the case, this could certainly cause the emission region to appear significantly more compact.
Differential phase signals are also relatively faint and translate into photocentre shifts that, even at a maximum magnitude of 0.0125 au, do not extend significantly beyond the stellar radius of 0.0123 au. The photocentre profile shows a significant displacement between the central channel photocentre position and the continuum photocentre at the zero position (i.e. the centre of Fig. 6.4). When taking into account the closure phase information, this displacement can be explained in terms of an uncertainty on the relative location of the continuum photocentre with respect to the star. The position of the star, which in Fig. 6.4 is located somewhere within the red circle determined from the closure phases, is still consistent with the shift measured for some of the photocentres on a 1σ level.
The photocentre profile features a blue arm that is extended along the semi-major axis of the continuum disk, whereas the displacements across the red wing appear to be more in line with the axis of the redshifted jet component. However, the scale of the error bars on the individual points in both wings prevent us from definitively associating the profile with either of these alignments. Given the large uncertainties, it is certainly possible to interpret the profile as essentially Keplerian, possibly tracing the Brγ emission coming from a wind that was launched from the rotating base of the disk near the inner rim. Not only would such a case be consistent with

the large spatial extent of the Brγ emission region, but also with the velocity profiles obtained with ALMA by Podio et al. (2020) and Güdel et al. (2018) from the large-scale CO and other molecular line emission, which also indicate blushifted emission along the south-east axis.

6.5. TW Hya

The Brγ emission line in the GRAVITY spectrum of TW Hya (Fig. 6.5) shows an excess of blueshifted emission, which is also seen in a spectrum recorded with SINFONI (Goto et al., 2012) with a similar (R=4000) spectral resolution as GRAVITY and further confirmed in high resolution (R=45000) (Sokal et al., 2018) observations made with IGRINS between 2015 and 2017.

At the centre of the feature we find that the Brγ emission region originates in area with 0.029 au (5.16 R_*) half flux radius, which falls off to 0.016 au (2.85 R_*) in the extreme blue wing and 0.022 au (3.91 R_*) at the lowest point in the red wing. As such TW Hya is the only source in the sample that clearly shows a decline in size towards the edges of the line beyond the uncertainty on the individual points.

We also find that the emission region in all channels is significantly more compact than the co-rotation radius of 0.05 au and slightly smaller than the magnetospheric radius of 0.037 au estimated from stellar parameters and an assumed magnetic field strength of 1 kG. As most of the observational evidence actually suggests the magnetic field to be of the order of up to 1.5 kG (e.g. Bouvier et al. (2007), Donati et al. (2011), Johnstone et al. (2014)), we can adjust the estimate of the truncation radius to 0.046 au and still find it to be less extended, but close to the co-rotation radius, which is expected for magnetospheric accretion. This agreement and the compact nature of the Brγ half flux region when compared to the co-rotation radius are making a compelling case for the idea that Brγ emission in TW Hya indeed originates from the magnetosphere. This is further supported by the size profile. The decrease in HWHM would be expected under a magnetospheric accretion scenario as line components with the highest velocity are likely tracing gas in free fall towards the stellar surface.

This very important result, presenting the Brγ emission region as the first direct measurement of a spatially resolved magnetosphere, was previously reported in Gravity Collaboration et al. (2020). Based on the same data, they found a Brγ region size of 0.021 au and thus something even more compact, although the deviation ultimately comes down to methodology and data correction. Even though a Gaussian disk was used as a geometric model in both cases, they performed their analysis on an average of the three central channels of the line and used previous ALMA measurements to fix their inclination at the level of the outer disk (7°, see e.g. Andrews et al. (2016)), while we refer to the GRAVITY measurements of the NIR continuum to perform

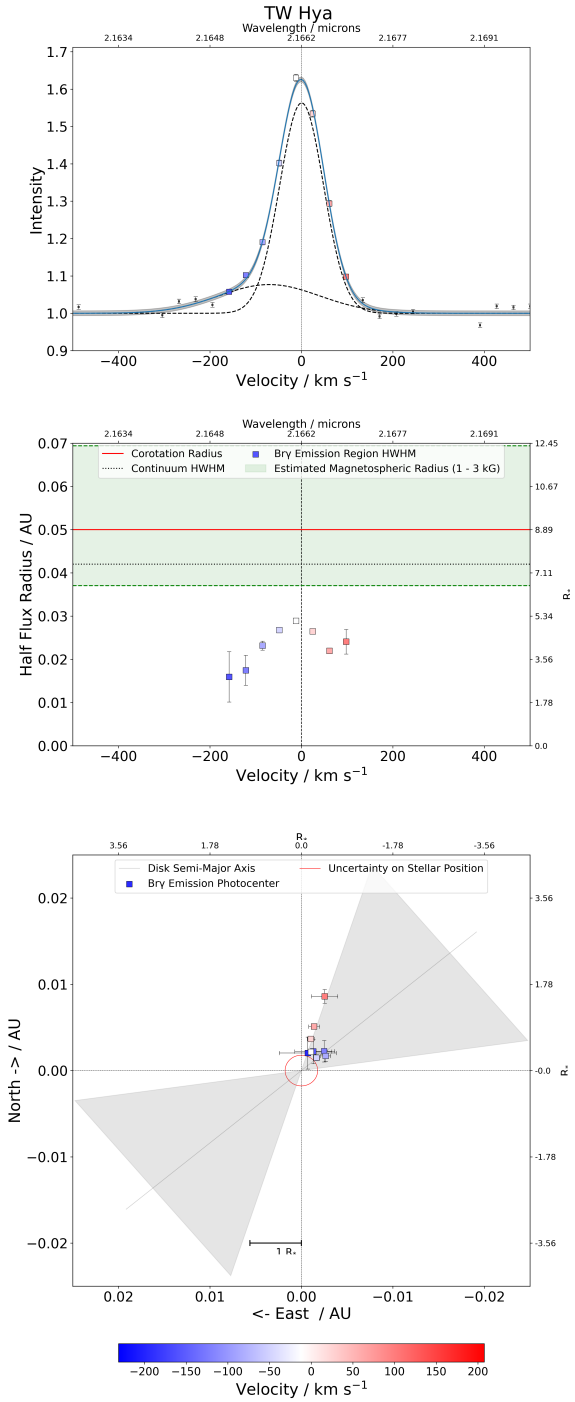

Figure 6.5.: Spectrum (top), size (middle), and photocentre shift (bottom) profiles for TW Hya. Shaded regions indicate uncertainties.

our fit for a slightly more inclined (14°) disk. Another key difference is the spectral correction that we applied to align telescope spectra with each other and with the telluric lines. As the interferometric quantities are recomputed based on the corrected spectra, the realignment can have a significant enough impact on the visibilities and differential phases to account for deviations such as this.

It is notable that the magnetospheric radius at B=1.5 kG extends beyond the K-band continuum half flux radius, whereas the dust sublimation radius was estimated to fall between 0.02 and 0.04 au (Gravity Collaboration et al., 2021b). This might indicate that dust grains exist up to the truncation radius and that the magnetosphere is playing a part in truncating not just the gaseous disk, but also the dusty disk, which was also suggested by Eisner et al. (2006) based on their Keck Interferometer observations of this target.

The photocentre profile across the line is highly compact, concentrating in an area within 0.01 au (1.78 R_*) around the continuum photocentre. Since the dispersion of closure phases at Brγ wavelengths is small, it is reasonable to assert that, given the maximum shift of 0.009 au and an average shift of less than 0.003 for the central channels compared to a stellar radius of 0.006 au, the Brγ photocentre across the line coincides with the position of the central star. This suggests that most of the different photocentre velocity components of Brγ emission, observed almost pole-on, are well centred on the stellar position. Little can be inferred directly from such a distribution. At very low inclination, any centrosymmetric brightness distribution is likely to lead to a similarly compact profile centred on zero, meaning only in combination with more conclusive evidence, as presented above, does it support the magnetospheric accretion scenario. It is still noticeable that the distribution, and indeed the differential phase signals at the individual baselines, appear to show slightly larger shifts in the red wing of the line. In the case of an inclined magnetosphere with two accretion columns, the opposite could be naively expected in a pole-on configuration, as infalling gas at the far side of the star at the highest blueshifted velocities would be blocked by the star itself, which should lead to a shift away from the centre for the blue components. The absence of a stronger shift in the blue arm could indicate that the configuration of the magnetic field in TW Hya is close to an axisymmetric scenario with a small obliquity angle between dipole and rotational axes. Such a case would be in line with the relatively small difference in inclination between the inner NIR continuum disk and the outer disk and also the lack of blueshifted absorption. However, a previous study by Johnstone et al. (2014) indicates a substantially tilted dipole, with an obliquity between 10° and 40°, respectively, and it is unclear whether this still would be consistent with such a scenario.

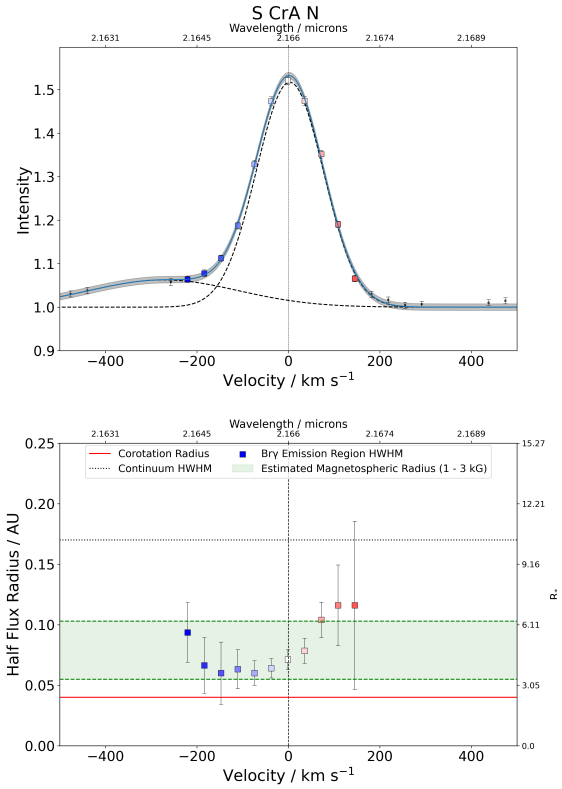

Figure 6.6.: Spectrum (top) and size (bottom) profile for S CrA N. Due to the poor quality of the phase data we chose not to include an analysis of the photocentre shift distribution for this object. Shaded regions indicate uncertainties.

6.6. S CrA N

We observe a similarly asymmetric spectral line as for most of the previous sources, although for S CrA (Fig. 6.6) it appears at a higher blueshift, with a broad high velocity component centred at -273 km/s.

The equivalent width of -8.7 Å is consistent with measurements of the Brγ line taken in 2008 with NIRSPEC, as presented in Sullivan et al. (2019), who reported -7.2 Å. However, they also report a significantly weaker mass-accretion rate of $12.8 \cdot 10^{-8}\,M_\odot yr^{-1}$ when compared to the estimate of $27.72^{+28.96}_{-13.57} \cdot 10^{-8}\,M_\odot yr^{-1}$ we derived from our equivalent width. The NIRSPEC K-band spectrum around the Brγ feature is visually consistent in shape with our GRAVITY observations and shows the same asymmetry, arguably even more so than the previously published work (Gravity Collaboration et al., 2017) on the same GRAVITY data, which was at the time not corrected for the misalignment between the four telescopes. S CrA was also investigated by Gahm et al. (2018) with the UVES spectrograph of the VLT, who fitted a magnetospheric accretion model to their spectroscopic data and found an even higher mass-accretion rate of $50 \cdot$

$10^{-8}\,M_{\odot}yr^{-1}$.

The spectral correction we applied also affects the shape and position of the Brγ signals in the visibilities. In Gravity Collaboration et al. (2017) their unusual shape and the misalignment between the visibility peaks at different baselines with the position of the line in the spectrum was presented as a possible indicator of the presence of different kinetic signatures in the data. In our spectrally corrected data, we do no longer find this misalignment for most of the baselines to any significant degree. Except for the shortest baseline, the peaks are sufficiently aligned with the spectral line and are well represented by a single peaked Gaussian shape. For the UT3-UT2 baseline with a length of 41 m, we still find a visibility shape that is strongly offset towards the blue wing and decreases much more quickly in the red, imitating the asymmetry in the spectrum. This could be indicative of a large-scale component in the system that is overresolved at the longer baselines, although this in itself would not explain the lack of signal in the red wing at this baseline.

At a number of combinations of channels and baselines, the pure line emission region is completely unresolved, as indicated by the fact that the computation of the pure line visibility yields results that are consistent with 1 within the uncertainties for those wavelengths at those baseline lengths. For the purpose of determining the region size, such points were discarded so that the fits of the ellipsoid are based purely on those baselines and channels for which the region is marginally resolved. While this correction is reflected in the error bars on the region size in each channel, the results in those cases also overestimate the true size and should thus be considered as an upper limit.

With this in mind it is difficult to comment on the trend of the size across the different velocity channels since for S CrA we find that it is mainly the outer parts of the wing, and the red wing in particular, which are affected by this issue. While the size profile shows an increase from 0.071 au (4.4 R_*) at 0 km/s to 0.104 au (6.4 R_*) in the extreme red and 0.094 (5.7 R_*) in the extreme blue channel, the uncertainties and upper limit nature of those results must put some doubt on any possible interpretation.

Even at the lowest extent in the central channels, the region extends outside the range of the co-rotation radius at 0.04 au (2.4 R_*). While the large uncertainties in the line wings again suggest that it is problematic to overstate this case for the higher velocity ranges, we consider it unlikely that the degree of overestimation is sufficiently large to mask an emission point of origin within the co-rotation radius.

Due to the poor quality of the differential phases, we cannot present a photocentre shift profile as for our other sample objects and have to rely largely on the visibilities for interpretation. As such, even when taking into account the degrading quality of the fits in the edges of the line, neither the absolute size of the emission region nor the size profile across the line appear char-

acteristic for magnetospheric accretion. It is likely that additional Brγ emitting components are indeed present in the system, as the peculiar shape of the UT3-UT2 visibility implied. This was in principle also the argument put forward in Gravity Collaboration et al. (2017), where they found a size of the semi-major axis of a Brγ Gaussian disk of (0.54 ± 0.07) mas at the centre of the line, which would translate to (0.087 ± 0.011) au. Given the obvious impact of the spectral correction on the visibilities, this is still very much consistent with the current results, although in the previous work the size of the region declined throughout the line rather than reach a minimum close to the line centre. S CrA is associated with a large-scale jet (Peterson et al., 2011) and could also be driving an outflow on smaller scales which contributes to the Brγ feature of the system, which might contribute to the blueshifted excess in the spectrum. The -273 km/s at the centre of the broad, blueshifted component fit the typical velocities found in small-scale jets (see e.g. Takami et al. (2003)). There they also found a positional displacement in Hα in S CrA N as part of their spectro-astrometic survey. While they argue that this displacement at a position angle of 153° is likely caused by the companion, we do note that baseline UT4-UT3 at a similar PA of 132° consistently yields the largest size for the Brγ emission region across all of the spectral channels. Given the separation between S CrA N and S CrA S of 1.3 arcseconds, the visibility measurements would not be contaminated by this visual companion.
However, differentiating between such stellar outflow or a wind being launched from the rotating inner disk as primary drivers of Brγ in S CrA N is challenging given the lack of robust differential phase data to trace the kinematics of the gas.

6.7. DoAr 44

DoAr 44 (Fig. 6.7) exhibits a symmetric line shape with peak line-to-continuum flux ratio of only 1.19, making it the weakest Brγ emitter in the sample. Similar to the case of S CrA N, the pure line emission region is completely unresolved at a number of channels for certain baselines, with pure line visibilities reaching values of 1 within the uncertainties. The so affected channel-baseline combinations were disregarded in the ellipse fitting process, as with a geometric Gaussian disk model these can only be associated with FWHMs of 0 arcseconds. The two outermost channels that meet the selection criterion are most affected by the reduced number of data points to fit the ellipse to, leading to disproportionately large error bars compared to the inner four channels. Even then, only for three of those four channels do we resolve the emission region under all six baselines simultaneously, which consequently makes those three channels the most robust estimators of the true region size that should be compared against the co-rotation radius of 0.05 au.
The emission region has a half flux radius of 0.05 au, which remains relatively constant between

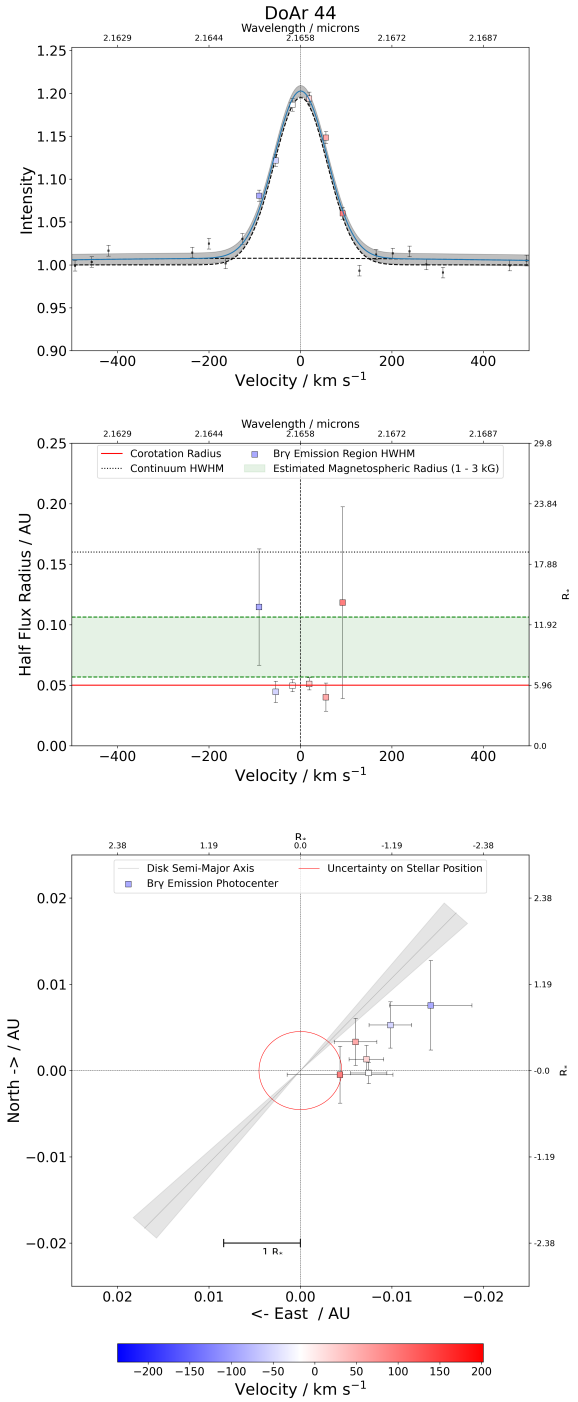

Figure 6.7.: Spectrum (top), size (middle), and photocentre shift (bottom) profiles for DoAr 44. Shaded regions indicate uncertainties.

the centre channels within the uncertainties. With Brγ emission coming from a region similar in extent to the co-rotation radius, it is likely that magnetospheric accretion is a driving mechanism behind a large part of the total line emission and that a significant portion of the emission originates in the accretion columns of the magnetosphere. At about 5.9 R_*, this size falls into the range of values typically associated with magnetospheres (Bouvier et al., 2007).

Our results are in agreement with those previously reported by Bouvier et al. (2020), who published a dedicated paper on a multi-instrument campaign on DoAr 44, including these GRAVITY interferometric observations. There they reported an upper limit to the emission region size of 0.047 au, which, when taking into account the impact of our additional spectral correction, is consistent with what we found.

The differential phase signals are faint, the resulting distribution of Brγ component photocentres hints at a separation of blue and red arms similar to a possible rotational profile, but the uncertainties prevent us from showing this conclusively. The maximum shift in the most blueshifted channel is of a magnitude of 0.016 au (1.9 R_*), while the red and centre channels cluster around an area at about 0.005 au (0.59 R_*) from the continuum photocentre. The closure phases show a weak offset in the continuum of around 0.9° which is still consistent with a shifted continuum photocentre of around that magnitude, meaning the observed Brγ emission could in truth be centred on the position of the star. This is also in agreement with the findings of Bouvier et al. (2020), who reported a continuum offset of 50 μas, which almost exactly corresponds to the offset of the white channel in Fig. 6.7.

Despite the relatively compact emission region, the photocentre profile appears less concentrated than the similarly compact case of TW Hya, which is likely rooted in the relatively higher inclination (32 ± 4)° of the inner disk when compared to the pole-on case. The profile appears also to be almost perfectly aligned with the semi-major axis of the inner disk (137 ± 4)°, which would be typical for a disk in rotation, but is not necessarily associated with a rotating magnetosphere. This could be explained by an additional wind component launched from the disk-magnetosphere interface, but in that case a blue excess in the line shape similar to what was observed in AS 353, for example, would be expected. As it stands, the alignment is either coincidental or the contribution from the wind is too weak to clearly modulate the line shape.

7. The GRAVITY Brγ T Tauri survey, part three: Radiative transfer simulations of magnetospheric accretion, and summary

Note: The contents of this chapter are direct citations from ***"The GRAVITY young stellar object survey IX. Spatially resolved kinematics of hot hydrogen gas in the star-disk interaction region of T Tauri stars" - Gravity Collab.: J. A. Wojtczak, L. Labadie et al.*** *(Gravity Collaboration et al., 2023b), specifically Section 6 and 7.*
Here I present the analysis of the radiative transfer simulation of the axisymmetric magnetospheric accretion model. The model was used to compute synthetic interferometric observables, which could then be used to establish reference points for the behaviour of the spectrally dispersed interferometric observables across the line profile. A summary of the most important findings of the GRAVITY Brγ T Tauri survey and its main conclusions are also given at the end of the chapter.

7.1. Comparison to radiative transfer simluations

Based on the results presented in Chapters 5 and 6, the objects of our sample can be broken down into three distinct categories: For two of them (TW Hya and DoAr 44) we found an emission region size that is of the order of the co-rotation radius or smaller, and also either of the order of, or smaller than, the truncation radius we estimated from the equivalent width.
Two of the other objects (AS 353 and DG Tau) showed emission regions that extend beyond 10 R_*, far exceeding both the co-rotation radius and also the range of truncation radii at magnetic field strengths of 1-3 kG.
The remaining T Tauri stars (VV CrA, S CrA N, and both epochs of RU Lup) do not fit clearly into either of those two groups, featuring Brγ emission regions with HWHMs either larger than the co-rotation radius, but consistent with the estimated range of truncation radii, or smaller than the co-rotation radius, but larger than even the upper limit of the truncation radius computed for a 3 kG field.
In this section, we discuss these results in the context of different Brγ origin mechanisms in

T Tauri stars. We begin by first introducing our work on a radiative transfer model of magnetospheric accretion in order to establish a baseline for the expected spectral, size and photocentre profiles for Brγ emission originating exclusively from the magnetosphere. We then proceed to consider how deviations from these baseline profiles in the form of additional components of extended Brγ emission would be able to account for those results which are not well explained by the magnetospheric accretion scenario.

7.1.1. Radiative transfer models of magnetospheric accretion

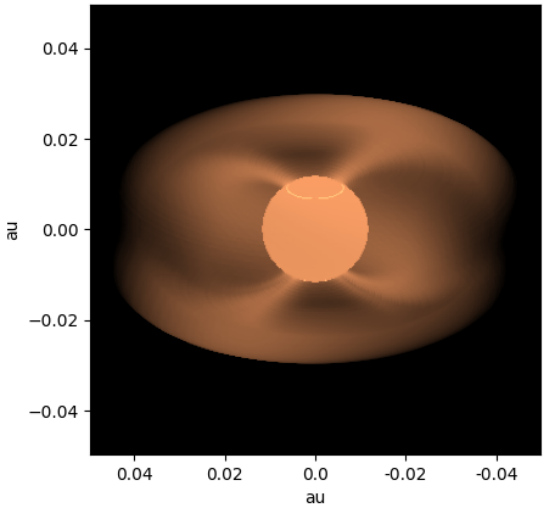

Figure 7.1.: Brγ emission region image of the magnetospheric accretion region of an RU Lup-like system at the Brγ peak wavelength, obtained from radiative transfer modelling with MCFOST. Depicted here are the accretion columns at the line centre, the star and the shock region at high latitude, as well as a contribution coming from a faint magnetospheric continuum. The model is axisymmetric, i.e. the magnetic axis is aligned with the stellar rotational axis, i.e. the vertical axis in the image above.

Estimates of the co-rotation and the truncation radii serve as simple criteria to differentiate between objects for which Brγ emission originates on spatially compact scales, consistent with the magnetospheric accretion scenario, and those showing an extended emission region, where other mechanisms are likely to contribute to a significant degree. Beyond this, it is challenging to assess the implications of the complete set of interferometric observables without being overly speculative. To provide us with a more complete idea of the expected signatures, and to aid us in the interpretation of the line shapes, the size profiles and the photocentre shift profiles, we additionally investigated the predictions of radiative transfer models of the magnetospheric accretion region (Tessore et al., in prep). We explored a number of model images, see Fig. 7.1, showing

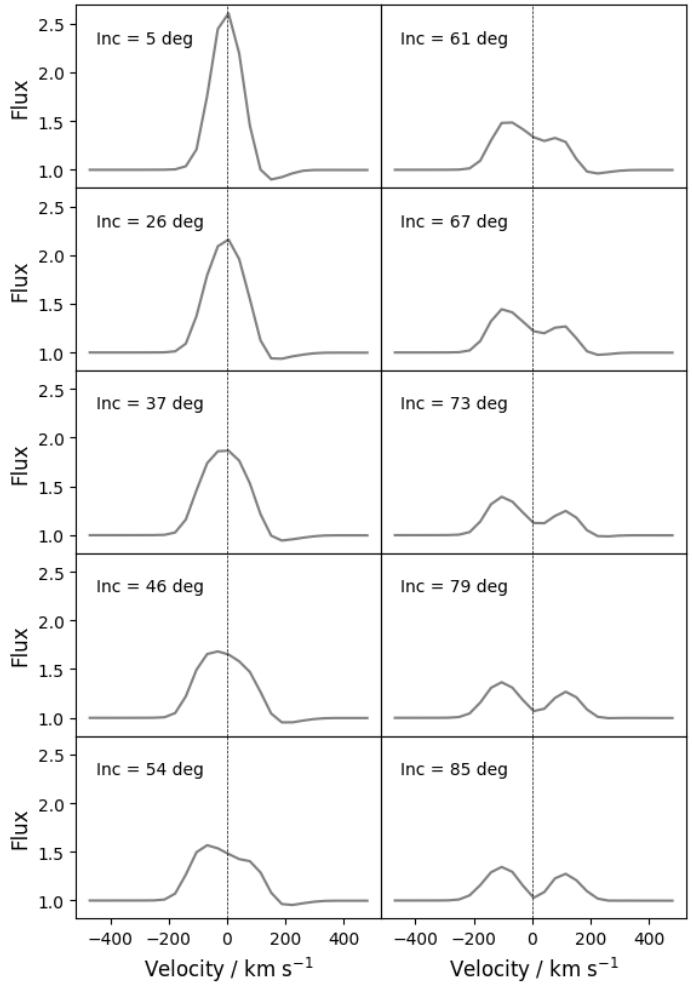

Figure 7.2.: Brγ spectral line profiles produced by the radiative transfer models at different inclinations of the magnetosphere. As we move to higher inclinations, the peak line-to-continuum flux ratio decreases and the line broadens. The inverse P Cygni profile with a redshifted absorption feature disappears beyond inclinations of 54°, as the accretion columns cover less of the stellar surface and the shock region. The blue- and redshifted velocity components of the rotating magnetosphere are increasingly separated, leading to a double peaked profile at high inclinations. We note that the synthetic data were convolved with a Gaussian and brought to the spectral resolution of GRAVITY.

the magnetospheric emission region at different inclinations and different radial velocities across the Brγ line. The model features an axisymmetric magnetosphere, meaning the magnetic dipole is aligned with the rotational axis of the star. While it has been shown in the past that a dipole tilt is common in T Tauris (e.g. Johnstone et al. (2014)), we consider the axisymmetric model

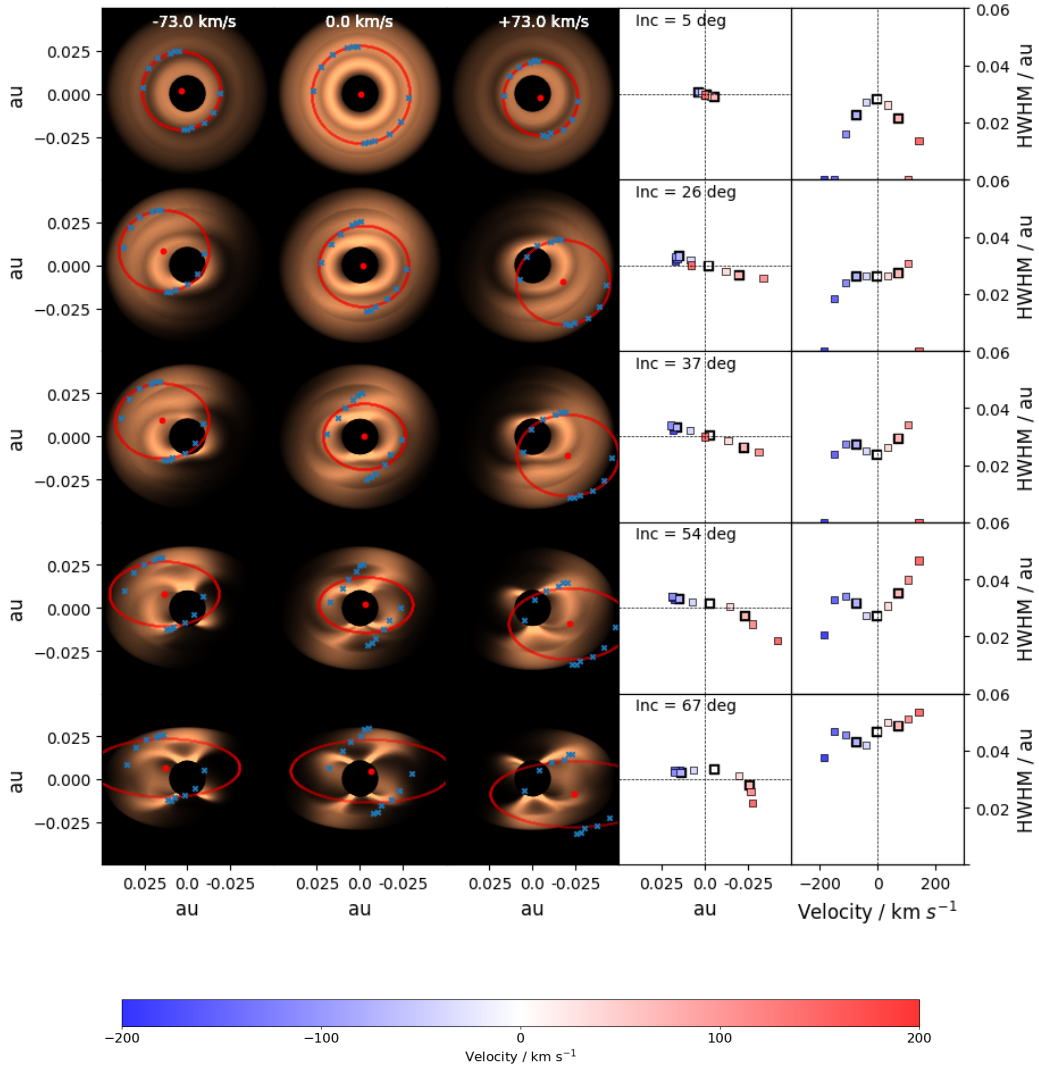

Figure 7.3.: Model images and derived quantities of the Brγ emission region.

The three columns on the left show the continuum-subtracted Brγ emission region image at three different velocities, while the two columns on the right show the photocentre shift profile and the size profile across all velocity components of the Brγ line, for a range of inclinations between 5° and 67°. The model images correspond to the blue, white and red channels marked with a bold black outline, and the photocentres and region sizes in those particular channels are defined by the red dots and the semi-major axes of the red ellipses, respectively. Only the semi-major axis of the ellipse is left as a free parameter of the fit, which emulates the approach taken with the observational data. Fig. 7.4 shows the corresponding profiles if inclination and position angle are also free parameters of the fit.

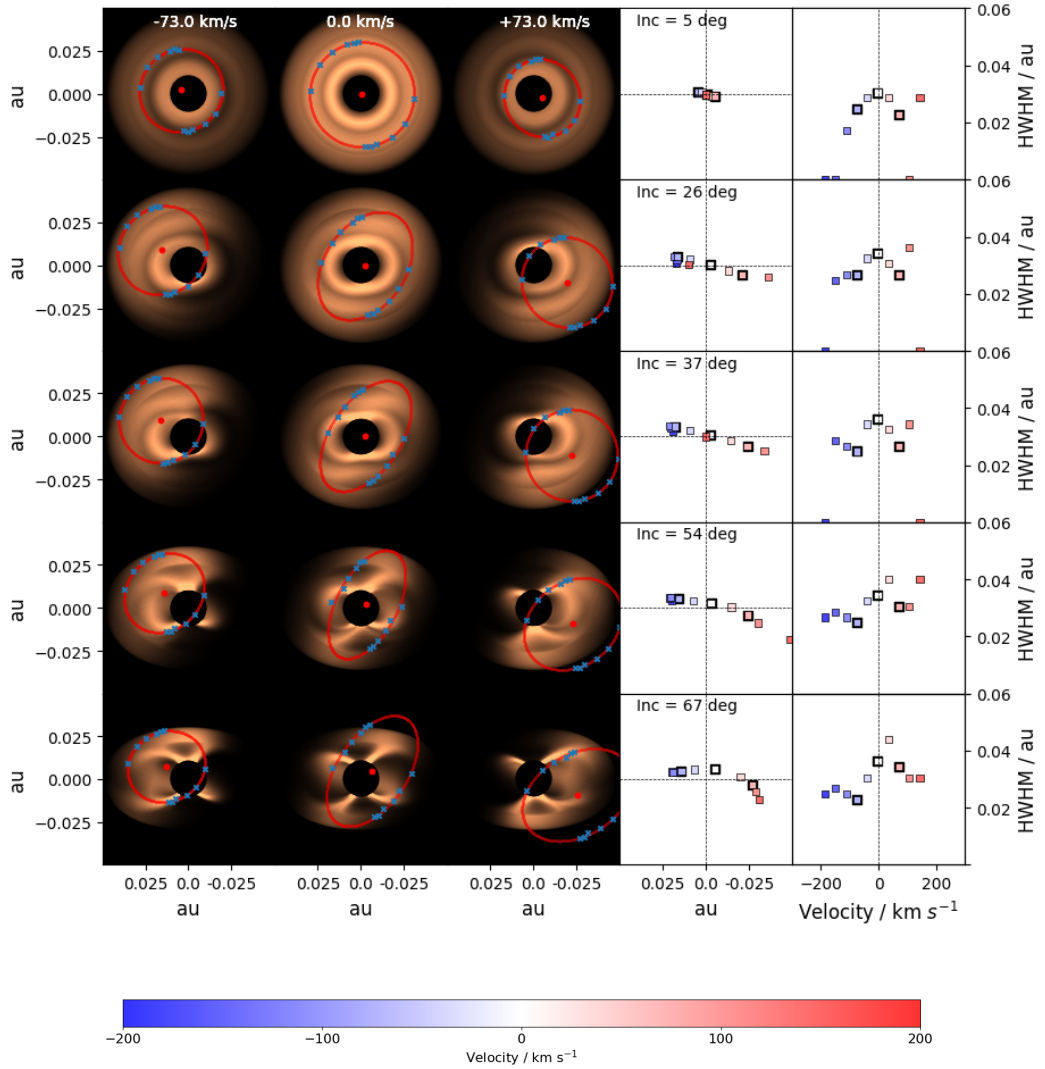

Figure 7.4.: Model images, photocentre, and size profiles at different inclinations as in Fig. 7.3, but in this version the position angle and inclination of the red ellipse are free parameters of the fit. This approach does not match the data treatment and suffers from a lack of constraints along the axis of the uv coverage gap, but finds better fitting solutions at high inclinations. We note that while the size profile is different between the two approaches, the photocentre profile is not affected by this and identical to Fig. 7.3.

still as a first step to establish broad interferometric trends and their dependencies on the model parameters.

Each of the image cubes represents the magnetosphere at a specific set of stellar and magnetospheric properties, including the stellar radius, mass-accretion rate, magnetospheric temperature and the temperature of the shock region. We set the parameters to emulate one of our sample targets in order to produce a set of synthetic observables analogous to those obtained from the GRAVITY observations. We subsequently applied the methodology laid out in Chapter 3 to determine the half-flux radius of a Gaussian disk and photocentre shift in each channel, so that the synthetic data were treated in the same way as the observational data.

To complement this, we chose the physical model of the magnetosphere to represent an RU Lup-like system at R_*=2.5 $R_\odot$ and an intermediate accretion rate of $\dot{M} = 5 \cdot 10^{-8}\ M_\odot yr^{-1}$ at a mass of 0.8 $M_\odot$ and a rotation period of 3.7 days. The magnetospheric temperature was set to 7500 K, with a shock region heated to 8000 K and a total magnetospheric radius of 4.57 R_* (0.053 au), consisting of a truncation radius of 3.37 R_* (0.039 au) and a magnetospheric width of 1.2 R_* (0.014 au).

The model intensity distribution (Fig. 7.1) features Brγ radiation coming from the emission line itself as well as a continuum contribution consisting of a photospheric component, the shock region and a faint magnetospheric continuum. It does not include an extended continuum component, such as the inner regions of a dusty disk. While this affects the direct comparison between synthetic and observational total observables, the pure line quantities remain unchanged. As detailed in Chapter 3, in depth knowledge about the exact composition of the continuum is not required in order to recover the pure Brγ line visibilities and differential phases.

A model spectrum was computed by integrating the image fluxes at each wavelength. At low inclinations it shows a single peaked profile with a shallow absorption feature in the red wing, caused by infalling optically thick gas obscuring part of the stellar surface and the shock region. This inverse P Cygni profile, which is considered to be a characteristic feature of hot hydrogen emission lines produced in accretion columns observed at face-on configurations (Bouvier et al., 2007), is visible in the model up to inclinations of 54° at velocities of 150 km/s up to 200 km/s, see Fig. 7.2. At the lowest modelled inclination of 5°, the emission line extends over a velocity range of about ± 150 km/s, whereas beyond 54°, the profile becomes double peaked and the range expands to ± 220 km/s.

When observed close to pole-on, the image of centrosymmetric accretion flows forms a disk-like structure with an intensity distribution that features rings of variable brightness, decreasing from the stellar surface to the edge of the magnetosphere. At such a low inclination, it is reasonably well approximated in principle by a geometric Gaussian disk model, given that the 'hole' left by the star in the continuum-subtracted images (Fig. 7.4 and 7.3, left side panel) is unresolved at

typical GRAVITY baselines. As we move to higher inclinations, centrosymmetry is lost and the internal geometry of the intensity distribution becomes complex, although the outline is still well demarcated by an inclined ellipse in the centre channel. In the blue and red wings of the line, Brγ emission is concentrated in regions away from the centre, so that the synthetic visibilities and consequently the fitted ellipse are tracing the corresponding substructures within the total magnetosphere.

For an inclination of 5°, the model system exhibits a decrease in size from the centre channel, with a half-flux radius of 0.032 au (2.75 R_*), to higher velocities, where the region can be as compact as 0.016 au (1.38 R_*). At higher inclinations, this trend becomes essentially inverted, with the centre channel forming a minimum and an increasing HWHM towards the line edges. In this case illustrated in Fig. 7.3, the ellipse position angle and inclination were fixed to be in line with the magnetosphere, following the approach we took with the GRAVITY data when fixing the ellipse fit at the PA and inclination of the NIR continuum disk. We revoked this assumption in Fig. 7.4. The results indicate that the exact choice of methodology potentially can have a large impact on the recovered trends across the line at the various inclinations. When all the parameters of the ellipse are left free for fitting, the size profile at higher inclinations broadly retains the original decrease in HWHM seen at 5° inclination, even if some of the individual channels show some fluctuations.

The best fit result of the ellipse for the 5° inclination suggests that the half-flux radius of the Gaussian disk underestimates the actual spatial extent of the full Brγ emission region by a factor of about 2/3 at the centre of the line. There the 0.032 au derived from the geometric model fall short in comparison to a magnetosphere with a defined size of 0.053 au. This discrepancy appears less pronounced at higher inclinations, although the comparison is not necessarily meaningful, as the intensity distribution in those cases is no longer well approximated by a simple geometric model. So while the ellipse fits based on the Gaussian disk do yield size estimates on roughly the appropriate order of magnitude, it is clear that a geometric Gaussian disk or ring model is not well suited to represent the realities of a system of accretion columns at higher inclinations, even for an axisymmetric magnetosphere.

The photocentre in each velocity channel was determined from a fit of the synthetic differential phases to again ensure consistency with the approach taken with the GRAVITY data. As a consistency check, we also computed the photocentre directly by calculating the barycentre of the intensity distribution, and found excellent agreement between the results of the two methods. The so obtained photocentre shift profiles are highly compact at inclinations of 5° (Fig. 7.3 and 7.4, centre panel), as at such a low angle the system of funnel flows is essentially centrosymmetric for the model of an axisymmetric magnetosphere. The maximum magnitude of shift in such a case is close to 0.007 au at 5° , which corresponds to 0.6 R_*. As the inclination

increases, we see a more extended profile, similar to a disk in Keplerian rotation, which begins to bend inwards at the edges at inclinations above 54°. The global maximum photocentre shift is thus found at moderate inclinations and remains relatively stable from 37° to 54° at 0.034 au or 2.9 R_*. At low to intermediate inclinations, the quasi-rotational profile is aligned at an angle of about 60° relative to the 'north' (i.e. the vertical) axis. In this the photocentre profile of the rotating magnetosphere is distinct from a rotating disk, as in the latter case the profile would be aligned with the disk semi-major axis.

7.1.2. Comparison of model to observational data

Whilst the model cube was set up to be comparable to an RU Lup-like system, it is still useful to compare the broader trends against the rest of the sample. The range of inclinations covered by the seven objects starts at the almost face-on case of TW Hya and goes up to $(49 \pm 4)°$ for DG Tau, with most of the objects being observed at low inclinations between 20° and 30°. In such cases, the spectral line is single peaked with a slight asymmetry caused by redshifted absorption at low inclinations, and a blueshifted line peak at intermediate inclinations. This behaviour is not consistent with the observed emission lines from the GRAVITY sample, as clearly visible absorption features in the red wing or shifts of the peak emission away from the centre are never detected in the observational data. Conversely, the asymmetric broadening of the base of the emission line, observed in four of the seven targets, is not reproduced by the model.

The size profile of the model shows that, at those low to moderate inclinations represented by the majority of sample objects, the HWHM either decreases towards the line edges, or remains relatively flat. The photocentre profile is either very clustered within a radius of 1 R_*, if observed face-on, or rotational and well aligned along a specific axis at an angle to the disk PA. Both of these trends together are roughly consistent with only the two weakest accretors. For the other objects we measure, within the error bars, either flat or increasing sizes at higher velocities. Only the two epochs of RU Lup exhibit a clear U-shape, such as can be seen in the model. However, in the model this feature only appears at significantly higher inclinations than those determined for the RU Lup system.

Most of the objects show photocentre profiles with higher orders of complexity than a simple alignment along one axis. One notable exception here is AS 353, for which the photocentre profile agrees with the model prediction in that it shows both a single axis rotational profile, but also a misalignment between that photocentre axis and the disk PA. However, for this target the emission region size is highly extended far beyond typical truncation radii, indicating that these photocentre profiles are not unique to the case of a rotating magnetosphere.

Overall the model trends are most accurately replicated by the data for TW Hya. Both the photocentre clustering and the smaller half-flux radii at higher velocities correspond very well to

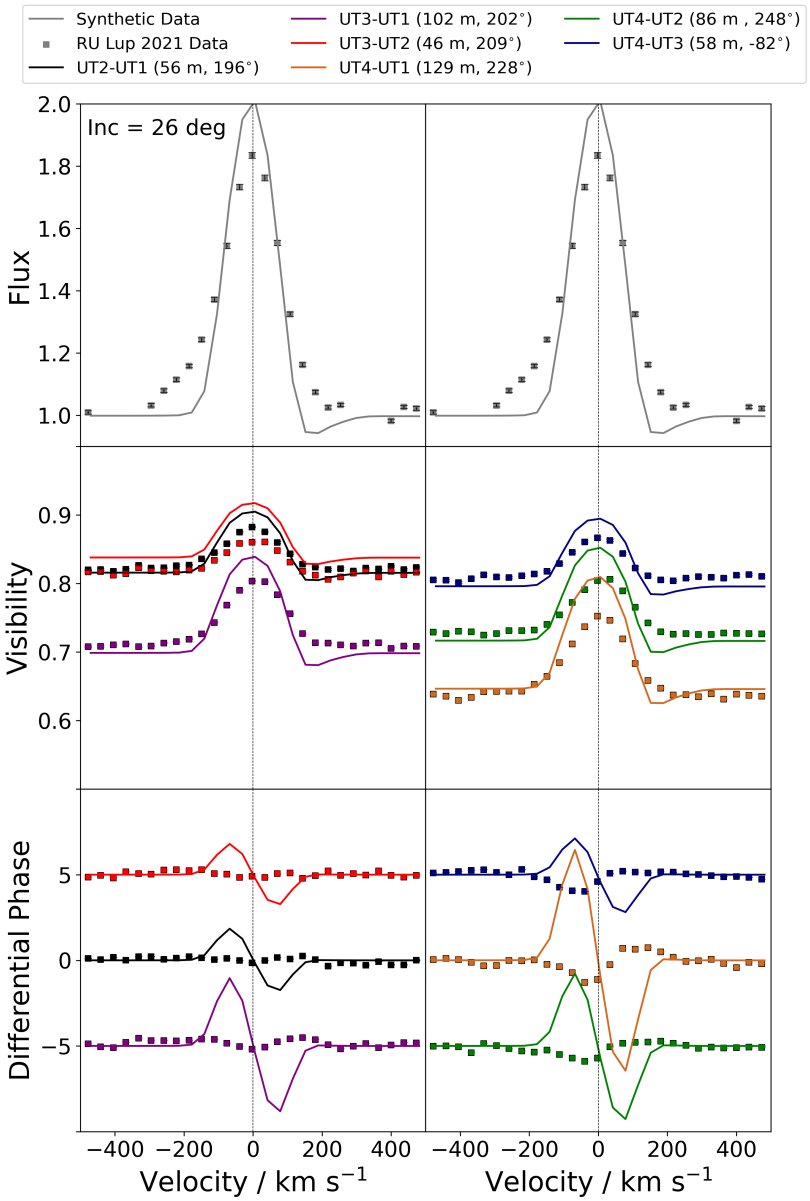

Figure 7.5.: Synthetic observables (solid lines) computed from the radiative transfer images of the magnetosphere, compared to the observational data of RU Lup from 2021. A Brγ spectrum was computed from integrating the image fluxes at different wavelengths. Synthetic visibility amplitudes and phases were obtained from Fourier transformation of the images. In order to ensure comparability with the total observables recorded by GRAVITY, an additional continuum disk contribution, taking into account parameters like disk size, disk flux and halo flux, was included through a form of post processing.
The figure shows the synthetic data for disk parameters chosen in accordance with the results reported in Gravity Collaboration et al. (2021b).

what is depicted in Figures 7.3 for a 5° inclination, further strengthening the argument for a Brγ emission region dominated by magnetospheric accretion (Gravity Collaboration et al., 2020). Still, even for this object, the inverse P Cygni profile that is predicted by the models is curiously absent from the observation, as is the case across the entire sample. It is possible that in TW Hya the asymmetric line shape is rather an expression of the absorption in the red wing rather than of an excess in the blue wing. The relatively narrow emission line in TW Hya, which matches up well with the range of ±200 km/s predicted by the model, could support this notion. We detect a notably larger range of velocities in emission for the other objects with strong asymmetric features, where the emission region size indicated spatially extended Brγ emission on a scale far beyond the magnetosphere.

DoAr 44 is another candidate for a Brγ emission region that is strongly shaped by magnetospheric accretion, although in this case the comparison against the model profiles is not as conclusive as for TW Hya. At the higher inclination of 32° of DoAr 44, the size profile derived from the model is more impacted by the methodology behind the emission region fit, although Fig. 7.3 shows profiles which are relatively flat for the centre channels at 26° and 37°. This would be consistent with what is seen in Fig. 6.7. The photocentre profile of DoAr 44 can be interpreted as quasi-rotational, although the low number of selected channels with sufficient flux and the relatively large uncertainties on the photocentre positions prevent this from being conclusive. Whether the GRAVITY spectrum of DoAr 44 shows the expected redshifted absorption is open to interpretation due to the relatively high dispersion among the continuum-level data points. At this level of inclination, the absorption peak would already be significantly less pronounced than in the pole-on case of TW Hya, see Fig. 7.2, so that the discrepancy between observed spectral line and model line shape is not large. The model thus seems to again support the idea that Brγ emission in DoAr 44 is indeed largely stemming from magnetospheric accretion processes, as was also proposed by (Bouvier et al., 2020)

VV CrA presents itself as something of an edge case here due to the very large uncertainties associated with the HWHMs and photocentre offsets. It appears that at least for the central channels the region is more compact (6.56 R_*) than the co-rotation radius (7.25 R_*), yet we also find a magnetospheric radius between 2.86 and 5.36 R_* for 1 and 3 kG magnetic fields, respectively. As the emission region extends further than what we would consider a reasonable upper limit on the truncation radius, the Brγ emission does not seem to trace the magnetosphere. For the remaining objects, comparisons between images and observations indicate that Brγ emission is not well described by only the magnetospheric accretion model. We see strong asymmetries in the line shapes, with moderate to high amounts of excess blueshifted emission, which are not explained by magnetospheric accretion alone. This is also true for the size profiles across the line, which appears either flat or U-shaped, with a minimum at the centre. Such profiles can be

seen in the model when fixing inclination and position angle for the ellipse fit (Fig. 7.3), but generally at higher inclinations than those measured for our sample objects. The photocentre profiles equally show a high degree of complexity, with either multiple alignments in different parts of the line or shift magnitudes far beyond the magnetosphere. We also must account for the possibility that some of the discrepancies between models and observations certainly arise from the axisymmetric nature of the model, given that non-aligned cases are common and obliquity angles between stellar dipole and rotational axis are typically on orders of 10° (McGinnis et al., 2020). This would likely affect the photocentre shift profiles the most, whereas the impact on the size profile is not trivial to evaluate intuitively.

To facilitate a more detailed comparison between the model of the RU Lup-like system and the data of the RU Lup observations, we made use of a custom developed tool which allowed us to derive the spectral and interferometric observables at a uv coverage set to correspond to the actual observation of RU Lup in 2021. The tool has the ability to modify the observables in such a way that they reflect the impact of varying the physical and geometric properties of the system, such as the inclination of the magnetosphere. These modifications also include the possible addition of a continuum disk contribution to compensate for the lack of a K-band emitting dusty disk in the original model. The full set of parameters that can be manipulated to produce the spectrum, visibility amplitudes and differential phases are: the common inclination and position angle of a system of continuum disk and magnetosphere, the size of the disk and the flux percentages coming from either the disk or an unresolved halo component.

Fig. 7.5 shows the synthetic data versus the observational data from 2021. In this case, the continuum disk size, disk flux, halo flux, position angle and inclination were set to the values reported in Gravity Collaboration et al. (2021b). At those parameters, the peak flux agrees with the observational results, but the line shape is lacking the broad base seen in the RU Lup data. The absorption feature in the red wing of the model spectrum translates to a similar dip in the model visibilities, as the obscuration of the stellar surface increases the relative weight of flux coming from a more extended area. The synthetic visibilities reproduce the observational continuum visibilities, but overestimate the Brγ peak, suggesting that the model is significantly more compact than the emission region that is reflected in the observational data. This is also reflected in the size profile (Fig. 7.6), where we also see that the change across the line is essentially inverted for the model when compared to the observational profile. The synthetic differential phases exhibit S-shaped signals at all baselines, with two phase peaks with opposite signs at red- and blueshifted velocities. The amplitude of these peaks ranges from 1° to 5°, which is an order of magnitude larger than the signals we detect in the observational data. This translates into a far more extended photocentre shift profile than the comparatively compact observed shifts for RU Lup in 2021, and also shows a clear alignment along one axis. The model here fails to re-

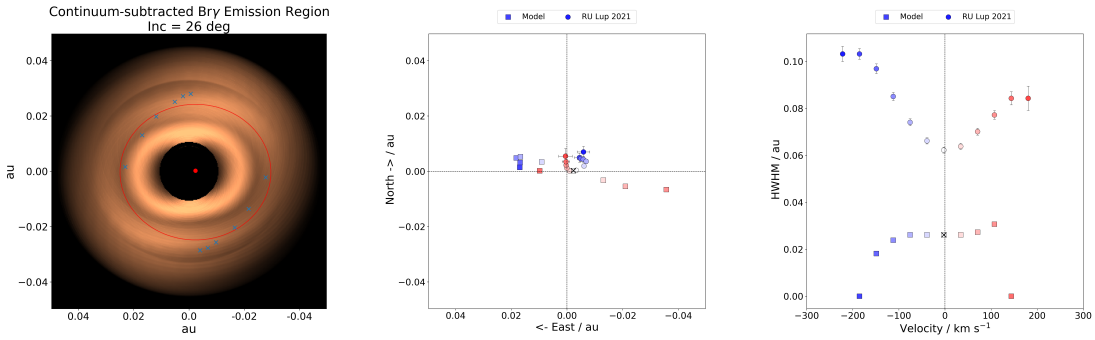

Figure 7.6.: Model image and derived quantities for an RU Lup-like system.

Left: A continuum subtracted model image of the magnetosphere at 26° inclination, representing the pure line emission region at the central channel of the Brγ line. The size of the region and its photocentre, depicted here as ellipse and red dot, were both determined from the synthetic observables in a process analogous to the way the GRAVITY data were treated.

Centre: The model photocentre shift profile across the line, compared to the results for RU Lup 2021. The model profile is largely aligned along a single axis, while the observational profile shows a significantly higher degree of complexity.

Right: Variation of emission region size across the line. While the size of the magnetosphere is an input parameter of the model, the change of the half flux radii at different velocities still provides a useful baseline to which the trends in the sample can be compared. The observational profile shows a region more than twice the size of the model HWHM at the central channel, growing larger at the line edges, whereas the model predicts a decline in size in the wings of the line.

produce the curved shape of the observational photocentre profile. We also see that the S-shapes produced by the model are essentially inverted in sign when compared to the observational data, indicating that the sense of rotation of the model is also essentially inverted with respect to the observed RU Lup system.

We also made an attempt to reproduce the observational data as closely as possible by fitting the model parameters, and found that we were not able to produce synthetic data in agreement with flux, visibilities and differential phases simultaneously. It is possible to reproduce the visibilities quite accurately, but only at a significantly higher inclination than what was found for RU Lup, and in such case the line flux would be severely underestimated. It is possible to find a much better agreement between synthetic and observed differential phases, mostly by manipulating the position angle of the system, but only at the expense of the visibilities. We were also not able to reproduce the broad base of the spectral line through any combination of parameters.

It is possible that a non-axisymmetric model, featuring a tilted magnetosphere, is better suited to resolve some of these discrepancies. The photocentre shift profile in particular, and its dependency on the inclination, is likely to be affected by the formation of preferential funnel flows per hemisphere, as is predicted in such a case. However, even such a modification to the model

is able to reconcile the observed large-scale emission in some objects with the compact scale of typical magnetospheres, nor would it account for the broad base of the emission lines or explain Brγ emission coming from beyond the co-rotation radius.
With this in mind, based on the observational results and the work done on the model cube, we reaffirm our original classification of our sample objects: sources for which magnetospheric accretion is the main driver of Brγ emission (TW Hya and DoAr 44), those which show spatially extended emission, likely predominantly originating in a disk or stellar wind (DG Tau and AS 353), and those that exhibit features not consistent with the model, but with characteristic sizes still of the order of the 4-7 R_* range associated with typical magnetospheres. For the latter group, a mixed contribution to the total Brγ flux coming from multiple emission components is likely responsible for the detected size and photocentre profiles.

7.2. Extended Brγ emission: Disk and stellar winds

While hydrogen line emission in T Tauri stars is strongly associated with the magnetic heating mechanisms in the accretion flows, magnetospheric accretion alone can only account for Brγ radiation produced in a compact region close to the stellar surface. This implies that spatially extended emission must arise from one or multiple other components in the system. In the context of Herbig Ae/Be type YSOs, the hot accretion disk itself is readily proposed as a possible source of Brγ emission (e.g. Kraus et al. (2008), Tambovtseva et al. (2016)), given the hot temperature environments found in the inner disk of intermediate mass objects. This idea has been extended to the case of the T Tauri stars in the early studies published by Eisner et al. (2010) and Eisner et al. (2014), who chose a Keplerian disk model and an infall/outflow model when attempting to reproduce their interferometric data and found no significant difference between the two in terms of the quality of their fit. However, computations of the radial temperature profile in the inner disk of T Tauri stars (Bertout et al., 1988) suggest disk temperatures, even at distances of 0.02 au, do not exceed 4000 K and thus fall short of the 8000 - 10000 K range we would expect from a strong Brγ emitter. By contrast, it has been shown that in magnetically driven winds hydrogen gas can be heated to temperatures of 10^4 K via ambipolar diffusion very quickly after being launched (Garcia et al., 2001b). This makes a wind a suitable candidate for an extended Brγ emitting component in the inner disk system. Such a wind might come in the form of an actual disk wind, launched from the surface of the inner disk, or originate from the polar region of the star as a stellar wind (e.g. Ferreira et al. 2006, Matt and Pudritz 2005). Interactions between stellar and disk winds, which can occur simultaneously, can also lead to material being ejected from the interface region between disk and stellar wind (Zanni and Ferreira, 2013). Ultimately it is unclear whether it would be possible to distinguish between

different types of outflow purely based on interferometric observations, as wide opening angles may lead to certain overlap of the possible scales of wind-driven emission. For the purpose and in the context of this discussion, we only refer to a wind as a Brγ emission component that is spatially extended beyond the magnetosphere and not differentiate any further. In any case, given that the rotation of the accretion disk is likely to transfer to and kinematically dominate the launch region of a disk wind, such a scenario could potentially reconcile the low temperatures of the accretion disk with the quasi-rotational photocentre profiles that we found for some of the our objects with extended emission regions.

Disk and stellar winds as Brγ emission sources have in the past also been discussed for Herbig Ae/Be stars: Kurosawa et al. (2016) examined spectro-interferometric data taken with VLTI AMBER, the predecessor to GRAVITY, and modelled the Brγ feature and associated interferometric observables with both a magnetosphere and a disk wind. Garcia Lopez et al. (2015) similarly explored AMBER data on the Herbig star VV Ser and found that a disk wind model was able to best reproduce the interferometric data, but did not match the line shapes, which were better reproduced by a bipolar outflow model. Weigelt et al. (2011) examined the scenario of a wind launched from a rotating disk for a Herbig Be star and produced model images for a Brγ disk wind with which they were able to reproduce their interferometric observables. The images they present show changes in the intensity distribution across the line that appears very similar to a rotating magnetosphere observed at low inclination, and would likely lead to a similarly rotational photocentre profile. Wilson et al. (2022) presented a spectroscopic study on hydrogen emission lines in a number of T Tauri stars, including DG Tau, which they compared against radiative transfer models of accretion with an additional stellar wind. Their model was able to reproduce the characteristics of the Hα line, but showed significant divergence from the observed infrared emission lines, including the Brγ feature.

Most objects in the GRAVITY T Tauri sample show emission lines which are either comparable in width to those derived from the radiative transfer model for low to moderate inclinations, or are asymmetric to the point that they are best described by a superposition of two Gaussians. Of the two Gaussians, one is typically broader and shifted to a higher blueshifted velocity, whereas the second one is comparatively narrow and centred. The narrow component is across the sample consistently similar in width to the magnetospheric model emission line, extending between $\pm$ 200 km/s, whereas the broad component appears at quite different widths and positions for the different targets, and can change significantly even for the same object between two epochs (see Fig. 6.2).

It is possible that the asymmetry is a manifestation of a multi-component Brγ emission region, consisting of a magnetospheric accretion component and additional outflow components in the form of disk or stellar winds. Such an interpretation would help to explain the prevalence of

the asymmetries and broad bases of the line shapes throughout the sample, given that the presence of outflows is generally expected in accreting objects due to their role in managing angular momentum in the system. This is especially true for objects with known associated large-scale jets, such as AS 353, DG Tau, and RU Lup. We note that AS 353 and RU Lup feature emission beyond the co-rotation radius as well as broad high velocity Gaussian components centred between -150 km/s to -50 km/s, which is similar to what has been reported by Garcia et al. (2001a) for the high velocity component of an atomic wind close to the star.

In AS 353, Brγ radiation was detected up to a HWHM of more than 13 R_*, which is about twice as far out as the co-rotation radius of the system. The photocentre profile is quasi-rotational, which would match the idea of a wind base in rotation. However, it is not clear if the scale of the photocentre profile is consistent with such an extended wind, as even the most displaced photocentre exhibits a shift magnitude of less than 2 R_*.

In RU Lup we equally observe Brγ emission from outside the co-rotation radius, but at 6.3 R_* in 2018 and 5 R_* in 2021 the emission region HWHM is still consistent with typical magnetospheric scales. If there is an additional wind present in the system, its contribution to the total Brγ output would likely be comparatively weaker than in the case of AS 353. The strong U-shape in the size profile at both epochs could also be explained in the context of a wind. In the case of a magneto-centrifugally driven wind, observed at low inclination, an accelerated flow of hydrogen ejected at a wide opening angle would reach higher velocities at more extended spatial scales. The complex photocentre profile of RU Lup is also not well explained by either a rotating wind or a rotating axisymmetric magnetosphere alone, as both of these scenarios on their own should produce a profile with a singular axis alignment. Whether a combination of a rotating magnetosphere and a disk wind could lead to an RU Lup-like profile is a question that ultimately requires more advanced modelling to answer.

The line shape observed in DG Tau is peculiar insofar as that it is one of only two objects in the sample for which the blueshifted excess is not at all detected, despite the fact that it has one of the largest emission region HWHMs of 12.9 R_* and is also the only object which shows Brγ radiation originating beyond the NIR continuum HWHM. The line extends almost to a range of ± 250 - 300 km/s and is as such broader than predicted by the magnetospheric accretion model. It is possible that inclination effects play a part here, but since DG Tau is observed at a similar inclination as AS 353, this alone would not account for the discrepancy in line shape between the two objects. Either way, the case of DG Tau casts some doubt on whether the Gaussian decomposition into broad and narrow components can be straightforwardly tied to physical emission components. Within the uncertainties, the photocentre profile can be interpreted as effectively rotational and well aligned with the disk profile, which also supports the idea of a wind launched from a rotating base, especially since in this case we know the photocentre profile mimics the

one reported for the large-scale rotating CO disk.
Overall five of the seven objects show signs of extended emission. For two of them (DG Tau and AS 353) the Brγ feature is likely driven predominantly by a rotating wind, whereas two (RU Lup and S CrA N) could see a more even ratio between the Brγ flux originating from the magnetosphere and the flux originating in an extended component, based on the region size compared to the co-rotation radius and how well rotation alone describes the photocentre profile. The case of VV CrA is not conclusive due to the large uncertainties on the photocentre positions and half-flux radii, although overall the observables also indicate a mixed origin of Brγ emission.
In the broader context of the analysis of the Brγ emission size as a function of mass accretion (see Fig. 5.1), we remind that the accretion rates were derived using the empirical relationship of Alcalá et al. (2014), established from a population with significantly weaker accretion properties than most of the objects of our sample show. However, the validity of this relationship for our study is well supported by the fact that it remains unchanged when including results for stronger accretors from Muzerolle et al. (1998) and essentially Calvet et al. (2004) (see panel C.7 for Brγ in Alcalá et al. (2014)). Still, the strong dispersion of the experimental points translates into large uncertainties on the coefficients a and b in Eq. 5.1, itself resulting in large error bars reported on the mass-accretion rates. In the light of our results, we propose that improved constraints on the connection between line luminosity and accretion rate could potentially be obtained through further quantitative estimates of the balance between mass inflow and outflow mechanisms (e.g. magnetospheric accretion vs. disk winds) in the inner disk.

7.3. Summary: The GRAVITY Brγ T Tauri survey

We presented spectro-interferometric data for a sample of seven T Tauri stars, observed in the K-band with VLTI GRAVITY between 2017 and 2021, focussing on the Brγ hydrogen emission line at 2.16 μm. For the first time, we were able to spatially resolve the innermost star-disk interaction regions for these objects, which are home to complex and time-variable phenomena, with an unprecedented accuracy of down to $\sim$ 0.001 au scales, improving upon previous campaigns, such as presented in Eisner et al. (2014), by an order of magnitude.
Based on the Brγ spectra, spectrally dispersed interferometric visibilities, and differential phases, we determined the HWHM of a geometrical Gaussian disk model in a number of spectral channels of the line, probing the change of the emission region size at different radial velocities. We also extracted the relative photocentre shift of the pure Brγ emission region with respect to the continuum photocentre from the differential phases and showed the distribution of Brγ emission photocentres in the different wavelength channels and corresponding velocities. Based on these results, we commented on generalised trends within the sample and attempted to identify dis-

tinct groups of objects based on their characteristics. These results were interpreted with respect to the likely origin of Brγ radiation in the respective systems, especially in the context of magnetospheric accretion, which is thought to be a major driver of Brγ emission in T Tauri stars. To assist in the interpretation and to help distinguish Brγ emission produced in accretion flows from other potential mechanisms, we used a radiative transfer model of an axisymmetric accreting magnetosphere to establish characteristic interferometric signatures which could serve as baselines against which to compare our observational results. To summarise the most important findings and conclusions:

- Out of a sample of seven objects in total, five exhibit Brγ emission lines with asymmetric line shapes. These lines feature a broad base with significant excess in the blue wing and can be decomposed into a broad high-velocity Gaussian and a narrow low-velocity Gaussian component. The lines of the remaining two sources (DG Tau and DoAr 44) are well approximated by a single Gaussian function.

- Across the sample, two objects (TW Hya and DoAr 44) show emission coming predominantly from within the co-rotation radius and Gaussian disk HWHMs that are comparable with the typical magnetospheric radii of around 5 R_*. This is in agreement with previous findings in Gravity Collaboration et al. (2020) and Bouvier et al. (2020).

- For another two objects (DG Tau and AS 353), Brγ half-flux radii extend to scales outside the co-rotation radius and beyond 10 R_*. We expect that other, spatially extended, sources of Brγ emission are present in these systems and are major, possibly dominant, contributors to the total line-flux output. Winds are likely candidates for such components. DG Tau is also the only source in the sample for which the Brγ HWHM is larger than the NIR continuum HWHM. Strong jets were previously reported for both of these objects.

- Brγ emission region sizes for the remaining objects are of the order of 4 to 7 R_*, but the data indicate that Brγ emission is nonetheless extending to outside the co-rotation radius or beyond the upper limit of estimated truncation radii for plausible magnetic field strengths. Such behaviour can indicate simultaneous emission from both a magnetospheric and a more extended component, possibly featuring a wind launched from close to the disk-magnetosphere interface region.

- The photocentre profiles can be roughly classified based on whether they show a quasi-rotational alignment of photocentres along a single axis, similar to what would be expected from a disk in Keplerian rotation, or if they exhibit more complex patterns. Large uncertainties on the position of the photocentres complicate this classification. Out of the seven

objects, one (AS 353) shows a distribution of photocentres across the line that most resembles a rotational profile. Two other objects (DG Tau and DoAr 44) can be interpreted as quasi rotational when their uncertainties are taken into account. One (TW Hya) shows an indistinct clustering of points within a single stellar radius that would be consistent with a rotating system observed at a close to pole-on configuration.

- The synthetic data derived from the radiative transfer models allowed us to identify trends across the line that match the observations of TW Hya and DoAr 44 in terms of their size and photocentre profiles. At intermediate inclinations, the photocentre profile of the rotating axisymmetric magnetosphere shows a rotational profile that is misaligned with the disk semi-major axis by about 30°. At higher inclinations, we found that methodological effects when determining the region size can have a large impact on the derived profile.

In conclusion, we find that the observational data fit the case of magnetospheric accretion best for the two weakest accretors in the sample (TW Hya and DoAr 44), while objects with higher mass-accretion rates also appear to feature significant influences from more spatially extended Brγ emission origins, which may come in the form of disk or stellar winds. Observations at very high angular resolution, such as those that only long baseline interferometry is able to provide in the foreseeable future, will be vital for any attempt to disentangle the different contributions in order to improve our understanding of the underlying processes in the star-disk interaction region. In particular, we are looking forward to the possibilities that will be unlocked by the implementation of the GRAVITY+ project, as the upgrade in sensitivity will make new reservoirs of potential sources available for future investigations. Additionally, multi-technique campaigns which can, for example, include polarimetric measurements of the magnetic field topologies, as well as repeated observations of individual sources to probe the time variability of the innermost regions, will offer great opportunities to gain new insights into the connection between multiple phenomena in the inner disk and strengthen the depth of the analysis.

8. Combined Accretion-ejection models for RU Lup

Note: The contents of this chapter are direct citations from ***"The interplay between disk wind and magnetospheric accretion mechanisms in the innermost environment of RU Lup" - J.A. Wojtczak, B. Tessore, L.Labadie et al.*** *(Wojtczak et al. (2024), in production), specifically Sections 1,2, 4, 5,and 6.*

Here I present in detail the results pertaining to the advanced radiative transfer simulations of magnetospheric accretion and disk wind models, using the methodology described in Chapter 4 of this thesis. A total of six different model variations, including pure axisymmetric and non-axisymmetric magnetospheric accretion models, pure disk wind models, and combined wind-magnetosphere hybrid models, were computed over a large parameter grid, and then used to compute synthetic interferometric observables from simulated images produced with the radiative transfer code MCFOST. These synthetic observables were compared against the GRAVITY data obtained for the young star RU Lup in 2021 in order to explore whether hybrid models would, in principle, be capable of explaining the behaviour of the observables at different velocities across the line. The essential result of this study was that the characteristic sizes and line profiles could be reproduced by a magnetospheric accretion-disk wind hybrid model, but the photocenter shift profiles were not well reproduced by any of the models explored here. Potential explanations for this issue are presented in the discussion, which concludes this chapter.

8.1. Introduction

Given the apparent limitations of the axisymmetric magnetospheric accretion scenario to explain many of the spectro-interferometric signatures obtained with GRAVITY, it is obvious that a more complex model is needed to approximate the observations. Firstly, the assumption of axisymmetry in the model could be questioned. It is well established that the magnetic dipole in many magnetically active YSOs is tilted with respect to the stellar rotational axis (Donati et al., 2007; Johnstone et al., 2014), meaning real observed systems typically exhibit non-axisymmetric magnetospheric geometries. However, while a non-zero dipole tilt may very well have some degree of impact on the interferometric signatures, it is not clear how this in itself would resolve the

discrepancy regarding the extended emission region size with regards to the comparatively small co-rotation radius. It is more likely that an additional large scale Brγ emission component, such as in the form of a disk wind being launched from the magnetosphere-disk interface, is needed to address this issue.

Such winds, among other outflows, have been thoroughly discussed in the context of young stars for decades due to their connection to large scale jet structures that have been observed around multiple YSO systems, like RU Lup or AS 353 (Takami et al., 2003; Whelan et al., 2021), as well as their presumed role in managing excess angular momentum in star formation (Hartmann and Stauffer, 1989; Matt and Pudritz, 2005). Winds constitute a strong contributor to mass loss and thus disk dispersal in YSOs as these objects evolve towards the main sequence (Alexander et al., 2014). As such, accretion and ejection are fundamentally related, and mass ejection rates typically proportional to the accretion rate. Both are known to decline with the age of the YSO as the system matures out of its pre-main sequence (PMS) phase (see e.g. Watson et al. (2016)). In Gravity Collaboration et al. (2023b), we showed that the younger systems from among the sample, with higher accretion rates, deviated from the pure magnetospheric accretion scenario more strongly. The idea of a wind component potentially acting as an additional emitter of Brγ radiation in younger systems, then diminishing in relative strength with increasing age, could serve as a possible explaination of the distinction found among the sample objects.

Previous theoretical works by, for example, Garcia et al. (2001b); Lima et al. (2010) suggest that a magnetically driven wind, launched through magnetohydrodynamical (MHD) processes, could reach temperatures on the order of 10^4 K close to the disk surface. Such an MHD wind could thus provide a sufficiently hot and dense environment to produce a significant amount of Brγ radiation on spatial scales close to the magnetosphere but larger than the co-rotation radius (Romanova and Owocki, 2015). MHD wind models have in the past been tested predominantly against spectroscopic observational data (Wilson et al., 2022; Weber et al., 2020), whereas interferometric studies that incorporate radiative transfer simulations are so far scarce. Works that feature models of wind or accretion based hydrogen emission have largely been restricted to Herbig Ae/Be stars (e.g. Weigelt et al. (2011); Kurosawa et al. (2016)), although more recent contributions have begun to focus on connecting simulations and interferometry in the context of classical T Tauri stars (Tessore et al., 2023; Gravity Collaboration et al., 2023b).

In this chapter, we build not only on our own previous work, but expand upon the body of interferometric studies of inflow/outflow mechanisms in general (e.g. Eisner et al. (2010)). For the first time, we combine sophisticated modelling efforts of the NIR signatures of disk winds and magnetospheric accretion in T Tauri stars with the unparalleled spatial resolution of long-baseline interferometry. We re-investigate the comparison of synthetic spectroscopic and interferometric observables to VLTI GRAVITY observational data for the exemplary case of

the young star RU Lup in the light of this comprehensive modelling approach. The goal of the analysis is to determine whether these types of complex wind-magnetospheric accretion hybrid models are suited to address the previously found discrepancies between the simple accretion scenario and the RU Lup data.

8.2. Observational results on RU Lup

RU Lup is a classical T Tauri star, located in the Lupus star forming region at a distance of 157.5 pc (Gaia Collaboration, 2020). An interferometric study with ALMA resolved the large scale disk structure in the 1.25 mm continuum and found the system to be at an almost pole-on configuration with an inclination of only 18.8° (Huang et al., 2018). RU Lup has a known large scale outflow component in the form of a jet whose blue-shifted component has been determined to be at a position angle of 229° North to East (Whelan et al., 2021). It is generally considered to be a strong accretor, with mass accretion rates in the literature ranging up to $30 * 10^{-8}\ M_{\odot} yr^{-1}$ (Siwak et al., 2016). Stock et al. (2022) proposed that the accretion rate of RU Lup, as estimated from an empirical relationship between line luminosity and accretion luminosity for certain tracing spectral lines, can vary by as much as a factor of two over a 15 day period, making accretion in RU Lup potentially also highly variable.

RU Lup was observed with GRAVITY in April 2018 and May 2021, combining the four 8.2 m Unit Telescopes (UTs) of the VLTI to record spectrally dispersed interferometric fringes with 6 baselines. The observations made use of GRAVITY's single field mode, delivering simultaneously low spectral resolution (R ~ 22) fringe tracker (FT) and high spectral resolution (R ~ 4000) science channel (SC) data of RU Lup across the near-infrared (NIR) K-band between 1.98 μm and 2.4 μm. The effective baseline lengths of the observation range from 46.48 m (UT3-UT2) up to 128.5 m (UT4-UT1), translating into maximum angular resolutions in the K-band between around 4.6 and 1.7 mas, since the angular resolution scales with the projected baseline length B as $\frac{\lambda}{2B}$. In both 2018 and 2021, the total observation time ran for a little over an hour, preceded by a single calibrator measurement in each case.

In the following we summarise the most important results from the GRAVITY continuum and Brγ line studies on RU Lup (Gravity Collaboration et al., 2021b, 2023b). The continuum visibility data for RU Lup was fitted with a multi-component geometrical model (Berger and Segransan, 2007). It consists of a point source to account for the star itself, a ring-like region which represents the interferometrically partially resolved region around the inner dusty rim, and an extended component which we refer to as the "halo". The halo component is thought

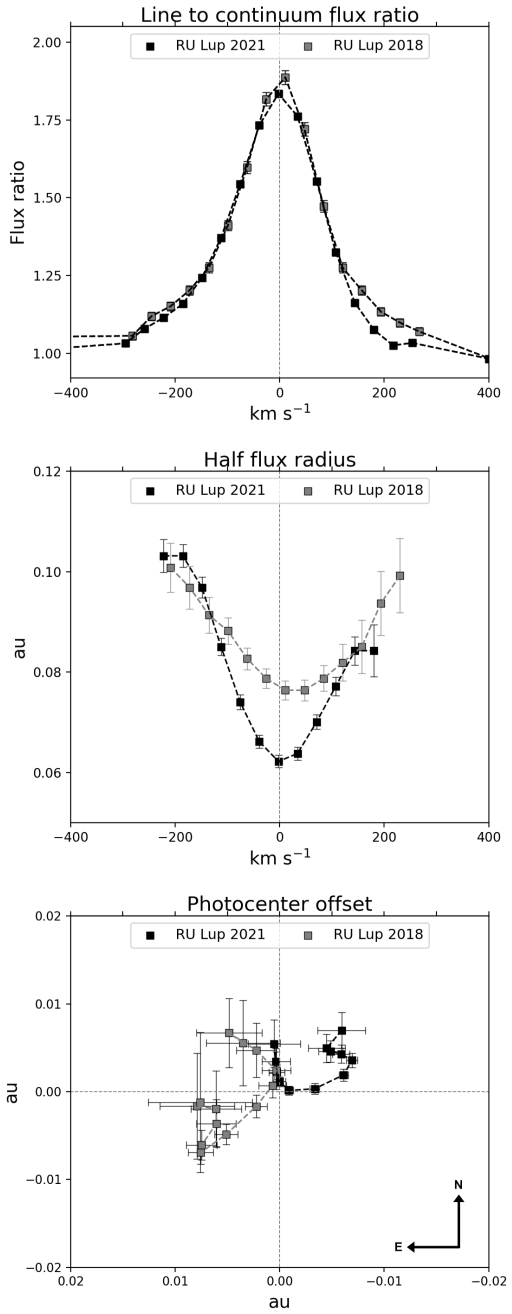

Figure 8.1.: Previous results for CTTS RU Lup, derived from VLTI GRAVITY observations in 2018 and 2021. Shown here are (from top to bottom) the line-to-continuum flux ratio of the Brγ spectral line, the characteristic size of the emission region across the velocity channels of the line, and the corresponding positions of the emission region photocenters.

to represent the large scale scattered light emission from the disk. It takes into account K-band continuum flux contributions which appear in the spectrum, but are spatially overresolved at the projected baseline lengths of the telescope configuration. The relevance of the halo and the continuum disk will be further detailed in Section 2.1.1. The ring-like morphology of the compact environmental component was chosen due to the association of the K-band continuum emission with the hot dusty wall at the sublimation radius. The continuum analysis yielded a halo contribution of 30 ± 10 % and a ring contribution of 12 ± 3 % to the total continuum emission. The fit of the ring region, for which a Gaussian brightness profile was assumed, yielded a size in the form of a half width at half maximum (HWHM), or half flux radius, of 0.21 ± 0.06 au in 2018 and 2021. The inclination of the inner disk continuum was determined to be 16^{+6}_{-8} degrees for the 2018 data and 20^{+6}_{-8} degrees for 2021 data. The position angles of the ring were constrained at 99 ± 31 degrees and 101 ± 31 degrees for 2018 and 2021, respectively.

The Brγ line profile shows a small variation in its equivalent width (-16.82 Å to -13.47 Å) from 2018 to 2021, and features an asymmetric shape with blueshifted excess emission and no visible inverse P Cygni characteristic. The visibility data was fitted using a geometrical Gaussian disk model. As such, we presumed that the brightness distribution of the emission region could be described by a disk-like morphology with a centrally peaked brightness profile, which then falls off as a Gaussian function with increasing distance from the center. In this manner we obtained spectrally dispersed characteristic sizes, again in the form of a half flux radius, for up to 13 velocity channels across the emission line. Similarly, we derived the positional offset of the barycenter of the brightness distribution (i.e. the photocenter) for the same spectral channels from the continuum-subtracted differential phase data. Both the visibility and differential phase data were corrected for continuum contributions, meaning the resulting quantities describe the pure line Brγ emission region. Hereby we found that the Brγ half flux radii (2018: 6.32 R_*, 2021: 5.01 R_* in the centre channel) were more extended than the co-rotation radius (R_{co} = 3.31 R_* for P_*=3.7 d, R_*=2.6 $R_\odot$, and M=0.6 $M_\odot$, as assumed in Gravity Collaboration et al. (2021b) and Gravity Collaboration et al. (2023b)), by a factor of more than 1.5. In addition, the emission region sizes were increasing towards the high velocity channels, which is was inconsistent with the centrally peaked size profile predicted by the simple axisymmetric accretion model. The distribution of emission region photocenters across the line showed no clear alignment with the known jet axis or the model profile. The magnitude of the displacements was significantly smaller, by a factor of about 4 in the most extreme channel, than that obtained from the synthetic model data. Figure 8.1 shows the observational results obtained for the Brγ emission region.

These clear deviations from the simple magnetospheric accretion scenario make RU Lup a suitable test case to investigate the effect of an additional Brγ emitting disk wind on the synthetic observables. The low inclination configuration, confirmed by GRAVITY, promises to be

particularly advantageous compared to some of the other objects from the GRAVITY T Tauri sample for which we found similar results, given that it more clearly separates the accretion and ejection emission regions when the system is viewed near pole-on. In this work we will focus on the comparison of the new radiative transfer simulations to the 2021 dataset, since the fundamental trends in the observable profiles are retained between 2018 and 2021. In both cases, we detect an asymmetric line, a spatially extended emission region with increasing sizes at high velocities and a compact multi-axial distribution of emission region photocenters across the Brγ line.

For a more detailed description of the reduction process, and a more thorough discussion on the results for both continuum and line emission data, we refer to Gravity Collaboration et al. (2021b, 2023b).

8.3. Radiative transfer simulations with MCFOST

The images were computed across 101 wavelengths centered on the line position, with a channel width of 0.723 Å. We chose to compute the atomic populations and radiative transfer on a spherical grid with a logarithmic distribution of points in the radial direction to maximize the density of cells in the central regions of the image, where the relatively complex brightness distribution of the star-magnetosphere system is located. As the axisymmetric magnetospheric model and the wind model are also symmetric with respect to rotation about the stellar axis, they were computed on a 2D spherical grid in order to save on computation time. By contrast, the non-axisymmetric magnetospheric accretion models required the use of a 3D spherical grid due to the azimuth-dependence of the hemispheric accretion flows under a tilted magnetic dipole. On the 2D grids we set the number of radial and polar angle grid points to 150 each, while on the 3D grids an additional 64 points in azimuth are included. We confirm, based on comparative simulations of an axisymmetric model on both a 2D and 3D grid, that resolution effects due to the smaller number of azimuth points do not affect the results. The extent of the grid constitutes a cut-off for the contributions coming from the outer regions of the wind, so the grid needs to be sufficiently large to include all significant flux, but should not be larger than necessary for the sake of computational time efficiency. To ensure this, the outer edge of the grid was tied to a multiple of the outer radius of the model. The exact number depends on the model used and was chosen by manually increasing the grid size until further increases did not significantly change the resulting line profile any longer. The effective range of grid sizes for the models discussed in section 8.4 lies between 36 and 47 R_*. The final images were produced for multiple inclinations and, where applicable, azimuth angles. The field of view of the image was also anchored to the outer radius of the model. It is again set to be sufficiently wide to capture the entire flux at any

possible inclination, but as small enough to minimise the resulting file sizes. The pixel size was, due to similar considerations as for grid size and field of view, set to a constant 0.03 au per pixel, meaning the number of pixels per image varies with the radial size of the chosen model.

The atomic hydrogen model used here includes the ground state and 15 excited bound states, leading to a total of 101 discrete bound-bound transitions and 15 bound-free transitions, of which the latter will contribute to the total system continuum emission while the former produces discrete spectral line emission. While this hydrogen model file contains a large number of other prominent hydrogen lines, such as Hα, we only consider line emission produced by the Brγ electronic 7-4 transition at a vacuum wavelength of 2.16612 μm.

8.4. Comparison to GRAVITY RU Lup data

In this section, we present a number of different models in an attempt to recreate the observational profiles obtained from the GRAVITY data for RU Lup from 2021. As relevant observables we consider here the line-to-continuum flux ratio, the characteristic emission region size obtained by fitting a geometric Gaussian disk model to the visibilities, and the photocenter shift of the emission region as reconstructed from the differential phases. In order to ensure comparability, we modify the model flux ratio as detailed in Chapter 4 by assuming an additional disk and halo continuum contribution to the total flux. We further fix the inclination both the image itself and of the geometric Gaussian disk at 20° to remain consistent with the treatment of the GRAVITY data.

Exploring the possible model variations is challenging given the large potential parameter space and the computational demands of MCFOST. Even a basic large scale model grid search over the entire parameter range is currently not possible within the technical capacities available and would require a substantial additional optimisation effort that is beyond the scope of this work. Instead, we utilise a mixed approach. We first consider the effect of isolated individual parameter variations from a common reference model to identify those quantities with the strongest response. This analysis indicates that there is a clear distinction between parameters which influence primarily the line flux, but have minor impact on the interferometric quantities, and those that strongly affect also the characteristic size and photocenter shift. We refer to Chapter 4 for a more thorough discussion of those results. Second, we employ a semi-manual fitting routine which involves running partial model grids for which we vary only a subset of the total model parameters simultaneously within a manually defined bracket of possible values. The best fitting models from those partial grids were then determined by χ^2 minimisation. This process was then iterated on by computing a new partial grid with different parameter variations

Table 8.1.

	Mag. accretion I Axisymmetric (MA I)	Mag. accretion II Non-axisymmetric (MA II)	Disk wind I Single peaked (DW I)	Disk wind II Double peaked (DW II)	Hybrid model I Cool + compact (HM I)	Hybrid model II Hot + extended (HM II)
R_* [$R_\odot$]	2.5	2.5	2.5	2.5	2.4	2.5
M_* [$M_\odot$]	0.8	0.8	0.8	0.8	1.2	0.8
T_* [K]	4050	4050	4050	4050	4050	4050
P_* [days]	7	7	7	7	9.05	7
R_{co} [R_*]	5.71	5.71	5.71	5.71	8.1	5.71
R_{mi} [R_*]	7	7	-	-	6	7
δR_m [R_*]	2	2	-	-	1	2
$\dot{M}_{acc}$ [10^{-8} $M_\odot yr^{-1}$]	23	23	-	-	10	23
T_{mag} [K]	8600	8600	-	-	7100	8600
R_{wi} [R_*]	-	-	7.1	9.1	7.1	9.1
δR_w [R_*]	-	-	5	3	8	3
d_{fp} [R_*]	-	-	15	15	15	15
R_{dd} [R_*]	-	-	14.5	13	13	13
β_{wind}	-	-	0.62	0.05	0.2	0.05
α_{wind}	-	-	0.4	0.7	0	0.7
z_{crit} [au]	-	-	0.0516	0.02	0.005	0.02
M_{loss} [10^{-8} $M_\odot yr^{-1}$]	-	-	5.1	12	10	12
β_{ma} [deg]	0	30	-	-	0	0

Table 8.2.: RU Lup model configurations compared to VLTI GRAVITY data. Descriptions of the physical nature of the respective model parameters are given in Section 4.3 for the accretion model and in Section 4.4 for the disk wind model.

to check if the χ^2 could be further improved.

Given that the instrumental error on the data points computed by the GRAVITY pipeline lie on the order of less than 2%, even the reduced χ^2 is typically very large. We rely on these quantities exclusively as relative indicators in order to rank different parameter combinations and models against each other and do not derive any statement on the global statistical significance of the models from them. With the simplified nature of our models and the limitations on the parameter exploration in mind, we do not necessarily expect to find a model that is a full quantitative match of the observational data. Instead, the idea is to determine whether the main trends derived from the observation can be reproduced in principle on an acceptable level, and to this end we prioritise achieving a good visual fit over a more quantitative approach.

In this section, we describe in more detail two variants each of a pure magnetospheric accretion model, a pure disk wind model and of a hybrid combination of both models. Table 8.1

summarises the parameters of the different models.

8.4.1. Scenario 1: Pure magnetospheric accretion model

As a starting point, we revisit the case of the simple axisymmetric magnetospheric accretion model from Gravity Collaboration et al. (2023b). In this work we explore a significantly expanded parameter space for this scenario, resulting in the model configuration depicted in the left column of Fig. 8.2 and referred to as MA I in Table 8.1. The normalised line flux is single peaked, with a center channel line-to-continuum flux ratio of 1.76, compared to the observational peak flux ratio of 1.83. The line width between model and observation is comparable at the 50% flux mark, with a model full width at half maximum (FWHM) of 168 km/s versus the observational profile at 187 km/s. At the base of the line, where the observational asymmetry is most pronounced, we note a larger disparity, with a width at 10% flux (W10%) of 320 km/s in the model versus a W10% of 420 km/s in the GRAVITY data. Visually this difference is clearly localised in the blue wing of the line, where the model profile lacks the excess amount of blueshifted Brγ emission that we detect in the observation. By contrast, the red wing of the line is well reproduced by the model.

In the center channel, the fit of the Gaussian disk geometric model yields a characteristic size of 0.055 au. As such, the half flux radius sits at half the outer magnetospheric radius of 9 R_*, which at $R_* = 2.5\ R_\odot$ translates to 0.11 au. This result is again comparable to the observational center channel half flux radius of 0.061 au, although still beyond the estimated 1σ fit uncertainty of 0.001 au. The increase in characteristic size in the wings, however, which we see in the observational data, is not recovered by this accretion model. From the observation we derive a maximum size of 0.1 au at the extreme blue end of the wavelength range, while the model profile is centrally peaked and drops off to 0.045 au in the corresponding channel.

In the photocenter profile, the offset magnitude ranges up to ± 0.022 au, which is by about a factor of two larger than the largest photocenter shift we obtain observationally. The distribution of photocenters across the line has a similar "crescent"-like shape, where the offsets at the most extreme velocities become smaller in magnitude again, but compared to the GRAVITY data the high velocity channels are still mostly aligned along a similar axis as the low velocity channels. The alignment of the overall model photocenter distribution appears almost perpendicular to the observational one, but the large uncertainty of the PA estimate obtained with GRAVITY (± 30°) leaves some ambiguity about the relative orientation.

Our second magnetospheric accretion model, referred to as MA II in Table 8.1 and depicted in the right column of Fig. 8.2 for an azimuth angle of -90°, addresses the question concerning the effect of a tilted magnetic dipole on the synthetic observables. Most of the fundamental parameters are unchanged with respect to MA I, but the model variant now features an obliquity

of 30°. The change results in an overall drop in line flux , with the peak flux reduced to 1.71 and the FWHM to 152 km/s. At an azimuth angle of -90 degrees , this predominantly affects the red wing of the line profile. For the same angle, the centrally peaked shape of the size profile is flattened to a relatively constant size of 0.051 au across the line. A similar effect is seen for the photocenter profile, where the crescent arch is also compressed, although the maximum shift magnitude remains close to 0.022 au.

The introduction of the dipole tilt breaks the axisymmetric nature of MA I. The image and resulting synthetic observables now depend on a selected azimuth angle, which effectively traces the rotation of the magnetosphere. At -90° in azimuth, the observer's line of sight is aligned with the two hemispheric funnel flows at non-zero inclinations. In Fig. 8.3 we concentrate on two specific examples at ± 45°, which in conjunction with the -90° plot from Fig. 8.2 cover the relevant potential differences. From these Figures is clear that even qualitatively the nature of the impact of a dipole tilt depends on the azimuth. The localisation of the variation in flux ratio between axisymmetric and non-axisymmetric model changes between the red and blue wing as we move from negative to positive azimuth angles. The flattening of the size profile only appears at negative azimuths, while the positive orientations retain the centrally peaked shape. At +45° azimuth, the photocenter distribution is more strongly aligned with the disk axis, which signifies a shift of about 30° towards East relative to -90° azimuth, and also to the axisymmetric case.

While the dipole tilt can clearly affect the overall shape of the observable profiles, its impact on the sizes and photocenter shift magnitudes at this level of inclination is even in the best case on the order of 10% or less. In itself, this is not sufficient to fully resolve the limitations of the pure magnetospheric model in matching the GRAVITY data, as the discrepancies between model and data described for the non-axsisymmetric scenario largely remain the same.

8.4.2. Scenario 2: Pure disk wind model

We further present two distinct pure disk wind models in order to explore the question as to whether the RU Lup GRAVITY data might be better described by a disk wind rather then the magnetospheric accretion scenario. Both models, referred to as DW I and DW II in Table 8.1 and depicted in Figure 8.4, are mainly differentiated by the wind velocity, as represented by a difference in the β_{wind} paramter of 0.62 (DW I) to 0.05 (DW II). In practical terms, the differing wind velocities result the line profile of DW I being single peaked, whereas the Brγ line in DW II appears strongly double peaked.

The DW I model manages to replicate the central channel line flux ratio almost exactly at 1.83, although the line is more narrow at an FWHM of only 152 km/s and a W10% of 231 km/s. The width at the base of the line in particular is then underestimated by a factor of almost two when compared to the W10% of 420 km/s of the observational data.

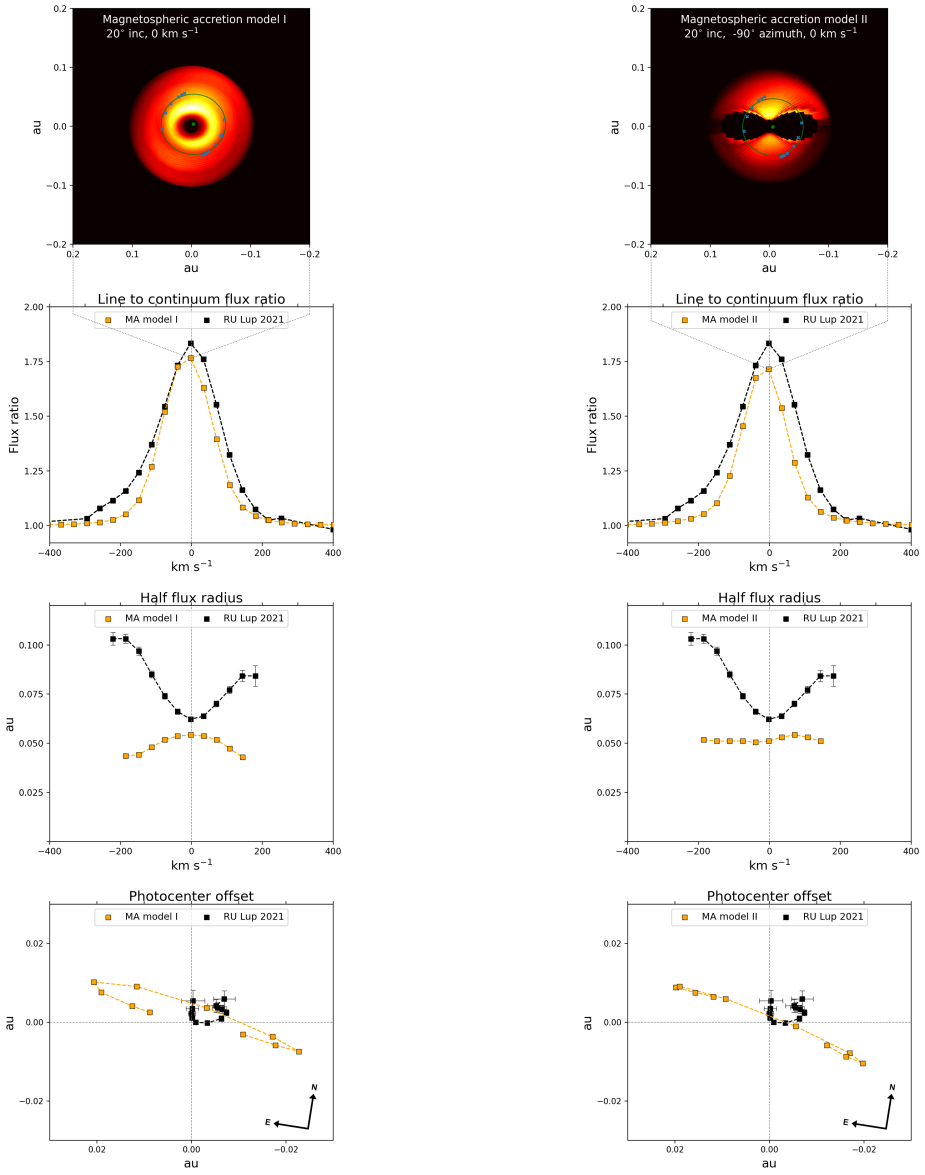

Figure 8.2.: **Left, from top to bottom:** Center channel image, line-to-continuum flux ratio, characteristic size and photocenter shift per velocity channel of the Brγ emission region of the **axisymmetric magnetospheric accretion** model. The ellipse depicted in the image signifies the half flux radius of the geometric Gaussian disk model used to derive the characteristic size. **Right: Non-axisymmetric variant** of the magnetospheric accretion model with an obliquity of 30°, viewed at an azimuth angle of -90°.
In this depiction the stellar rotational axis, not the North axis, is aligned with the vertical coordinate axis. The observational photocenters were rotated by -9° with respect to Fig. 8.1 to put them in the same frame of reference.

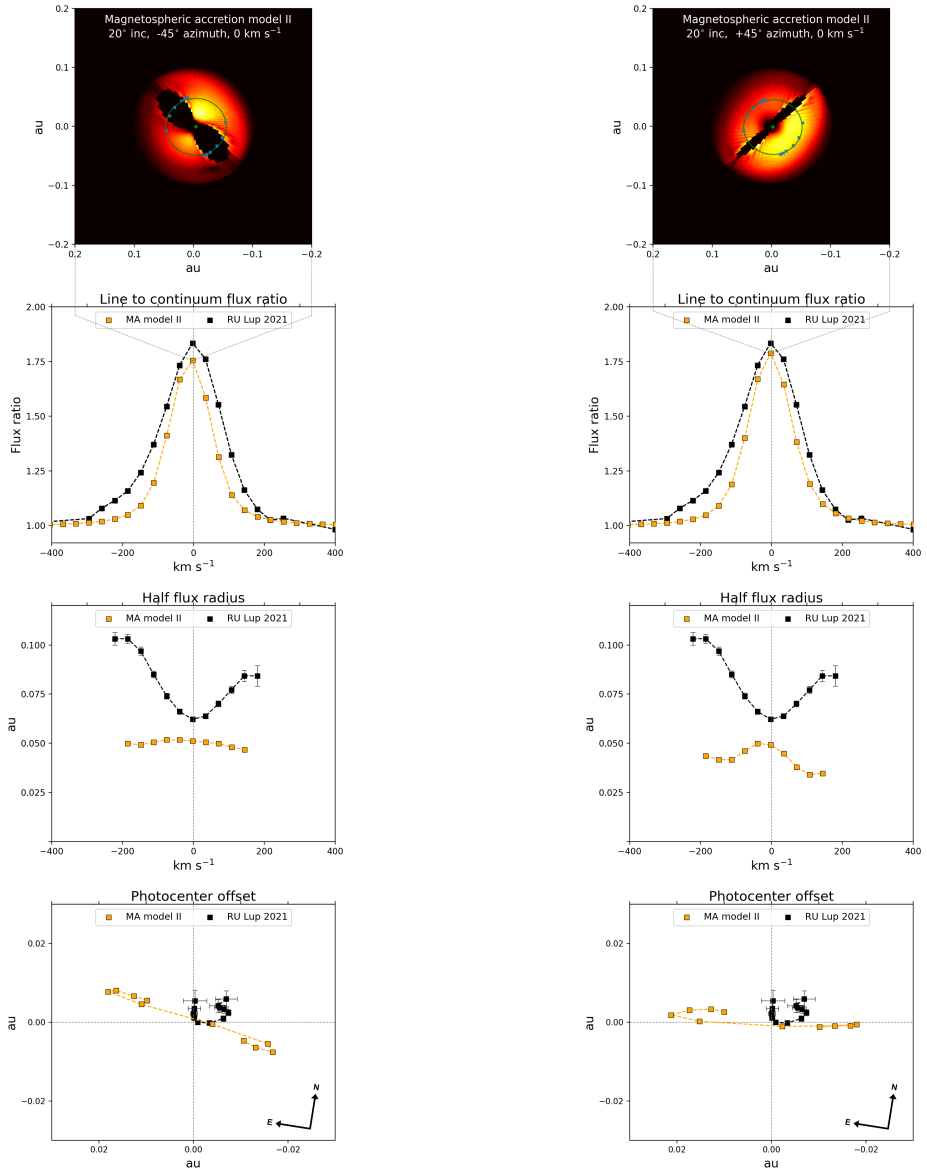

Figure 8.3.: **Left, from top to bottom:** Center channel image, line-to-continuum flux ratio, characteristic size and photocenter shift per velocity channel of the Brγ emission region of the **non-axisymmetric magnetospheric accretion** model with an obliquity of 30°, viewed at an azimuth angle of -45°. The ellipse depicted in the image signifies the half flux radius of the geometric Gaussian disk model used to derive the characteristic size. **Right:** The same model, viewed at an azimuth angle of +45 °.
In this depiction the stellar rotational axis, not the North axis, is aligned with the vertical coordinate axis. The observational photocenters were rotated by -9° with respect to Fig. 8.1 to put them in the same frame of reference.

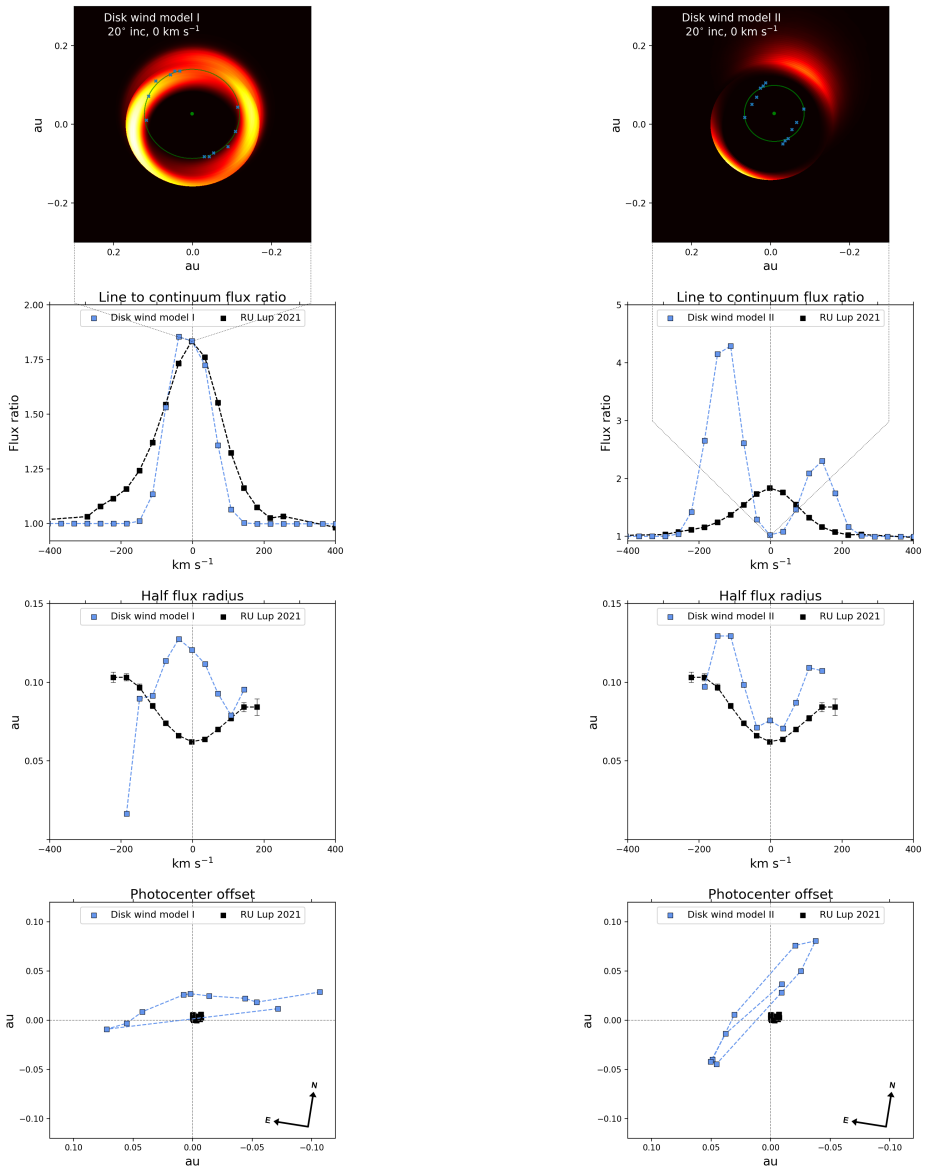

Figure 8.4.: **Left, from top to bottom:** Center channel image, line-to-continuum flux ratio, characteristic size and photocenter shift per velocity channel of the Brγ emission region of the centrally peaked disk wind model (DW I). The ellipse depicted in the image signifies the half flux radius of the geometric Gaussian disk model used to derive the characteristic size. **Right:** The corresponding observables for the double peaked disk wind model (DW II).
In this depiction the stellar rotational axis, not the North axis, is aligned with the vertical coordinate axis. The observational photocenters were rotated by -9° with respect to Fig. 8.1 to put them in the same frame of reference.

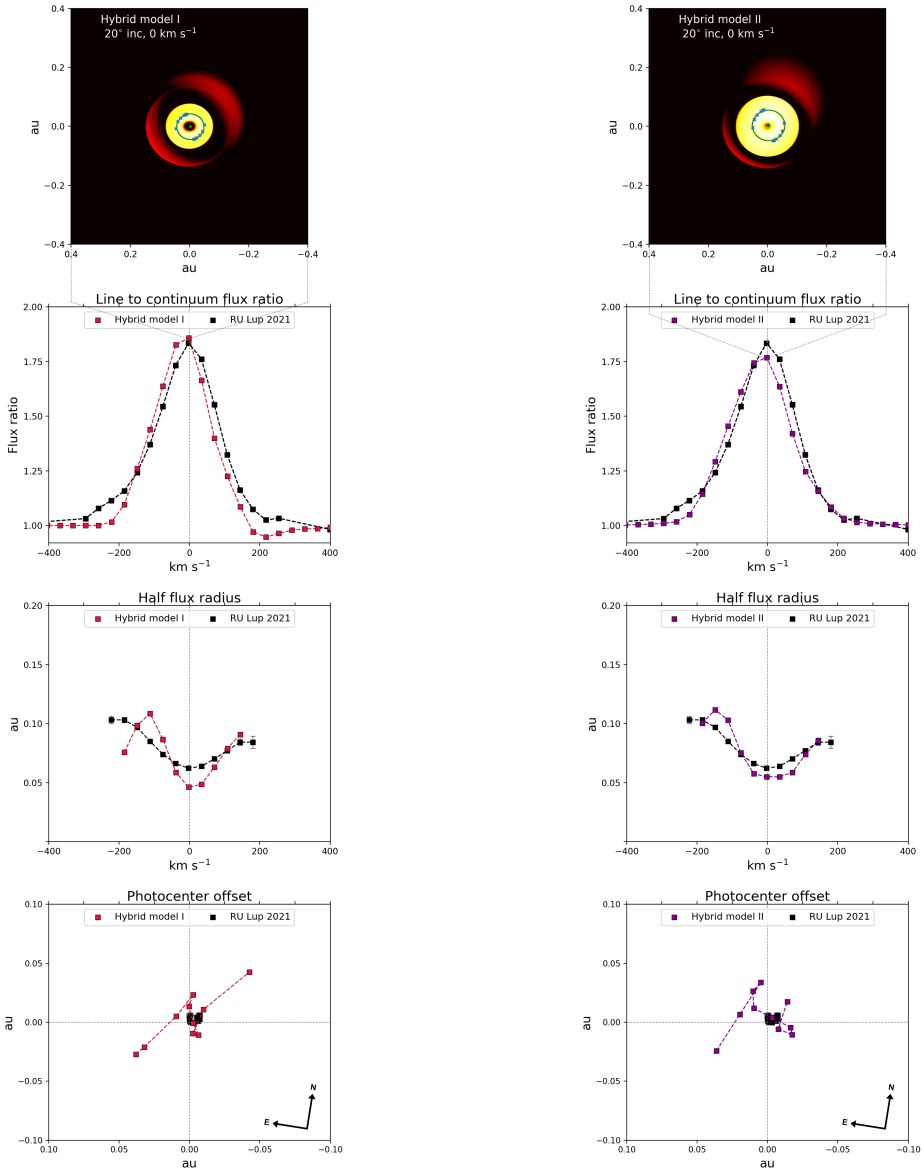

Figure 8.5.: **Left, from top to bottom:** Center channel image, line-to-continuum flux ratio, characteristic size and photocenter shift per velocity channel of the Brγ emission region of the first hybrid model, featuring a relatively cool and compact magnetosphere (HM I). The ellipse depicted in the image signifies the half flux radius of the geometric Gaussian disk model used to derive the characteristic size. **Right:** The corresponding observables for the second hybrid model, featuring a more extended and hotter magnetosphere (HM II).

In this depiction the stellar rotational axis, not the North axis, is aligned with the vertical coordinate axis. The observational photocenters were rotated by -9° with respect to Fig. 8.1 to put them in the same frame of reference.

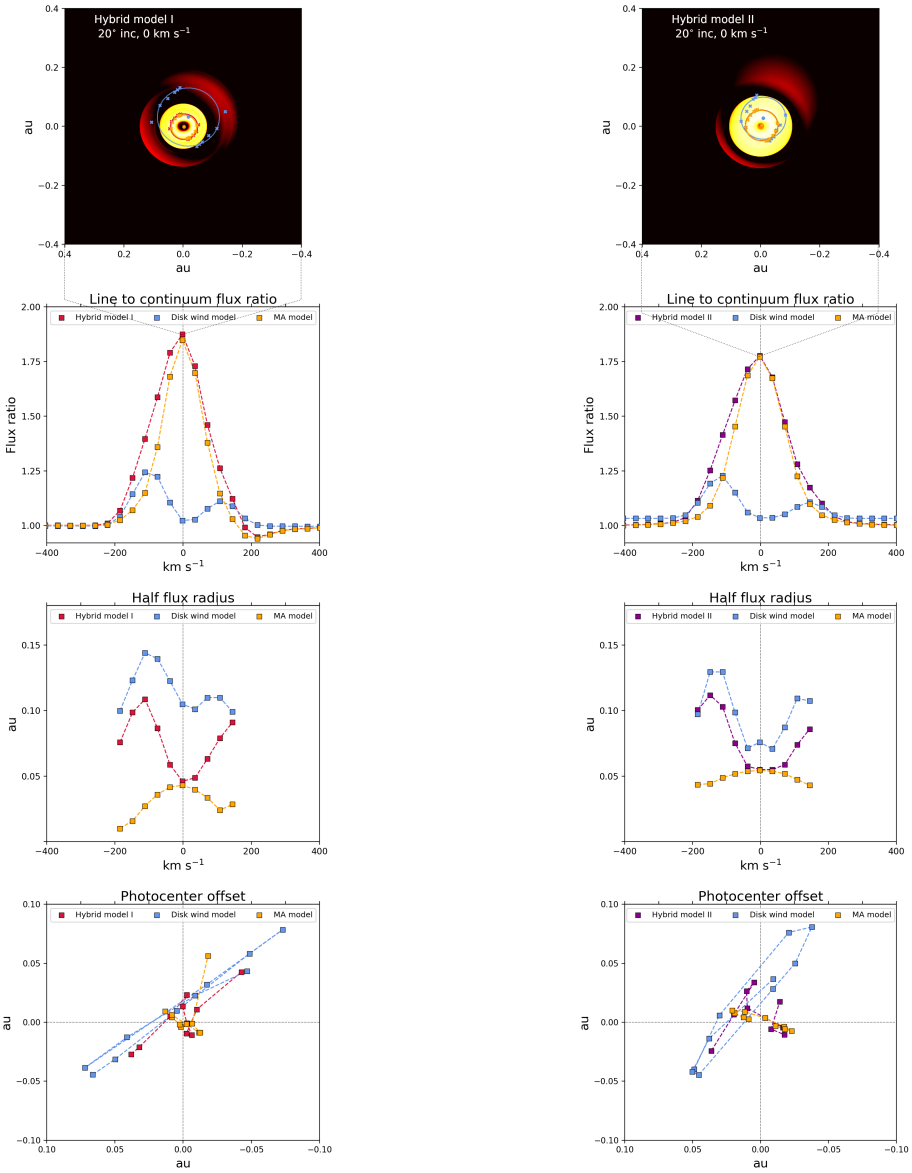

Figure 8.6.: Decomposition of the synthetic observables into their constituent model component profiles for the first **(left, HM I)** and second **(right, HM II)** hybrid model.
In this depiction the stellar rotational axis, not the North axis, is aligned with the vertical coordinate axis. The observational photocenters were rotated by -9° with respect to Fig. 8.1 to put them in the same frame of reference.

The size profile follows the centrally peaked shape of the Brγ line itself, although the central half flux radius of the model overestimates the observational data by again a factor of two (0.121 au compared to 0.061 au, respectively). The large drop in size in the bluest channel in this case is

a result of the low line flux at high velocities, which can threaten the integrity of the observable computation as the extraction of the pure line quantities requires division by a $(F_{L/C} - 1)$ term.

The jumps in the photocenter positions at the most extreme velocities are likely equally caused by this effect, although we note that even at the center channels, the shift magnitude is on the order of 0.025 au and thus almost three times as large as the most extreme observational offsets. At high velocities this discrepancy can grow to a factor of five, leaving the DW I profile profile much more extended than the observational profile.

The main purpose of the DW II model is to illustrate that the disk wind model can in principle reproduce the rising sizes at high velocities. The parameters of DW II were specifically selected to emulate the characteristic size profile of RU Lup as much as possible, which in this case comes at the expense of the line profile fit. The increase in size from a center channel half flux radius of 0.07 au to a maximum size of 0.13 in the blue wing requires the line profile to be double peaked, which does not agree with the observational data. Additionally, while the center channel sizes are close to the observational profile, those obtained in the wings of the profile are then larger by about 20%. The entire photocenter distribution is rotated by about 45° with respect to DW I, where the photocenters were mostly aligned parallel to the disk axis. Given that the shift magnitudes are comparable between both disk wind models, we find a similarly large disparity between model and observation for DW II as for DW I.

8.4.3. Scenario 3: Hybrid models

Finally, we introduce a pair of hybrid scenarios in which we combine the disk wind and magnetospheric accretion region into a single common model brightness distribution. While both models, which in Table 8.1 are referred to as HM I and HM II and which are depicted in Figures 8.5 and 8.6, differ in a number of parameters, we first and foremost distinguish between them primarily based on the co-rotation criterion. For the model HM I, which is characterised by a cooler and more compact magnetospheric configuration than HM II, the size, rotational period and stellar parameters were selected to allow the magnetosphere to be truncated within the co-rotation radius. For HM II, we disregard this requirement and attempt to achieve the best fit to the data regardless of whether the co-rotation criterion is respected.

For HM I we find a center channel flux ratio of 1.85 along with a FWHM of 180 km/s and a W10% of 340 km/s. Flux ratio and FWHM deviate from the observational results by less than 5%, although we see that W10% is still underestimated. However, visually the disparity in the line base can no longer be clearly attributed to the lack of blue excess emission, but is also caused by the presence of an inverse P Cygni feature in the red wing which we do not detected observationally. On the contrary, the line flux in the blue wing is reproduced well up to velocities of about -150 km/s before it diverges significantly from the RU Lup data.

The center channel characteristic size of 0.047 underestimates the observational result by less than 25%, while the model still reproduces the increase in size towards the edges of the line. In the red wing the observational result is well matched at 0.09 au, although in the blue wing we do note a drop in size below -150 km/s, which does not agree with the data.

The largest photocenter shifts at high velocities show a displacement magnitude of 0.045 au, which is still four times larger than the largest shifts observed for RU Lup. However, only the highest velocities show such a strong photocenter offset, whereas above -150 km/s the largest shift is already only about half as large (0.023 au). There is also a clearly visible change in the alignment of the profile at the same velocities. While the high velocity channels are aligned at an angle of about 45° relative to the disk axis, the remaining channels show photocenter offsets which are almost perfectly oriented along the stellar rotational axis.

The left column of Figure 8.6 depicts the decomposition of the three model observables of HM I into their the constituent components. In the blue wing the wind becomes the dominant contributor to the line flux below -150 km/s, whereas in the red wing the influence is more mixed, as the inverse P Cygni feature of the magnetosphere still appears clearly in the combined line profile. The decomposition of the interferometric quantities shows that the shape in the wings largely follows the wind, but the combined region characteristic size is adjusted downwards by the magnetospheric component. Equally, we see that the alignment of the photocenters at low velocities results from a superposition of differently aligned shift vectors between wind and magnetosphere. The high velocity channels follow the 45° alignment of the disk wind profile, although the magnetospheric influence again reduced the magnitude of the shift compared to the pure wind component.

For HM II, the center channel flux ratio and FWHM (1.77 and 209 km/s, respectively) fit the observation similarly well as they did for HM I, but the W10% is now increased to almost 400 km/s, which compares more favourably to the observational W10% of 420 km/s. The line shape lacks the P Cygni characteristic of HM I, which improves the fit in the red wing to give an almost perfect match to the data points at velocities above +150 km/s. The flux ratio in the blue wing remains close to the observational ratio down to to almost -200 km/s in this model.

The deviation in center channel size is reduced to about 7% and the sharp drop off in half flux radius at -150 km/s is much attenuated to provide an overall visually clearly improved fit to the data. In the photocenter shift profile of HM II, the largest offsets outside the extreme blue spectral channel are reduced in magnitude. In the red, the maximum offset is now 0.023 au, compared to the more than 0.06 au in the same channel of HM I. By contrast, the low velocity channels appear to feature photocenter shifts that are larger by up 20% in magnitude with respect to their corresponding offsets in HM I, and the axis of alignment does no longer coincide with the stellar rotational axis but is rather at a -45° degree angle relative to the disk axis.

From the decomposition of HM II shown in the right column of Fig. 8.6 we see that the magnetospheric component in itself lacks the P Cygni characteristic and that it produces a line that is about 25% broader when compared to HM I, while the relative contribution of the wind component is similar. The characteristic sizes of both wind and magnetospheric component are closer to the combined profile than before, and the dominance of the magnetosphere in the center channels is even greater as now up to three channel total characteristic sizes are almost fully defined by the magnetospheric component. This is again equally true for the low velocity channels of the photocenter shift profile, where the decomposition shows that the alignment of the total profile is also close to identical to the alignment of the magnetospheric photocenter offsets. A plot showing the mass density, temperature and velocity fields of HM II is included in Appendix B.1.

8.5. Discussion

In Section 8.4 we presented results for a total of six different model combinations, featuring two variants each of a pure magnetospheric accretion model, a pure parametric disk wind model, and a hybrid combination of both. The synthetic spectro-interferometric observables derived from these model images indicate that neither the magnetospheric accretion model nor the disk wind model are individually capable of reproducing the observational interferometric data obtained for RU Lup in 2021 with VLTI GRAVITY. While it is to some degree possible to approximate either the GRAVITY spectrum or the characteristic sizes of the emission region with specific components and parameter settings, a combination of wind and magnetosphere is ultimately required to reconcile model and observation. Both of the hybrid scenarios provide significantly better fits to the observational data and do not only reproduce the trends in principle, but come close to matching the normalised line flux and characteristic sizes.

In this section, we discuss the most relevant of these results. This includes general commentary as to the interpretation of certain model behaviours described in Section 8.4. We further explore to which degree the parameters chosen for these scenarios are plausible and in agreement with previously reported findings for RU Lup. Finally, we re-examine the case of the photocenter shift, which is not well reproduced by any of the model variants.

8.5.1. Non-axisymmetric magnetospheric accretion models

The axisymmetric magnetospheric configuration used for the MA I model is concept identical to the radiative transfer model presented in Gravity Collaboration et al. (2023b). The principal difference lies in the extent of the parameters space explored, which was strongly expanded upon during the course of this work. The resulting best fitting model MA I is hotter, with a maximum

funnel temperature of 8600 K, larger at an outer extent of 9 R_* and accretes more matter per unit time at $\dot{M}_{acc} = 23 \cdot 10^{-8}\ M_\odot\ \mathrm{yr}^{-1}$ compared to the original model at 7500 K, 4.57 R_* and $5 \cdot 10^{-8}\ M_\odot\ yr^{-1}$, respectively.

Considering the impact on the synthetic observables, we note that the line profile itself is affected most by the change in parameters. The higher magnetospheric temperature and the increase in density are responsible for an increased magnetospheric contribution to the total continuum emission in the system. In practical terms, this additional contribution effectively removes the inverse P Cygni absorption feature that we expect in the red wing of magnetospheric accretion lines at low inclination, and which for example is present in the magnetospheric component of HM I. Indeed, such an absorption feature was also present in the old model, even though observationally no clear inverse P Cygni dips were detected for RU Lup or any of the other sources investigated in Gravity Collaboration et al. (2023b). In conjunction with a generally broader line profile, this change improves the fit to the observational profile visibly. We discuss the physical plausibility of this magnetospheric continuum emission component again in Section 8.5.3 in the context of the hybrid models.

The trend in sizes across the line is essentially retained between the old model and MA I. For the old configuration we found a central characteristic size of 0.032 au, which is about 60% of the model radius of 4.57 R_* (0.053 au). A comparison to the corresponding result for MA I, where we found a characteristic size of about 50% the outer model radius (0.055 au half flux radius versus 0.11 au in R_{mo}), suggests that beyond the simple increase in size there is also a redistribution of flux across the emission region towards the center associated with the parameter change. We do not note any significant difference in shift magnitudes or angle alignments between the photocenter positions of MA I and the old model.

The introduction of the dipole tilt has a significant effect on the geometry of the Brγ brightness distribution, although the effective impact on the synthetic observables is tied strongly to its azimuth dependency. There is a qualitative change in the derived sizes across the line as we move from negative to positive azimuth angles (Fig. 8.3). This behaviour is caused by the interplay between the system inclination and the position of the two hemispheric accretion flows relative to the observer's line of sight. At -90° azimuth, the upper hemisphere accretion column is inclined away from the observer, while at +90° azimuth it is inclined toward the observer. The latter case seems to favour the centrally peaked size profile, while the former shows that the sizes remain more constant at different velocities. However, the reason why the characteristic sizes are slightly larger at negative azimuth is not easily deduced, as there is also the baseline configuration to consider. While for the axisymmetric models the orientation of the baselines has a negligible impact, the azimuth dependency can change how their configuration probes the two hemispheric columns.

On the other hand, due to the nature of the photocenter shift computation, the effect of the baseline orientation on the derived offset position remains negligible even in the non-axisymmetric case. The differently oriented photocenter profiles at different azimuth angles can in this case then be directly attributed to the variation in the brightness distribution. There is once again a principal distinction between positive and negative azimuth angles, as the former lead to photocenter shift distributions that are more preferentially aligned with the disk axis, whereas the latter retain essentially the same angle of about 30° relative to the disk axis that was observed in the axisymmetric model.

While there is no obvious mechanism at play here that would directly explain why these models are associated with these specific alignments, the detection of different photocenter alignments at different azimuths is in itself noteworthy. We observe a similar change in the orientation of the photocenter profiles between the 2018 and 2021 datasets. In addition, the observational size profile appears relatively more flat in 2018, whereas the 2021 data shows a stronger dip at low velocities (Fig. 8.1). The difference in center channel size between both epochs is on the order of 0.02 au, which is similar to the level of size variation we derive at different azimuth angles. We do note that this azimuth-dependent change in half flux radius primarily affects in the wings of the Brγ feature rather than the center.

Still, these azimuth-dependent effects may indicate that the two GRAVITY observations probe the RU Lup system at different points during its rotation. So while the switch to the non-axisymmetric dipole configuration does not resolve the fundamental limitations of the axisymmetric scenario with regards to fitting the RU Lup data, the inclusion of a tilted dipole offers one way to address the apparent time dependency of the observational results.

8.5.2. Disk wind models

The shortcomings of the pure wind models DW I and DW II are obvious, as they either fail to reproduce the behaviour of the characteristic sizes in the wings of the line or they produce a type of double peaked line profile inconsistent with the RU Lup data. The single peaked profile of DW 1 essentially replicates the fundamental characteristics of the magnetospheric accretion model. At the same time, it provides a worse fit to the data in terms of line width and especially photocenter shifts, thus offering no advantage over the magnetospheric accretion model. The double peaked configuration is more relevant, as it is the only type of low inclination model capable of matching trend of increasing sizes at high velocities. Indeed, DW II is identical in terms of model parameters to the disk wind component of the hybrid model HM II, where we successfully emulate the observational sizes in the wings by combining it with a hot magnetospheric central region. The line-to-continuum ratio depicted in Fig. 8.4 appears much larger than in the decomposition in Fig. 8.6 due to the lack of the magnetospheric continuum contribution, as will

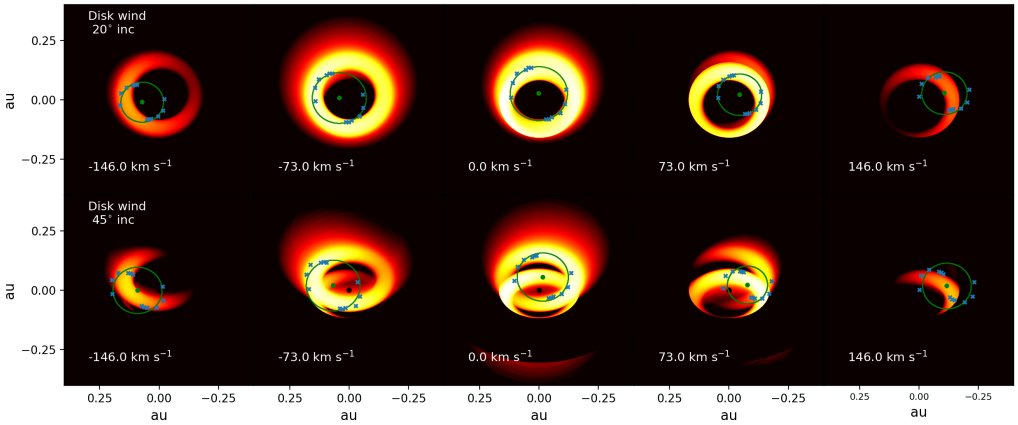

Figure 8.7.: Images of the disk wind model DW I at different velocities across the Brγ line and at 20° (top row) and 45°(bottom row) inclination. The green ellipses depict the HWHM of the Gaussian disk model used to derive the characteristic sizes of the emission region. The Gaussian model is fixed at 20° inclination in both cases to remain consistent with the treatment of the original GRAVITY data. It is centered on the photocenter of each image, as recovered from the differential phases. The blue points signify the HWHMs obtained for the individual six baselines of the GRAVITY UT configuration that was used to observe RU Lup in 2021.

be discussed in Section 8.5.3.

We remind that we consider the half flux radii obtained with the Gaussian disk model to be characteristic sizes first and foremost, and do not preoccupy ourselves with their exact relationship to the true physical size of the emission region for the purpose of this work. Still, it is worth pointing out for the sake of prudence that the disk wind model images essentially depict a ring-like region, which we fit with a disk-like geometric model. This may create a greater discrepancy between physical size of the region and characteristic size, especially in the wings of the line. Figure 8.7 shows the HWHM of the Gaussian disk as an ellipse around the photocenter, compared to the underlying emission region. Especially at higher velocities, the relationship between both becomes more abstract, which may be a result of the mismatch in model morphologies. While this is of no concern to the comparison with the GRAVTIY data due to the consistent approaches between model and observational data treatment, a geometric ring model may better serve to derive values closer to the spatial extent of the true wind region.

8.5.3. Physicality of the hybrid model parameters

It is immediately obvious from Fig. 8.5 that the hybrid approach is superior to any of the other models detailed in this work in terms of matching the observational data. It can both reproduce the general trends that we see in the observational line and characteristic size profiles, and even

in the case of HM II fit the observational data reasonably well, given the limitations of the semi-manual fitting approach described in Section 8.2. However, as the models are parametric in nature, there is a danger of enforcing a physically implausible parameter configuration in order to achieve a certain result. In this section we discuss the selected parameters in the context of the available literature on RU Lup.

While an examination of the physicality is difficult for parameters without explicit connection to quantifiable observables, there are those for which observational evidence or implicit constraints are more readily available. Chief among them are the stellar parameters, which are only partially shared between the hybrid models. For HM I and II the stellar mass was set to 1.2 M_* and 0.8 M_*, respectively, the stellar radii to 2.4 R_* and 2.5 R_*, and the stellar temperature to 4050 K. These masses are well within the broad range of possible values proposed by Alcalá et al. (2017). They estimate stellar mass and mass accretion rates from four different evolutionary models for pre-main sequence stars, thus yielding four different mass estimates between 0.43 M_* and 1.21 M_*. They also report a stellar radius of 2.39 ± 0.55 R_* and a photospheric temperature of 4060 ± 187 K.

The mass accretion rate for HM I was set to $10 \cdot 10^{-8}$ $M_\odot\ yr^{-1}$ and for HM II to $23 \cdot 10^{-8}$ $M_\odot\ yr^{-1}$. This agrees with our own estimates of the accretion rate for RU Lup based on the GRAVITY Brγ data. In Gravity Collaboration et al. (2023b) we used the empirical accretion luminosity to line luminosity relationship given by Alcalá et al. (2014) to determine $M_{acc} = 13.38^{+15.79}_{-6.66} \cdot 10^{-8}$ $M_\odot\ yr^{-1}$ for the 2021 data and $17.31^{+20.78}_{-8.54} \cdot 10^{-8}$ $M_\odot\ yr^{-1}$ for the 2018 data of RU Lup. The highest estimate available in the literature was found by Siwak et al. (2016) at $30 \cdot 10^{-8}$ $M_\odot\ yr^{-1}$.

Since the magnetospheric accretion model does not treat the gas temperature in the funnel flows self-consistently, one needs to be cautious to choose a maximum accretion flow temperature consistent with observations. Hard limits to the chosen combination of accretion rate and temperature can be easily enough determined by looking at extreme cases. At either very low mass accretion rates or temperatures ($\leq$ 6000 K, $\leq 10^{-9}$ $M_\odot\ yr^{-1}$) barely any Brγ emission is produced and the image is almost completely continuum dominated. Increasing temperature and accretion rate simultaneously will lead to veiling effects as the gas starts emitting in the continuum and becomes increasingly optically thick. This behaviour was already observed in the magnetospheric accretion study of Muzerolle et al. (2001). They found that, for all the investigated hydrogen transitions, a critical threshold was reached at temperatures $\geq$ 10000 K and accretion rates of $\geq 10^{-6}$ $M_\odot\ yr^{-1}$, at which point the emission line is turned into an absorption feature. At lower densities however, the gas never becomes sufficiently optically thick for this effect to occur. In their work they derive optimal ranges of mass accretion rates and temperatures for T Tauri stars from the continuum luminosity and the Paβ/Brγ line ratios. For our hybrid mod-

els, we paired the mass accretion rate of HM I ($\log(M_{acc})$=-7) with a maximum magnetospheric temperature of 7100 K and the accretion rate of HM II ($\log(M_{acc})$=-6.6) with a temperature of 8600 K. According to Fig. 16 in Muzerolle et al. (2001), the excluded temperature ranges for $\log(M_{acc}$=-7) are given as below 6500 K and above 10000 K, and for $\log(M_{acc}$=-6.6 below 6000 K and above 9500 K. Our chosen accretion and temperature parameters for both hybrid models lie well within this range.

Fang et al. (2018) showed for a population of T Tauri YSOs, RU Lup among them, that $\dot{M}_{wind}/\dot{M}_{acc}$ ratios can be on the order of slightly above 1, depending on the gas temperature, with a median ratio of 0.1 derived from a number of atomic emission lines for their sample. This is similar to the findings of Watson et al. (2016) and is consistent with the global mass loss rate we set for the hybrid models, where we use $\dot{M}_{loss}$=$\dot{M}_{acc}$ for HM I and $\dot{M}_{loss} \approx 0.5\ \dot{M}_{acc}$ for HM II. However, these values are derived for the low velocity component of the outflows, with velocities on the order of a few tens of km/s. For the high velocity component, which is more in line with the velocities we require for our wind components, Fang et al. (2018) presents maximum ratios is indeed on the order of 0.1 or less. This would suggest that our wind component is significantly stronger than what has been observed in these studies. We also note that the high $\dot{M}_{wind}/\dot{M}_{acc}$ ratios found for the low velocity component are based on more extended wind regions than the ones used in our models.

It may be useful to discuss the dark disk radius, which in both hybrid models is set to 13 R_*, in the context of gas and dust in in the innermost parts of the disk. Historically, the simplified view of inner disk opacities assumes that the close environment of a young star is divided into an inner optically thin purely gaseous disk and an outer optically thick dusty region, divided by the sublimation radius (Natta et al., 2001). Although some studies propose that the opacities of the gaseous cavity inwards of the sublimation radius behave in a more complex manner than this image suggests (see e.g. Muzerolle et al. (2004)), the gaseous inner disk is only likely to become optically thick if the accretion rate is sufficiently large. If we, in first order, assume that in our case the midplane within the inner cavity is close to transparent to Brγ radiation, then the change in opacity would be predominantly connected to the presence of dust. In Gravity Collaboration et al. (2021b), the K band continuum emission was traced to a region with a half flux radius of $0.21^{+0.07}_{-0.05}$ au using a geometric Gaussian ring model. The general assumption is that this region is a proxy for the hot inner dust wall, which is thought to dominate the disk continuum emission at NIR K-band wavelengths. In the same publication, we compared the K-band size to a sublimation radius derived from a simple model of dust absorption and emission (Monnier and Millan-Gabet, 2002), and this way found a smaller value of 0.05 to 0.1 au. At a dark disk radius of 13 R_* (0.15 au), the disk in the hybrid models becomes transparent just in between these two regions.

We set the rotation period in HM I to 9.05 days and in HM II to 7 days, which is consistent with known general distributions of rotational periods in low mass YSOs. These can range up to about 10 days, as was shown in a number of studies based on the data from the Kepler space telescope (e.g. Rebull et al. (2020)). However, for the specific case of RU Lup, the rotational period has been estimated to be on the lower end of this dispersion. Stempels et al. (2007) investigated the periodicity of radial velocity variations for this object and derived a stellar period of 3.71 days, consistent with earlier photometric periodicity studies, e.g. by Hoffmeister (1965) and Drissen et al. (1989). Frasca et al. (2017) used the VLT X-Shooter spectrograph to determine the v sin(i) of RU Lup to be 8.5 km/s, which translates to a stellar period of 5.1 days when using the inclination fitted from the GRAVITY NIR continuum data (20^{+6}_{-8} degrees, see Gravity Collaboration et al. (2023b)). Even using the highest deviation of 26 degrees within the stated 1σ range will only yield a rotational period of 6.5 days in this case. It is not clear why our best fit models point to stellar periods that are significantly slower than known observational results, but the question of the model stellar period is ultimately also tied to the size of the magnetosphere, and thus to the accretion regime of RU Lup.

8.5.4. The accretion regime of RU Lup

The fundamental distinction between the two hybrid models HM I and HM II lies with how they treat the co-rotation criterion. HM I represents a parameter combination that fully respects the criterion. The sizes, stellar parameters and rotational period were selected so that $R_{mo} < R_{co}$. The magnetosphere is then truncated on the order of the co-rotation radius R_{co}, which is consistent with the idea of stable magnetospheric accretion. In numerical MHD simulations, a further distinction arises between the regimes of stable ($0.7\ R_{co} \leq R_{mo} \leq R_{co}$) and unstable ($R_{mo} < 0.7\ R_{co}$) accretion (Romanova and Owocki, 2015). If the magnetospheric truncation is more compact, then the disk can penetrate into the magnetosphere and the gas is accreted from close to the star along a set of spontaneously forming accretion tongues. Additionally, for $R_{mo} > R_{co}$, angular momentum considerations dictate that the accreting matter would be at least partially ejected at the disk-magnetosphere interface and thus lead to less steady, more time-variable accretion (Blinova et al., 2016). This is referred to as the "propeller regime".

For HM II, we decided to relax the co-rotation criterion and set the truncation radius and the stellar period independently to obtain the best possible fit to the GRAVITY data. The chosen truncation radius of 7+2 R_* compares to a co-rotation radius of 5.72 R_* at the selected $P_{rot} = 7$ days. In Romanova and Owocki (2015), a "fastness parameter" $w_s = \left(\frac{R_{mi}}{R_{co}}\right)^{(3/2)}$ is used to distinguish between different accretion regimes, and also between strong and weak propellers. They define a system in a weak propeller regime as one where $w_s \approx 1$, while a w_s at multiples of 1 indicates a strong propeller with ejection exceeding the remaining accretion. Our configuration

of HM II translates into a fastness parameter of 1.35, which would indicate that - if we straightforwardly apply these concepts to our analytical model - it still exists in the regime of a weak propeller. HM II could then still be consistent with a system that is principally in accretion, even if some material is ejected at the magnetospheric boundary.

However, this would contradict the idea that RU Lup is in a regime of unstable accretion, as was proposed by Siwak et al. (2016). Their examination of RU Lup photometric data from MOST observations taken in 2012 and 2013 show highly irregular light curves for this object. Based on this lack of a clear periodicity in the brightness variability, they argue that the chaotic behaviour is the result of a randomised distribution of temporary accretion hot spots on the stellar surface caused by the unstable accretion tongues. This is in agreement with the theoretical predictions of unstable accretion light curves from numerical simulations (Romanova et al., 2008b), and indeed this regime of unstable accretion is associated predominantly with higher accretion rates such as found for RU Lup. It is not clear whether the remaining accretion in a system in the propeller regime might produce a similar effect.

Another question as to whether the analytical stable accretion model yields plausible physical characteristics involves the magnetic field. While we do not set a magnetic field strength explicitly, the chosen stellar parameters, mass accretion rate and truncation radius can be implicitly related to a magnetic dipole field strength. Using the formulation in Hartmann et al. (2016), we can determine the field strength in kG via

$$B_{kG} = \left(\frac{R_{tr} M_{0.5}^{(1/7)} \dot{M}_{-8}^{(2/7)}}{18 \gamma R_2^{(12/7)}} \right)^{(7/4)} , \tag{8.1}$$

where $M_{0.5}$ is the stellar mass in units of 0.5 $M_\odot$, $\dot{M}_{-8}$ the mass accretion rate in units of 10^{-8} $M_\odot$ yr^{-1}, R_2 the stellar radius in units of 2 $R_\odot$, and γ is an uncertain factor ≤ 1. Assuming the most favourable case with $\gamma = 1$, and using the inner magnetospheric radius as truncation radius (i.e. 6 R_* for HM I and 7 R_* for HM II), the field strength for HM I comes out to 1.5 kG, whereas for HM II we compute a 2.6 kG dipole field. Although there are no published measurements of the RU Lup field in the literature, a default assumption for the magnetic fields of T Tauris stars is a range of about 1 to 2 kG, so the implicit field strength of the HM II configuration would be atypically large. We do note, however, that this formula is approximate and based on simplifications of the mechanics involved. If indeed the accretion process in RU Lup is complex beyond the case of simple stable magnetospheric accretion, as the previous considerations imply, then these magnetic field values should not be adopted without question.

The question of the RU Lup accretion regime is ultimately not easily answered. The stable analytical accretion model is also only an approximation of a more complex truth, and the fact that some of the parameters we derive from it are not immediately consistent with other observations is not unexpected. Another example for a potential additional effect that is not considered at all

outside certain numerical simulations is the idea of a failed disk wind, meaning a wind that is launched close the disk-magntosphere interface, but which fails to escape the gravitational field of the star. Instead, the wind material falls back onto the magnetosphere and is accreted onto the star, effectively enlarging the magnetospheric emission region and masking a more compact actual magnetosphere in the process (Takasao et al., 2022)).

A different and more technical potential explanation for the size of the best fitting magnetosphere may lie with the treatment of the observational data rather than with the models themselves. Unlike the continuum data in Gravity Collaboration et al. (2021b), the visibility modelling of the Brγ line emission data did not consider the effects of a large scale halo component that might account for a significant part of the line flux. Such a halo component, which may for example reflect the influence of Brγ photons scattered on the disk surface, was omitted from the treatment as the primary intent behind Gravity Collaboration et al. (2023b) was to compare general trends among a number of objects for a simple geometric approach. Including a halo would effectively reduce the derived characteristic size for the resolved emission region compared to the results presented in Fig. 8.1. Whether this effect could be sufficiently strong to reduce the observational characteristic sizes to a point where we may be able to fit them similarly well as we did with HM II, without exceeding the co-rotation radius, is at this point entirely speculative and would depend on a number of other factors. Still, it may be a point worth considering for future investigations into similar questions.

8.5.5. The photocentre shift problem and the possible role of other emission components

One of the primary issues of the model analysis in Gravity Collaboration et al. (2023b) was that the synthetic photocenter positions obtained from the images were offset by a factor four to five when compared to the GRAVITY photocenter shifts. Neither the consideration of a dipole tilt, nor the introduction of an additional wind component, have done much to resolve this issue. On the contrary, the photocenter profile associated with the disk wind shows even substantially larger photocenter shifts than the magnetosphere. As a consequence, the hybrid photocenter profiles become even more elongated, as shown via the decomposition in Fig. 8.6.

The divergence between the observational and synthetic profiles is potentially rooted in some aspect of the observed system that is not reflected in the models, such as the presence of an additional Brγ emission component. Such a component could, for example, come in the form of a hot MHD stellar wind, launched along the open magnetic field lines from the polar regions of the star (Ferreira et al., 2006). However, it is not clear whether such a stellar wind would even address the issue of the photocenters in principle, let alone be consistent overall with the GRAVITY data. In a low inclination system such as RU Lup, a collimated outflow, launched

from the stellar pole, almost directly along the line of sight would be expected to cause significant blueshifted absorption, whereas GRAVITY on the contrary picked up blueshifted excess emission in the Brγ spectrum. Given that the redshifted stellar wind component is also likely to be at least partially blocked by the star itself at this inclination, there should be a substantial difference in both characteristic size and photocenter shift profiles between the red and the blue arm. It is equally not clear whether such a collimated wind could simultaneously reproduce the increase in size in the wings and the more compact distribution of photocenters.

Any component that may help to resolve the question of the overestimated photocenter shifts fundamentally needs to lead to a decrease in offset magnitudes without an accompanying reduction in characteristic size. This would be achieved by a system that remains relatively centrosymmetric across the line at scales even on the order of below the truncation radius, but then features asymmetries in the extreme close environment of the star. A disk like structure with weak or no rotation, viewed at low inclination, may provide the necessary degree of centrosymmetry across the line, but lacks the asymmetric elements. In this context we could consider again the possibility that RU Lup may be in the regime of unstable accretion. If the gaseous matter penetrating the magnetosphere behaved essentially as such a disk, then the formation of accretion tongues very close to the star could introduce the necessary asymmetry that would lead to offsets in the photocenter positions. Answering this question would require some dedicated modelling, as without knowledge of the relative Brγ flux between the tongues and the remaining emission region, it is difficult to comment on whether this would be a viable solution. This is also true for the introduction of a halo component, which is another possible way to address this question. The halo may have a in principle similar compressing effect on the photocenter shifts, assuming that it itself is largely centrosymmetric. Whether this effect could be sufficiently large to explain the degree of divergence we detect between model and observation is again a question of the flux ratios between halo and resolved region. Still, as of now, these ideas may hold the most promise to resolve the issue of the photocenter shifts.

8.6. Summary: Combined accretion-ejection models for RU Lup

We computed the spectro-interferometric characteristics of six models of the Brγ line emission region in the innermost environment of low mass young stars. These models featured different configurations of emission components in the form of disk wind outflows and magnetospheric accretion. From the synthetic model data, which included the normalised line-to-continuum flux ratio, the interferometric visibilities, and the differential phases, we determined characteristic sizes and the position of the emission region photocentres for ten spectral channels across the Brγ line. We then compared these synthetic quantities to observational results derived from

VLTI GRAVITY data for the classical T Tauri star RU Lup.

Our goal was to explain a number of features in the observational data that were not well reproduced by previous modelling efforts presented in Gravity Collaboration et al. (2023b). Specifically, we tried to determine whether the addition of a larger scale outflow component onto an accreting magnetosphere would deliver results consistent with an asymmetric line profile with blueshifted excess emission, an increase in characteristic radii towards the high velocity wings of the line profile, and a compact distribution of photocentres across the line. To summarise the most important results of this paper:

- Both axisymmetric and non-axisymmetric magnetospheric accretion models produce either centrally peaked or flat characteristic size profiles across the line. No parameter configuration leads to a size increase at high velocities and a minimum size at the line centre, as observed for RU Lup. While it is possible to fit the central component of the Brγ line with a hot magnetosphere, the blueshifted excess emission that we detect observationally cannot be emulated.

- The variability in equivalent width, peak flux ratio, and photocentre shifts that we find between the 2018 and 2021 epochs of the observation is on the order of the variation that we detect when comparing the line profile of the non-axisymmetric magnetospheric accretion model at different azimuth angles. This could indicate that between 2018 and 2021 we are in observing a tilted dipole at different phases during the stellar rotational period.

- Only disk wind models with sufficiently fast winds to produce double peaked spectral features at the spectral resolution of GRAVITY are associated with an increase in emission region sizes at high velocities. We do not manage to reproduce both the centrally peaked line profile and the increase in the size profile simultaneously with a disk wind alone.

- Hybrid models, combining a strong magnetospheric component that dominates the central channels of the line and a fast double peaked wind component, can reproduce the trends in both line profile and sizes at the same time as parameters that appear mostly in agreement with previous observational findings on the physical characteristics of RU Lup. The magnitude of the model photocentre shifts overestimates the observational photocentre profile across all model variations by factor of four or more, including the hybrid models.

- Our best fitting hybrid model manages to well reproduce the 2021 Brγ spectral line and characteristic sizes across the line. Still, in that case, the truncation radius exceeds the co-rotation radius by more than 50%, meaning that part of the gas is found beyond the centrifugal barrier, where it is expected to be expelled and not accreted.

In conclusion, we find that the success of the hybrid approach to modelling the Brγ region strongly supports the idea of a multi-component emission environment for certain class II low mass YSOs with large mass accretion rates such as RU Lup. Discrepancies between the expected magnetospheric accretion characteristics and our best fitting parameters likely indicate that the accretion-ejection process in RU Lup is more complex than what is captured by our analytical models. Another explanation may lie in the potential effects of a possible unresolved Brγ halo component, which was not included in the treatment of the GRAVITY data in Gravity Collaboration et al. (2023b). Neglecting the halo when deriving the observational results would potentially lead to an overestimation of the size and underestimation of the photocentre shift magnitudes, depending on the flux ratio between resolved and unresolved region. If that is indeed the case, it may be possible to attain a similarly good fit to the remodelled data with a smaller magnetosphere that respects the co-rotation criterion.

9. Conclusions and outlook

The advent of optical long-baseline interferometry has brought with it an age of exciting discoveries across multiple fields of active astrophysical research, be it the study of young stars, exoplanets, or supermassive black holes. The latter has risen to particular prominence in recent years through the Nobel prize-winning work of Reinhard Genzel and others, which is intimately connected to the development of GRAVITY. Still, for all the technical advances that have allowed us ever closer looks into the smallest regions around distant stars, much of the methodology behind the analysis of interferometric data is still firmly rooted in the same concepts that have accompanied the technique for much of the past 30 years ore more. At the beginning of this project, my own perception was that infrared interferometry was predominantly the domain of size measurements, and that for all its great advantages, the limitations of the method appeared immovable. Sparse uv coverage with four (or less) telescope arrays necessitated the use of geometric modelling with all its potential pitfalls, and true image reconstruction was only realistically possible for a small number of objects due to the coordinated effort required to obtain enough data for a single target.

When I began my work on what would become the GRAVITY Brγ T Tauri survey, there was an apparent disconnect between the observational results and the physics potentially governing the Brγ emission region in these objects. The study seemed to rely strongly on a single parameter - the co-rotation radius - as the defining criterion to decide whether any one object in the sample would confirm the magnetospheric accretion scenario. At the time, I had no knowledge of the analytical model of magnetospheric accretion, and the technology to implement non-LTE radiative transfer atomic line simulations for accretion tracer lines was not widely available at all. Without these tools, the interpretation of the behaviour of the emission region across multiple velocity channels was challenging at best, especially when it came to the photocenter shift profiles. Most of my attempts to intuit what the distribution of the photocenter offsets could look like in a system of funnel flows turned out to be naive and quite detached from the results we would eventually obtain through RT simulations. However, that is not to disparage the traditional approach of interferometry. Even ignoring the introduction of the accretion model, the T Tauri survey in the end was able to achieve its goal and delivered important results concerning the relative scale of the emission regions between different accretion stages, as well as concerning the expected profiles of photocenter offsets in these objects. While, in absence of the model, it

was not clear what likely photocenter signature of magnetospheric accretion would be, the study showed that these types of objects at least exhibited profiles with high degrees of complexity, or no clear structure at all. The common presence of the blushifted "bump" in the emission spectrum was equally an important first indicator that the emission region might be composed of different potential emission sources.

Still, the adoption of the RT simulations clearly pushed the project ahead in tremendous ways and opened up possibilities that, up to this point, seemed out of reach. Through the use of the analytical models, it became possible to explore a direct link between physical characteristics of the emission region, and the interferometric results. For the first time, non-LTE radiative transfer simulations, a physical model of magnetospheric accretion, and the particular lens of interferometry were combined to derive a baseline in terms of interferometric observables that allow us to not just compare the central, but the complete spectrally dispersed data set. It is fair to say that only with the use of radiative transfer models did we actually make proper use of the high spectral resolution offered by GRAVITY. Not only were we able to show that indeed many of the observed profiles did not fit the pure magnetospheric accretion case, but also eventually to confirm that a spatially extended outflow in the form of a wind component may offer a possible answer to some of the questions posed by GRAVITY survey. While some confusion remains regarding the photocenter shifts, and the physicality of some of the parameters used to obtain this result, this should not detract from the fact that the simulation of combined accretion-ejection systems, as a next step in the synthesis between modelling and interferometric observations, was fundamentally successful as a proof-of-concept.

However, there are still a good number of ways in which this project could be advance even further. I will present a brief outlook on these possible paths forward here:

- Improvements to the computational method used by MCFOST: The deterministic ALI solver delivers the most accurate results of all the non-LTE algorithms, but at the expense of computational time. Given the very practical limitations imposed by hour long run times on the amount of models produced, it was not possible to fully automate the fitting procedure of models to data, and a substantial manual effort was required instead. If it were possible to cut down on the computation time to the point that a proper fitting routine could be implemented, it would dramatically improve the chances that the use of RT models could be extended to a large numer of different objects. One idea here would be to follow, in a sense, a hybrid approach concerning the non-LTE solution method: An automated MCMC fitting routine could possibly explore a much larger parameter space if MCFOST computed the line transfer using the Sobolev approximation. A successful minimisation routine of this kind could restrict the parameter space already to a small number of models, which are then recomputed using the more accurate deterministic ALI

method.

- An additional stellar wind model could be implemented in MCFOST. The impact of such a wind, either on its own or in addition to the disk wind, could then be explored in order to see if it offers a solution to the photocenter problem.

- The parametric model fitting could be applied to other sources from the GRAVITY T Tauri survey sample. It would be especially interesting to see if the observational results could be reproduced with the hybrid models even at higher inclination, in a scenario where the there is overlap along the line of sight between the two components.

- On the side of the data treatment, the visibility data could be re-valuated by including an overresolved halo component in the visibility model, just as was done in the continuum study on these objects. Such a halo could reflect the scattered light contribution of Brγ photons being scattered by the dusty disk.

- More objects could be added to the sample. While observations of Brγ line emission in T Tauris are difficult, the implementation of GRAVITY Plus with it's increased sensitivity and better AO system will unlock a whole new reservoir of additional observable sources. A larger sample is more suited to identify correlations between characteristics like accretion rate and size of the emission region, and may confirm the hypothesis that transitional systems are more likely to be dominated by magnetospheric accretion in their Brγ emission, while younger systems with higher accretion rates also exhibit stronger outflow components.

All of these ideas are well worth pursuing, and I encourage future scientists to make use of, and expand upon, the methodology presented in this thesis, as well as the capacity of MCFOST to compute the hydrogen line transfer regions for accretion-wind systems. The features that were implemented over the course of this work into MCFOST are now available as part of the public MCFOST package. It is clear to me that the synthesis of radiative transfer simulations and interferometry is the way forward to provide new and robust ways to interpret the spectacular data sets produced by top tier instruments as the VLTI, and to use them to their fullest extent. While this project has come to a satisfying and promising conclusion, I sincerly hope that it will prove to be only the beginning of these efforts.

A. T Tauri GRAVITY data

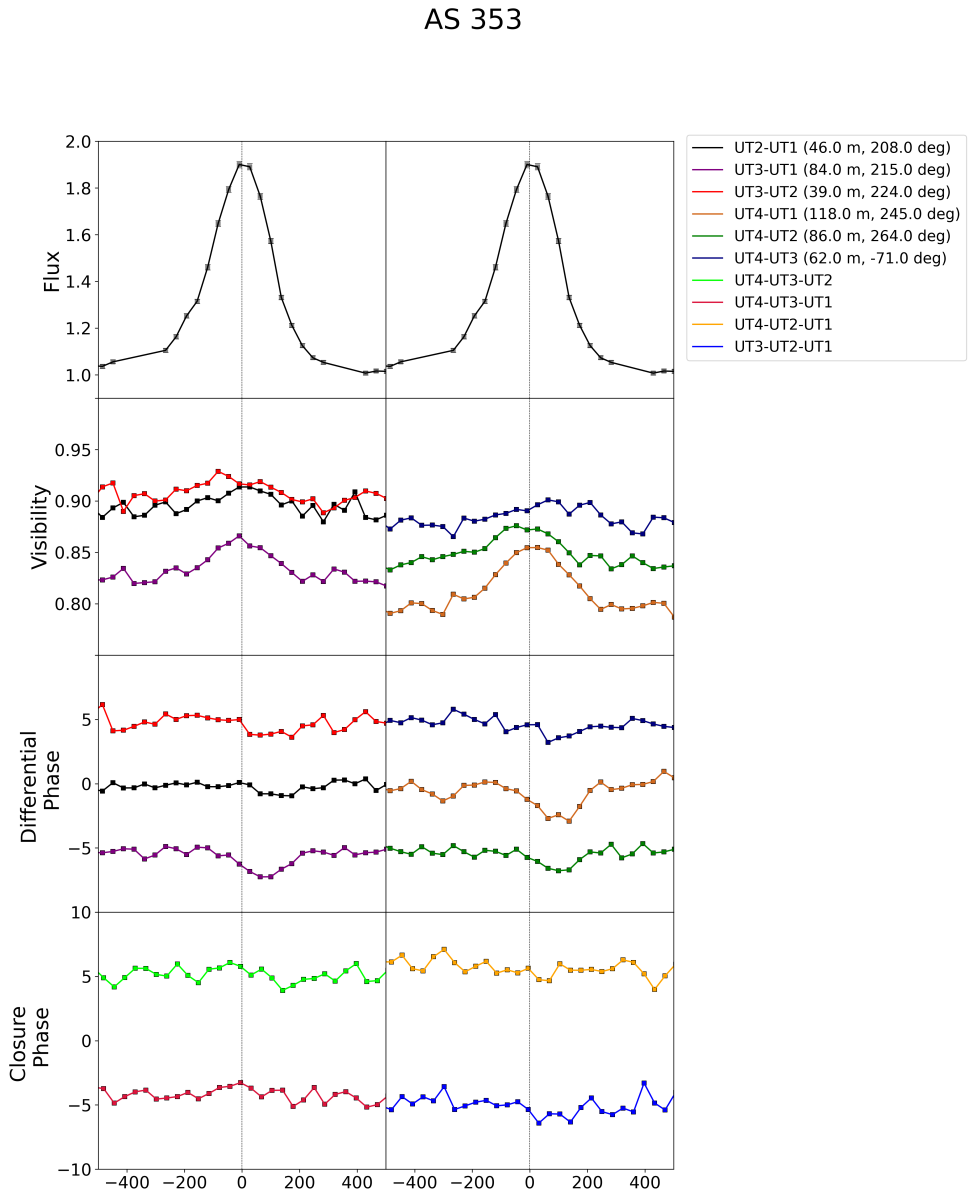

Figure A.1.: Observational data for AS 353. Differential phases and closure phases have been shifted by ±5 deg at certain baselines.

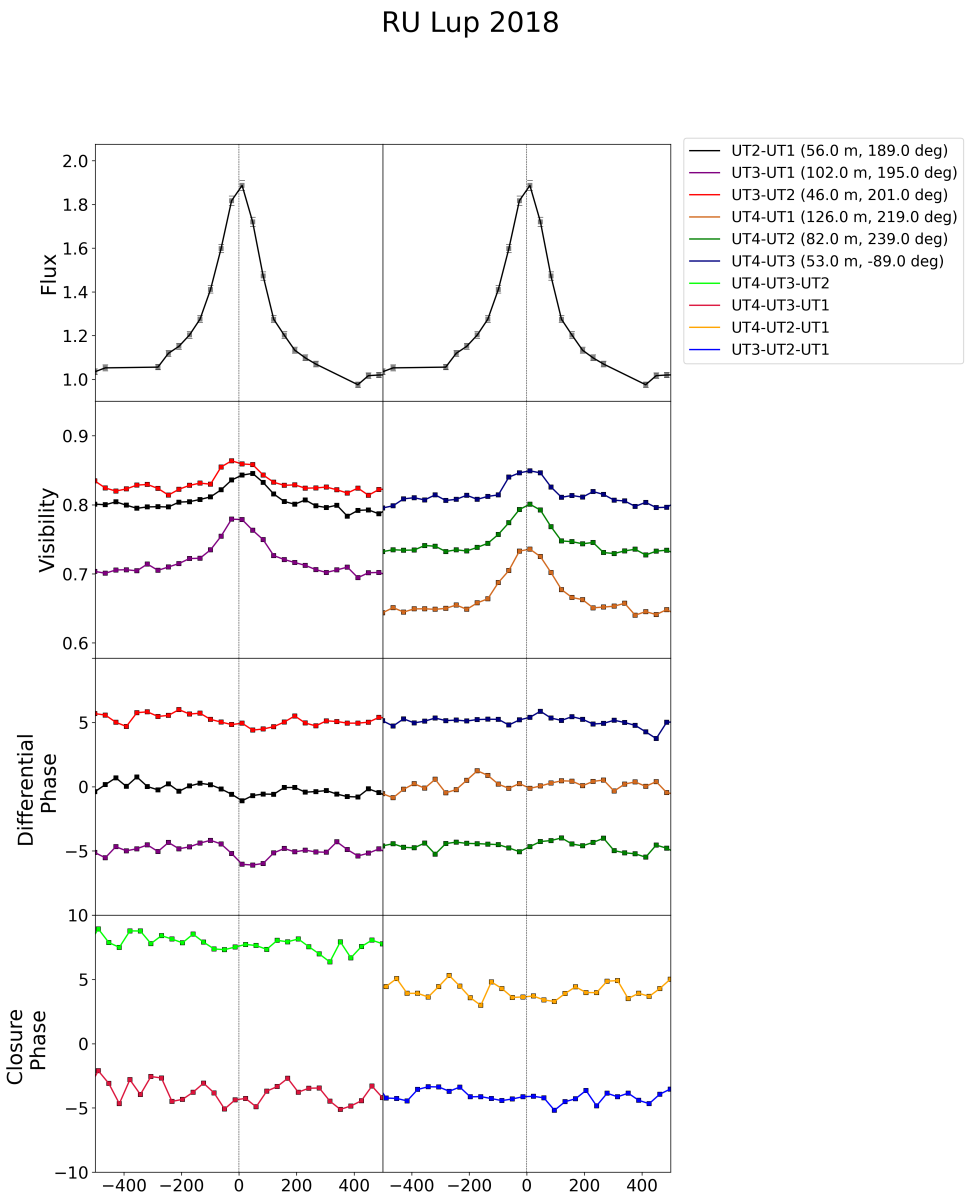

Figure A.2.: Observational data for RU Lup 2018. Differential phases and closure phases have been shifted by ±5 deg at certain baselines.

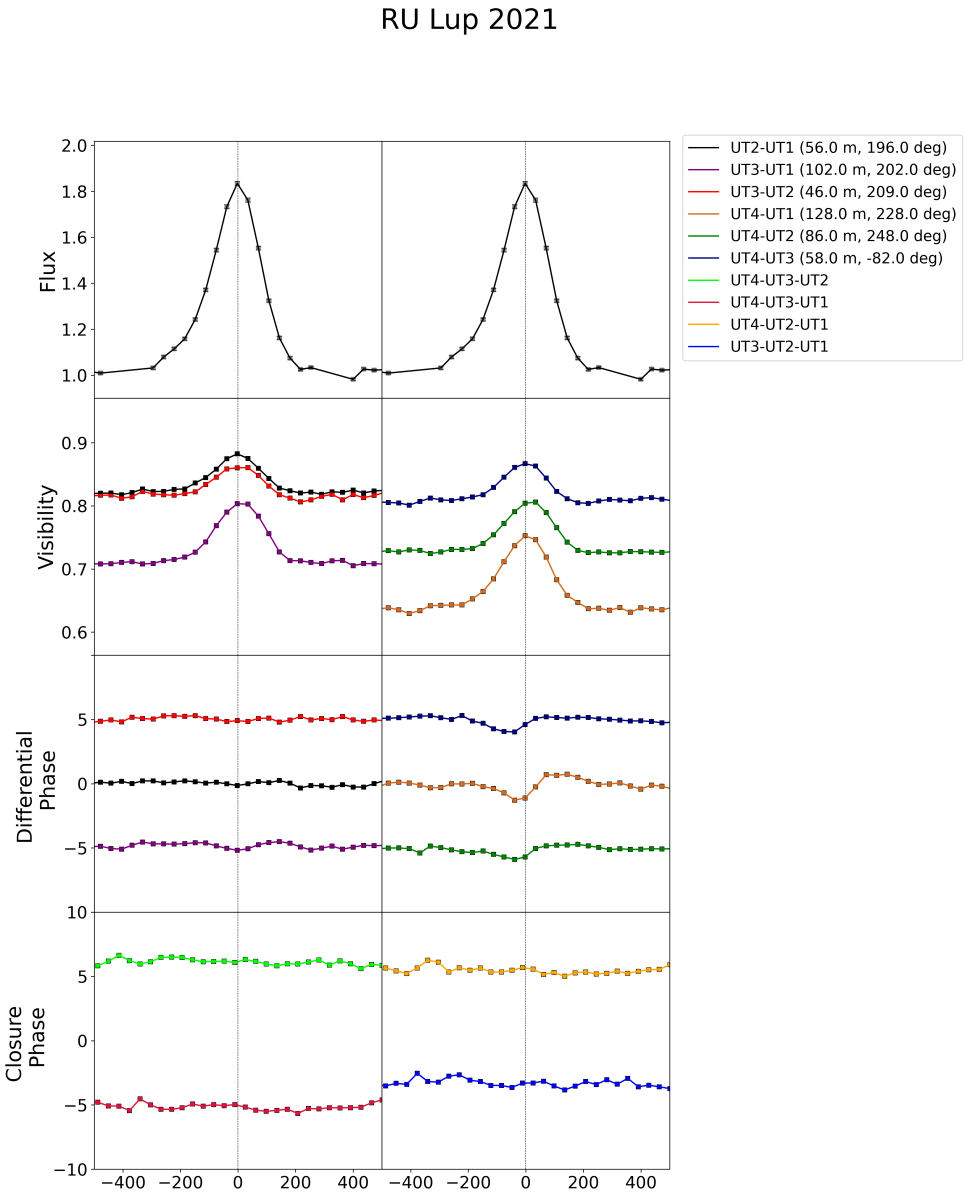

Figure A.3.: Observational data for RU Lup 2021. Differential phases and closure phases have been shifted by ±5 deg at certain baselines.

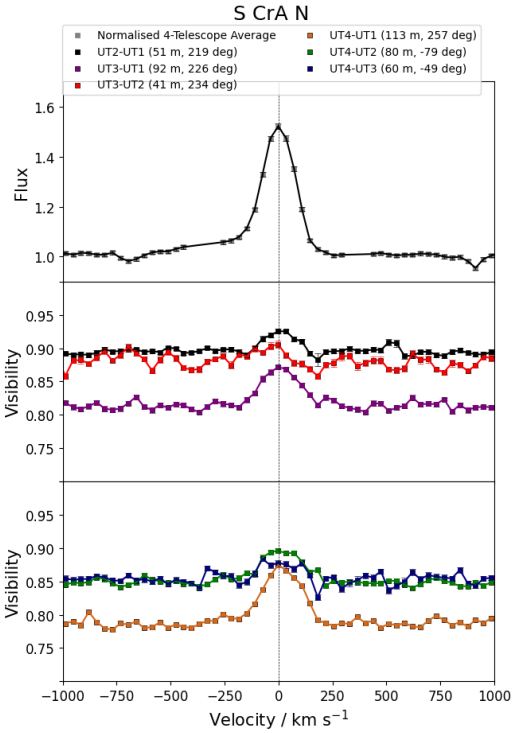

Figure A.4.: Observational data for S CrA. Differential phases and closure phases were omitted due to poor data quality.

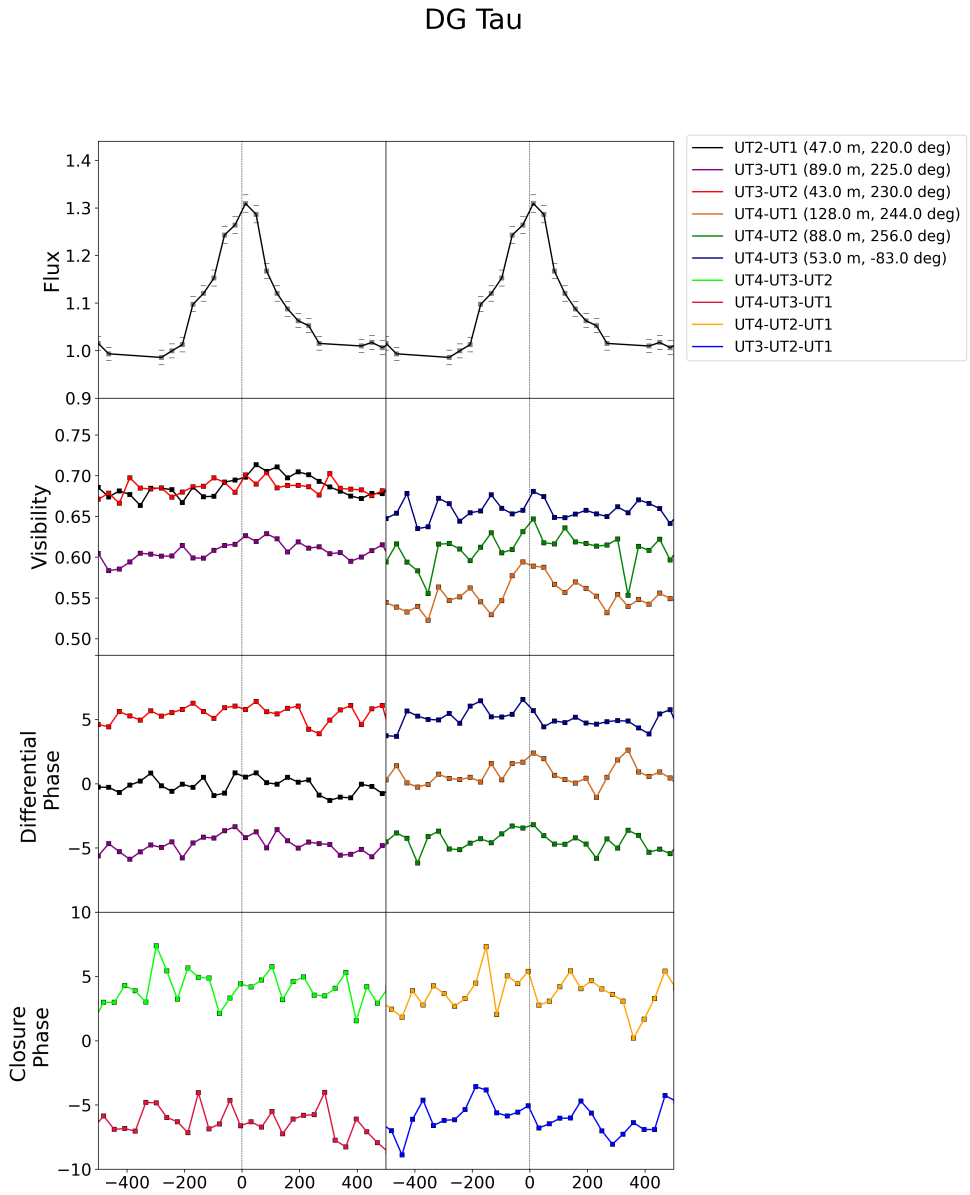

Figure A.5.: Observational data for DG Tau. Differential phases and closure phases have been shifted by ±5 deg at certain baselines.

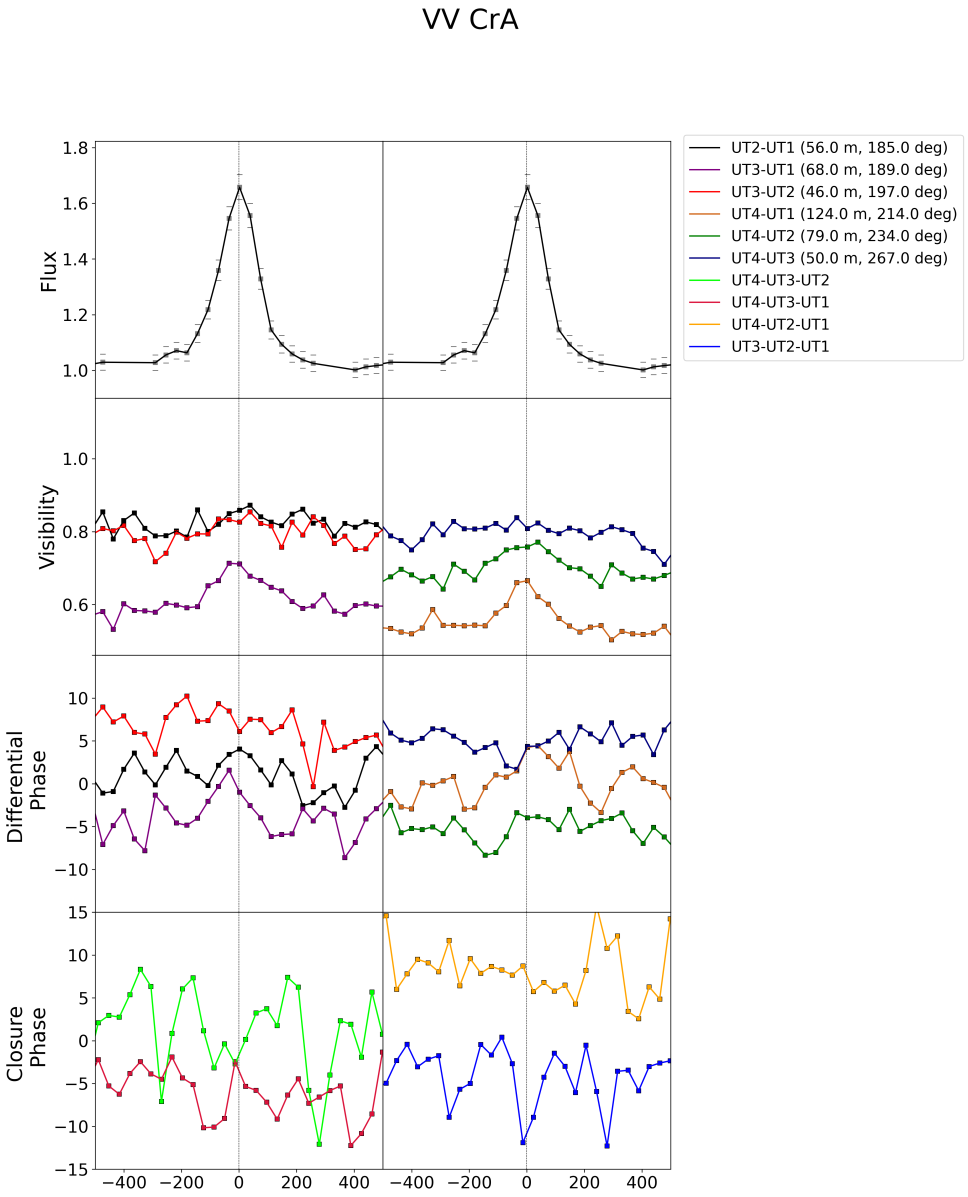

Figure A.6.: Observational data for VV CrA. Differential phases and closure phases have been shifted by ±5 deg at certain baselines.

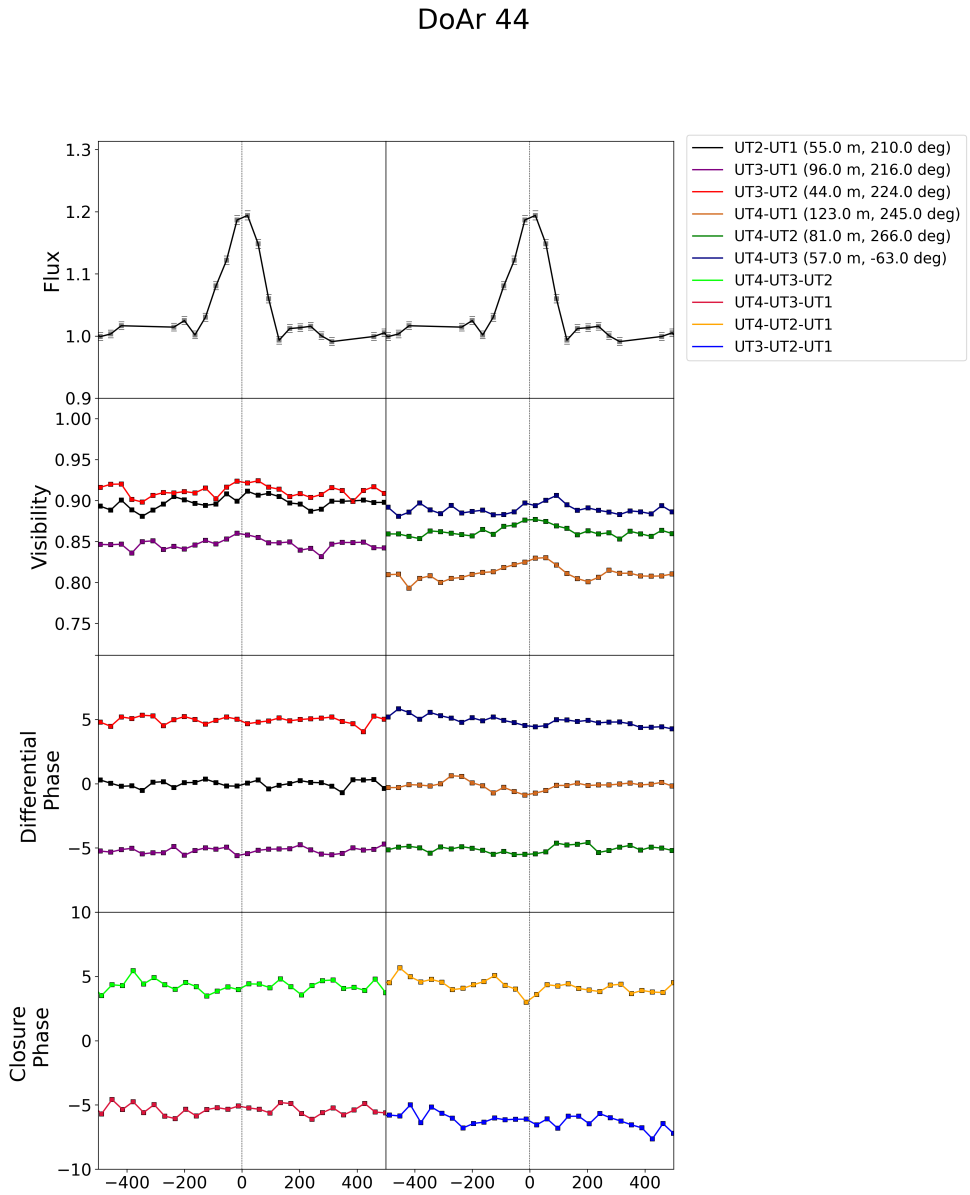

Figure A.7.: Observational data for DoAr44. Differential phases and closure phases have been shifted by ±5 deg at certain baselines.

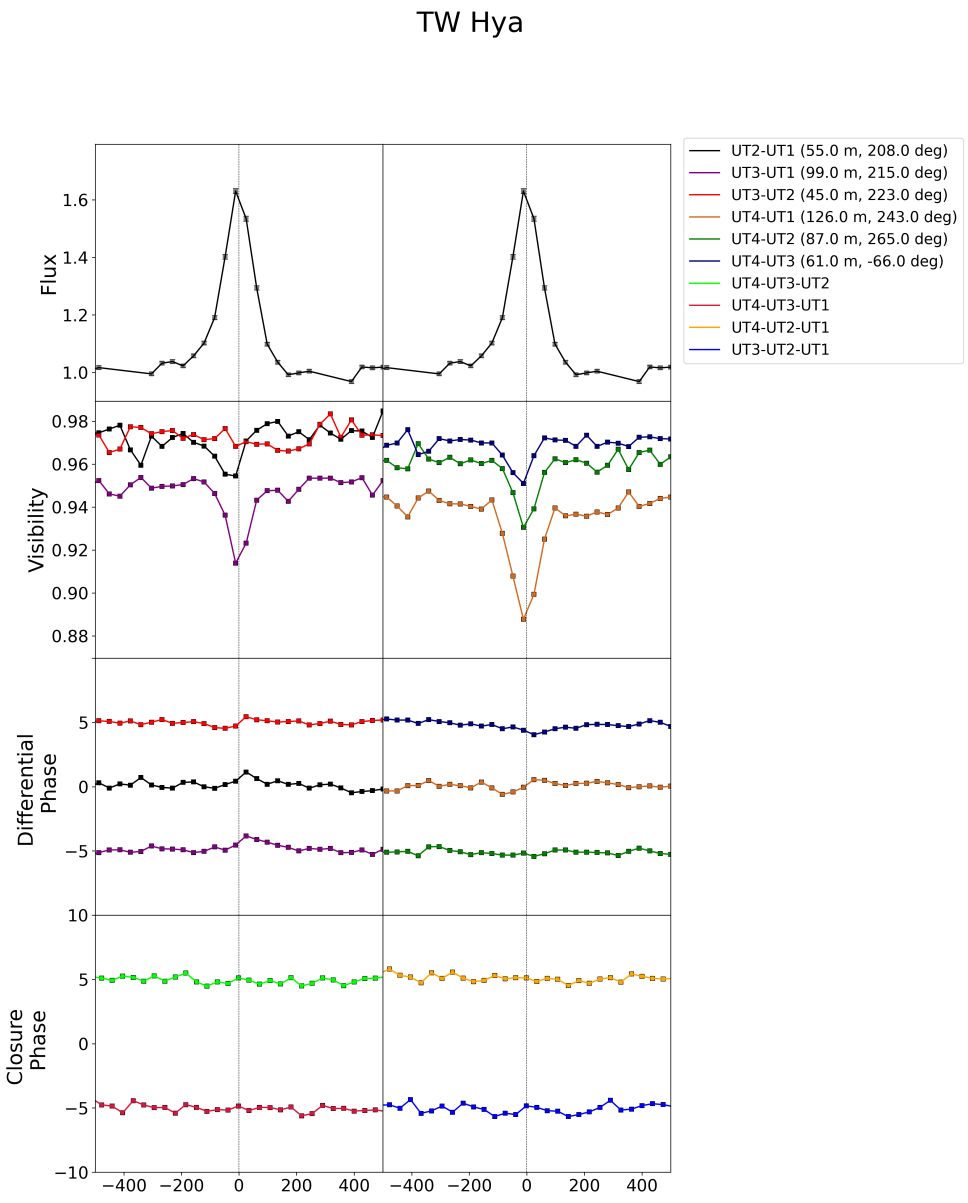

Figure A.8.: Observational data forTW Hya. Differential phases and closure phases have been shifted by ±5 deg at certain baselines.

B. Radiative transfer simulations

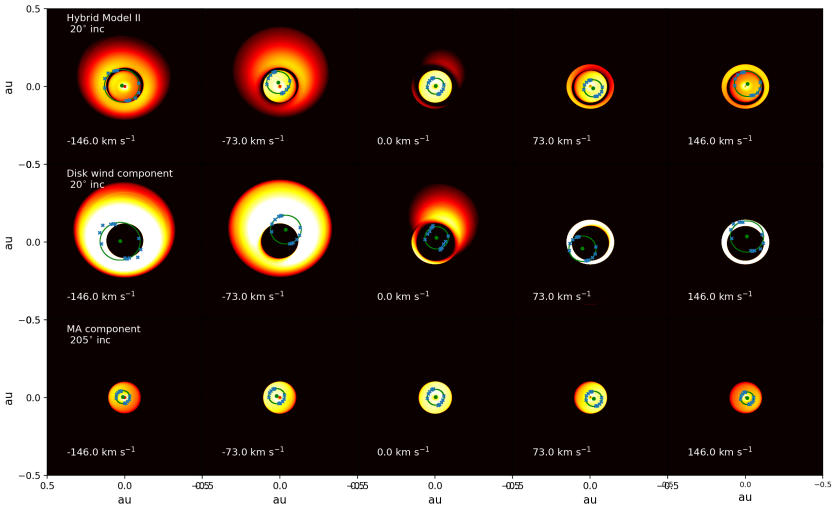

Figure B.1.: Channel maps for HM II and its individual components

B.1. Grid profiles for HM II

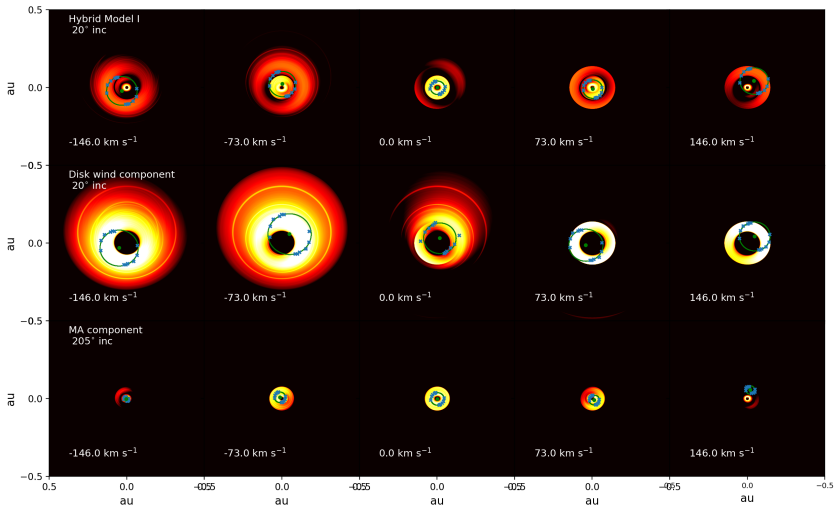

Figure B.2.: Channel maps for HM I and its individual components

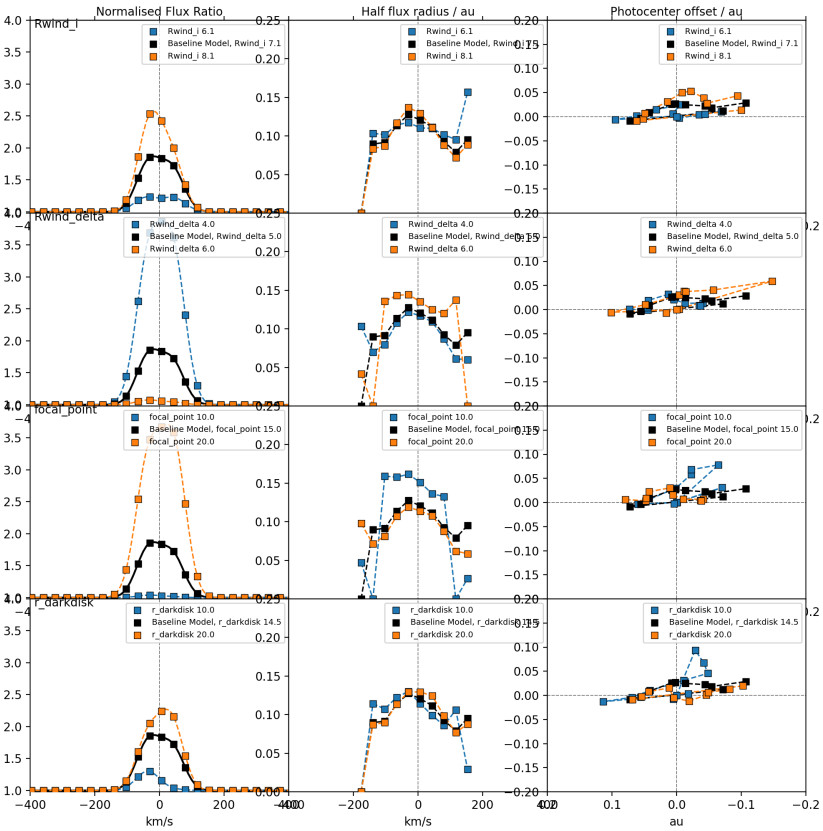

Figure B.3.: Observable response to parameter variations for the wind model.

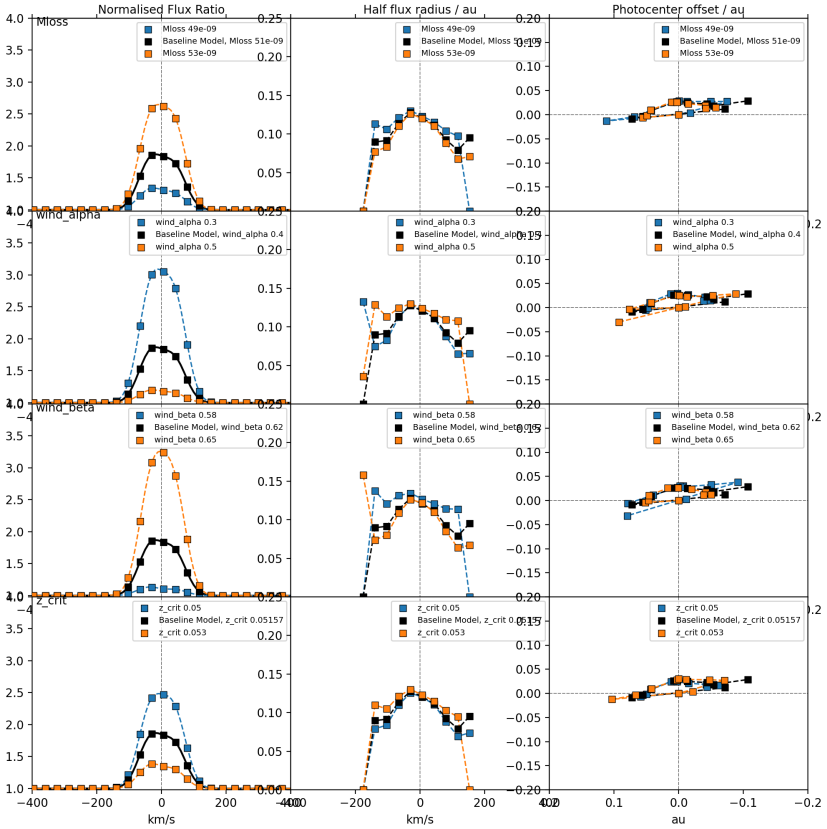

Figure B.4.: Observable response to parameter variations for the wind model.

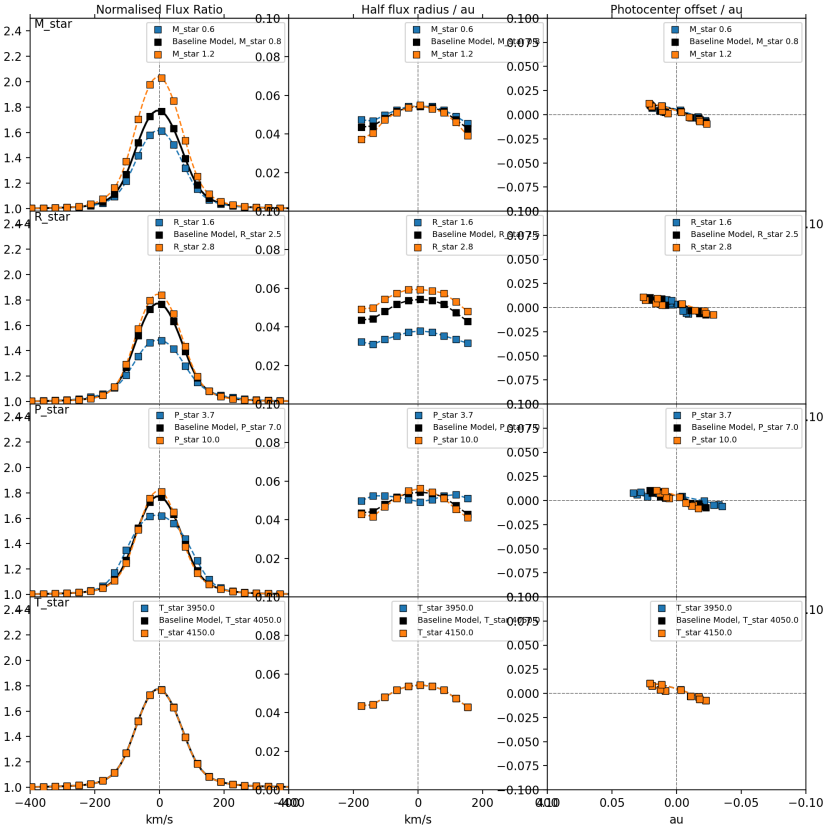

Figure B.5.: Observable response to parameter variations for the wind model.

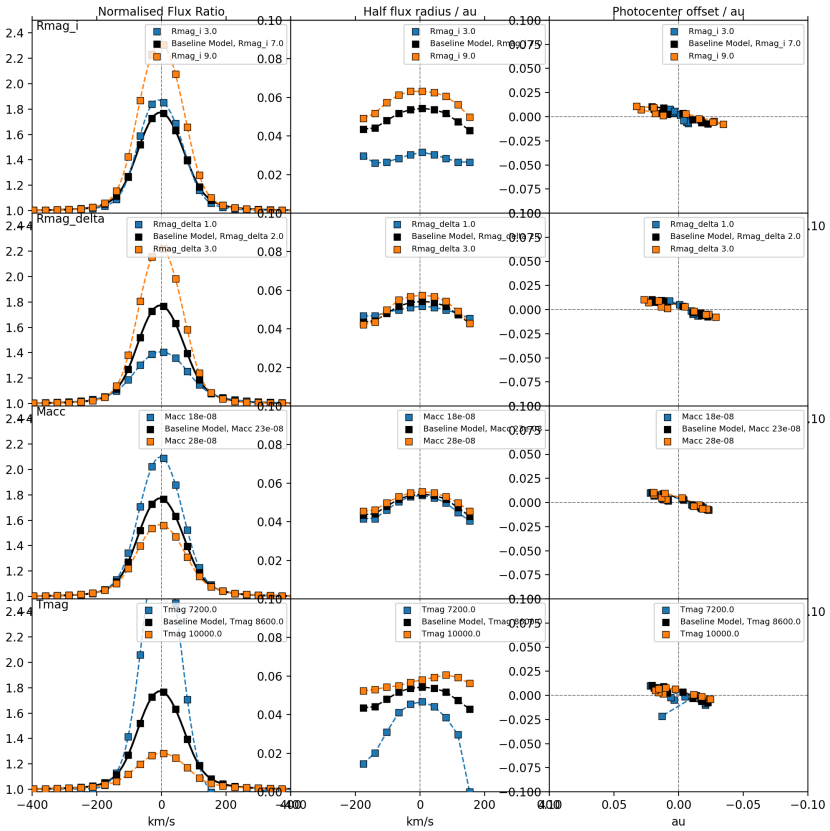

Figure B.6.: Observable response to parameter variations for the wind model.

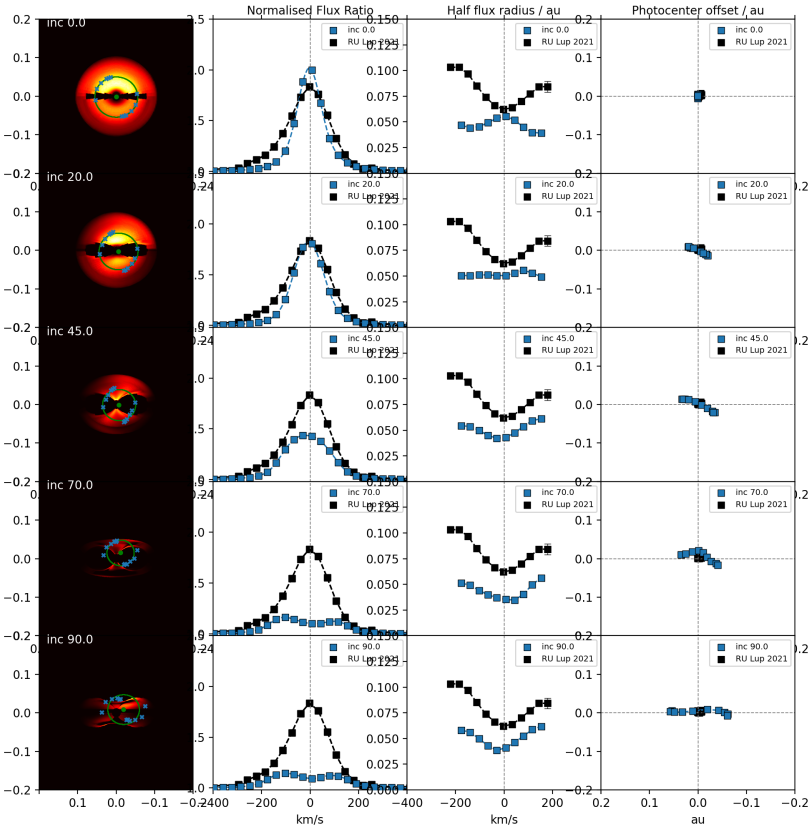

Figure B.7.: Observable dependency on azimuth angle of the non-axisymmetric magnetospheric accretion model with 15 deg obliquity.

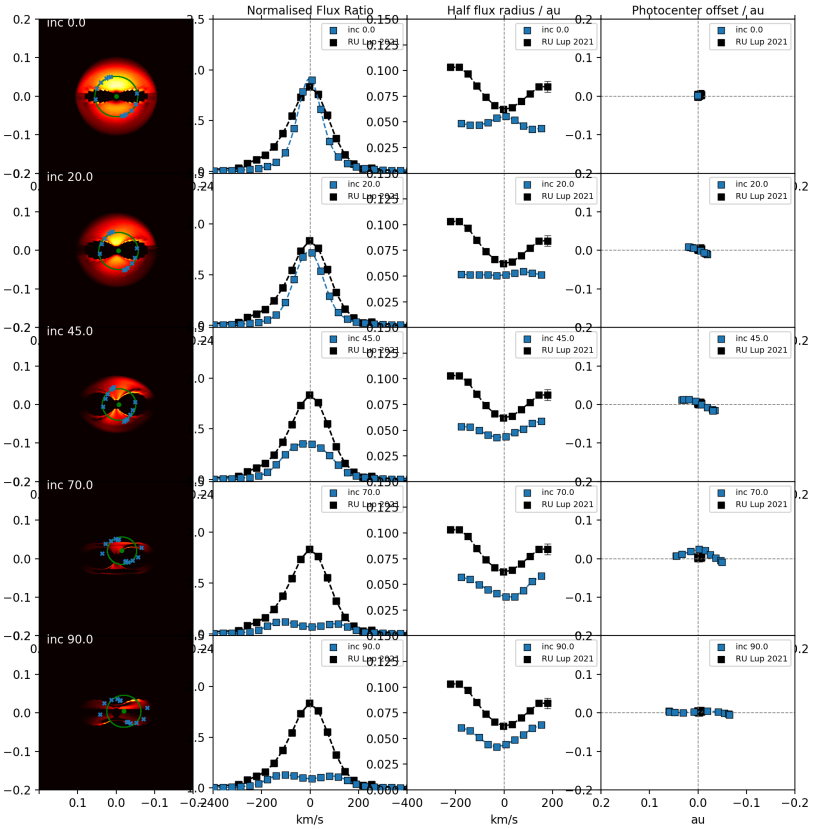

Figure B.8.: Observable dependency on azimuth angle of the non-axisymmetric magnetospheric accretion model with 30 deg obliquity.

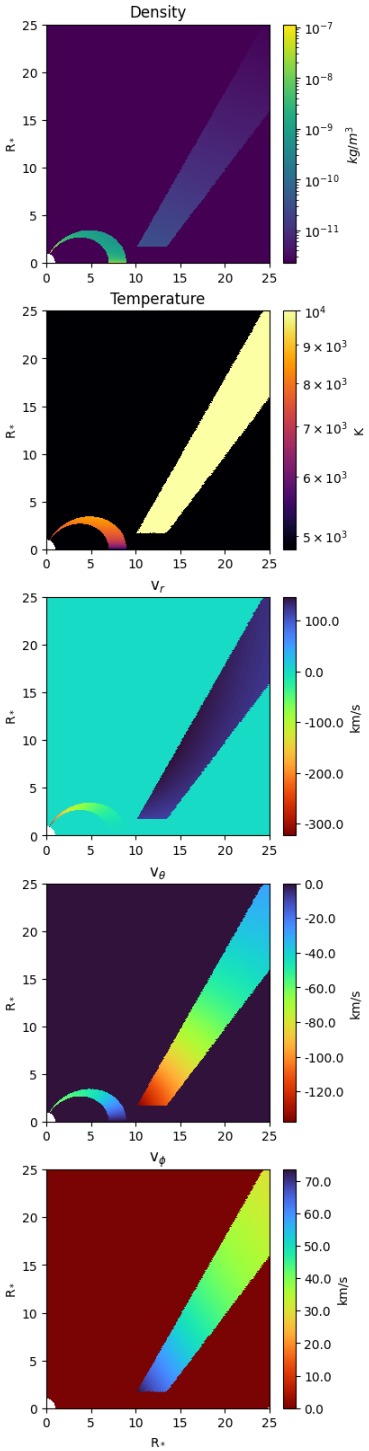

Figure B.9.: 2D model profiles for hybrid model II. Shown are, from top to bottom: Mass density, temperature, and the three spherical components of the velocity field.

Acknowledgements

Now, at the conclusion of this project, as I turn towards the customary practise of giving acknowledgments to the people who supported me throughout the years, I find myself thinking about all the names, past and present, who have accompanied me on this path. It is easy enough to think of those wo are still with me today, but in truth there is an even greater number of those who have come and gone, who moved on towards other projects or a different life outside academia altogether, yet for some time made vital contributions to my work and life at the university. As I consider them all, I realise that no list could ever be exhaustive, nor could any words ever repay the full debt of gratitude that I owe to them all. I apologise profoundly to all those who I may fail to include here.

Above all I wish to thank my supervisor, Lucas Labadie, for his ongoing support throughout the many years we have worked together, beginning with my Bachelor's project up to the completion of this thesis. Again, I could never give a full account of all the things I have learned under his guidance. Instead, I shall simply say "Thank you".

The same sentiment I extend to all my great colleages from the Institut de Planétologie et d'Astrophysique de Grenoble (IPAG), with whom I was lucky enough to cooperate closely over the past 4 years. With no particular regard to the order of importance, I want to give thanks to Karine Perraut, Jerome Bouvier, Catherine Dougados, Evelyne Alecian, whose scientific expertise has guided me throughout my project and without whom I could not have succeeded. I also thank the great people of the SPIDI team, Anthony Soulain, William Dethier, George Pantolmos, as well as Hugo Nowacki, who have not only influenced my work, but above all have welcomed me warmly as I spent a month in France to collaborate on this project. Last but not least, I wish to thank Benjamin Tessore, who has tirelessly supported me with his scientific and personal expertise, and without whom much of my work simply would not exist.

I also thank my dear colleagues of PHI institute at the University of Cologne, many of which I have come to consider friends over the years. While this list cannot possibly be complete, I wish to thank Rebekka Grellmann in particular, who has supported me from my first day in the institute and continued to do so long after she herself moved on to other things. I also must mention

Christan Straubmeier, Lukas Steiniger, Matthias Subroweit, Elaheh Hosseini, Sanny Ahmed and Birka Zimmermann for their immense moral support especially in these last stressful months.

Finally, and certainly not least of them all, I give thanks to my family, as without their continued moral support in even the most difficult of times, none of this would have been possible at all.

Again, these are only some of the many people I whose company and cooperation I was lucky to share over the years. To all of them, and many more not mentioned here, I say again "Thank you!".

List of Figures

42figure.caption.23

List of Tables

Glossary

ATs Auxilliary Telescopes. 45, 46

BCI Beam Combining Instrument. 48

CHARA Center for High Angular Resolution. 45

CIAO Coudé Infrared Adaptive Optics. 47

ESO European Southern Observatory. 45

FT fringe tracker. 49

KI Keck Interferometer. 46

LBTI Large Binocular Telescope Interferometer. 46

MACAO Multi-Application Curvature Adaptive Optics. 47

mas milliarcseconds. 45

MATISSE Multi AperTure mid-Infrared SpectroScopic Experiment. 47

MUSE Multi-Unit Spectroscopic Explorer. 45

NAOMI New Adaptive Optics Module for Interferometry. 47

PIONIER Precision Integrated Optics Near Infrared ExpeRiment. 47

SC science channel. 49

SPHERE Spectro-Polarimetric High-contrast Exoplanet REsearch. 45

UTs Unit Telescopes. 45, 46

VISIR VLT imager and spectrometer for the mid infrared. 45

VLT Very Large Telescope. 45

VLTI Very Large Telescope Interferometer. 45

Bibliography

Agra-Amboage, V., Cabrit, S., Dougados, C., Kristensen, L. E., Ibgui, L., and Reunanen, J. (2014). Origin of the wide-angle hot H_2 in DG Tauri. New insight from SINFONI spectro-imaging. , 564:A11.

Alcalá, J. M., Manara, C. F., Natta, A., Frasca, A., Testi, L., Nisini, B., Stelzer, B., Williams, J. P., Antoniucci, S., Biazzo, K., Covino, E., Esposito, M., Getman, F., and Rigliaco, E. (2017). X-shooter spectroscopy of young stellar objects in Lupus. Accretion properties of class II and transitional objects. , 600:A20.

Alcalá, J. M., Natta, A., Manara, C. F., Spezzi, L., Stelzer, B., Frasca, A., Biazzo, K., Covino, E., Randich, S., Rigliaco, E., Testi, L., Comerón, F., Cupani, G., and D'Elia, V. (2014). X-shooter spectroscopy of young stellar objects. IV. Accretion in low-mass stars and substellar objects in Lupus. , 561:A2.

Alencar, S. H. P., Bouvier, J., Walter, F. M., Dougados, C., Donati, J. F., Kurosawa, R., Romanova, M., Bonfils, X., Lima, G. H. R. A., Massaro, S., Ibrahimov, M., and Poretti, E. (2012). Accretion dynamics in the classical T Tauri star V2129 Ophiuchi. , 541:A116.

Alexander, R., Pascucci, I., Andrews, S., Armitage, P., and Cieza, L. (2014). The Dispersal of Protoplanetary Disks. In Beuther, H., Klessen, R. S., Dullemond, C. P., and Henning, T., editors, *Protostars and Planets VI*, pages 475–496.

Andrews, S. M., Wilner, D. J., Zhu, Z., Birnstiel, T., Carpenter, J. M., Pérez, L. M., Bai, X.-N., Öberg, K. I., Hughes, A. M., Isella, A., and Ricci, L. (2016). Ringed Substructure and a Gap at 1 au in the Nearest Protoplanetary Disk. , 820(2):L40.

Bai, X.-N. (2017). Global Simulations of the Inner Regions of Protoplanetary Disks with Comprehensive Disk Microphysics. , 845(1):75.

Banzatti, A., Pascucci, I., Edwards, S., Fang, M., Gorti, U., and Flock, M. (2019). Kinematic Links and the Coevolution of MHD Winds, Jets, and Inner Disks from a High-resolution Optical [O I] Survey. , 870(2):76.

Berger, J. P. and Segransan, D. (2007). An introduction to visibility modeling. , 51(8-9):576–582.

Bertout, C., Basri, G., and Bouvier, J. (1988). Accretion Disks around T Tauri Stars. , 330:350.

Bessolaz, N., Zanni, C., Ferreira, J., Keppens, R., and Bouvier, J. (2008). Accretion funnels onto weakly magnetized young stars. , 478(1):155–162.

Blandford, R. D. and Payne, D. G. (1982). Hydromagnetic flows from accretion disks and the production of radio jets. , 199:883–903.

Blinova, A. A., Romanova, M. M., and Lovelace, R. V. E. (2016). Boundary between stable and unstable regimes of accretion. Ordered and chaotic unstable regimes. , 459(3):2354–2369.

Bouvier, J. (2013). Observational studies of stellar rotation. In Hennebelle, P. and Charbonnel, C., editors, *EAS Publications Series*, volume 62 of *EAS Publications Series*, pages 143–168.

Bouvier, J., Alencar, S. H. P., Harries, T. J., Johns-Krull, C. M., and Romanova, M. M. (2007). Magnetospheric Accretion in Classical T Tauri Stars. In Reipurth, B., Jewitt, D., and Keil, K., editors, *Protostars and Planets V*, page 479.

Bouvier, J., Covino, E., Kovo, O., Martin, E. L., Matthews, J. M., Terranegra, L., and Beck, S. C. (1995). COYOTES II: SPOT properties and the origin of photometric period variations in T Tauri stars. , 299:89.

Bouvier, J., Perraut, K., Le Bouquin, J. B., Duvert, G., Dougados, C., Brandner, W., Benisty, M., Berger, J. P., and Alécian, E. (2020). Probing the magnetospheric accretion region of the young pre-transitional disk system DoAr 44 using VLTI/GRAVITY. , 636:A108.

Calvet, N. and Hartmann, L. (1992). Balmer Line Profiles for Infalling T Tauri Envelopes. , 386:239.

Calvet, N., Muzerolle, J., Briceño, C., Hernández, J., Hartmann, L., Saucedo, J. L., and Gordon, K. D. (2004). The Mass Accretion Rates of Intermediate-Mass T Tauri Stars. , 128(3):1294–1318.

Camenzind, M. (1990). Magnetized Disk-Winds and the Origin of Bipolar Outflows. *Reviews in Modern Astronomy*, 3:234–265.

Curiel, S., Raga, A., Raymond, J., Noriega-Crespo, A., and Canto, J. (1997). HST Images of the High-Excitation Herbig-Haro Object HH 32. , 114:2736.

Cutri, R. M., Skrutskie, M. F., van Dyk, S., Beichman, C. A., Carpenter, J. M., Chester, T., Cambresy, L., Evans, T., Fowler, J., Gizis, J., Howard, E., Huchra, J., Jarrett, T., Kopan, E. L., Kirkpatrick, J. D., Light, R. M., Marsh, K. A., McCallon, H., Schneider, S., Stiening, R., Sykes, M., Weinberg, M., Wheaton, W. A., Wheelock, S., and Zacarias, N. (2003). VizieR Online Data Catalog: 2MASS All-Sky Catalog of Point Sources (Cutri+ 2003). *VizieR Online Data Catalog*, page II/246.

Dame, T. M. and Thaddeus, P. (1985). A wide-latitude CO survey of molecular clouds in the northern Milky Way. , 297:751–765.

Donati, J. F., Gregory, S. G., Alencar, S. H. P., Bouvier, J., Hussain, G., Skelly, M., Dougados, C., Jardine, M. M., Ménard, F., Romanova, M. M., and Unruh, Y. C. (2011). The large-scale magnetic field and poleward mass accretion of the classical T Tauri star TW Hya. , 417(1):472–487.

Donati, J. F., Jardine, M. M., Gregory, S. G., Petit, P., Bouvier, J., Dougados, C., Ménard, F., Collier Cameron, A., Harries, T. J., Jeffers, S. V., and Paletou, F. (2007). Magnetic fields and accretion flows on the classical T Tauri star V2129 Oph. , 380(4):1297–1312.

Drissen, L., Bastien, P., and St. -Louis, N. (1989). Linear Polarization of T Tauri Stars. I. Variability of Southern Stars. , 97:814.

Dullemond, C. P. and Monnier, J. D. (2010). The Inner Regions of Protoplanetary Disks. , 48:205–239.

Edwards, S. (1994). Accretion Disks, Energetic Outflows, and the Origin of Stellar Angular Momentum. In *American Astronomical Society Meeting Abstracts*, volume 185 of *American Astronomical Society Meeting Abstracts*, page 99.02.

Edwards, S., Fischer, W., Hillenbrand, L., and Kwan, J. (2006). Probing T Tauri Accretion and Outflow with 1 Micron Spectroscopy. , 646(1):319–341.

Edwards, S. and Snell, R. L. (1982). A search for high-velocity molecular gas around T Tau stars. , 261:151–160.

Eisenhauer, F., Monnier, J. D., and Pfuhl, O. (2023). Advances in Optical/Infrared Interferometry. , 61:237–285.

Eislöffel, J. and Mundt, R. (1998). Imaging and Kinematic Studies of Young Stellar Object Jets in Taurus. , 115(4):1554–1575.

Eisner, J. A., Chiang, E. I., and Hillenbrand, L. A. (2006). Spatially Resolving the Inner Disk of TW Hydrae. , 637(2):L133–L136.

Eisner, J. A., Hillenbrand, L. A., and Stone, J. M. (2014). Constraining the sub-au-scale distribution of hydrogen and carbon monoxide gas around young stars with the Keck Interferometer. , 443(3):1916–1945.

Eisner, J. A., Hillenbrand, L. A., White, R. J., Bloom, J. S., Akeson, R. L., and Blake, C. H. (2007). Near-Infrared Interferometric, Spectroscopic, and Photometric Monitoring of T Tauri Inner Disks. , 669(2):1072–1084.

Eisner, J. A., Monnier, J. D., Woillez, J., Akeson, R. L., Millan-Gabet, R., Graham, J. R., Hillenbrand, L. A., Pott, J. U., Ragland, S., and Wizinowich, P. (2010). Spatially and Spectrally Resolved Hydrogen Gas within 0.1 AU of T Tauri and Herbig Ae/Be Stars. , 718(2):774–794.

Espaillat, C., D'Alessio, P., Hernández, J., Nagel, E., Luhman, K. L., Watson, D. M., Calvet, N., Muzerolle, J., and McClure, M. (2010). Unveiling the Structure of Pre-transitional Disks. , 717(1):441–457.

Fang, M., Pascucci, I., Edwards, S., Gorti, U., Banzatti, A., Flock, M., Hartigan, P., Herczeg, G. J., and Dupree, A. K. (2018). A New Look at T Tauri Star Forbidden Lines: MHD-driven Winds from the Inner Disk. , 868(1):28.

Ferreira, J. (2013). Braking down an accreting protostar: disc-locking, disc winds, stellar winds, X-winds and Magnetospheric Ejecta. In Hennebelle, P. and Charbonnel, C., editors, *EAS Publications Series*, volume 62 of *EAS Publications Series*, pages 169–225.

Ferreira, J., Dougados, C., and Cabrit, S. (2006). Which jet launching mechanism(s) in T Tauri stars? , 453(3):785–796.

Fossati, L., Schneider, F. R. N., Castro, N., Langer, N., Simón-Díaz, S., Müller, A., de Koter, A., Morel, T., Petit, V., Sana, H., and Wade, G. A. (2016). Evidence of magnetic field decay in massive main-sequence stars. , 592:A84.

Frasca, A., Biazzo, K., Alcalá, J. M., Manara, C. F., Stelzer, B., Covino, E., and Antoniucci, S. (2017). X-shooter spectroscopy of young stellar objects in Lupus. Atmospheric parameters, membership, and activity diagnostics. , 602:A33.

Gahm, G. F., Petrov, P. P., Tambovsteva, L. V., Grinin, V. P., Stempels, H. C., and Walter, F. M. (2018). S Coronae Australis: a T Tauri twin. , 614:A117.

Gaia Collaboration (2020). VizieR Online Data Catalog: Gaia EDR3 (Gaia Collaboration, 2020). *VizieR Online Data Catalog*, page I/350.

Garcia, P. J. V., Cabrit, S., Ferreira, J., and Binette, L. (2001a). Atomic T Tauri disk winds heated by ambipolar diffusion. II. Observational tests. , 377:609–616.

Garcia, P. J. V., Ferreira, J., Cabrit, S., and Binette, L. (2001b). Atomic T Tauri disk winds heated by ambipolar diffusion. I. Thermal structure. , 377:589–608.

Garcia Lopez, R., Tambovtseva, L. V., Schertl, D., Grinin, V. P., Hofmann, K. H., Weigelt, G., and Caratti o Garatti, A. (2015). Probing the accretion-ejection connection with VLTI/AMBER. High spectral resolution observations of the Herbig Ae star HD 163296. , 576:A84.

Glindemann, A. (2011). *Principles of Stellar Interferometry*.

Goto, M., Carmona, A., Linz, H., Stecklum, B., Henning, T., Meeus, G., and Usuda, T. (2012). Kinematics of Ionized Gas at 0.01 AU of TW Hya. , 748(1):6.

Gravity Collaboration, Ganci, V., Labadie, L., Klarmann, L., de Valon, A., Perraut, K., Benisty, M., Brandner, W., Caratti O Garatti, A., Dougados, C., Eupen, F., Garcia Lopez, R., Grellmann, R., Sanchez-Bermudez, J., Wojtczak, A., Garcia, P., Amorim, A., Bauböck, M., Berger, J. P., Caselli, P., Clénet, Y., Coudé Du Foresto, V., de Zeeuw, P. T., Drescher, A., Duvert, G., Eckart, A., Eisenhauer, F., Filho, M., Gao, F., Gendron, E., Genzel, R., Gillessen, S., Heissel, G., Henning, T., Hippler, S., Horrobin, M., Hubert, Z., Jiménez-Rosales, A., Jocou, L., Kervella, P., Lacour, S., Lapeyrère, V., Le Bouquin, J. B., Léna, P., Ott, T., Paumard, T., Perrin, G., Pfuhl, O., Heißel, G., Rousset, G., Scheithauer, S., Shangguan, J., Shimizu, T., Stadler, J., Straub, O., Straubmeier, C., Sturm, E., van Dishoeck, E., Vincent, F., von Fellenberg, S. D., Widmann, F., and Woillez, J. (2021a). The GRAVITY young stellar object survey. VIII. Gas and dust faint inner rings in the hybrid disk of HD141569. , 655:A112.

Gravity Collaboration, Garcia Lopez, R., Natta, A., Caratti o Garatti, A., Ray, T. P., Fedriani, R., Koutoulaki, M., Klarmann, L., Perraut, K., Sanchez-Bermudez, J., Benisty, M., Dougados, C., Labadie, L., Brandner, W., Garcia, P. J. V., Henning, T., Caselli, P., Duvert, G., de Zeeuw, T., Grellmann, R., Abuter, R., Amorim, A., Bauböck, M., Berger, J. P., Bonnet, H., Buron, A., Clénet, Y., Coudé Du Foresto, V., de Wit, W., Eckart, A., Eisenhauer, F., Filho, M., Gao, F., Garcia Dabo, C. E., Gendron, E., Genzel, R., Gillessen, S., Habibi, M., Haubois, X., Haussmann, F., Hippler, S., Hubert, Z., Horrobin, M., Jimenez Rosales, A., Jocou, L., Kervella, P., Kolb, J., Lacour, S., Le Bouquin, J. B., Léna, P., Ott, T., Paumard, T., Perrin, G., Pfuhl, O., Ramirez, A., Rau, C., Rousset, G., Scheithauer, S., Shangguan, J., Stadler, J., Straub, O., Straubmeier, C., Sturm, E., van Dishoeck, E., Vincent, F., von Fellenberg, S.,

Widmann, F., Wieprecht, E., Wiest, M., Wiezorrek, E., Woillez, J., Yazici, S., and Zins, G. (2020). A measure of the size of the magnetospheric accretion region in TW Hydrae. *Nature*, 584(7822):547–550.

Gravity Collaboration, Garcia Lopez, R., Perraut, K., Caratti O Garatti, A., Lazareff, B., Sanchez-Bermudez, J., Benisty, M., Dougados, C., Labadie, L., Brandner, W., Garcia, P. J. V., Henning, T., Ray, T. P., Abuter, R., Amorim, A., Anugu, N., Berger, J. P., Bonnet, H., Buron, A., Caselli, P., Clénet, Y., Coudé Du Foresto, V., de Wit, W., Deen, C., Delplancke-Ströbele, F., Dexter, J., Eckart, A., Eisenhauer, F., Garcia Dabo, C. E., Gendron, E., Genzel, R., Gillessen, S., Haubois, X., Haug, M., Haussmann, F., Hippler, S., Hubert, Z., Hummel, C. A., Horrobin, M., Jocou, L., Kellner, S., Kervella, P., Kulas, M., Kolb, J., Lacour, S., Le Bouquin, J. B., Léna, P., Lippa, M., Mérand, A., Müller, E., Ott, T., Panduro, J., Paumard, T., Perrin, G., Pfuhl, O., Ramirez, A., Rau, C., Rohloff, R. R., Rousset, G., Scheithauer, S., Schöller, M., Straubmeier, C., Sturm, E., Thi, W. F., van Dishoeck, E., Vincent, F., Waisberg, I., Wank, I., Wieprecht, E., Wiest, M., Wiezorrek, E., Woillez, J., Yazici, S., and Zins, G. (2017). The wind and the magnetospheric accretion onto the T Tauri star S Coronae Australis at sub-au resolution. , 608:A78.

Gravity Collaboration, Perraut, K., Labadie, L., Bouvier, J., Ménard, F., Klarmann, L., Dougados, C., Benisty, M., Berger, J. P., Bouarour, Y. I., Brandner, W., Caratti O Garatti, A., Caselli, P., de Zeeuw, P. T., Garcia-Lopez, R., Henning, T., Sanchez-Bermudez, J., Sousa, A., van Dishoeck, E., Alécian, E., Amorim, A., Clénet, Y., Davies, R., Drescher, A., Duvert, G., Eckart, A., Eisenhauer, F., Förster-Schreiber, N. M., Garcia, P., Gendron, E., Genzel, R., Gillessen, S., Grellmann, R., Heißel, G., Hippler, S., Horrobin, M., Hubert, Z., Jocou, L., Kervella, P., Lacour, S., Lapeyrère, V., Le Bouquin, J. B., Léna, P., Lutz, D., Ott, T., Paumard, T., Perrin, G., Scheithauer, S., Shangguan, J., Shimizu, T., Stadler, J., Straub, O., Straubmeier, C., Sturm, E., Tacconi, L., Vincent, F., von Fellenberg, S., and Widmann, F. (2021b). The GRAVITY young stellar object survey. VII. The inner dusty disks of T Tauri stars. , 655:A73.

Gravity Collaboration, Soulain, A., Perraut, K., Bouvier, J., Pantolmos, G., Caratti O Garatti, A., Caselli, P., Garcia, P., Lopez, R. G., Aimar, N., Amorin, A., Benisty, M., Berger, J. P., Bourdarot, G., Brandner, W., Clénet, Y., de Zeeuw, T., Davies, R., Drescher, A., Eckart, A., Eisenhauer, F., Schreiber, N. M. F., Gendron, E., Genzuel, R., Gillessen, S., Heißel, G., Henning, T., Hippler, S., Horrobin, M., Jocou, L., Kervella, P., Labadie, L., Lacour, S., Lapeyrere, V., Le Bouquin, J. B., Léna, P., Lutz, D., Mang, F., Ott, T., Paumard, T., Perrin, G., Sanchez, J., Scheithauer, S., Shangguan, J., Shimizu, T., Straub, O., Straubmeier, C., Sturm, E., Tacconi, L. J., Vincent, F., van Dishoeck, E., Widmann, F., Wieprecht, E., Wiezorrek, E.,

and Yazici, S. (2023a). The GRAVITY young stellar object survey. X. Probing the inner disk and magnetospheric accretion region of CI Tau. , 674:A203.

Gravity Collaboration, Wojtczak, J. A., Labadie, L., Perraut, K., Tessore, B., Soulain, A., Ganci, V., Bouvier, J., Dougados, C., Alécian, E., Nowacki, H., Cozzo, G., Brandner, W., Caratti O Garatti, A., Garcia, P., Garcia Lopez, R., Sanchez-Bermudez, J., Amorim, A., Benisty, M., Berger, J. P., Bourdarot, G., Caselli, P., Clénet, Y., de Zeeuw, P. T., Davies, R., Drescher, A., Duvert, G., Eckart, A., Eisenhauer, F., Eupen, F., Förster-Schreiber, N. M., Gendron, E., Gillessen, S., Grant, S., Grellmann, R., Heißel, G., Henning, T., Hippler, S., Horrobin, M., Hubert, Z., Jocou, L., Kervella, P., Lacour, S., Lapeyrère, V., Le Bouquin, J. B., Léna, P., Lutz, D., Mang, F., Ott, T., Paumard, T., Perrin, G., Scheithauer, S., Shangguan, J., Shimizu, T., Spezzano, S., Straub, O., Straubmeier, C., Sturm, E., van Dishoeck, E., Vincent, F., and Widmann, F. (2023b). The GRAVITY young stellar object survey. IX. Spatially resolved kinematics of hot hydrogen gas in the star-disk interaction region of T Tauri stars. , 669:A59.

Güdel, M., Eibensteiner, C., Dionatos, O., Audard, M., Forbrich, J., Kraus, S., Rab, C., Schneider, C., Skinner, S., and Vorobyov, E. (2018). ALMA detects a radial disk wind in DG Tauri. , 620:L1.

Haniff, C. (2007). An introduction to the theory of interferometry. , 51(8-9):565–575.

Hartmann, L. (2009). *Accretion Processes in Star Formation: Second Edition*.

Hartmann, L., Avrett, E., and Edwards, S. (1982). Wave-driven winds from cool stars. II - Models for T Tauri stars. , 261:279–292.

Hartmann, L., Calvet, N., Gullbring, E., and D'Alessio, P. (1998). Accretion and the Evolution of T Tauri Disks. , 495(1):385–400.

Hartmann, L., Herczeg, G., and Calvet, N. (2016). Accretion onto Pre-Main-Sequence Stars. , 54:135–180.

Hartmann, L., Hewett, R., and Calvet, N. (1994). Magnetospheric Accretion Models for T Tauri Stars. I. Balmer Line Profiles without Rotation. , 426:669.

Hartmann, L. and Stauffer, J. R. (1989). Additional Measurements of Pre-Main-Sequence Stellar Rotation. , 97:873.

Herczeg, G. J. and Hillenbrand, L. A. (2008). UV Excess Measures of Accretion onto Young Very Low Mass Stars and Brown Dwarfs. , 681(1):594–625.

Hoffmeister, C. (1965). Bearbeitung von 22 sudlichen Veranderlichen Sternen. *Veroeffentlichungen der Sternwarte Sonneberg*, 6:123–155.

Huang, J., Andrews, S. M., Dullemond, C. P., Isella, A., Pérez, L. M., Guzmán, V. V., Öberg, K. I., Zhu, Z., Zhang, S., Bai, X.-N., Benisty, M., Birnstiel, T., Carpenter, J. M., Hughes, A. M., Ricci, L., Weaver, E., and Wilner, D. J. (2018). The Disk Substructures at High Angular Resolution Project (DSHARP). II. Characteristics of Annular Substructures. , 869(2):L42.

Hummer, D. G. and Voels, S. A. (1988). Collisional-radiative switching - A powerful technique for converging non-LTE calculations. , 192(1-2):279.

Iguchi, N. and Itoh, Y. (2016). High-Resolution Spectroscopy of Winds Associated with T Tauri Stars. *Research in Astronomy and Astrophysics*, 16(2):30.

Jankov, S., Vakili, F., Domiciano de Souza, A., J., and Janot-Pacheco, E. (2001). Interferometric-Doppler imaging of stellar surface structure. , 377:721–734.

Johns-Krull, C. M. (2007). The Magnetic Fields of Classical T Tauri Stars. , 664(2):975–985.

Johnstone, C. P., Jardine, M., Gregory, S. G., Donati, J. F., and Hussain, G. (2014). Classical T Tauri stars: magnetic fields, coronae and star-disc interactions. , 437(4):3202–3220.

Knigge, C., Woods, J. A., and Drew, J. E. (1995). The application of Monte Carlo methods to the synthesis of spectral line profiles arising from accretion disc winds. , 273(2):225–248.

Kraus, S., Hofmann, K. H., Benisty, M., Berger, J. P., Chesneau, O., Isella, A., Malbet, F., Meilland, A., Nardetto, N., Natta, A., Preibisch, T., Schertl, D., Smith, M., Stee, P., Tatulli, E., Testi, L., and Weigelt, G. (2008). The origin of hydrogen line emission for five Herbig Ae/Be stars spatially resolved by VLTI/AMBER spectro-interferometry. , 489(3):1157–1173.

Kurosawa, R., Harries, T. J., and Symington, N. H. (2006). On the formation of Hα line emission around classical T Tauri stars. , 370(2):580–596.

Kurosawa, R., Kreplin, A., Weigelt, G., Natta, A., Benisty, M., Isella, A., Tatulli, E., Massi, F., Testi, L., Kraus, S., Duvert, G., Petrov, R. G., and Stee, P. (2016). Probing the wind-launching regions of the Herbig Be star HD 58647 with high spectral resolution interferometry. , 457(2):2236–2251.

Kurosawa, R., Romanova, M. M., and Harries, T. J. (2011). Multidimensional models of hydrogen and helium emission line profiles for classical T Tauri stars: method, tests and examples. , 416(4):2623–2639.

Lacour, S., Dembet, R., Abuter, R., Fédou, P., Perrin, G., Choquet, É., Pfuhl, O., Eisenhauer, F., Woillez, J., Cassaing, F., Wieprecht, E., Ott, T., Wiezorrek, E., Tristram, K. R. W., Wolff, B., Ramírez, A., Haubois, X., Perraut, K., Straubmeier, C., Brandner, W., and Amorim, A. (2019). The GRAVITY fringe tracker. , 624:A99.

Le Bouquin, J. B., Absil, O., Benisty, M., Massi, F., Mérand, A., and Stefl, S. (2009). The spin-orbit alignment of the Fomalhaut planetary system probed by optical long baseline interferometry. , 498(3):L41–L44.

Lee, C.-F. (2020). Molecular jets from low-mass young protostellar objects. , 28(1):1.

Lee, C.-F., Ho, P. T. P., Li, Z.-Y., Hirano, N., Zhang, Q., and Shang, H. (2017). A rotating protostellar jet launched from the innermost disk of HH 212. *Nature Astronomy*, 1:0152.

Lima, G. H. R. A., Alencar, S. H. P., Calvet, N., Hartmann, L., and Muzerolle, J. (2010). Modeling the Hα line emission around classical T Tauri stars using magnetospheric accretion and disk wind models. , 522:A104.

Lynden-Bell, D. and Pringle, J. E. (1974). The evolution of viscous discs and the origin of the nebular variables. , 168:603–637.

Mahdavi, A. and Kenyon, S. J. (1998). The Bright Accretion Rings on Magnetic T Tauri Stars. , 497(1):342–353.

Manara, C. F. (2014). *The physics of the accretion process in the formation and evolution of Young Stellar Objects*. PhD thesis, Ludwig-Maximilians University of Munich, Germany.

Martin, S. C. (1996). The Thermal Structure of Magnetic Accretion Funnels in Young Stellar Objects. , 470:537.

Matt, S. and Pudritz, R. E. (2005). Accretion-powered Stellar Winds as a Solution to the Stellar Angular Momentum Problem. , 632(2):L135–L138.

McGinnis, P., Bouvier, J., and Gallet, F. (2020). The magnetic obliquity of accreting T Tauri stars. , 497(2):2142–2162.

Mendigutía, I. (2020). On the Mass Accretion Rates of Herbig Ae/Be Stars. Magnetospheric Accretion or Boundary Layer? *Galaxies*, 8(2):39.

Millour, F. (2014). Interferometry concepts. In *EAS Publications Series*, volume 69-70 of *EAS Publications Series*, pages 17–52.

Monnier, J. D. (2007). Phases in interferometry. , 51(8-9):604–616.

Monnier, J. D. and Millan-Gabet, R. (2002). On the Interferometric Sizes of Young Stellar Objects. , 579(2):694–698.

Muzerolle, J., Calvet, N., and Hartmann, L. (1998). Magnetospheric Accretion Models for the Hydrogen Emission Lines of T Tauri Stars. , 492(2):743–753.

Muzerolle, J., Calvet, N., and Hartmann, L. (2001). Emission-Line Diagnostics of T Tauri Magnetospheric Accretion. II. Improved Model Tests and Insights into Accretion Physics. , 550(2):944–961.

Muzerolle, J., D'Alessio, P., Calvet, N., and Hartmann, L. (2004). Magnetospheres and Disk Accretion in Herbig Ae/Be Stars. , 617(1):406–417.

Najita, J., Carr, J. S., and Mathieu, R. D. (2003). Gas in the Terrestrial Planet Region of Disks: CO Fundamental Emission from T Tauri Stars. , 589(2):931–952.

Natta, A., Prusti, T., Neri, R., Wooden, D., Grinin, V. P., and Mannings, V. (2001). A reconsideration of disk properties in Herbig Ae stars. , 371:186–197.

Ortiz-León, G. N., Dzib, S. A., Kounkel, M. A., Loinard, L., Mioduszewski, A. J., Rodríguez, L. F., Torres, R. M., Pech, G., Rivera, J. L., Hartmann, L., Boden, A. F., Evans, Neal J., I., Briceño, C., Tobin, J. J., and Galli, P. A. B. (2017). The Gould's Belt Distances Survey (GOBELINS). III. The Distance to the Serpens/Aquila Molecular Complex. , 834(2):143.

Pascucci, I., Cabrit, S., Edwards, S., Gorti, U., Gressel, O., and Suzuki, T. K. (2023). The Role of Disk Winds in the Evolution and Dispersal of Protoplanetary Disks. In Inutsuka, S., Aikawa, Y., Muto, T., Tomida, K., and Tamura, M., editors, *Protostars and Planets VII*, volume 534 of *Astronomical Society of the Pacific Conference Series*, page 567.

Peterson, D. E., Caratti o Garatti, A., Bourke, T. L., Forbrich, J., Gutermuth, R. A., Jørgensen, J. K., Allen, L. E., Patten, B. M., Dunham, M. M., Harvey, P. M., Merín, B., Chapman, N. L., Cieza, L. A., Huard, T. L., Knez, C., Prager, B., and Evans, N. J. (2011). The Spitzer Survey of Interstellar Clouds in the Gould Belt. III. A Multi-wavelength View of Corona Australis. , 194(2):43.

Pinte, C., Harries, T. J., Min, M., Watson, A. M., Dullemond, C. P., Woitke, P., Ménard, F., and Durán-Rojas, M. C. (2009). Benchmark problems for continuum radiative transfer. High optical depths, anisotropic scattering, and polarisation. , 498(3):967–980.

Pinte, C., Ménard, F., Berger, J. P., Benisty, M., and Malbet, F. (2008). The Inner Radius of T Tauri Disks Estimated from Near-Infrared Interferometry: The Importance of Scattered Light. , 673(1):L63.

Pinte, C., Ménard, F., Duchêne, G., and Bastien, P. (2006). Monte Carlo radiative transfer in protoplanetary disks. , 459(3):797–804.

Podio, L., Garufi, A., Codella, C., Fedele, D., Rygl, K., Favre, C., Bacciotti, F., Bianchi, E., Ceccarelli, C., Mercimek, S., Teague, R., and Testi, L. (2020). ALMA chemical survey of disk-outflow sources in Taurus (ALMA-DOT). III. The interplay between gas and dust in the protoplanetary disk of DG Tau. , 644:A119.

Prato, L., Greene, T. P., and Simon, M. (2003). Astrophysics of Young Star Binaries. , 584(2):853–874.

Rebull, L. M., Stauffer, J. R., Cody, A. M., Hillenbrand, L. A., Bouvier, J., Roggero, N., and David, T. J. (2020). Rotation of Low-mass Stars in Taurus with K2. , 159(6):273.

Rei, A. C. S., Petrov, P. P., and Gameiro, J. F. (2018). Line-dependent veiling in very active classical T Tauri stars. , 610:A40.

Rice, E. L., Prato, L., and McLean, I. S. (2006). An Association in the Aquila Star-forming Region: High-Resolution Infrared Spectroscopy of T Tauri Stars. , 647(1):432–443.

Romanova, M. M., Kulkarni, A. K., Long, M., and Lovelace, R. V. E. (2008a). Modeling of Disk-Star Interaction: Different Regimes of Accretion and Variability. In Wijnands, R., Altamirano, D., Soleri, P., Degenaar, N., Rea, N., Casella, P., Patruno, A., and Linares, M., editors, *A Decade of Accreting MilliSecond X-ray Pulsars*, volume 1068 of *American Institute of Physics Conference Series*, pages 87–94.

Romanova, M. M., Kulkarni, A. K., and Lovelace, R. V. E. (2008b). Unstable Disk Accretion onto Magnetized Stars: First Global Three-dimensional Magnetohydrodynamic Simulations. , 673(2):L171.

Romanova, M. M. and Owocki, S. P. (2015). Accretion, Outflows, and Winds of Magnetized Stars. , 191(1-4):339–389.

Romanova, M. M. and Owocki, S. P. (2016). Accretion, Outflows, and Winds of Magnetized Stars. In *The Strongest Magnetic Fields in the Universe: Space Sciences Series of ISSI*, volume 54, page 347.

Rutten, R. J. (2003). *Radiative Transfer in Stellar Atmospheres*.

Rybicki, G. B. and Hummer, D. G. (1991). An accelerated lambda iteration method for multi-level radiative transfer. I. Non-overlapping lines with background continuum. , 245:171–181.

Scicluna, P., Wolf, S., Ratzka, T., Costigan, G., Launhardt, R., Leinert, C., Ober, F., Manara, C. F., and Testi, L. (2016). Understanding discs in binary YSOs - detailed modelling of VV CrA. , 458(3):2476–2491.

Setterholm, B. R., Monnier, J. D., Davies, C. L., Kreplin, A., Kraus, S., Baron, F., Aarnio, A., Berger, J.-P., Calvet, N., Curé, M., Kanaan, S., Kloppenborg, B., Le Bouquin, J.-B., Millan-Gabet, R., Rubinstein, A. E., Sitko, M. L., Sturmann, J., ten Brummelaar, T. A., and Touhami, Y. (2018). Probing the Inner Disk Emission of the Herbig Ae Stars HD 163296 and HD 190073. , 869(2):164.

Sicilia-Aguilar, A., Banzatti, A., Carmona, A., Stolker, T., Kama, M., Mendigutía, I., Garufi, A., Flaherty, K., van der Marel, N., and Greaves, J. (2016). A 'Rosetta Stone' for Protoplanetary Disks: The Synergy of Multi-Wavelength Observations. , 33:e059.

Siwak, M., Ogloza, W., Rucinski, S. M., Moffat, A. F. J., Matthews, J. M., Cameron, C., Guenther, D. B., Kuschnig, R., Rowe, J. F., Sasselov, D., and Weiss, W. W. (2016). Stable and unstable accretion in the classical T Tauri stars IM Lup and RU Lup as observed by MOST. , 456(4):3972–3984.

Sokal, K. R., Deen, C. P., Mace, G. N., Lee, J.-J., Oh, H., Kim, H., Kidder, B. T., and Jaffe, D. T. (2018). Characterizing TW Hydra. , 853(2):120.

Solf, J. and Boehm, K. H. (1993). High-Resolution Long-Slit Spectral Imaging of the Mass Outflows in the Immediate Vicinity of DG Tauri. , 410:L31.

Sperling, T., Eislöffel, J., Fischer, C., Nisini, B., Giannini, T., and Krabbe, A. (2021). Evolution of the atomic component in protostellar outflows. , 650:A173.

Stempels, H. C., Gahm, G. F., and Petrov, P. P. (2007). Periodic radial velocity variations in RU Lupi. , 461(1):253–259.

Stock, C., McGinnis, P., Caratti o Garatti, A., Natta, A., and Ray, T. P. (2022). Accretion variability in RU Lup. , 668:A94.

Sullivan, K., Prato, L., Edwards, S., Avilez, I., and Schaefer, G. H. (2019). S and VV Corona Australis: Spectroscopic Variability in Two Young Binary Star Systems. , 884(1):28.

Tabone, B., Cabrit, S., Bianchi, E., Ferreira, J., Pineau des Forêts, G., Codella, C., Gusdorf, A., Gueth, F., Podio, L., and Chapillon, E. (2017). ALMA discovery of a rotating SO/SO_2 flow in HH212. A possible MHD disk wind? , 607:L6.

Takami, M., Bailey, J., and Chrysostomou, A. (2003). A spectro-astrometric study of southern pre-main sequence stars. Binaries, outflows, and disc structure down to AU scales. , 397:675–691.

Takasao, S., Tomida, K., Iwasaki, K., and Suzuki, T. K. (2022). Three-dimensional Simulations of Magnetospheric Accretion in a T Tauri Star: Accretion and Wind Structures Just Around the Star. , 941(1):73.

Tambovtseva, L. V., Grinin, V. P., and Weigelt, G. (2016). Brackett γ radiation from the inner gaseous accretion disk, magnetosphere, and disk wind region of Herbig AeBe stars. , 590:A97.

Tessore, B., Pinte, C., Bouvier, J., and Ménard, F. (2021). Atomic line radiative transfer with MCFOST. I. Code description and benchmarking. , 647:A27.

Tessore, B., Soulain, A., Pantolmos, G., Bouvier, J., Pinte, C., and Perraut, K. (2023). Spectroscopic and interferometric signatures of magnetospheric accretion in young stars. , 671:A129.

Uitenbroek, H. (2001). Multilevel Radiative Transfer with Partial Frequency Redistribution. , 557(1):389–398.

Venuti, L., Stelzer, B., Alcalá, J. M., Manara, C. F., Frasca, A., Jayawardhana, R., Antoniucci, S., Argiroffi, C., Natta, A., Nisini, B., Randich, S., and Scholz, A. (2019). X-shooter spectroscopy of young stars with disks. The TW Hydrae association as a probe of the final stages of disk accretion. , 632:A46.

Watson, D. M., Calvet, N. P., Fischer, W. J., Forrest, W. J., Manoj, P., Megeath, S. T., Melnick, G. J., Najita, J., Neufeld, D. A., Sheehan, P. D., Stutz, A. M., and Tobin, J. J. (2016). Evolution of Mass Outflow in Protostars. , 828(1):52.

Weber, M. L., Ercolano, B., Picogna, G., Hartmann, L., and Rodenkirch, P. J. (2020). The interpretation of protoplanetary disc wind diagnostic lines from X-ray photoevaporation and analytical MHD models. , 496(1):223–244.

Weber, M. L., Ercolano, B., Picogna, G., and Rab, C. (2022). The interplay between forming planets and photoevaporating discs I: forbidden line diagnostics. , 517(3):3598–3612.

Weigelt, G., Grinin, V. P., Groh, J. H., Hofmann, K. H., Kraus, S., Miroshnichenko, A. S., Schertl, D., Tambovtseva, L. V., Benisty, M., Driebe, T., Lagarde, S., Malbet, F., Meilland, A., Petrov, R., and Tatulli, E. (2011). VLTI/AMBER spectro-interferometry of the Herbig Be star MWC 297 with spectral resolution 12 000. , 527:A103.

Whelan, E. T., Pascucci, I., Gorti, U., Edwards, S., Alexander, R. D., Sterzik, M. F., and Melo, C. (2021). Evidence for an MHD Disk Wind via Optical Forbidden Line Spectroastrometry. , 913(1):43.

White, R. J. and Ghez, A. M. (2001). Young Binary Stars in Taurus-Auriga. In Zinnecker, H. and Mathieu, R., editors, *The Formation of Binary Stars*, volume 200, page 332.

White, R. J. and Hillenbrand, L. A. (2004). On the Evolutionary Status of Class I Stars and Herbig-Haro Energy Sources in Taurus-Auriga. , 616(2):998–1032.

Wilson, T. J. G., Matt, S., Harries, T. J., and Herczeg, G. J. (2022). Hydrogen emission from accretion and outflow in T Tauri stars. , 514(2):2162–2180.

Wojtczak, J. A., Tessore, B., Labadie, L., Perraut, K., Bouvier, J., Dougados, C., Nowacki, H., Soulain, A., Alécian, E., Pantolmos, G., Ferreira, J., Straubmeier, C., and Eckart, A. (2024). The interplay between disk wind and magnetospheric accretion mechanisms in the innermost environment of ru lup.

Zanni, C. and Ferreira, J. (2013). MHD simulations of accretion onto a dipolar magnetosphere. II. Magnetospheric ejections and stellar spin-down. , 550:A99.